

# Compressor Rotating Stall, Surge, and Its Control

Lead Guest Editor: Feng Lin

Guest Editors: Ronald Mailach, Yutaka Ohta, and Pietro Zunino



---



## **Compressor Rotating Stall, Surge, and Its Control**

International Journal of Rotating Machinery

---

## **Compressor Rotating Stall, Surge, and Its Control**

Lead Guest Editor: Feng Lin

Guest Editors: Ronald Mailach, Yutaka Ohta, and Pietro Zunino



Copyright © 2018 Hindawi. All rights reserved.

This is a special issue published in "International Journal of Rotating Machinery." All articles are open access articles distributed under the Creative Commons Attribution License, which permits unrestricted use, distribution, and reproduction in any medium, provided the original work is properly cited.

## **Editorial Board**

H. Joon Ahn, Republic of Korea  
Ryoichi Samuel Amano, USA  
Sourabh V. Apte, USA  
Farid Bakir, France  
Hans Joerg Bauer, Germany  
Gerard Bois, France  
Christopher Earls Brennen, USA  
Alessandro Corsini, Italy  
Luis Gato, Portugal

Awatef Hamed, USA  
Jechin Han, USA  
Hooshang Heshmat, USA  
Dimitrios T. Hountalas, Greece  
Norihiko Iki, Japan  
Tariq Iqbal, Canada  
Funazaki Ken-ichi, Japan  
Akira Murata, Japan  
M. Razi Nalim, USA

Eddie Ng Yin Kwee, Singapore  
Yutaka Ohta, Japan  
Ion Paraschivoiu, Canada  
Paolo Pennacchi, Italy  
Sergio Preidikman, USA  
Meinhard T. Schobeiri, USA  
Terrence W. Simon, USA  
Seung Jin Song, Republic of Korea

# Contents

## Oscillatory Tip Leakage Flows and Stability Enhancement in Axial Compressors

Feng Lin  and Jingyi Chen

Review Article (14 pages), Article ID 9076472, Volume 2018 (2018)

## Observations of the Growth and Decay of Stall Cells during Stall and Surge in an Axial Compressor

Adam R. Hickman and Scott C. Morris

Research Article (11 pages), Article ID 6329382, Volume 2017 (2018)

## Observations on Rotating Instabilities and Spike Type Stall Inception in a High-Speed Multistage Compressor

Johannes Schreiber, Benoit Paoletti, and Xavier Ottavy

Research Article (11 pages), Article ID 7035870, Volume 2017 (2018)

## Investigation of Performance and Rotor Tip Flow Field in a Low Speed Research Compressor with Circumferential Groove Casing Treatment at Varying Tip Clearance

Matthias Rolfs, Martin Lange, and Ronald Mailach

Research Article (14 pages), Article ID 4631751, Volume 2017 (2018)

## Transition Process from Diffuser Stall to Stage Stall in a Centrifugal Compressor with a Vaned Diffuser

Nobumichi Fujisawa and Yutaka Ohta

Research Article (13 pages), Article ID 2861257, Volume 2017 (2018)

## Experimental and Numerical Investigations of Surge Extension on a Centrifugal Compressor with Vaned Diffuser Using Steam Injection

Chuang Gao, Weiguang Huang, Tianhua Zheng, Kang Yang, Haosen Yang, and Yun Cao

Research Article (16 pages), Article ID 9159516, Volume 2017 (2018)

## Active Flow Control in a Radial Vaned Diffuser for Surge Margin Improvement: A Multislot Suction Strategy

Aurélien Marsan, Isabelle Trébinjac, Stéphane Moreau, and Sylvain Coste

Research Article (12 pages), Article ID 4120862, Volume 2017 (2018)

## Application of System Identification for Modeling the Dynamic Behavior of Axial Flow Compressor Dynamics

Marco P. Schoen and Ji-Chao Lee

Research Article (14 pages), Article ID 7529716, Volume 2017 (2018)

## Review Article

# Oscillatory Tip Leakage Flows and Stability Enhancement in Axial Compressors

Feng Lin  and Jingyi Chen

*Institute of Engineering Thermophysics, Chinese Academy of Sciences, Beijing, China*

Correspondence should be addressed to Feng Lin; [fenglinfenglin@hotmail.com](mailto:fenglinfenglin@hotmail.com)

Received 20 April 2017; Revised 7 October 2017; Accepted 14 December 2017; Published 6 June 2018

Academic Editor: Paolo Pennacchi

Copyright © 2018 Feng Lin and Jingyi Chen. This is an open access article distributed under the Creative Commons Attribution License, which permits unrestricted use, distribution, and reproduction in any medium, provided the original work is properly cited.

Rotating stall axial compressor is a difficult research field full of controversy. Over the recent decades, the unsteady tip leakage flows had been discovered and confirmed by several research groups independently. This paper summarizes the research experience on unsteady tip leakage flows and stability enhancement in axial flow compressors. The goal is to provide theoretical bases to design casing treatments and tip air injection for stall margin extension of axial compressor. The research efforts cover (1) the tip flow structure at near stall that can explain why the tip leakage flows go unsteady and (2) the computational and experimental evidences that demonstrate the axial momentum playing an important role in unsteady tip leakage flow. It was found that one of the necessary conditions for tip leakage flow to become unsteady is that a portion of the leakage flow impinges onto the pressure side of the neighboring blade near the leading edge. The impediment of the tip leakage flow against the main incoming flow can be measured by the axial momentum balance within the tip range. With the help of the theoretical progress, the applications are extended to various casing treatments and tip air recirculation.

## 1. Background and Motivation

Modern high-performance axial compressors in gas turbines, especially in aeroengines, are mostly unshrouded due to the high rotating speed of the shafts, which means that the tip clearance is necessary. The tip clearance brings additional complication into the corner of rotor blade and the casing. In 1996, Lakshminarayana [1] published a comprehensive illustration on the flow structures within rotor blade passages. The shock, the tip leakage flow (TLF), and the tip leakage vortex (TLV) are the three flow structures that are unique to the blade tip region. Two boundary layers, the end-wall boundary layer at casing and the blade surface boundary layer, provide a battle ground for all these flows interacting with each other. Please note that TLF is different from TLV in that in some cases only a portion of the TLF would be revolved into TLV and the rest of the TLF would either mix with the incoming main flow or leak again through the tip gap of the neighboring blade.

Lakshminarayana's illustration is meant to present the situation at compressor's design condition. It would become

even more complicated when the compressor is throttled to close-to and near stall conditions, which will be the main theme of this paper. The tip clearance not only changes the flows structures at the design condition but also alters the Stall Inception and stalling behaviors. We noticed the debate on whether or not the stalling mechanism requires a nonzero tip clearance. Vo et al. [2] hypothesized that spikes (one of the two basic types of stall precursors) emerged when the interface between the TLF and the main flow spilled out of the leading edge of rotor blade. This hypothesis thus can only be true when the tip clearance is not zero. Pullan et al. [3] argued that spikes can be recognized as a vortex tube spanning from blade's suction surface near the tip to the casing, a result of blade leading edge separation due to high incident angle of the incoming main flow, which can happen even with zero tip clearance.

As a matter of fact, most modern axial compressors are tip critical; that is, their rotating stall is initiated at the tip region. In other words, as long as the tip clearance is not zero, the tip leakage flow takes part in Stall Inception process. Thus, the hypothesis from either side of the debate is applicable to the

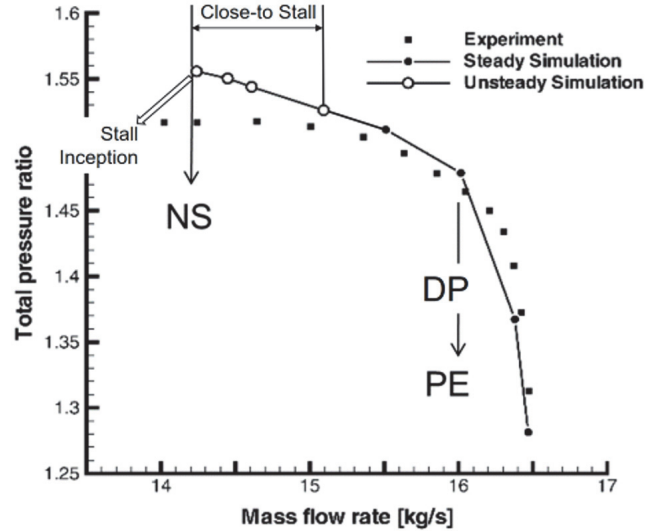
compressors we are dealing with daily. Pullan's argument, the flow separation at rotor blade's suction surface near leading edge as the cause of the rotating stall, is a continuation of the traditional Emmons' model [4] that is widely accepted in engineering practices.

More than ten years ago, we started to study the tip flow structures at near stall and estimate the location of the interface between the incoming main flow (MF) and TLF. At first, we were able to repeat the finding of others [4–7] that TLF would become oscillatory at operating points close to stall limit, while the whole compressor is completely stable. This brings an unexpected benefit, making the tip air injection become closed-loop without sensing spikes. We then realized that this had been done several years before us without knowing the existence of the oscillatory tip leakage flow [8–10]. In order to estimate the MF/TLF interface location, axial momentum equation within the tip region was then integrated over a sequence of control volumes, which ended up with a curve of cumulative axial momentum distribution along blade's axial chord. This curve resembles a bell shape, whose peak point marks the “boundary” between main flow dominated region and the TLF dominated region. This makes it possible to compare the ability to extend the stall margin for various casing treatments, which is very helpful in screening out of bad designs from a large pool of casing treatment candidates in early design stage.

Note that the purpose of this paper is not to review the entire research field of compressor instability. Day [11] presented an excellent review recently as a Scholarly Lecture in the annual conference of International Gas Turbine Institute in 2017. In this paper, the tip leakage flow structure at close-to and near stall is reviewed in Section 2, followed by the features of oscillatory TLF in both low- and high-speed compressors (Section 3). The role of axial momentum and the “bell-shaped” curve are explained in Section 4. The applications of both the “bell-shaped” curve and the oscillatory TLF are reviewed in Section 5. Conclusions are given in the last section for convenience, together with discussions on future work.

## 2. The Tip Leakage Flow Structure in Close-to and Near Stall

It is necessary to clarify a few terms before reading further. As a compressor is throttled from large flow rate to stall, it would experience several steps. Figure 1 illustrates them along a typical compressor characteristic. Several points are identified in the figure. The point of peak efficiency (PE) is where the efficiency reaches the maximum, while the design point (DP) is the point that the compressor is designated to work. While these two often referred to the same point, there are occasions where these two are different. For instance, when a compressor has to work on a designated flow rate to match the other components in the same system (e.g., a gas turbine), its DP would be different from PE. For the cases studied in this paper, DP and PE are the same because all the cases are single rotors. This ensures that the flow angles around the blade are well organized, which forms a fair ground for comparison against the rest of the off-design points.



“Stall Inception” is very important, as stall precursors only happen in Stall Inception. Near stall is a point that belongs to the segment of close-to Stall, in which no spike would be formed yet. Therefore, according to the opinion of this paper’s authors, the oscillation of tip leakage vortex or the Rotating Instability is NOT part of Stall Inception, although it may trigger spikes or modal waves that later eventually initiate rotating stall.

The flow structure in the tip region is the key to understand the mechanism behind the flow phenomena. The early efforts included Adamczyk et al. (1993) [20] and Suder and Celestina (1996) [21]. At off design conditions, a large “blockage,” that is, a low-energy region within the blade passage, was found due to vortex breakdown caused by the shock. Their excellent work was so much ahead of their time that no much more knowledge in this regard had been gained since then until unsteady oscillatory TLF was found and confirmed.

The modern powerful tools of unsteady Navier-Stokes solvers empower us to revisit this flow structure at a level much closer to stall and from a viewpoint of unsteady flow. One of the rotors was Darmstadt Rotor 1, which is a transonic rotor of a single-stage transonic compressor rig at Technische Universität Darmstadt [22, 23]. The comparison of experimental and computational characteristics is depicted in Figure 1 [12]. Note that the steady simulation fits well with the test curve. While overpredicting the total pressure rise up to 2.5%, the unsteady simulation was able to make the computed stall limit very close to that of the test result (less than 1.5% of the test flow rate at stall). Figure 2 depicts the regions of influences by tip leakage flows. At PE, the loading is distributed over about 80% of the blade chord. The shock is attached to the leading edge and the tip leakage vortex flows out of the blade passage. At NS, the loading fluctuates within the first half of the blade chord. The shock is detached from the blade leading edge and interacts with the tip leakage vortex, causing a large “blockage” as seen in Adamczyk’s paper [20]. Note that the pictures at NS are only one instant of the oscillatory movement.

Particles were released within the tip gap to trace the trajectories of TLF in numerical results. Figure 3 compares them at PE and at one of the instants at NS. They are the 3D views of those in Figure 2. For the one at NS, a schematic is plotted in Figure 4 to summarize the flows at NS for clarity. It can be seen that the TLF are divided into two parts along the blade chord based on the location of shock on the suction surface. The first portion of TLF forms the vortex core and flows through the blade passage, while the second portion goes across the blade passage and hits the pressure side of the neighboring blade. It then splits there, a part of which leaks over the blade tip one more time.

### 3. The Unsteady Features of Oscillatory Tip Leakage Flow

The fact that the tip leakage vortex impinges the pressure side of the neighboring blade is believed to be one of the necessary conditions for TLF oscillation. Deng et al. [7] were the first to notice this in our research group when simulating

a low-speed rotor. This had later been observed in several other compressor rotors, including Darmstadt Rotor 1 as shown in Figures 2 and 3 and NASA Rotor 67 in Figure 5. The top row of Figure 5 lists six instantaneous contours of static pressure coefficients with the last one almost exactly repeating the first one. The bottom row is the corresponding pressure coefficient distribution in the pressure side of the blade. The low-pressure spot on the pressure side is marked as A1, which is clearly casted by the low pressure core of the tip leakage vortex. At time 0/30T, where “T” represents the time interval to store data set by the time-accurate CFD solver, A1 is located at the leading edge. Because of it, the pressure difference across the tip clearance is low, which weakens the tip leakage vortex and pushes the TLF/MF interface downstream. As time goes on (e.g., at 20/30T and 30/30T), the low-pressure spot A1 moves towards the trailing edge, while the high pressure regains its control on the leading edge causing the first half of the TLF/MF interface to swing back. Close to the end of one period, the low-pressure spot A1 moves out of the blade chord, the TLF/MF interface returns to its starting position, and a new A1 emerges at the leading edge of the pressure side. The entire process repeats. The frequency of this oscillation is calculated as 0.586 BPF (Blade Passing Frequency) for this particular rotor in rotor relative frame.

The features of the aforementioned unsteady process were observed in compressor experiments. The first feature was that the location of the highest amplitude should be at the leading edge of the pressure side, neither at the spot where the shock/vortex interact nor at the shock itself. It is not even at the starting place of the tip leakage vortex. Figure 6 depicts the comparison of the root mean square (RMS) of static pressure distribution at casing. The left was the result of phase-locked RMS obtained from experiments of Darmstadt Rotor 1, while the right was the numerical simulation [12]. Both match well with each other.

The second feature is signature frequency bands of the casing static pressure measurements. Figure 7 demonstrates the relation between rotating relative frame and the casing stationary frame using numerical results. The top row shows the time series and its frequency spectrum for a probe fixed on the rotor relative frame. The first peak at 3056.68 Hz or 0.57 BPF is the main frequency and the second peak is its harmonic. The second row is the data taken from a probe at the same axial location but fixed on the casing. The frequency components are much richer due to the modulation of frequencies between the relative frame and the rotor rotating frame. Figure 8 compares the frequency spectra between the experiments and CFD simulations [12]. Note that the test results contain noises from turbulent, the variations of the blade geometry and/or assembly, and so forth; thus the frequency spectra appear as a few signature bands, not as pronounceable individual peaks.

The comparison of the oscillatory TLF introduced here and Rotating Instability as described in [8] is of interest. Since there is no chance to study the compressors that were reported to possess Rotating Instability such as those in [8, 24], we are not able to justify whether or not these two are the same. However, there are at least two features that are common to both phenomena: (1) both embark a

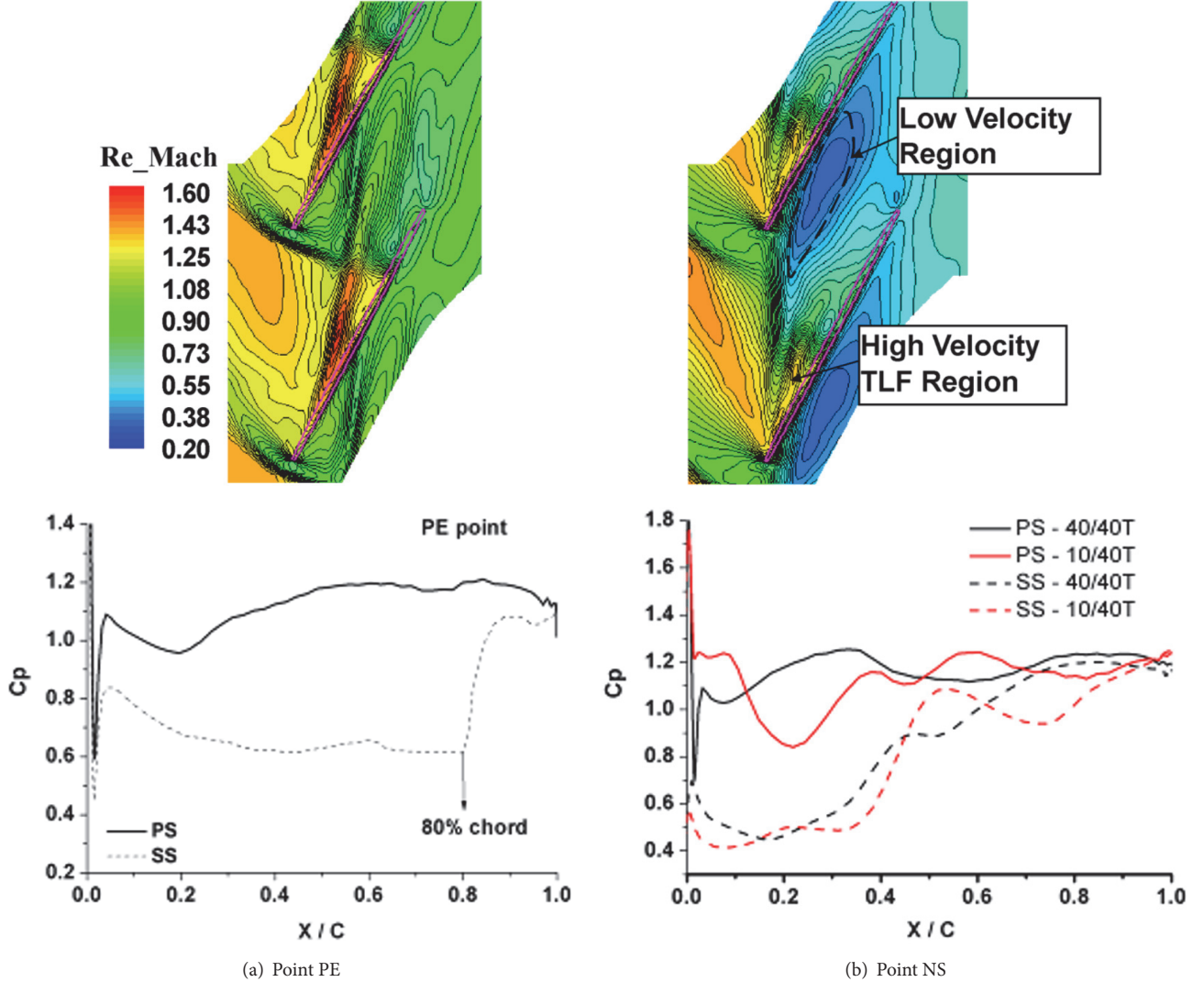


FIGURE 2: The top two pictures show the relative Mach number contours at 99% span, a plane at the middle of the tip clearance, at points PE and NS. The bottom two pictures depict the blade loadings using the surface pressure coefficient distributions along the blade's axial chord. ([12]). Figure reproduced from LIN et al. (2010).

signature frequency band; (2) the frequency band is about 0.5 BPF. Regardless of whether this frequency is measured in the rotor rotating frame or in the casing stationary frame, as long as it is about 0.5 BPF, it would appear as the tip leakage vortices (TLV) alternate their trajectories between neighboring blade passages. That is, when one TLV is within the blade passage, its neighboring one would impinge the blade's pressure surface. Both features were observed in our low-speed compressor.

#### 4. The Role of Axial Momentum and the “Bell-Shaped” Curve

According to Vo's hypothesis [2], it is necessary to be able to estimate the location of the interface between the incoming main flow (MF) and the tip leakage flow (TLF). Since such an MF/TLF interface exists in the rotor's rotating reference frame, how it looks like on the casing stationary reference

frame becomes crucial to experimentists. Cameron et al. [14] demonstrated that on casing the complex 3D curvy oscillatory surface of MF/TLF in the rotor rotating frame can be observed as a straight line on the casing stationary frame, as seen in Figure 9 [14]. This is because, when observed at casing, the spatial and temporal variations within the rotor frame are all naturally averaged. Figure 9(a) depicts the experimental result of the casing streaklines, which was taken from a transparent window when the compressor was operating at Point B. In Figure 9(b), on the left, it is the computational result of one instant showing the streaklines on casing, while on the right the resultant streaklines after spatial and temporal averaged display flow patterns qualitatively the same as those of experiments. The rotor under investigation was the transonic rotor in University of Notre Dame in USA, abbreviated as ND-TAC.

Cameron et al. [14] then proposed a simple model to estimate the location of the MF/TLF interface on casing, as

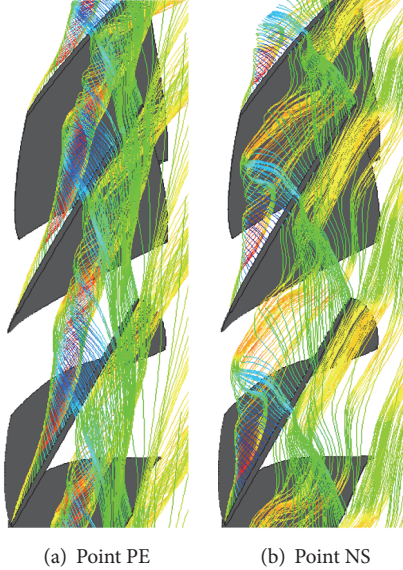


FIGURE 3: Streaklines that depict the TLF structures ([12]). Figure reproduced from LIN et al. (2010).

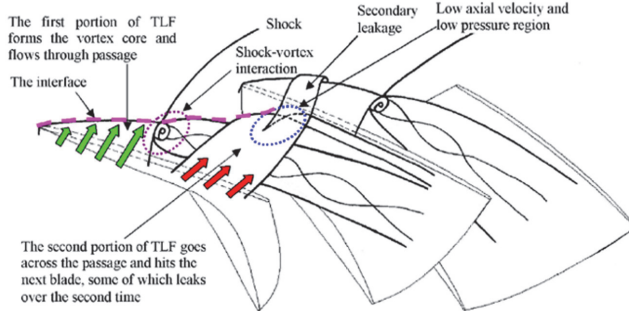


FIGURE 4: The schematic of TLF structure at NS ([12]). Figure reproduced from LIN et al. (2010).

illustrated in Figure 10. The axial momentum equation near the tip clearance was simplified as the balance between the pressure due to main flow and the axial momentum due to tip leakage jet. The details of derivation, which can be found in [14, 15], are omitted here due to the space limitation of this paper. Despite its simplicity, the trend of  $X_{zs}$  versus the compressor's incoming flow coefficient fitted well with that of the throttling process, which suggests that this simple model did capture some physics embedded in the stalling mechanism.

Since the MF/TLF interface is a 3D surface, such as the one in Figure 11, it is not surprising that using  $X_{zs}$  alone is not sufficient to correlate it to stall. A control volume approach is thus proposed to include the 3D effect into a new model [16, 19]. Unfortunately, it is impossible to establish an analytical equation like the one for  $X_{zs}$  due to the complexity of the 3D unsteady flow. The new model is indeed a method of postdata processing based on 3D unsteady Reynolds-Averaged Navier-Stokes solutions. It starts with the same strategy as the  $X_{zs}$  equation: observing the flows within the rotor while sitting

on the casing stationary reference frame. The details can be described below.

Consider a series of discrete control volumes installed at the tip region between the casing and the rotor passage tip as illustrated in Figures 12 and 13. If we integrate all the linear momentum in axial direction, according to the Newton's second law, such an integral would be equal to the total axial force acting on the control volume. Because this is done on a fixed and stationary control volume, it is equivalent to pitch-wise smear the spatial variation. For unsteady cases, the total axial linear momentum at every time instant should first be averaged before spatial integration. The end result is a number representing the net axial force on the control volume, as measured by an observer on casing stationary frame. If this number is positive, it means that the net axial force on this control volume is pushing the fluid downstream. If it is negative, it means that the net force is pushing the fluid upstream. Therefore, the control volume approach proposed here makes the justification of the flow stability become simple. The key is where the net force is zero. The closer this location is to the leading edge, the easier the compressor would run into stall.

The rotor in Figure 12 is NASA Rotor 67. The smooth casing is placed on the left, while the casing treated with 6 grooves is on the right. The bottom row depicts the entropy contours on the suction surface of the blade, indicating the radial depth of influence by the tip leakage flow. This is how the depth of the control volumes is decided. For instance, in the case of Figure 12, the control volumes are taken as deep as up to 90% span. A volumetric illustration of a typical control volume is given in Figure 13. Considering only the axial direction, the momentum equation in a finite control volume form can be written as

$$\int_{z-} P_{z-} dA_- + \int_{z+} P_{z+} dA_+ + \int_{CS} P_{CS} dA_{CS} \Big|_z$$

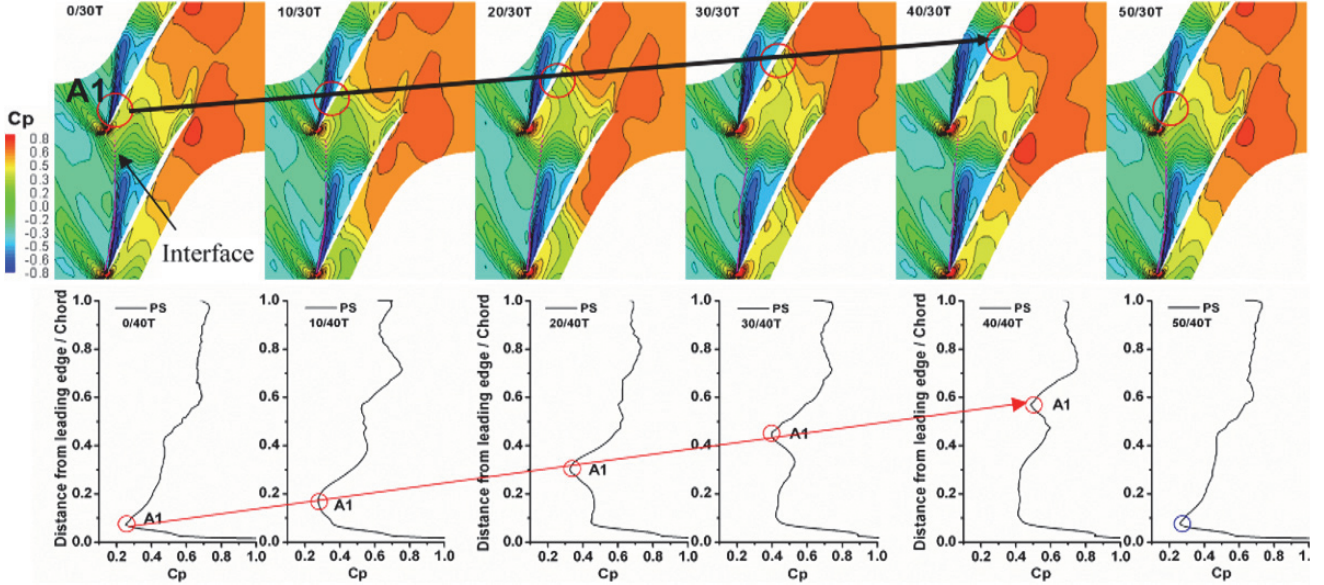


FIGURE 5: Snapshots of 6 instantaneous moments during one period of TLD oscillation for Rotor 67 ([13]). “T” represents the time interval to store the data set by the time-accurate CFD solver. Figure reproduced from DU et al. (2010).

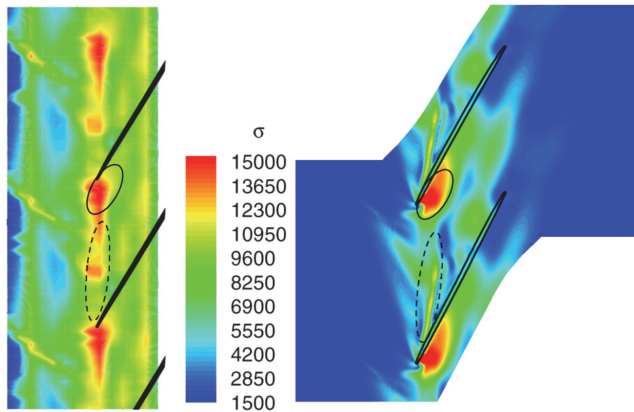


FIGURE 6: Experimental verification of ([12]). Figure reproduced from LIN et al. (2010).

$$\begin{aligned}
 & + \int_{BT} P_{BT} dA_{BT} \Big|_z + \int_{CS} \tau_{CS} dA_{CS} \Big|_z \\
 & + \int_{BT} \tau_{BT} dA_{BT} \Big|_z + F_{blade-Z} \\
 = & \int_{Z_-} \rho W_z (\vec{W} \cdot \vec{n}) dA_{z_-} \\
 & + \int_{Z_+} \rho W_z (\vec{W} \cdot \vec{n}) dA_{z_+} \\
 & + \int_{BT} \rho W_z (\vec{W} \cdot \vec{n}) dA_{BT} \\
 & + \int_{CS} \rho W_z (\vec{W} \cdot \vec{n}) dA_{CS}
 \end{aligned} \tag{1}$$

Here,  $z$  refers to axial direction. Each control volume covers one pitch. The two periodic surfaces of each control volume are ignored in the equation due to the periodic boundary conditions for the single passage simulation.

By adding the right-hand side of the above equation together and averaging it over the oscillation period, we will obtain the net axial momentum (or force) on the control volume. Plotting all the net forces for all the control volumes, we obtain a distribution curve of local net axial momentum (or force) (Figure 14(a)). Two curves in the plot are for peak efficiency (PE) and near stall (NS) points, respectively. The location where the net momentum is zero for PE is at 38% axial chord, while the one for the NS is at 14%, much closer to leading edge as expected. In Figure 14(b), the curves of cumulative axial momentum for both the smooth casing (SC) and the 6-groove casing treatment (CG6 as in Figure 12) at the NS point of SC are given (the comparison between them will be explained later). The cumulative axial momentum is equal to the cumulative distribution of the net force acting on the enlarged control volume from the inlet of the first control volume gradually to the outlet of the last control volume on the curve. This cumulative momentum curve reaches its peak at which the local momentum curve crosses the zero. After that, the local momentum becomes negative and the net momentum starts to decrease. Therefore, the curve forms a bell shape. It is thus called “bell-shaped curve” or simply “bell curve” for brevity.

The peak of the bell curve divides the tip region into two. The one in the front (near the leading edge) is dominated by the incoming main flow, while the other one on the back is dominated by the tip leakage flow. The location of the peak is more valuable than the peak value itself because the peak value involves the blade force that is so complicated that it is hard to explain the meaning of the peak value in general. If needed, it has to be carefully examined case by case.

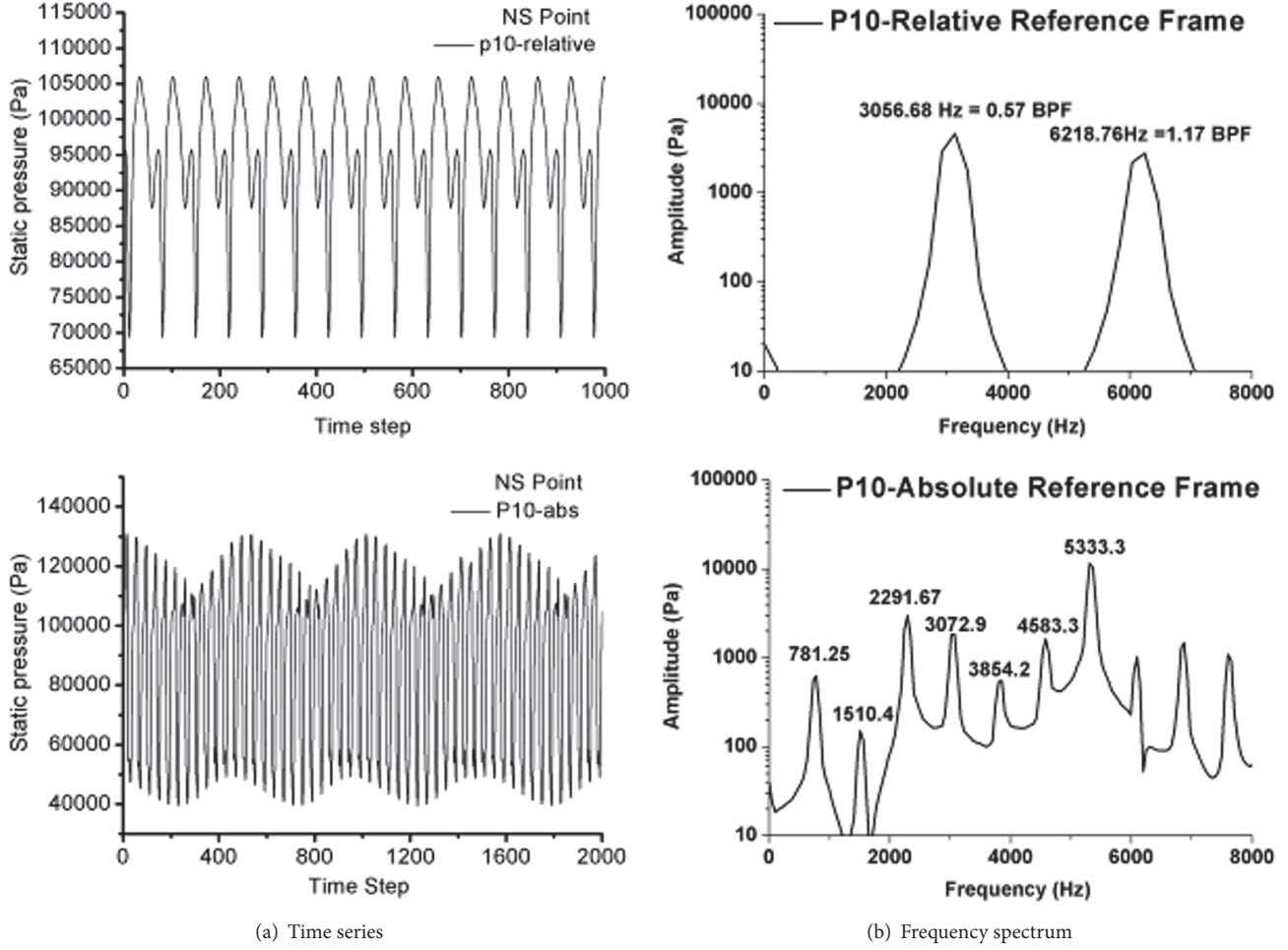


FIGURE 7: The relation between relative and absolute frames at NS ([12]). Figure reproduced from LIN et al. (2010).

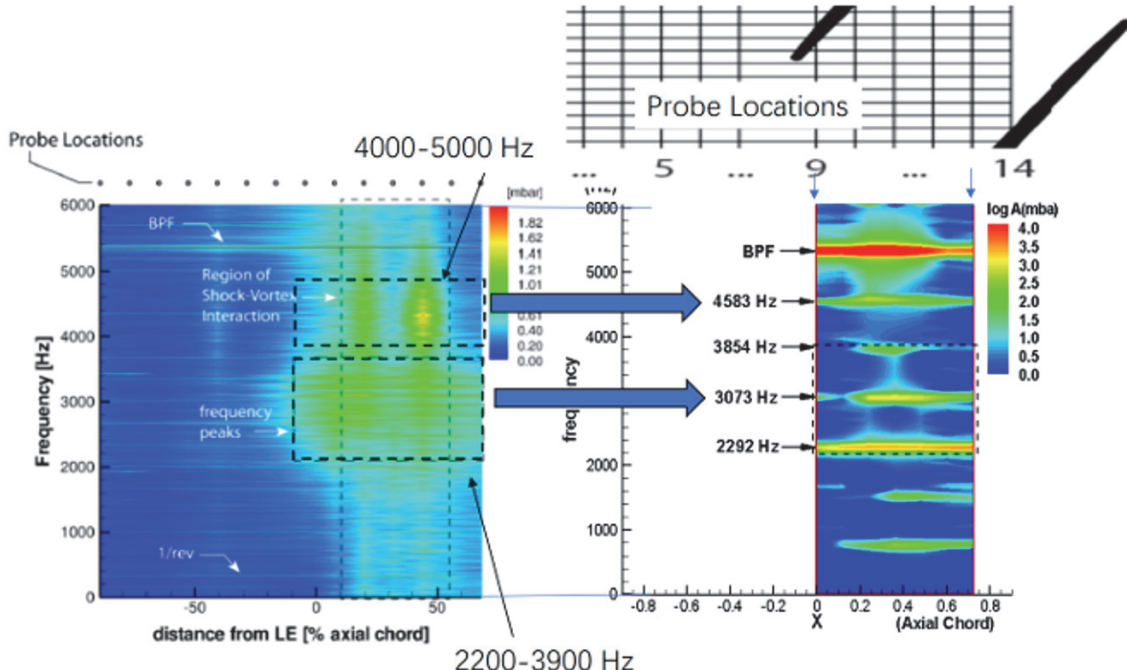


FIGURE 8: The comparison of frequency spectra between experiments (left) and simulations (right) at NS ([12]). Figure reproduced from LIN et al. (2010).

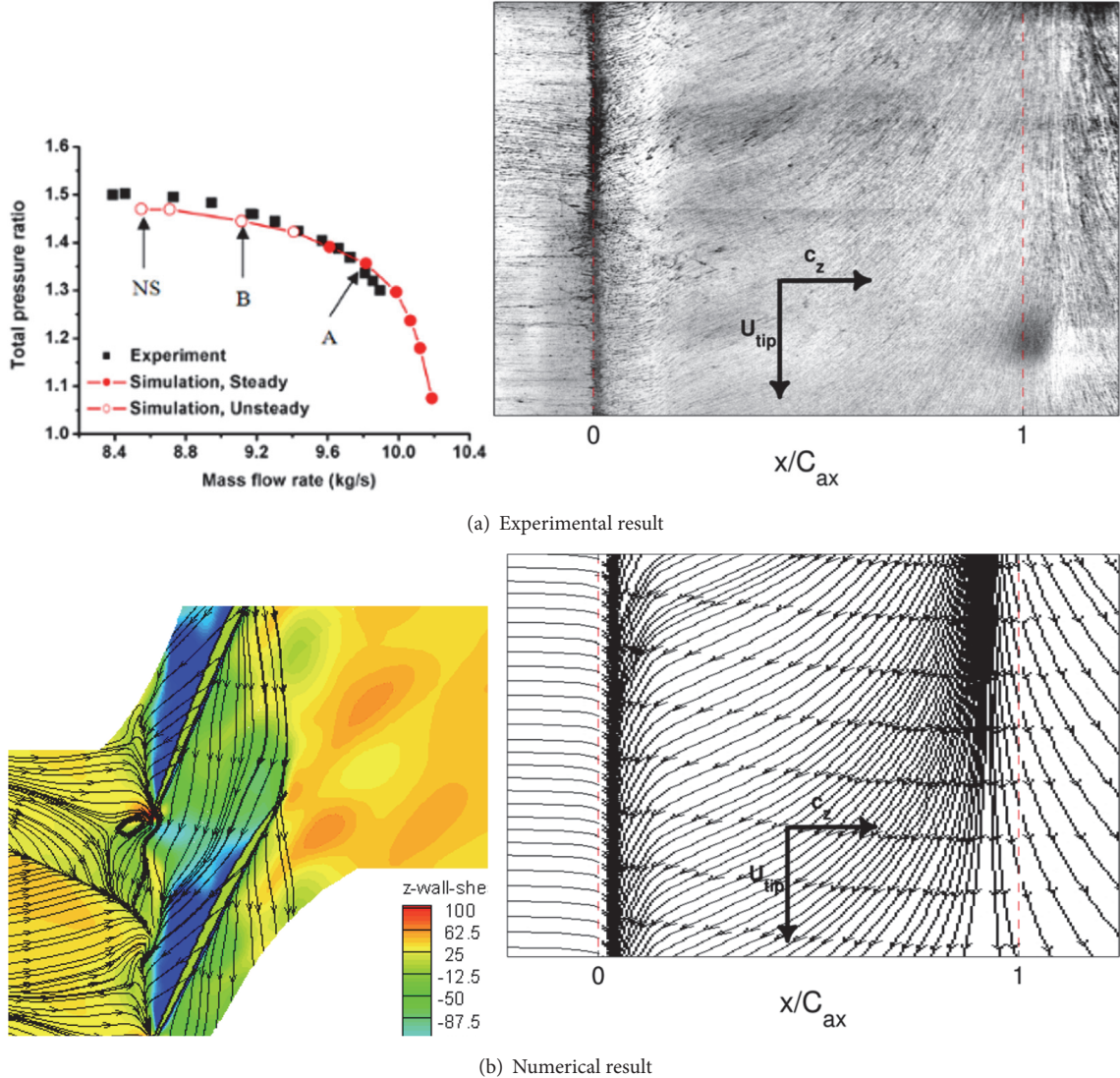


FIGURE 9: The MF/TLF interface as observed in the rotor rotating frame and at casing stationary frame ([14]). Figure reproduced from CAMERON et al. (2013).

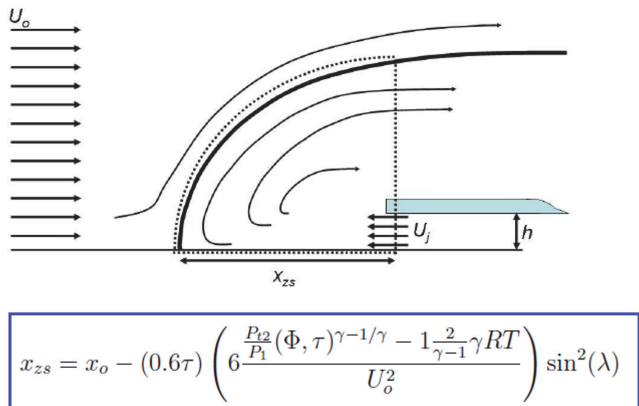


FIGURE 10: The simplified model of axial momentum balance on casing and its vicinity (illustrated based on the information in [15]). Figure reproduced from BENNINGTON et al. (2008).

To demonstrate the usefulness of the bell curves, seven points were chosen on the same characteristic of Rotor 67 and seven bell curves were generated, which corresponded to the throttling process of the rotor [16]. Figure 15 depicts the results. One can see that the locations of the peak move exactly as expected towards the leading edge monotonically as the rotor is throttled to near stall.

Figure 14(b) also depicts the comparison of the two bell curves for the smooth casing and the treated casing, respectively. Both are at the same flow coefficient, that is, the near stall point of smooth casing. It is clear that the 6-groove casing treatment is able to move the peak location further downstream compared to the smooth casing. Therefore, one can predict that the CG6 would extend the stall margin of the rotor by comparing the bell curves at the near stall point with smooth casing, without even being numerically calculated to CG6's own stall limit. The

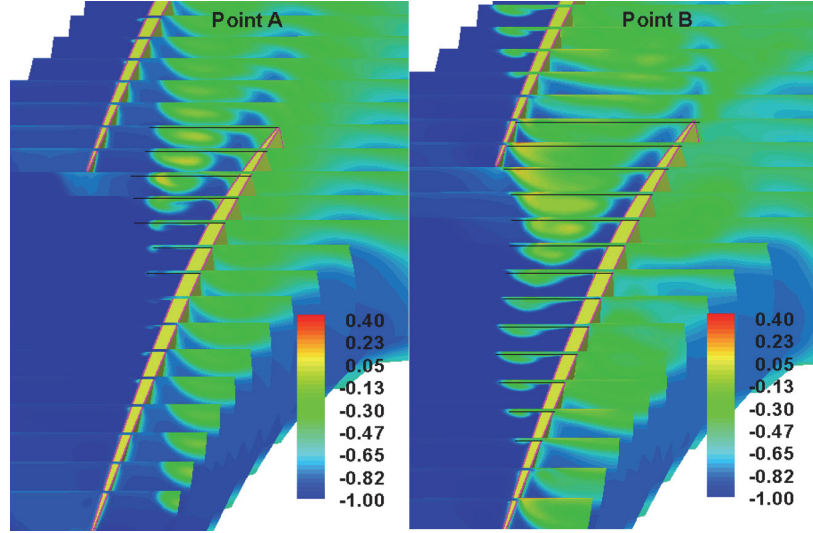


FIGURE 11: The axial-radial slices of entropy contours that show the 3D complex surface of MF/TLF interface ([14]). Points A and B are the ones marked on the left of Figure 9(a). Figure reproduced from CAMERON et al. (2013).

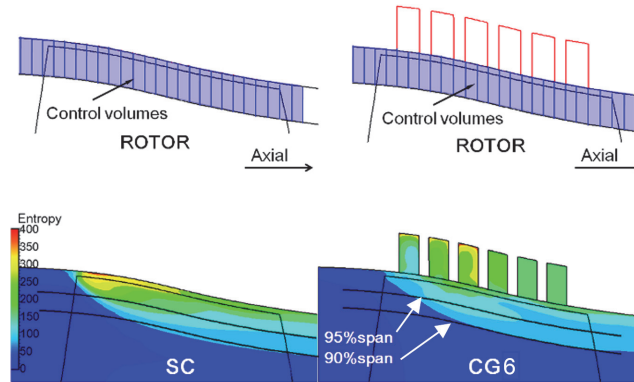


FIGURE 12: The installment of control volumes ([16]). Figure reproduced from NAN et al. (2014).

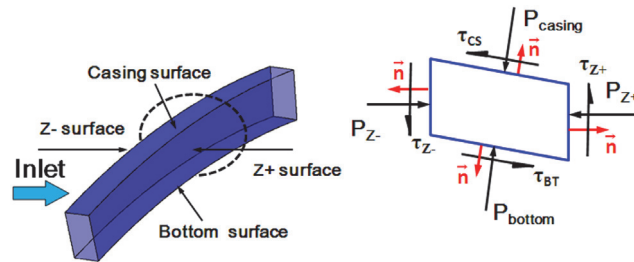


FIGURE 13: The volumetric illustration of typical control volumes ([16]). Figure reproduced from NAN et al. (2014).

feature could greatly reduce the need of unsteady CFD simulations when it comes to design or optimize casing treatments.

Both Figures 14 and 15 are CFD results. In the next section, we will provide examples that have experimental results to validate the bell curves and demonstrate how they can be used in design or optimization of casing treatments and tip air injections. However, it must be noted that the idea of bell curves relies on the hypothesis that rotating stall would

be triggered by the MF/TLF interface spillage out of the rotor leading edge. There is at least one counter example. Houghton et al. [25] showed that when testing the effect of single groove's axial location on the stall margin improvement (SMI), there are two peaks on the curve of SMI versus axial chord. The hypothesis of MF/TLF spillage cannot explain what happens in this case. However, other than this special case, the method of bell curves works well with many stability enhancement techniques.

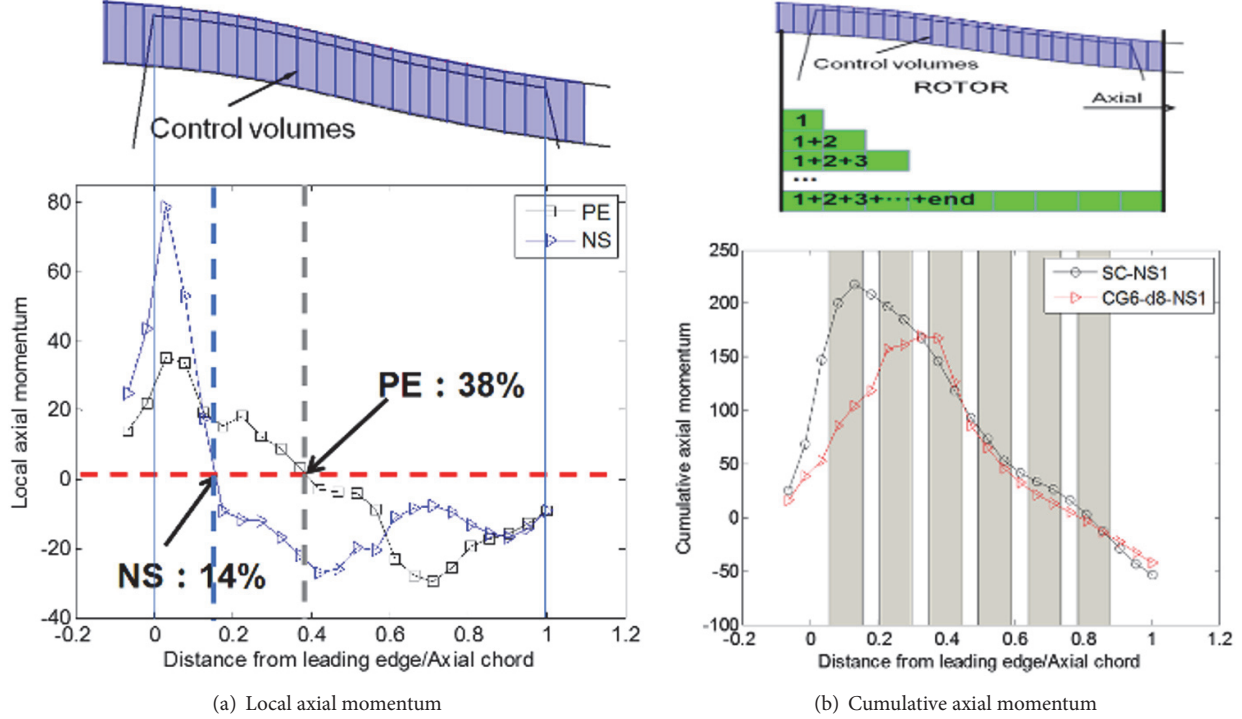


FIGURE 14: The net axial momentum distributions ([16]). Figure reproduced from NAN et al. (2014).

## 5. The Examples of Application

In this section, we will demonstrate how to apply the bell curves to design or optimize stability enhancement techniques. Every example had been experimentally validated.

**5.1. Casing Grooves.** The experimental data of the first example is taken from Ross [26], in which a set of casing grooves were tested. There are three grooves available on the especially decided casing (called variable casing treatment, or VCT). One can open or block any of the grooves to make 7 combinations of casing grooves, which are marked as 001, 010, and so forth on Figure 16. Number 1 means that the groove is open and number 0 means that the groove is closed. The seven SMIs together with that of the smooth casing were listed in Figure 16. The total eight bell curves were calculated and plotted together in one chart. The SMIs can be grouped into four groups, A, B, C, and D, each of which corresponds to two cases of casing grooves that exhibit similar SMIs. The order of SMI groups is A>B>C>D. The eight bell curves can also be grouped into four groups, each of which contains two bell curves whose peaks located almost at the same axial location. Furthermore, the order of the four groups of peaks along the axial chord corresponded EXACTLY to the order of SMI groups. The bell curves were plotted based on the CFD results at the same incoming flow coefficient as the NS point of smooth casing. At this point, the flow fields in most of the cases with grooves were still steady, which saved lots of computation time and expenses.

**5.2. Skewed Axial Slots.** Four skewed axial-slot casing treatments with different geometries were chosen to check the applicability of the bell curve (Table 1), which were named as CT-a, CT-b, CT-c, and CT-d for short. The data were taken from a large-scale low-speed compressor test rig [18]. In this study, each individual slot component covers exactly the tip chord of the blade and has a skew angle of 60° along the same direction of blade rotation. The depth of all slots is 10 mm. The comparison of the bell-shaped curves for these four CTs is shown in Figure 17. The experimental results are listed in Table 1. The trend of those peaks of the bell curves matches very well with the trend of SMIs.

**5.3. Tip Air Injection with Self-Recirculation.** Up to this point, the experiments were done prior to CFD and the bell curves, so the results were used for validation purposes. Hereby we are giving an example where the bell curves were done before the experiments and predicted the test results of SMI. A type of casing treatment (SELF-INJ), which recirculates the air from the trailing edge into the leading edge, was designed as shown in Figure 18. A high-fidelity time-resolved CFD simulation was done to predict its SMI by gradually rising the back pressure. The stall limit was recognized as the last point before the CFD collapsed. At the same time, the same CFD result at the near stall point of the smooth casing was used to construct the bell curve and compare it with those of the smooth casing, a double-grooved casing (generated separately for another paper [16]), a five-grooved casing, and a SAS casing. The resultant bell curves are depicted in

TABLE 1: The effectiveness for different axial slot schemes.

Configurations	Slots /passage	Slot width (% of $C_{ax}$ )	<b>SMI (EXP)</b>	
	CT-a	7	15%	<b>8.2%</b>
	CT-b	5	15%	<b>6.6%</b>
	CT-c	7	7.5%	<b>1.8%</b>
	CT-d	17	5%	<b>5.4%</b>

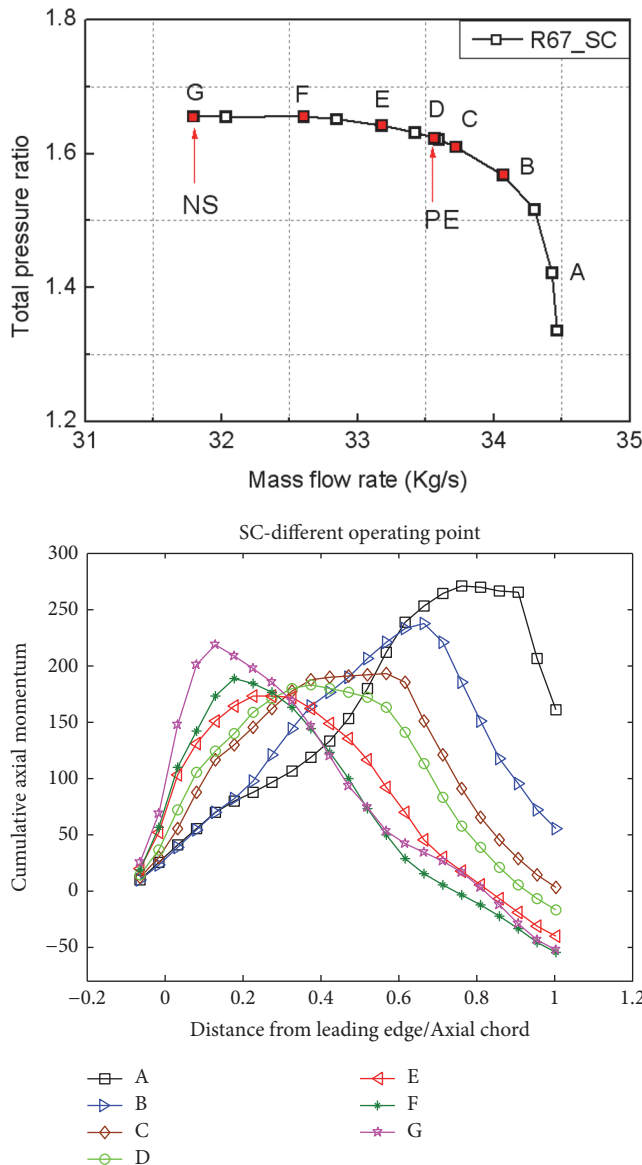


FIGURE 15: The bell curves during the throttling process of Rotor 67 ([16]). Figure reproduced from NAN et al. (2014).

TABLE 2:  $Z_{bp}$  in bell-shaped curves and the experimental SMI [19].

End-wall treatment	$Z_{bp}$	$\Delta Z_{bp}$	Experimental SMI
SC	0.273	-	-
SELF-INJ	0.341	0.068	5.26%
Double-groove CG13	0.274	0.064	5.28%
CG5	0.409	0.136	10.8%
SAS	0.544	0.271	27.4%

Figure 19 [19], which predicted that the SMI of SELF-INJ should be similar to the double-grooved CG13 (not shown in the figure), much less than the other two casing treatments. The test results are given in Table 2 [19], which confirmed the prediction in Figure 19.

## 6. Summary and Future Work

Research on oscillatory TLF and its applications are reviewed in this paper. The oscillatory TLF is a phenomenon that has been observed and studied by many researchers. As one of the research teams worldwide, we offered both CFD and test results and explained them from a view angle of flow structure at near stall. Since the oscillation of TLF was considered as a consequence of the axial momentum imbalance, a novel control-volume-based method, the bell curve, is proposed to estimate the axial momentum balance between the main flow and the tip leakage flow. The bell curve was then applied to make comparison of SMIs for various casing treatment methods and other stability enhancement methods that involve tip leakage flows.

These research efforts have been centered on one single purpose, that is, enlarging the stall margin of axial compressors. However, towards this goal, there is still a long way to go. Four ideas are proposed here for future research:

- (1) Momentum transport in radial direction from PE to NS
- (2) Identification of critical stage in multistage environment

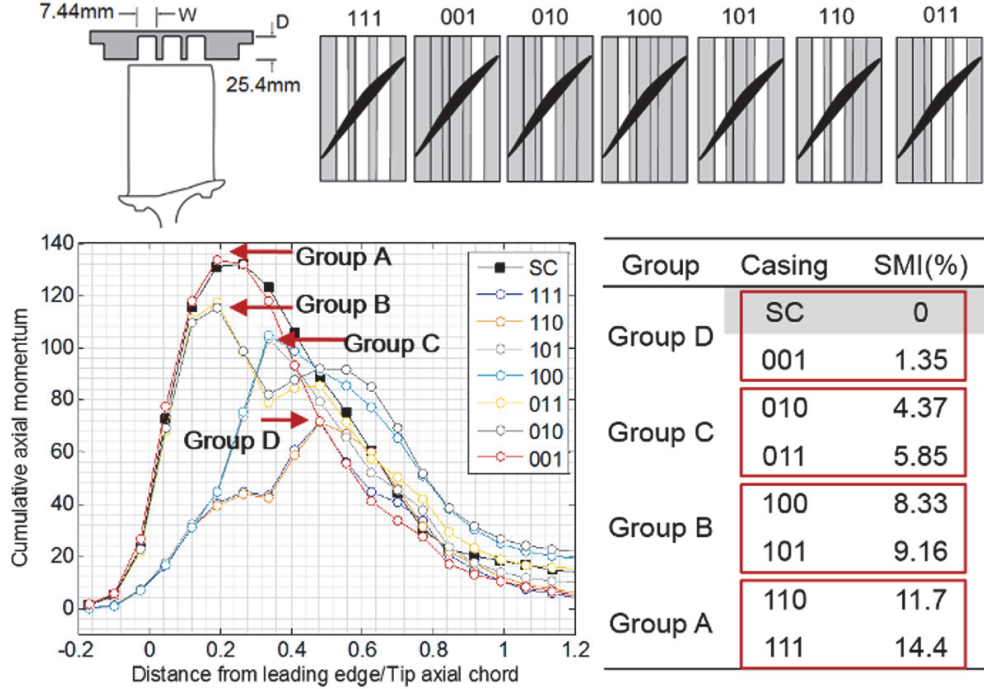


FIGURE 16: The bell curves for prediction of VCT ([17]). Figure reproduced from NAN (2014).

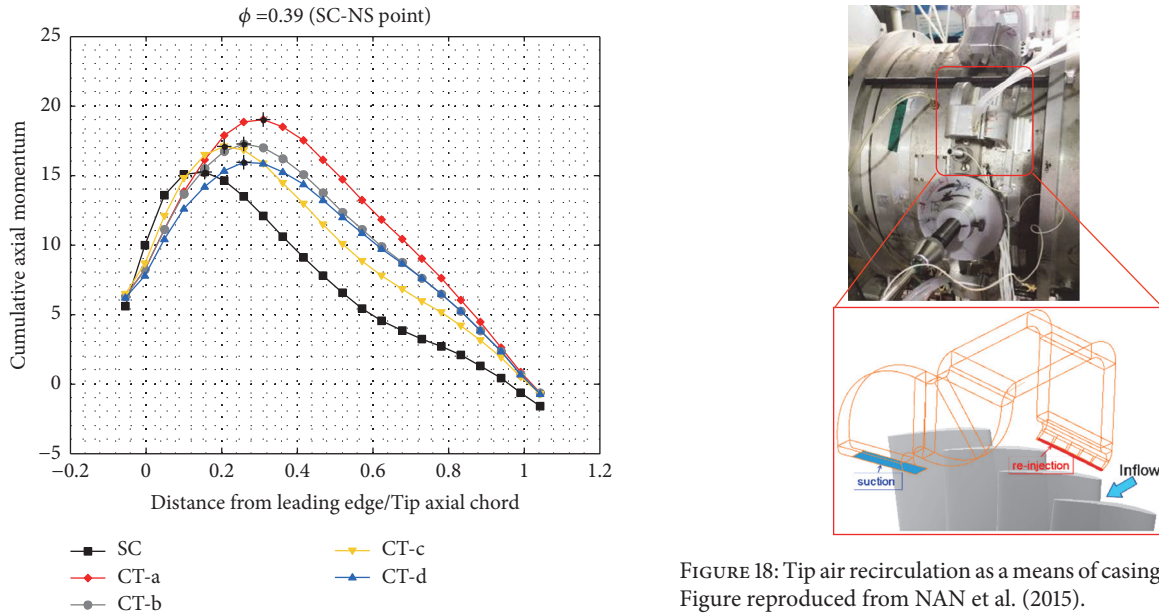


FIGURE 17: The bell-shaped curves for the four different axial-slots configurations together with that of the smooth casing ([18]). Figure reproduced from MA (2016).

- (3) Integrated optimization of casing treatment and blade design for high-pressure compressors
- (4) Active control of heavily loaded low-pressure compressors

The first idea is to extend the momentum analysis from tip region to all radial section of the blade span through the

throttling process from PE to NS. It will help to understand the blade loading transition as a compressor approaches to stall. The second is to extend the current research from single rotors to multistages. These two ideas are basic research. The third and fourth ideas are for high-pressure compressor and low-pressure compressor, respectively. They are the applications of the first two ideas, with a hope to design safer modern compressors.

FIGURE 18: Tip air recirculation as a means of casing treatment ([19]). Figure reproduced from NAN et al. (2015).

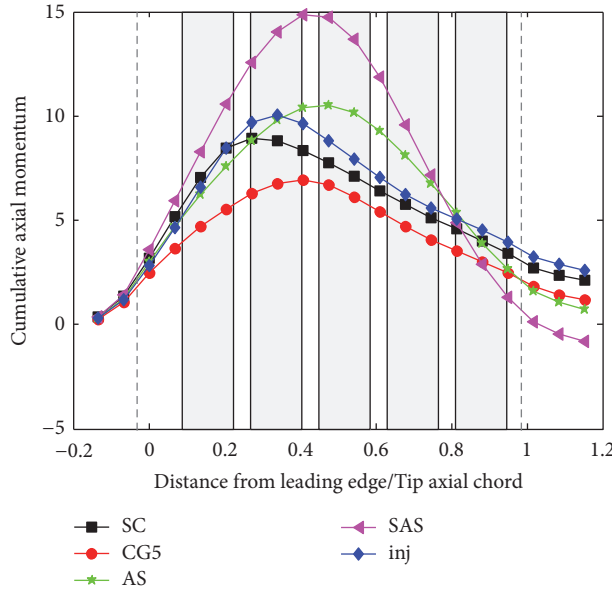


FIGURE 19: The bell-shaped curves for the studied casing treatments ([19]). Figure reproduced from NAN et al. (2015).

## Nomenclature

- $\rho$ : Density
- $\sigma$ : Root mean square of static pressure
- $\Phi$ : Mass flow coefficient of compressor
- $\tau$ : Shear stress on solid surfaces
- $A$ : Area
- $C_{ax}$ : Tip axial chord
- $h$ : Tip clearance
- $Mz$ : Axial momentum
- $F$ : Force
- $n$ : Unit vector normal to given surface
- $p$ : Static pressure
- $T$ : Time interval to store data in unsteady CFD
- $U$ : Absolute velocity
- $W$ : Relative velocity
- $X_{zs}$ : Axial location of zero shear region
- $Z$ : Axial direction
- $Z_{pb}$ : Axial location of bell curve peak.

## Superscripts and Subscripts

- $BT$  : Blade tip
- $CS$ : Casing surface
- $j$ : Leakage jet through the tip clearance
- $Z+$ : Positive axial direction
- $Z-$ : Negative axial direction.

## Abbreviations

- BPF: Blade passing frequency
- CFD: Computational fluid dynamics
- CT: Casing treatment
- DP: Design point
- IGTI: International Gas Turbine Institute

MF:	Main flow
NS:	Near stall point
PE:	Peak efficiency point
RMS:	Root mean square
SAS:	Skewed axial slots
SC:	Smooth casing
SFB:	Signature frequency band
SMI:	Stall margin improvement
TLF:	Tip leakage flow
TLV:	Tip leakage vortex
URANS:	Unsteady Reynolds-averaged Navier-Stokes
UTLF:	Unsteady tip leakage flow
VCT:	Variable casing treatment.

## Conflicts of Interest

The authors declare that they have no conflicts of interest.

## Acknowledgments

The support of the National Natural Science Foundation of China through Grants no. 51676184 and no. 51606189 is acknowledged. The authors thank many colleagues and former students at Chinese Academy of Sciences who have contributed and are still contributing their efforts to enrich this ongoing research experience.

## References

- [1] B. Lakshminarayana, *Fluid Dynamics and Heat Transfer of Turbomachinery*, John Wiley & Sons, 1995.
- [2] H. D. Vo, C. S. Tan, and E. M. Greitzer, “Criteria for spike initiated stall,” *ASME Journal of Turbomachinery*, vol. 130, no. 1, Article ID 011023, 2008.
- [3] G. Pullan, A. M. Young, I. J. Day, E. M. Greitzer, and Z. S. Spakovszky, “Origins and structure of spike-type rotating stall,” in *Proceedings of the ASME turbine Technical Conference and Exposition (GT '12)*, pp. 2567–2579, June 2012.
- [4] R. Mailach, I. Lehmann, and K. Vogeler, “Rotating instabilities in an axial compressor originating from the fluctuating blade tip vortex,” *Journal of Turbomachinery*, vol. 123, no. 3, pp. 453–460, 2001.
- [5] M. B. Graf, *Effects of Stator Pressure Field on Upstream Rotor Performance*, [Doctoral Thesis], Massachusetts Institute of Technology, 1996.
- [6] J. Bae, K. S. Breuer, and C. S. Tan, “Periodic Unsteadiness of Compressor Tip Clearance Vortex,” in *Proceedings of the ASME Turbo Expo Power for Land, Sea, and Air*, pp. 457–465, Vienna, Austria, 2004.
- [7] X. Deng, H. Zhang, J. Chen, and W. Huang, “Unsteady Tip Clearance Flow in a Low-Speed Axial Compressor Rotor With Upstream and Downstream Stators,” in *Proceedings of the ASME Turbo Expo Power for Land, Sea, and Air*, pp. 1371–1381, Reno, Nevada, USA, 2005.
- [8] N. Tahara, T. Nakajima, M. Kurosaki, Y. Ohta, E. Outa, and T. Nisikawa, “Active stall control with practicable stall prediction system using auto-correlation coefficient,” in *Proceedings of the 37th Joint Propulsion Conference and Exhibit*, Salt Lake City, UT, USA.
- [9] M. Dhingra, Y. Neumeier, J. V. Prasad, A. Breeze-Stringfellow, H. Shin, and P. N. Szucs, “A Stochastic Model for a Compressor

- Stability Measure," in *Proceedings of the ASME Turbo Expo: Power for Land, Sea, and Air*, pp. 833–843, Barcelona, Spain, 2006.
- [10] D. Christensen, P. Cantin, D. Gutz et al., "Development and Demonstration of a Stability Management System for Gas Turbine Engines," in *Proceedings of the ASME Turbo Expo: Power for Land, Sea, and Air*, pp. 165–174, Barcelona, Spain, 2006.
- [11] I. J. Day, "Stall, surge, and 75 years of research," *Journal of Turbomachinery*, vol. 138, no. 1, Article ID 2478223, 2015.
- [12] F. Lin, J. Du, J. Chen, C. Nie, and C. Biela, "Flow Structures in the Tip Region for a Transonic Compressor Rotor," in *Proceedings of the ASME Turbo Expo 2010: Power for Land, Sea, and Air*, pp. 2561–2572, Glasgow, UK.
- [13] J. Du, F. Lin, H. Zhang, and J. Chen, "Numerical investigation on the self-induced unsteadiness in tip leakage flow for a transonic fan rotor," *Journal of Turbomachinery*, vol. 132, no. 2, 2010.
- [14] M. A. Bennington, M. H. Ross, J. D. Cameron et al., "An Experimental and Computational Investigation of Tip Clearance Flow and Its Impact on Stall Inception," in *Proceedings of the ASME Turbo Expo 2010: Power for Land, Sea, and Air*, pp. 501–512, Glasgow, UK.
- [15] M. A. Bennington, J. D. Cameron, S. C. Morris et al., "Investigation of Tip-Flow Based Stall Criteria Using Rotor Casing Visualization," in *Proceedings of the ASME Paper*, pp. 641–651, Berlin, Germany.
- [16] X. Nan, F. Lin, S. Wang, L. Liu, N. Ma, and J. Chen, "The Analysis of Axial Momentum of the Rotor Tip Flows for Axial Compressors With Circumferential Grooves," in *Proceedings of the ASME Turbo Expo Turbine Technical Conference and Exposition*, Düsseldorf, Germany, 2014.
- [17] X. Nan, *The compressor rotor tip control volume method and its application on circumferential groove casing treatment*, Doctoral Thesis [Doctoral, thesis], Chinese Academy of Sciences, 2014.
- [18] N. Ma, *Research on the Low-speed Modeling Similarity Criteria for High-speed compressors and the flow mechanisms of Axial-slot Casing Treatments*, Doctoral Thesis [Doctoral, thesis], Chinese Academy of Sciences, 2016.
- [19] X. Nan, N. Ma, Q. Lu, and F. Lin, "The Control Volume Analysis of the Effectiveness of Casing Treatments for a Low-speed Compressor," in *Proceedings of the International Gas Turbine Congress IGTC-2015-0260*, Tokyo, 2015.
- [20] J. J. Adamczyk, M. L. Celestina, and E. M. Greitzer, "The role of tip clearance in high-speed fan stall," *Journal of Turbomachinery*, vol. 115, no. 1, pp. 28–38, 1993.
- [21] K. L. Suder and M. L. Celestina, "Experimental and computational investigation of the tip clearance flow in a transonic axial compressor rotor," *Journal of Turbomachinery*, vol. 118, no. 2, pp. 218–229, 1996.
- [22] J. Bergner, M. Kinzel, H. Schiffer, and C. Hah, "Short Length-Scale Rotating Stall Inception in a Transonic Axial Compressor: Experimental Investigation," in *Proceedings of the ASME Turbo Expo 2006: Power for Land, Sea, and Air*, pp. 131–140, Barcelona, Spain.
- [23] C. Hah, J. Bergner, and H.-P. Schiffer, "Tip clearance vortex oscillation, vortex shedding and rotating instabilities in an axial transonic compressor rotor," in *Proceedings of the 2008 ASME Turbo Expo*, pp. 57–65, deu, June 2008.
- [24] J. März, C. Hah, and W. Neise, "An Experimental and Numerical Investigation Into the Mechanisms of Rotating Instability," in *Proceedings of the ASME Turbo Expo 2001: Power for Land, Sea, and Air*, p. V001T03A084, New Orleans, Louisiana, USA.
- [25] T. Houghton and I. Day, "Enhancing the stability of subsonic compressors using casing grooves," in *Proceedings of the ASME Paper*, pp. 39–48, Orlando, Fla, USA, June 2009.
- [26] M. Ross, *Tip clearance flow interaction with circumferential groove casing treatment in a transonic axial compressor*, [Doctoral, thesis], University of Notre Dame, 2013.

## Research Article

# Observations of the Growth and Decay of Stall Cells during Stall and Surge in an Axial Compressor

**Adam R. Hickman and Scott C. Morris**

*University of Notre Dame, Notre Dame, IN 46556, USA*

Correspondence should be addressed to Adam R. Hickman; adamrhickman@hotmail.com

Received 17 March 2017; Revised 1 July 2017; Accepted 27 July 2017; Published 13 September 2017

Academic Editor: Pietro Zunino

Copyright © 2017 Adam R. Hickman and Scott C. Morris. This is an open access article distributed under the Creative Commons Attribution License, which permits unrestricted use, distribution, and reproduction in any medium, provided the original work is properly cited.

This research investigated unsteady events such as stall inception, stall-cell development, and surge. Stall is characterized by a decrease in overall pressure rise and nonaxisymmetric throughflow. Compressor stall can lead to surge which is characterized by quasi-axisymmetric fluctuations in mass flow and pressure. Unsteady measurements of the flow field around the compressor rotor are examined. During the stall inception process, initial disturbances were found within the rotor passage near the tip region. As the stall cell develops, blade lift and pressure ratio decrease within the stall cell and increase ahead of the stall cell. The stall inception event, stall-cell development, and stall recovery event were found to be nearly identical for stable rotating stall and surge cases. As the stall cell grows, the leading edge of the cell will rotate at a higher rate than the trailing edge in the rotor frame. The opposite occurs during stall recovery. The trailing edge of the stall cell will rotate at the approximate speed as the fully developed stall cell, while the leading edge decreases in rotational speed in the rotor frame.

## 1. Introduction

The stable operation of an axial compressor at a given shaft speed is limited at low mass flows by compressor stall. Stall is characterized by a decrease in overall pressure rise and nonaxisymmetric throughflow. A region of low momentum fluid can develop in one or more rotor passages and rotate around the annulus. This region is often referred to as a stall cell. Rotating stall can lead to quasi-axisymmetric fluctuations in mass flow and pressure known as compressor surge. Axial compressors may enter periods of stable rotating stall and surge during operation at off-design conditions. This generally leads to decreased efficiency and increased blade vibration. This paper presents detailed unsteady experimental measurements from a transonic axial compressor in order to describe stall inception, stall cell development, and surging characteristics.

The inception of stall has been the topic of significant research for many years. Camp and Day [1] found that stall inception may occur locally from short length scale disturbances (spikes) or from long length scale disturbances (modes). The present work will focus on observations from

a compressor that exhibits spike-type stall inception. Vo [2] found that a criterion for spike-type stall inception is that the interface created from the approach flow and the reverse tip-leakage flow becomes parallel with the rotor leading edge plane. Later Cameron et al. [3] obtained measurements supporting this concept using the compressor used in the present work. Tan et al. [4] provide a comprehensive review on the current understanding of stall inception. They found that the most common type of stall inception for modern compressor designs is a spike-type. This is when the initial stall cell develops on the order of a few rotor revolutions. Stall will typically develop in a single blade passage initially. There have been findings to support the existence of prestall spikes prior to stall inception. Initial disturbances have been found by Weichert and Day [5] found that initial disturbances can occur within the rotor passage at approximately 10–25% chord from the leading edge. Yamada et al. [6] also found that unsteady flow phenomena appear inside the rotor passage at near-stall.

After stall inception, a stall cell will increase in circumferential and radial extent. The stall cell will span multiple rotor

passages as it rotates around the annulus. Cameron et al. [7] found that the leading edge of the stall cell will initially rotate at a slower rate in the laboratory frame. The trailing edge of the stall cell will initially rotate around the annulus at nearly the rotor speed. After a few revolutions the leading edge will increase in rotational speed and the trailing edge will decrease in rotational speed as the final size is reached. Day [8] gives a thorough review of the current understanding of rotating stall. Day found throughout many compressors described in the literature that smaller stall cells tend to travel faster in the laboratory frame than larger cells.

The system dynamics of stall and surge for a compression system has been studied extensively. Greitzer [9, 10] developed a lumped parameter model to predict the fluctuations in mass flow and plenum pressure during stall and surge. The Greitzer stall and surge model can be used to predict the point where, as a compressor reaches the stall limit, stall will transition to surge. In his work, Greitzer found that a single nondimensional parameter, termed the  $B$  parameter, was a good indicator to determine whether stall or surge would occur. Hickman and Morris [11] found that the poststall throttle point can also influence the onset of surge.

Surge can grow from rotating stall as the compressor interacts with compression system. Day [12] found that the flow breakdown around the rotor caused by a stall inception event is typically the reason for the onset of surge. Compressor surge is composed of multiple parts [13]. The developing stall cell produces an effective blockage of the compressor annulus. A sudden drop in pressure ratio and mass flow rate then follow [11]. Rotating stall may be present from stall inception until the surge recovery process, [14] depending on the compressor. The recovery process occurs where the compressor will recover from rotating stall briefly. During the brief stall recovery process, the pressure ratio returns to its prestall value. Another stall inception event and surge cycle repeat as the stall point is reached again [11].

Observations from measurements of stall inception, rotating stall, surge, and stall recovery are presented. This paper includes a description of the test facility and instrumentation used. Instantaneous shroud and rotor exit unsteady pressure contours are presented during transient events in order to better understand the process of stall inception and stall development. A comparison between stall and surge events is also given to describe how the onset of surge occurs [15].

## 2. Experimental Methods

**2.1. Compressor Test Facility.** Experiments were conducted using the Notre Dame Transonic Axial Compressor Facility (NDTAC). The NDTAC facility includes a butterfly valve and plenum upstream of the axial compressor and a second plenum and butterfly valve downstream. The upstream and downstream plenum volumes were approximately  $1.52 \text{ m}^3$  and  $0.70 \text{ m}^3$ , respectively. The NDTAC facility employed a magnetic bearing system where the rotor shaft was levitated by a series of magnets. This enabled the facility to safely operate in rotating stall for extended periods of time and surge for short periods.

TABLE 1: ND Stage 04 design parameters.

Quantity	Value
Tip dia. [m]	0.457
Inlet hub dia. [m]	0.343
Exit hub dia. [m]	0.368
Rotor axial chord [cm]	3.56
Rotor blade count	20
Stator count	43
$N_c$ [rpm]	14684
$U_{\text{tip}}$ [m/s]	352

The compressor used in the experiments was ND Stage 04, a single stage transonic axial compressor with a mean hub-to-tip ratio of approximately 0.78. Figure 1 shows the schematic of the cross-section of ND Stage 04. Table 1 shows the design parameters for this stage. This compressor stage includes an annular contraction that incorporates a perforated plate which provided an approximate 3.5% turbulence intensity to the stage. The test article included a rotor and stator configuration.

**2.2. Instrumentation.** Steady and unsteady instrumentation were utilized for this work. Figure 1 shows the measurement planes. Standard Kiel probes to measure steady-state total temperature and total pressure were located at  $3.2 c_{\text{ax}}$  upstream of the rotor leading edge and  $0.77 c_{\text{ax}}$  downstream of the rotor trailing edge. Unsteady instrumentation was located upstream, downstream, and over the rotor.

Constant temperature hot wires were used to measure the unsteady stage inlet velocity and track the development of the stall cell during transient events. A circumferential array of 4 hot wires spaced every  $90^\circ$  were positioned approximately  $8.9 c_{\text{ax}}$  upstream of the rotor leading edge at midspan of the flow path. The hot wires were  $5 \mu\text{m}$  tungsten wire probes and oriented normal to the flow and in the radial direction. Using the form of King's law presented by Bruun [16], a simple calibration was found to relate the voltage and flow velocity. The velocities from the four hot wires were averaged in order to estimate the time-resolved and the annulus average unsteady mass flow. The hot-wire frequency response was in excess of 100 kHz.

High-response pressure transducers were utilized for flow field measurements in the plenums and in the vicinity of the rotor. Figure 2 is a schematic of the locations of unsteady instrumentation around the rotor. The pressure sensors used in the experiments were silicon piezoresistive pressure sensors made by Kulite (model XTL-140-25A). These pressure transducers had a natural frequency of approximately 240 kHz. Kulite pressure transducers were located in the upstream and downstream plenums. A circumferential array of ten high-frequency pressure transducers, located approximately  $0.18 c_{\text{ax}}$  upstream of the rotor leading edge, were flush mounted to the flow surface of the shroud. This allowed tracking of the stall-cell development and calculation of the circumferential size of the stall cell. A line of thirteen

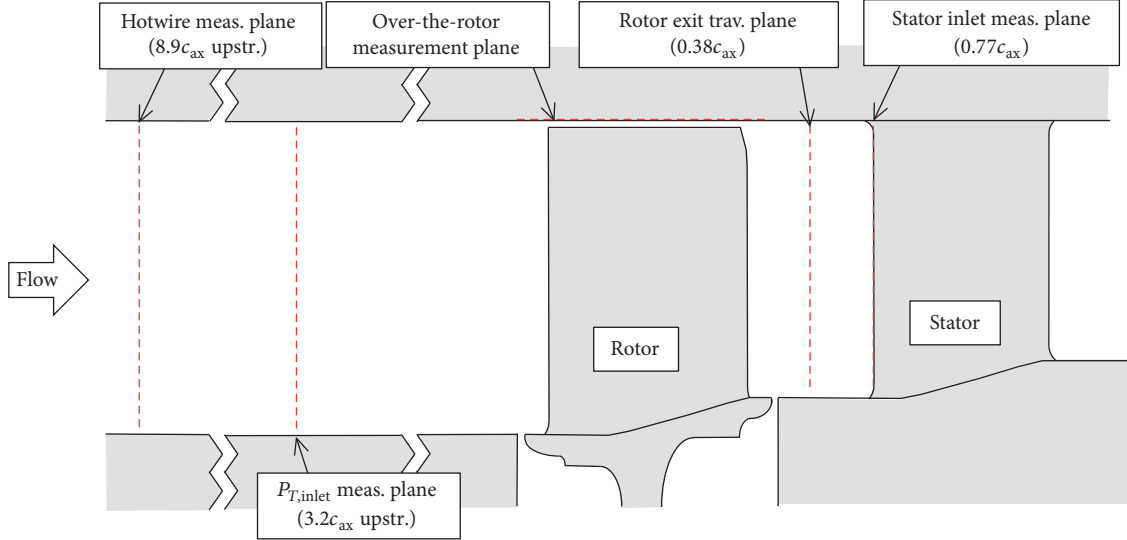


FIGURE 1: Cross-section of ND Stage 04.

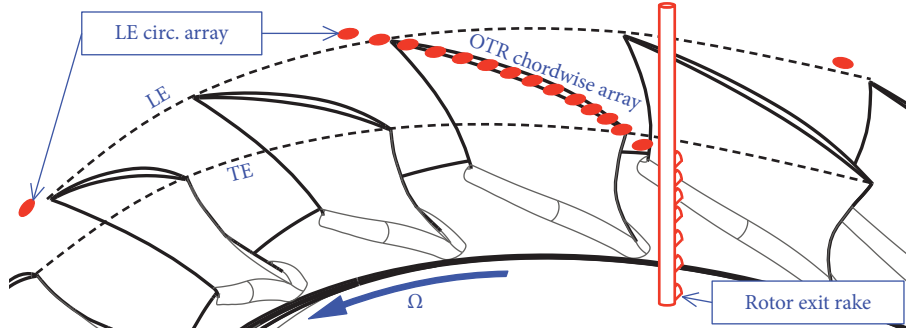


FIGURE 2: Schematic of near rotor unsteady instrumentation.

high-frequency pressure sensors was also located directly over-the-rotor (OTR) in a chord-wise array. The array of OTR transducers was flush mounted to the flow surface following the stagger angle of the rotor blade tip similar to Weichert and Day [5].

An unsteady total pressure rake was specifically designed for this work. The top of Figure 3(a) shows a photograph, and the bottom shows a schematic of the total pressure rake. The rake contained seven miniature Kulite transducers (XCQ-95-062) which were mounted into separate Kiel heads such that the transducer was directly exposed to the oncoming flow. Some have designed unsteady total pressure probes such that the transducer is in the body of probe [17]. Though this design can protect the sensor from dust and debris, it can limit the frequency response of the probe. The multiple sensors were positioned along the length of the probe and were concentrated towards the tip region of the rotor. It was installed at the rotor exit traverse plane shown in Figures 1 and 2. The unsteady total pressure rake was used to record unsteady total pressures simultaneously at multiple spanwise locations during stall and surge.

Because this was an unconventional design, a yaw sensitivity test was conducted for the developed unsteady total pressure rake. Figure 3(b) shows the total pressure normalized by the maximum as a function yaw angle for one of the transducers. All transducers contained nearly identical yaw sensitivity. The unsteady total pressure rake was found to have an acceptance angle limit of approximately  $\pm 20^\circ$ . Beyond the acceptance range, the measured pressure is biased low and drops gradually compared to a standard Kiel probe at approximately 0.4% per degree.

Unsteady instrumentation was sampled at rate of 200 kHz. It was found that the sampling rate and frequency response of the sensors were sufficient to measure the frequencies associated with stall inception and rotating stall events at the speeds considered. The maximum frequencies of interest were found to be under 20 kHz. The Kulite sensors were calibrated before the measurement program and were found to have an uncertainty less than 1% of the full-scaled values. Hot-wire measurements were also calibrated immediately prior to the measurements and were found to have an uncertainty of approximately 3% of the measured values.

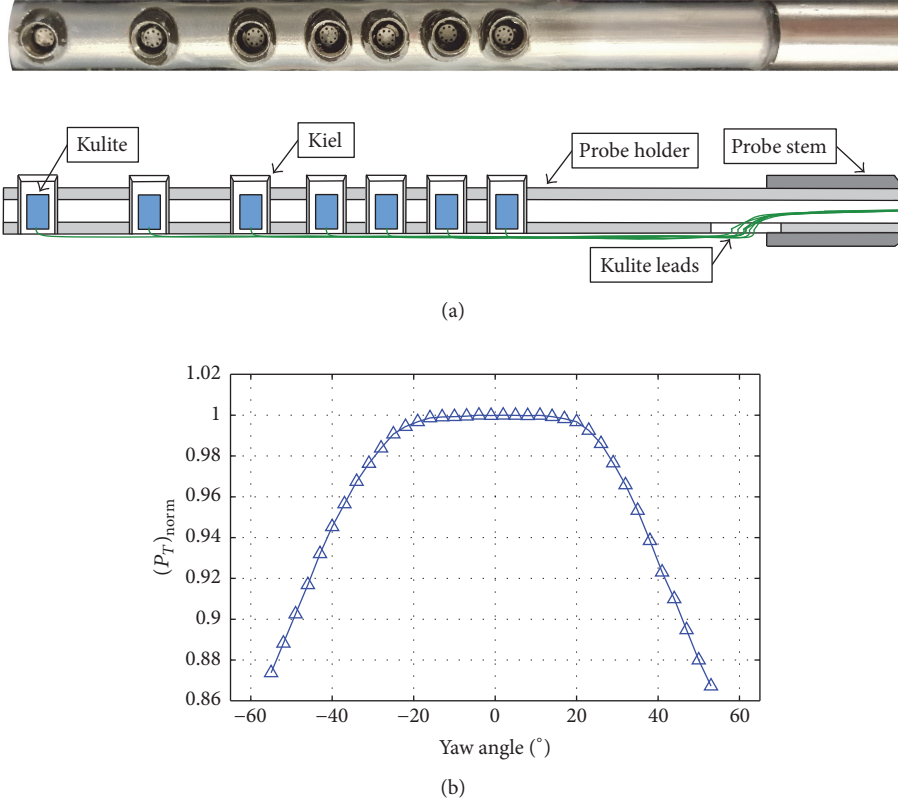


FIGURE 3: (a) Photograph and schematic of the unsteady total pressure rake and (b) the yaw response.

### 3. Steady and Unsteady Compressor Characteristics

This section presents the steady-state compressor characteristic and unsteady characteristics during two poststall events at 100% design speed. First, the steady-state normalized plenum pressure rise ( $\Delta P$ ) is shown as a function of flow coefficient ( $C_x/U$ ) for ND Stage 04 at 100% design speed in Figure 4. The unstalled branch of the steady characteristic contains a steep negative slope. The stall point was found at approximately  $C_x/U = 0.34$ . Upon throttling the compressor beyond stall, the mass flow and pressure rise decrease abruptly. A black dashed line connects the last stable prestall point to the initial stall point. The rotating stall branch of the steady-state compressor characteristic below the value of  $C_x/U = 0.29$  was approximated using data at lower speeds as discussed in Hickman and Morris [11]. This portion of the characteristic was used strictly for predictions of unsteady compressor characteristics and contains a nearly constant pressure rise as the mass flow decreases. The steady characteristic includes a stall/unstall hysteresis portion. Upon opening the valves, the characteristic deviates from the original path. The pressure rise remains relatively constant as the mass flow increases to approximately  $C_x/U = 0.32$ . This was found to be the critical recovery value for this compressor at 100% design speed. Upon opening the throttle valves beyond this point, the compressor recovered from rotating stall.

The measured unsteady compressor characteristics for a stall and surge case at 100% design speed are also shown in Figure 4. The markers along the measured curves indicate every 5 rotor revolutions. The unsteady events were recorded back-to-back with identical speeds and identical values of the upstream and downstream  $B$  Parameter ( $B_U = 2.52$ ,  $B_D = 1.71$ ). The single difference between the stall and surge case is the poststall throttle point. The ending throttle point for the stall case (blue) corresponded to the initial stall point. The compressor was “eased” into stall by closing the valves up to and not past the initial stall point. After the compressor stalled, the mass flow and pressure rise decreased past the initial stall point. The mass flow and pressure rise then increased, or rebounded, such that it did not surpass the critical recovery value of  $C_x/U$ . The compressor then entered stable stall.

For the surge case (red) in Figure 4, the poststall throttle point is denoted by the red dashed line. The compressor was throttled deeper into stall past the initial stall point. The decrease in pressure rise and mass flow are more dramatic. The rebounding motion of the compressor characteristic is such that it surpasses the critical recovery value of  $C_x/U$  and the compressor temporarily recovers from stall. The compressor then returns back to the initial stall point. Not shown in Figure 4 is that after the compressor is again brought to the stall point, another surge cycle begins similar to the first. A further analysis of the development of the stall cell and comparison between the stall and surge case will be discussed

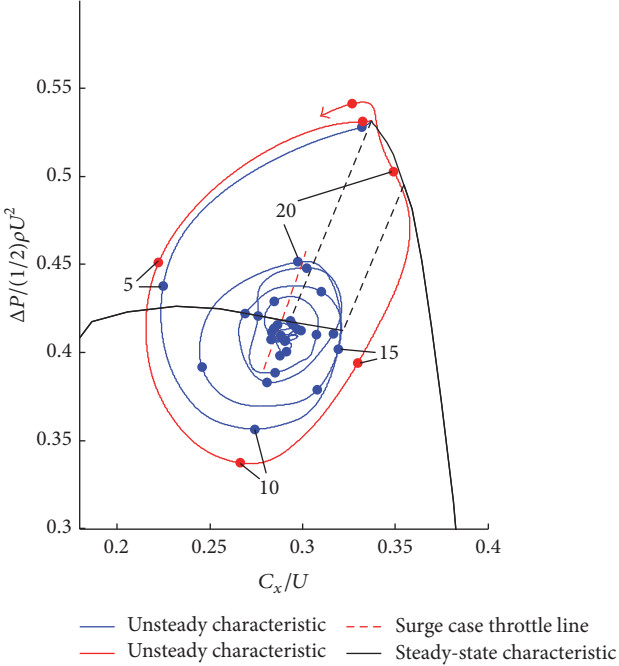


FIGURE 4: Steady and unsteady 100% corrected speed compressor characteristics.

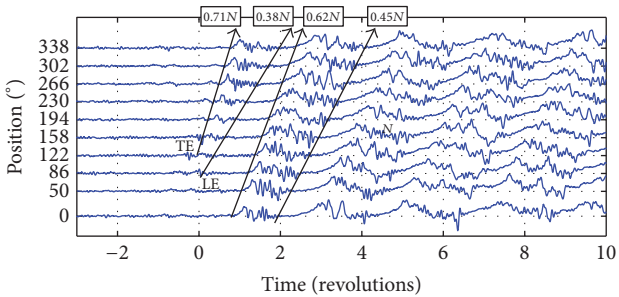


FIGURE 5: Time series from the circumferential array of static pressures upstream of the rotor leading edge.

in the following sections. All of the following data and results presented were acquired at the 100% design speed.

#### 4. Stall Inception and Stall-Cell Development Measurements

**4.1. Leading Edge Shroud Static Pressure Time Series.** Stall inception events were recorded using the unsteady instrumentation described in Section 2.2. Figure 5 shows the pressure traces from the circumferential array of high-frequency pressure transducers during a typical stall inception event at 100% corrected speed. The abscissa is plotted in units of rotor revolutions and extends from -3 to 10 revolutions. The ordinate represents both the circumferential position and magnitude of the fluctuations at the position. Time series are low-pass filtered at 15 times the shaft rate (15N), just below the blade passing frequency such that the development of the rotating stall cell can be tracked. It was found that

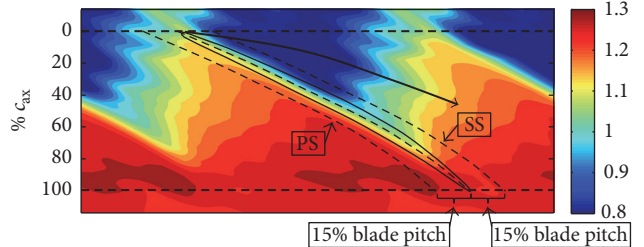


FIGURE 6: Ensemble average shroud static pressure at prestall conditions.

stall inception occurred in the same circumferential location repeatedly. This was most likely due to some slight asymmetry in the inlet flow path.

The origin of the time axis corresponds to the time when the fluctuations become greater than prestall fluctuations. At approximately revolution 0, a single stall cell or spike begins to form and rotate around the annulus. A static pressure rise occurs upstream of the blade row similar to Pullan et al. [18], which extends over the span of multiple blade passages. Initially, the trailing edge of the stall cell rotates at a rate of 0.71N and slows down in the laboratory frame as the stall cell increased in circumferential size. The leading edge rotates at 0.38N in the laboratory frame initially and increases rotational speed as the cell develops. These observations are consistent with short length scale, or “spike” type stall inception.

In the frame of the rotor the leading edge of the stall cell initially rotates at approximately 0.62N while the trailing edge rotates at only 0.29N. Thus, the stall cell grows on the leading edge side of the cell initially. Rotor passages at the leading edge of the stall cell stall at a faster rate relative to passages exiting the cell during the initial growth phase.

**4.2. Prestall Shroud Static Pressure.** To compare to stall inception measurements, the prestall phase-locked average shroud static pressure normalized by the inlet plenum pressure,  $P_{PU}$ , is presented in Figure 6. This contour corresponds to the shroud static pressure at the last stable operating point prior to stall inception. Evidence of the tip clearance vortex as discussed in Weichert and Day [5] can be seen by a low pressure core that extends from the suction side (SS) of the rotor leading edge towards the middle of the pressure side (PS) of the adjacent blade. The path is denoted by the black arrow in Figure 6.

**4.3. Stall Inception.** Prior to the earliest detectable signs by the circumferential array of high-frequency pressure transducers, evidence of stall inception can be seen within rotor passages. Figure 7 shows the shroud static (top) and rotor exit total (bottom) raw pressure time series. These data are measured using the OTR chord-wise array and unsteady total pressure rake described in Section 2.2. The centers of the contours in Figure 7 are at approximately revolution -0.8 at the 0° circumferential position. The raw data are displayed as a contour normalized by  $P_{PU}$ , where the ordinates are in space and the abscissa is in time. This gives an “instantaneous view” of the shroud static pressure and rotor exit total pressure,

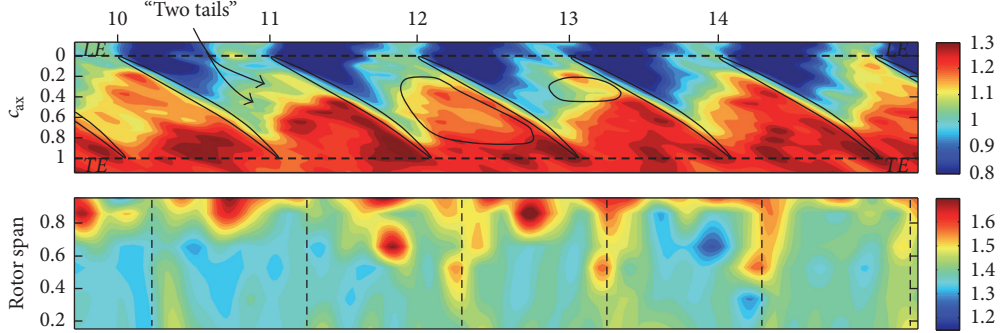


FIGURE 7: Instantaneous (space-time) shroud static and rotor exit pressure contour centered at revolution  $-0.8$  of Figure 5 at the  $0^\circ$  circumferential position.

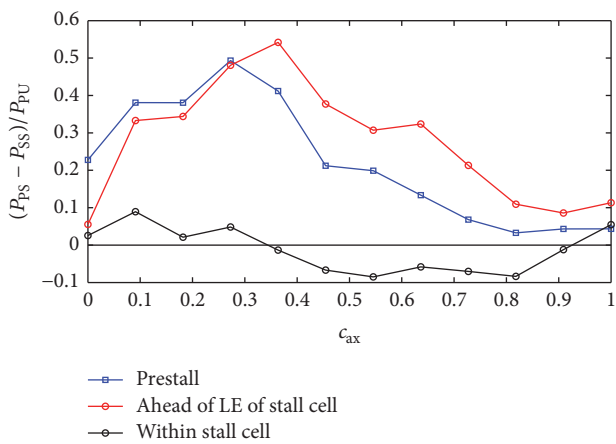


FIGURE 8: Rotor blade tip loading at prestall and poststall conditions.

assuming the flow field evolves slowly with respect to the blade passage time scale. Blade locations are overlaid for reference in the shroud contours. Approximate locations of the rotor wake are denoted with vertical dashed lines in the rotor exit contours. All instantaneous contours in this section are captured during the unsteady event shown in Figure 5, but the characteristics described in this section were found to be similar throughout the majority of stall inception events for this compressor.

Many repeatable features were found similar to Weichert and Day [5] such as the existence of the “two-tail” phenomenon. This feature can be seen in the shroud static pressure contour between blades 10 and 11 of Figure 7. This is an indication that the tip clearance vortex is disturbed. The two passages to the right show regions of low pressure. These regions are circled and indicate signs of prestall spikes. The blade loading for blades 12 and 13 decreases as a result of the low pressure regions. The rotor passage between blades 13 and 14 returns close to prestall values as compared to Figure 6.

The rotor exit pressure contours in Figure 7 show a large degree of unsteadiness from one passage to another. For this compressor, the vertical streaks of higher total pressure are typically associated with the blade wakes as these measurements are in the absolute frame. This contour shows no obvious signs of disturbed flow, and it will be shown that

the values closely resemble prestall values for this moment in time.

**4.4. Blade Lift and Spanwise Rotor Exit Total Pressure.** To better quantify instantaneous values, the blade loading was approximated and compared to prestall values. As there was no unsteady instrumentation on the rotor to calculate loading on the blade, the blade loading was approximated from the shroud static pressure measurements from the OTR chord-wise array. The dashed line to the left of the blade in Figure 6 was defined as the sample location for the pressure on the PS of the rotor blade. The sample location was approximately 15% of a blade pitch from the mean camber line of the blade. A similar method was used to define the pressure on the SS of the rotor blade. The difference between the PS and SS at each axial location was assumed to be the blade loading at the tip of the rotor.

This method was used to determine the blade loading during stable prestall operation and poststall events. Figure 8 shows the average blade loading for prestall conditions and two poststall conditions. Curves in this figure are plotted as blade loading normalized by  $P_{PU}$  as a function of axial location. The blue curve in Figure 8 is the average prestall blade loading prior to stall inception. During prestall conditions, the rotor blade is more highly loaded towards the leading edge of the blade and exhibits the highest loading at approximately  $0.27c_{ax}$ .

The blade lift at the rotor tip was approximated during the steady prestall operation and poststall events. The blade lift was found by integrating the blade loading curve along the axial direction. For poststall events, blade lift was calculated as individual blades passed by the over-the-rotor chord-wise array. Figure 9(a) shows the blade lift at the  $0^\circ$  circumferential position during the stall inception event shown in Figure 5. Values are normalized by the mean of the prestall lift. The prestall lift can fluctuate from unsteadiness in the flow through the rotor. Statistics were performed on the lift in the prestall region immediately prior to stall inception. The grey band in Figure 9(a) represents values bounded by plus and minus one standard deviation from the mean of the prestall region. The spanwise average total pressure was also calculated and is shown in Figure 9(b). Values are normalized by the mean of the prestall rotor exit total pressure. The

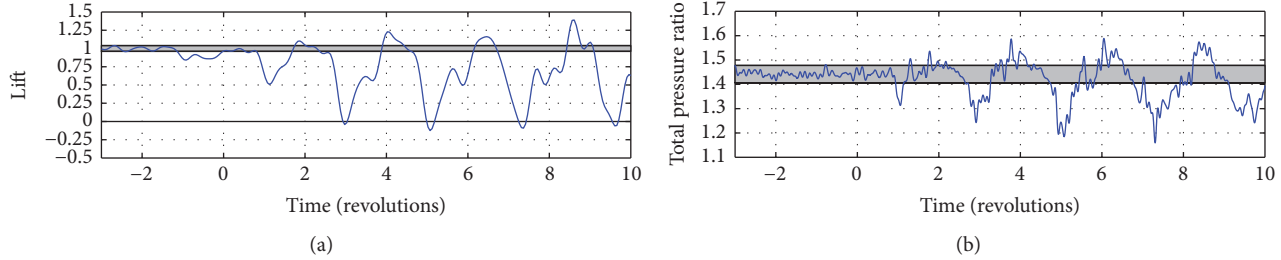


FIGURE 9: (a) Blade lift at rotor tip and (b) spanwise average rotor exit total pressure ratio at the  $0^\circ$  circumferential location.

spanwise average total pressure was found by averaging multiple pressures along the span measured by the unsteady total pressure rake at the  $0^\circ$  circumferential position. The grey band in Figure 9(b) also represents values bounded by plus and minus one standard deviation from the mean of the prestall region.

At approximately  $-0.8$  revolutions, corresponding to the instantaneous contours in Figure 7, there is a statistically significant decrease in lift at the tip. At the same moment in time, the spanwise average total pressure ratio shows no deviation from the prestall. The first moment that the compressor experiences a significant decrease in total pressure is at approximately revolution  $1.1$ , which corresponds to the first stall cell passing. By this time, the stall cell has grown in circumferential size and is clearly noticeable in Figure 5. This result agrees well with the work of Weichert and Day [5] that the first sign of stall inception spikes occurs within a rotor passage.

**4.5. Stall-Cell Development.** As the stall cell develops, blade lift and rotor total pressure fluctuate dramatically. The first instance the stall cell passes the OTR chord-wise array and unsteady total pressure rake is between revolutions  $0.8$  and  $1.7$ . The trailing edge of the stall cell is at approximately  $0.8$  revolutions and the leading edge is at approximately  $1.7$  revolutions. Moving forward in time, as the trailing edge of the stall cell propagates to the  $0^\circ$  circumferential location at  $0.8$  revolutions the lift and total pressure ratio begin to decrease. By revolution  $1$ , within the stall cell, the lift decreases to approximately  $50\%$  of the prestall value. The pressure ratio decreases to nearly  $1.3$ . The stall cell has not yet fully developed, and the decrease in lift and pressure ratio are not as drastic as future stall cell passing. At revolution  $1.7$ , ahead of the leading edge of the stall cell, the lift and pressure ratio are both slightly above prestall values. This suggests increased incidence and turning ahead of the stall cell.

It is useful to analyze the raw unsteady pressure time series to better visualize the growth of the stall cell. Figure 10 shows the instantaneous shroud static pressure and rotor exit total pressure contours during the first stall cell passing. Contours in Figure 10(a) are centered at revolution  $0.9$  and show the trailing edge of the stall cell. In this figure, passages to the left of blade  $7$  are exiting the stall cell and are in the process of recovering. The passages increase in blade loading and pressure ratio to the left of blade  $7$ . Passages to the right of blade  $7$  are stalled with little blade loading and pressure ratio.

Figure 10(b) shows the leading edge of the stall cell. This contour is centered at revolution  $1.1$ . Blade  $12$  exhibits

a relatively high pressure difference across the blade in the shroud static pressure contour. The rotor exit contour shows pressures near prestall values. To the left of blade  $12$ , the blade loading and rotor exit total pressure progressively decrease. Passages between blades  $10$  and  $12$  are entering the leading edge of the stall cell and are in the process of stalling. Passages to the left of blade  $10$  are stalled and show little pressure rise across the rotor.

Passages ahead of leading edge of the stall cell are shown in Figure 10(c), centered at revolution  $1.7$ . These blades show an increase in blade loading and pressure ratio above the prestall values as discussed previously. These passages are overpressured and are approaching the stall cell.

After rotor revolution  $2$ , the stall cell has become fully developed. Figure 9 shows the blade lift and pressure ratio for three more stall cell revolutions. Within the fully developed stall cell, the blade lift decreases to slightly below zero at revolutions  $3$ ,  $5.1$ , and  $7.3$ . The blade loading at approximately revolution  $3$  is shown in Figure 8 as the black curve. The blade loading between  $0.35c_{ax}$  and  $0.9c_{ax}$  is less than zero for this moment in time. This is evidence of localized back-flow through the rotor passage as the stall cell passes. The rotor total pressure ratio decreased as low as  $1.2$  within the stall cell (Figure 9(b)).

The blade lift increased significantly ahead of the stall cell at revolutions  $4$ ,  $6.4$ , and  $8.6$ . At revolution  $8.6$ , blade lift increased approximately  $40\%$  above prestall values. The blade loading at approximately revolution  $4.1$  is shown in Figure 8 as the red curve. The loading from the rotor leading edge to  $0.25c_{ax}$  is slightly below the average prestall loading. From  $0.25c_{ax}$  to the trailing edge of the rotor, the blade shows increased loading compared to the prestall. The rotor exit total pressure also increased significantly ahead of the developed stall cell as high as approximately  $1.59$  as shown in Figure 9(b).

## 5. Stall and Surge Time Series

The development of the stall cell was remarkably similar between cases when the compressor entered stable rotating stall and when the compressor surged. This section will provide a detailed comparison between the two unsteady events shown on the left of Figure 4.

Both the stall and surge cases exhibited a sharp decrease in  $C_x/U$  and  $\Delta P$  during the stall inception event. Figures 11(c) and 11(d) show a comparison of  $C_x/U$  and  $\Delta P$  between the stall and surge cases. In these figures, the blue curve is

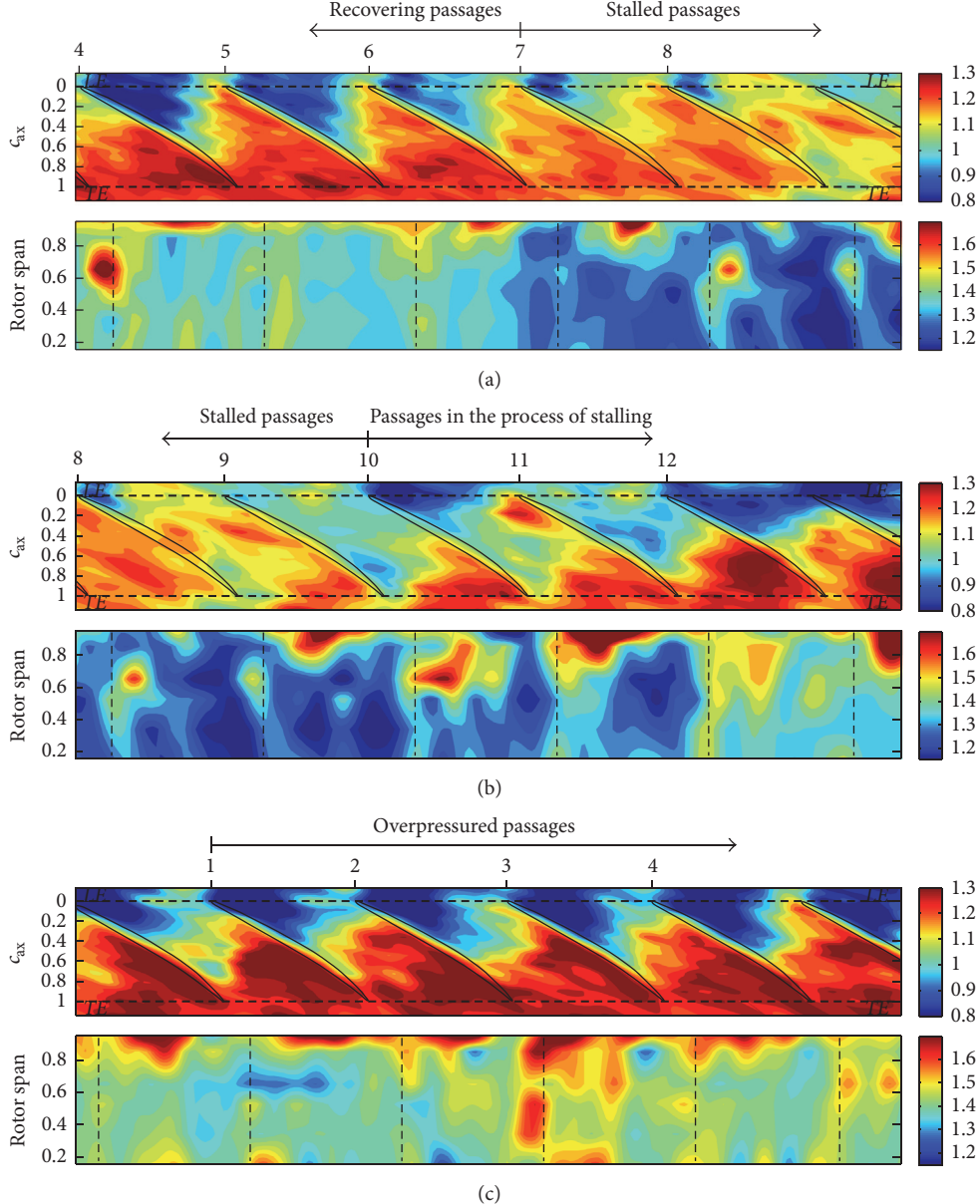


FIGURE 10: Instantaneous (space-time) shroud static and rotor exit pressure contours centered at revolution (a) 0.9, (b) 1.1, and (c) 1.8 of Figure 5 at the 0° circumferential position.

the 100% corrected speed stall case and the red curve is the 100% corrected speed surge case. The surge case shows a larger decrease in plenum pressure rise and mass flow compared to the stall case. The larger decrease produces a large enough return swing during the recovery to surpass the critical recovery value of  $C_x/U$  [11]. The critical recovery value of  $C_x/U$  is shown as the black line in Figure 11(c). The fluctuations in the stall case are just small enough such that the trajectory of the unsteady characteristic never surpasses the critical recovery value of  $C_x/U$ . This can be seen more clearly in Figure 4. The trajectory of the blue experimental curve approaches the critical recovery value of  $C_x/U$  on three occasions, but does not go above. It is the existence of a relatively

large stall/unstall hysteresis branch in the steady-state characteristic that allows this to occur.

Figures 11(a) and 11(b) show the low-pass filtered time traces of shroud static pressure and upstream hot wires for both the stall and surge cases. These figures illustrate the similarities between the two stall inception events. From rotor revolutions 0 to 14 the traces are similar. Stall inception occurs at approximately the same circumferential location. The initial growth and rotation rates of the stall cell during the first few revolutions between the two cases are nearly identical. At approximately revolution 5, the speed of the stall cell was 0.44N in the laboratory reference frame. At this point, the stall cell was at its largest size and rotating the

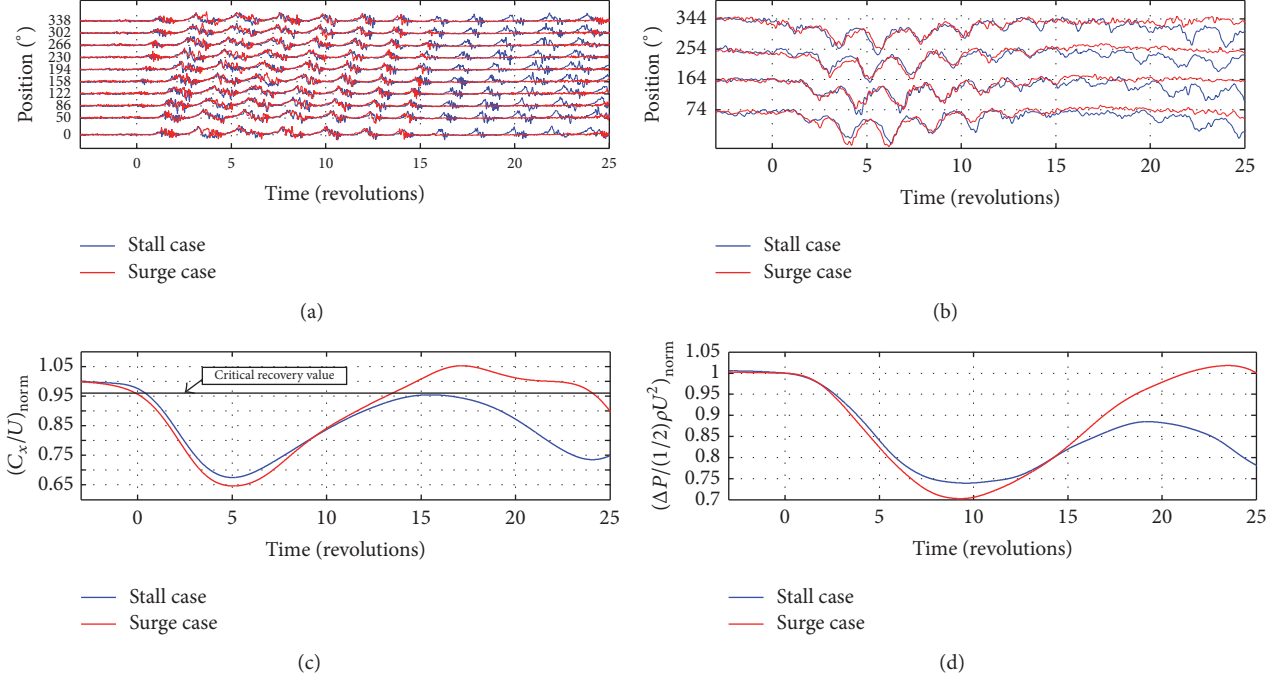


FIGURE 11: Time series of (a) circumferential array of static pressures upstream of the rotor leading edge, (b) circumferential array of hot wires upstream of the rotor leading edge, (c) annulus average mass flow, and (d) plenum-to-plenum pressure rise during stall (blue) and surge (red).

slowest. This coincides with the local minimum on the  $C_x/U$  trace in Figure 11(c). As the mass flow recovers, the stall cell then begins to decrease in circumferential size and increase in speed until approximately revolution 15 where  $C_x/U$  was at its local maximum for the stall case. The speed of the stall cell for the stall case at revolution 15 was approximately  $0.52N$ .

The shroud static pressure traces in Figure 11(a) for the surge case show a second peak for approximately half of a revolution of the stall cell between rotor revolutions 3 and 4. This second peak is most apparent in Figure 11(a) at the  $0^\circ$  circumferential position and at rotor revolution 4. This extra disturbance may have been due to the mass flow being slightly lower for the surge case. A decrease in mass flow may have increased the incidence angle possibly allowing for a second spike to briefly form at the leading edge of the main stall cell.

In the surge case, the critical recovery value of  $C_x/U$  was surpassed at approximately rotor revolution 13.5. It was at this point that the stall recovery process began for the compressor in the surge case. This is when the shroud static pressure traces and upstream hot-wire traces for the surge case begin to deviate from the stall case. With the compressor recovered from rotating stall, the plenum pressure rise recovered until the compressor was brought to the stall point again in the surge case. At revolution 24 of the surge case, a second stall inception event occurred and another surge cycle began. Figures 11(a) and 11(b) show how similar the stall inception events are for the stall and surge case. These results show it is purely the poststall throttling point in conjunction with the system dynamics that determine whether surge will grow from rotating stall. For a further analysis of the rotating stall case see Hickman and Morris [19].

## 6. Temporary Surge and Stall Recovery

During the temporary stall recovery at the end of the surge cycle, the leading edge and trailing edge of the stall cell will travel at different speeds. Figure 12(a) shows the shroud static pressure traces from the circumferential array for the surge case from rotor revolutions 10 through 18. The speeds of the leading edge and trailing edge of the stall cell are labeled. As the compressor begins to recover, the trailing edge of the stall cell rotates at approximately the same speed as when the cell was fully developed. The leading edge of the stall cell rotates at a faster rate in the laboratory frame as the cell is shrinking. In the rotor frame, the leading edge of the stall cell rotates more slowly until the leading edge and trailing edge meet and the stall cell disappears. This is very similar to a compressor recovering from stable rotating stall.

Data were acquired during the recovery from stable rotating stall. Figure 13 shows the unsteady characteristic for a rotating stall and stall recovery event. The markers along the solid blue curve represent every 2 rotor revolutions. The zero location was chosen as the approximate point where stall cell dies out. The unsteady characteristic during the stall event is shown as the blue dashed line for reference in Figure 13. In this case the compressor entered stable rotating stall by closing the valves. The valves were then opened and the compressor recovered from rotating stall. The solid blue line is the unsteady characteristic during the stall recovery event. The characteristic starts at the initial stall point and at approximately rotor revolution -2, the unsteady characteristic surpasses the critical recovery value of  $C_x/U$ , and the stall recovery process begins. The unsteady characteristic

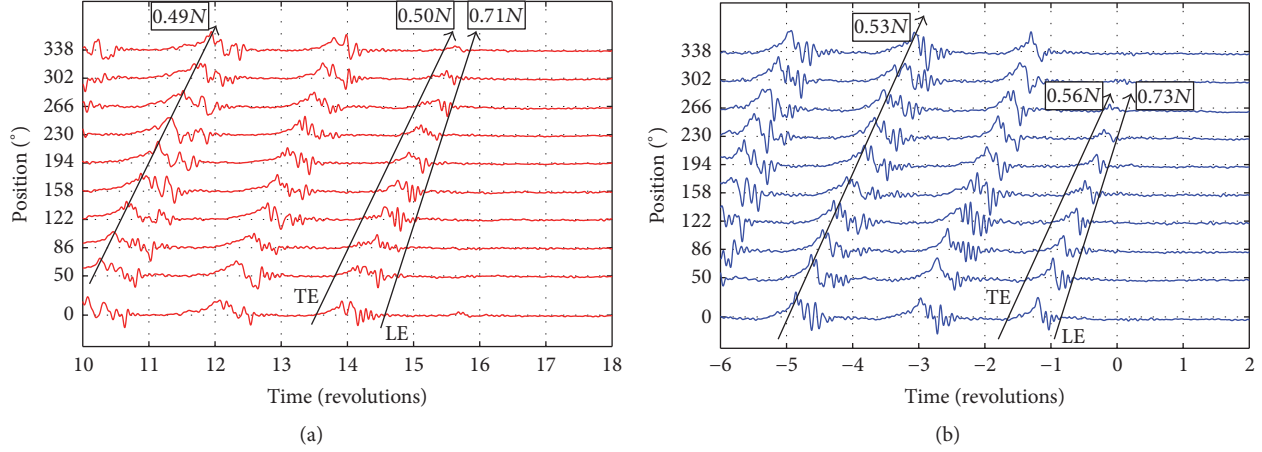


FIGURE 12: Time series of circumferential array of static pressures upstream of the rotor leading edge during (a) temporary recovery at the end of a surge cycle and (b) stall recovery with an opened outlet valve.

transiently attaches to the unstalled branch of the steady-state compressor characteristic.

In Figure 12(b) are the leading edge traces for the stall recovery event shown in Figure 13. The time axis corresponds to the labeled markers in Figure 13. The speeds of the trailing edge and leading edge of the stall cell during stall recovery are similar to the temporary stall recovery at the end of a surge cycle. The trailing edge rotates at approximately the same speed as the developed stall cell, while the stall cell decays at the leading edge. Figure 12 illustrates that stall recovery and temporary surge recovery are similar events.

## 7. Conclusions

Observations from unsteady measurements during stall inception, stall-cell development, rotating stall, and surge were presented. The first signs of stall inception spikes were found within rotor passages. As the stall cell grows after stall inception, the leading edge of the cell will rotate at a higher rate than the trailing edge in the rotor frame suggesting that the stall cell initially increases in size at the leading edge.

Blade loading at the tip and rotor exit total pressure ratio decrease dramatically within the stall cell. Blade lift can decrease to negative values within the stall cell suggesting back-flow. Ahead of the leading edge of the stall cell, the blade lift and rotor exit total pressure ratio surpass prestall values. This is a sign of higher incidence and turning ahead of the stall cell.

The compressor investigated stalls with a single full span stall cell. A single stall cell is also present during surge. There is a striking resemblance between the development of the stall cell for rotating stall and surge cases. The initiation location, initial speed, and initial growth rate of the stall cell are nearly indistinguishable between stall and surge cases. The unsteady event becomes a surge event when the critical recovery value of  $C_x/U$  is surpassed.

Temporary stall recovery at the end of a surge cycle and recovery from rotating stall are similar events. The trailing

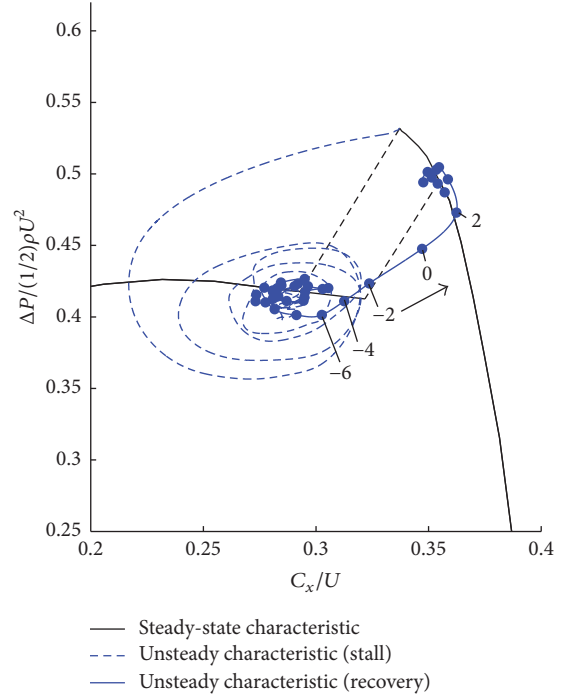


FIGURE 13: Unsteady compressor characteristic during stall and stall recovery.

edge of the stall cell will rotate at the approximate speed as the fully developed stall cell, while the leading edge decreases in rotational speed in the rotor frame. During recovery from compressor stall, the stall cell decays at the leading edge.

Compressor surge was long thought to be an axisymmetric phenomenon. This research has shown that while global fluctuations in mass flow and pressure are present during surge events, local asymmetric instabilities similar to those seen during rotating stall may also take place. Fully

understanding these instabilities may lead to new methods for delaying or mitigating their effects.

## Conflicts of Interest

The authors declare that they have no conflicts of interest.

## References

- [1] T. R. Camp and I. J. Day, "A study of spike and modal stall phenomena in a low-speed axial compressor," *Journal of Turbomachinery*, vol. 120, no. 3, pp. 393–401, 1998.
- [2] H. D. Vo, "Rotating stall suppression in axial compressors with casing plasma actuation," *Journal of Propulsion and Power*, vol. 26, no. 4, pp. 808–818, 2010.
- [3] J. D. Cameron, M. A. Bennington, M. H. Ross et al., "The influence of tip clearance momentum flux on stall inception in a high-speed axial compressor," *Journal of Turbomachinery*, vol. 135, no. 3, Article ID 051005, 2013.
- [4] C. S. Tan, I. Day, S. Morris, and A. Wadia, "Spike-type compressor stall inception, detection, and control," *Annual Review of Fluid Mechanics*, vol. 42, pp. 275–300, 2010.
- [5] S. Weichert and I. Day, "Detailed measurements of spike formation in an axial compressor," *Journal of Turbomachinery*, vol. 136, no. 5, Article ID 051006, 2013.
- [6] K. Yamada, H. Kikuta, M. Furukawa, S. Gunjishima, and Y. Hara, "Effects of tip clearance on the stall inception process in an axial compressor rotor," in *Proceedings of the ASME Turbo Expo 2013: Turbine Technical Conference and Exposition (GT '13)*, June 2013.
- [7] J. D. Cameron, S. C. Morris, S. T. Barrows, and J.-P. Chen, "On the interpretation of casing measurements in axial compressors," in *Proceedings of the 2008 ASME Turbo Expo*, pp. 653–665, American Society of Mechanical Engineers, New York, NY, USA, June 2008.
- [8] I. J. Day, "Stall, surge, and 75 years of research," *Journal of Turbomachinery*, vol. 138, no. 1, Article ID 2478223, 2015.
- [9] E. M. Greitzer, "Surge and rotating stall in axial flow compressors—part i: theoretical compression system model," *Journal of Engineering for Gas Turbines and Power*, vol. 98, no. 2, pp. 190–198, 1976.
- [10] E. M. Greitzer, "Surge and rotating stall in axial flow compressors—part ii: experimental results and comparison with theory," *Journal of Engineering for Gas Turbines and Power*, vol. 98, no. 2, pp. 199–211, 1976.
- [11] A. R. Hickman and S. C. Morris, "Stall and Surge Characteristics of a Two-Volume Compression System," in *Proceedings of the 52nd AIAA/SAE/ASEE Joint Propulsion Conference*, Salt Lake City, UT, USA, 2016.
- [12] I. J. Day, "Axial compressor performance during surge," *Journal of Propulsion and Power*, vol. 10, no. 3, pp. 329–336, 1994.
- [13] H. Schoenenborn and M. de Vries, "Aeroelasticity at reversed flow conditions-part III: reduction of surge loads by means of intentional mistuning," *Journal of Turbomachinery*, vol. 135, no. 3, Article ID 041009, 2013.
- [14] T. Abe, H. Mitsui, and Y. Ohta, "Coexisting phenomena of surge and rotating stall in an axial flow compressor," *Journal of Thermal Science*, vol. 22, no. 6, pp. 547–554, 2013.
- [15] A. R. Hickman, *The Transition From Rotating Stall to Surge in an Axial Compressor [Ph.D. thesis]*, University of Notre Dame-Turbomachinery Laboratory, 2017.
- [16] H. H. Bruun, *Hot-wire Anemometry: Principles and Signal Analysis*, Oxford University Press, 1995.
- [17] J. Lepicovsky and E. P. Braunscheidel, "Measurement of flow pattern within a rotating stall cell in an axial compressor," NASA/TM—2006-214270, NASA, 2006.
- [18] G. Pullan, A. M. Young, I. J. Day, E. M. Greitzer, and Z. S. Spakovszky, "Origins and structure of spike-type rotating stall," in *Proceedings of the ASME Turbo Expo 2012: Turbine Technical Conference and Exposition (GT '12)*, pp. 2567–2579, June 2012.
- [19] A. R. Hickman and S. C. Morris, "Characteristics of stable rotating stall cells in an axial compressor," in *Proceedings of ASME Turbo Expo 2017: Turbomachinery Technical Conference and Exposition*, pp. GT2017-GT64901, 2017.

## Research Article

# Observations on Rotating Instabilities and Spike Type Stall Inception in a High-Speed Multistage Compressor

Johannes Schreiber, Benoit Paoletti, and Xavier Ottavy

Laboratoire de Mécanique des Fluides et d'Acoustique, UMR CNRS 5509, Université de Lyon, Ecole Centrale de Lyon, UCB Lyon I, INSA, 36 Av. Guy de Collongue, 69134 Écully Cedex, France

Correspondence should be addressed to Johannes Schreiber; [johannes.schreiber@ec-lyon.fr](mailto:johannes.schreiber@ec-lyon.fr)

Received 17 March 2017; Revised 30 June 2017; Accepted 25 July 2017; Published 28 August 2017

Academic Editor: Feng Lin

Copyright © 2017 Johannes Schreiber et al. This is an open access article distributed under the Creative Commons Attribution License, which permits unrestricted use, distribution, and reproduction in any medium, provided the original work is properly cited.

This work investigates high-frequency measurements for the contribution to the understanding of different stall inception types in high-speed multistage compressors. A 3.5-stage high-speed axial multistage compressor is investigated with a 2 MW test rig in the Laboratoire de Mécanique des Fluides et d'Acoustique (LMFA) at Ecole Centrale de Lyon, France. Two different types of instabilities arise in this compressor as a function of shaft speed. At part speed, a controversy called “rotating instability” type flow field modulation is identified with the measurements. New results are the demonstration of the periodic behavior of this instability and the analogy to classical frequency modulation, periodic to one revolution of the instability. Furthermore, the amplitude of the instability is modulated by the time period of a rotor revolution. At nominal speed, the abrupt spike type stall inception is detected, taking usually less than five rotor revolutions.

## 1. Introduction

At the low mass flow rate end of the operating range, every axial compressor will ultimately experience rotating stall, one or several local rotating detached flow cell(s). This can be followed by surge, which is a system instability with a possible global flow reversal. There are two widely recognized rotating stall inception types for low- and high-speed axial compressors: modal and spike [1], though weak rotating perturbations can be present before the rotating stall inception, allowing a stable compression system operation. They are often reported as rotating instabilities in literature [2].

The need for detailed measurements in high-speed axial compressors and their analysis was clearly stated by Day [1] in 2015 reviewing 75 years of stall research and derived from flow features that can only be found in high-speed compressors. That environment poses a challenge in terms of measurement cost and technique but here the measurements are necessary to understand the instabilities arising in a real aircraft engine compressor. Numerical studies can be used for complementary flow field understanding but their limitations

(particularly induced by the use of RANS modeling) need to be considered.

The spike stall inception describes an onset mechanism starting from a local strong perturbation of the flow field in the tip region of a rotor. Recent numerical and experimental works converge towards explaining the typical increase and decrease in wall pressure by a vortex structure forming at the leading edge of the rotor blade and spanning to the casing (“tornado vortex”). Inoue et al. [3] identified this numerically at first, and recent numerical and experimental works by Pullan et al. [4] support those results. In high-speed compressors, the spike type structure evolves very quickly (a few rotor revolutions) into a rotating stall cell.

Rotating disturbances can be observed already at a mass flow rate greater than the stall inception point and appear as a regular modulation of the flow field prior to surge. This disturbance does not induce a significant flow blockage in the concerned rotor contrary to the rotating stall. They have been sometimes reported as high-frequency rotating stall [5] or pressure waves [6], with cells numbers and rotation speed higher than the ones observed with rotating stall.

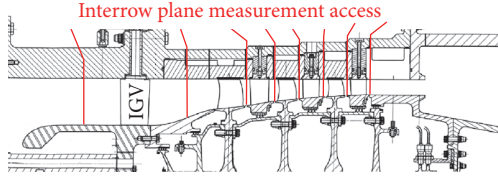


FIGURE 1: Meridian view of CREATE and measurement planes.

A certain controversy called rotating instability (RI) could be understood as a subtype of the rotating disturbances. The RI induces a characteristic frequency bump (or rake) in a pressure spectrum compared to a single peak for the rotating disturbances. The source mechanism of the RI appears to be closely related to the spike formation as demonstrated by Inoue et al. [7] and Yamada et al. [8]. The RI occurs mostly in low-speed compressors and with large rotor tip gaps. A flow separation has to occur at the leading edge of usually a rotor blade, causing a probable leading edge vortex. The flow separation can also be provoked by a corner separation in a case without tip gaps as identified by Beselt et al. [9]. What eventually induces the “unstable” behavior, causing the multiple frequencies, has to be identified yet.

Firstly, the high-speed multistage compressor test case and the experimental methods will be presented. Then, two types of instabilities will be discussed: spike and rotating instability. The high-frequency measurements allow a characterization of the abrupt spike type stall inception at nominal shaft speed. Furthermore, this work will present original results about the periodic behavior of a rotating instability at part shaft speed, contrary to what would be expected from the naming in literature.

## 2. Test Case (CREATE)

For this work, the research compressor *CREATE* (Compreseur de Recherche pour l’Etude des effets Aérodynamiques et TÉchnologiques) is investigated in the laboratory of fluid mechanics and acoustics (*LMFA*) at Ecole Centrale de Lyon, France. The geometry and rotation speed of the 3.5-stage high-speed axial research compressor are representative of high-pressure compressor median rear blocks of a modern turbojet engine, designed by Safran Aircraft Engines.

The compressor and the measurement planes are presented in Figure 1. The rotor shaft is driven at a design speed of 11543 rpm, whereby the flow is slightly transonic in the first stage and fully subsonic in the last two stages. More characteristics of *CREATE* are given in Table 1. The spatial circumferential periodicity of the 3.5 stages is reduced to  $2\pi/16$  by choosing all numbers of blades as a multiple of 16, as stated in Table 2. Consequently one temporal period corresponds to 1/16th of a rotor revolution. A profound knowledge-base has been acquired with *CREATE* for numerical and experimental methods aiming at flow field investigations in the high-speed multistage compressor environment [10–13]. Standard tip gap sizes are implemented compared to increased tip gaps in rotors 2 and 3 in the previous version of *CREATE*.

TABLE 1: Characteristics of *CREATE* at design point.

Casing diameter	0.52 m
Core speed	11543 rpm
Rotor 1 tip speed	313 m/s
Rotor 1 tip inlet relative Mach number	0.92

TABLE 2: Number of blades of *CREATE*.

Row	IGV	R1	S1	R2	S2	R3	S3
Number of blades per row ( $2\pi/16$ )	2	4	7	5	7	5	7

TABLE 3: Relative measurement uncertainties for high frequency static pressure measurements estimated for *CREATE* by [14].

	Weak gradient zones	Strong gradient zones
Rotor 1	0.47%	3.3%
Rotor 2	0.51%	3.0%
Rotor 3	0.60%	3.0%

## 3. Experimental Methods

The main characteristics of the high-frequency casing pressure measurements are summarized hereinafter. Furthermore, global performance measurements are conducted but not described in more detail here. Ottavy et al. [10] state more details about this test rig and give an exhaustive introduction of the experimental methods, whereas only a brief summary is given hereinafter.

**3.1. High-Frequency Wall Static Pressure Measurements.** High-frequency wall static pressure measurements have been carried out for a general description of the flow field and the study of the onset of instabilities near surge and the surge inception. For capturing all the unsteady features of the flow, the wall static pressure measurements have been acquired simultaneously with a frequency of 500 kHz using 48 sensors (Kulite: XTE-190). Six probes can be installed per interrow plane and 12 probes per rotor tip. The sensors, used without their protective grid, have a correct frequency-response up to about 160 kHz, where the BPFs of rotors 2 and 3 correspond to 15 kHz. More details about the high-frequency-response acquisition system are stated in the works of Gourdin et al. [11] and Courtiade [14], and the relative measurement uncertainty is given in Table 3.

**3.2. Data Treatment Methods.** The data treatment is done consistently in this work and defined hereinafter. The mass flow rate, isentropic efficiency, and pressure ratio are normalized by their respective maximum values or given as difference. Entropy, temperature, and pressure are normalized by their overall time-mean rise in the compressor according to (1). The time axis might be normalized by the rotating

frequency of the shaft. The nondimensional data is labeled “normalized” (or “norm.”)

$$X_{\text{norm}} = X_{\text{mes}} \times \frac{1}{\overline{X}_{\text{outlet}} - \overline{X}_{\text{inlet}}}. \quad (1)$$

Static variables are arithmetically averaged in space, whereas convected variables ( $X_c$ ) are weight-averaged by the axial velocity ( $V_{x_i}$ ) according to

$$\overline{X}_c = \frac{1}{N \cdot \overline{V}_x} \cdot \sum_{i=0}^{N-1} X_i \cdot V_{x_i}. \quad (2)$$

Temporal averages are performed as arithmetic averages.

In this work, rotating frequencies of flow structures are obtained with the help of cross-correlations between the signals of probes (e.g., signal 1 and signal 2) located at identical axial positions but different circumferential positions. The cross-correlation allows the estimation of the time lag between the passing of a flow structure in front of probe 1 and that in front of probe 2. The time lag is estimated between the maximum of the autocorrelation of signal 1 and the maximum of the cross-correlation between signals 1 and 2.

Knowing the circumferential distance between the probes ( $\Delta\theta_{12}$  in radians) and the time lag ( $\Delta t$  in seconds), a rotating frequency ( $\omega_{\text{flow structure}}$ ) can be calculated according to

$$\omega_{\text{flow structure}} = \frac{1}{2\pi} \cdot \frac{\Delta\theta_{\text{probes}}}{\Delta t}. \quad (3)$$

#### 4. Stall Inception in the Compressor CREATE

The stall inception type is a function of the rotor speed in this high-speed compressor. In this work it is therefore possible to present observations on rotating instabilities and spikes.

**4.1. Global Overview.** The global total pressure ratios at 80%, 90%, and 100% shaft rotation speed are presented in Figure 2 and give an overview of identified instabilities in this compressor. The pressure rise distributions reach a rather flat part towards the low mass flow rate before the system falls into surge (see “approximated surge line”). The often called “peak” of the pressure rise distribution is not exceeded here at any rotation speed. The measurements allow the detection of a spike type stall inception at 100% shaft speed and a rotating instability (RI) type stall inception at part shaft speed. This work will present observations concerning these two instabilities with detailed measurement data at 80% (representative of the part speed flow field) and 100% shaft rotation speed.

In this compressor and as usual in a well matched multistage compressor [1], the instability and stall inception occurs in rotor 1. The general characteristics of the instability onset are described with help of Figure 3 for 80% shaft speed on the left and 100% shaft speed on the right. Six signals are presented per speed. They are obtained from the high-frequency casing pressure probes that are positioned around the circumference at a plane just upstream of rotor 1. For these surge inception measurements, the outlet throttle valve

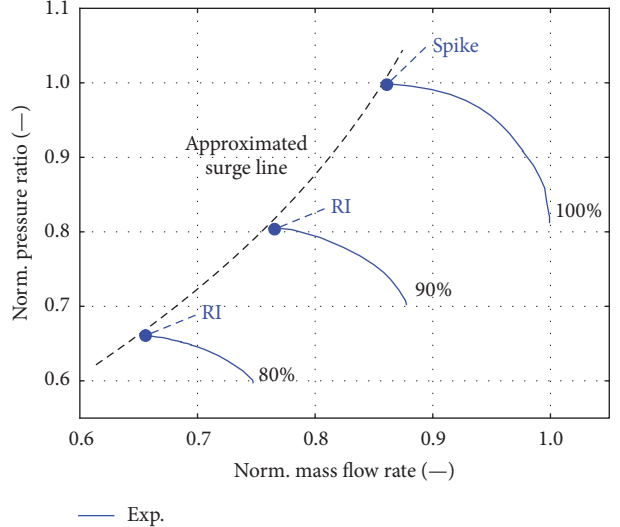


FIGURE 2: Experimental results for total pressure ratio at part and nominal rotation speeds.

is closed continuously and very slowly from a stable operating point, giving quasi-steady operating conditions and avoiding the generation of “steps” in the pressure signals when the throttle is closed step by step. The signals are low-pass-filtered below the BPF and they are shown for 23 rotor revolutions.

At both shaft speeds, a single rotating stall cell forms between rotations 14 and 18. The circumferential extension of the cell is growing rapidly during two rotations while the cell’s LE is rotating at  $0.6 \Omega$  (estimated with cross-correlations according to (3)). The compressor falls abruptly into surge between revolutions 18 and 20.

At 80% shaft speed, the instability is present in hundreds of rotations prior to the rotating stall cell (quantified later in Figure 7). It is seen as somewhat of noise in the signals here. The rotating stall cell forms (indicated with the black dashed circle) without any detectable trace of a spikelike flow perturbation in this compressor. The difference between the rotating stall cell and RI signature will be discussed with a wavelet analysis later on.

At 100% shaft speed, the typical increase and decrease related to a spike type perturbation are found [4]. The increase and decrease of the static pressure extend each over four rotor blade passing instances (not detailed here). At the first detection, the rotating speed of the spike is estimated to be  $0.9086 \Omega$  with the help of cross-correlations between the six signals, applying (3). The spike structure evolves within less than 2 rotor revolutions into a single rotating stall cell, which is forming at revolution 16. The whole stall inception process is abrupt at 100% shaft speed and takes less than 20 rotor revolutions in any measured case and a stall warning system could not react in this short span of time.

At all investigated shaft speeds, temporal mode 1 (normalized by the shaft rotating frequency) is present in the flow field in rotor 1. At 80%, this mode causes a modulation of the rotating instability and can be found as a wavelike modulation of the signals in Figure 3(a). At 100% shaft speed, mode 1

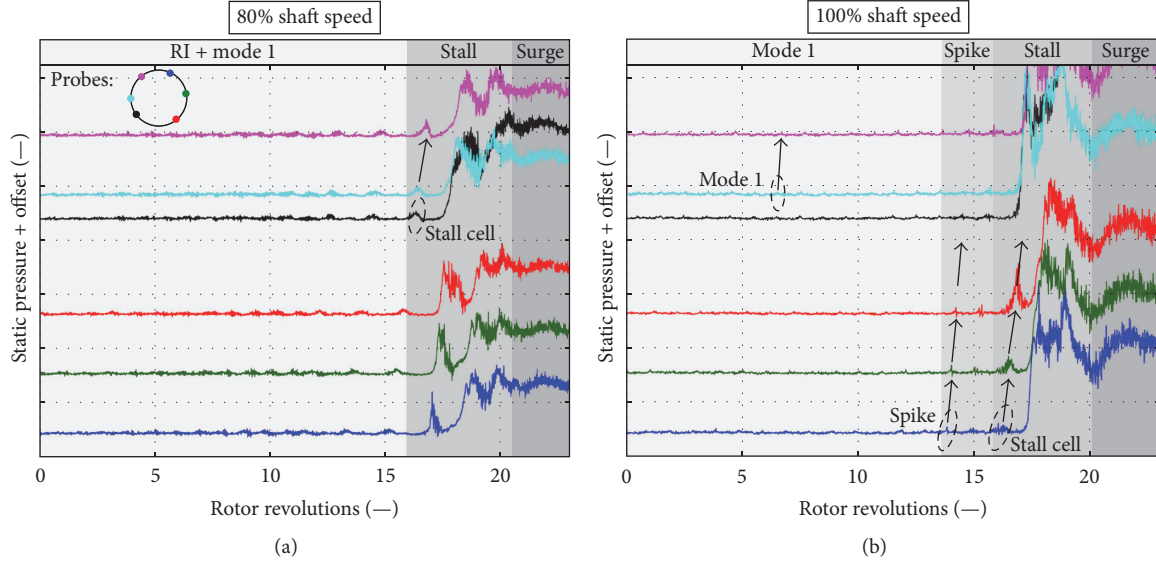


FIGURE 3: Static pressure signals (low-pass filtered below BPF) of six probes around the circumference upstream of the rotor 1 LE during stall inception at 80% (a) and 100% (b) shaft speed with an identical scale.

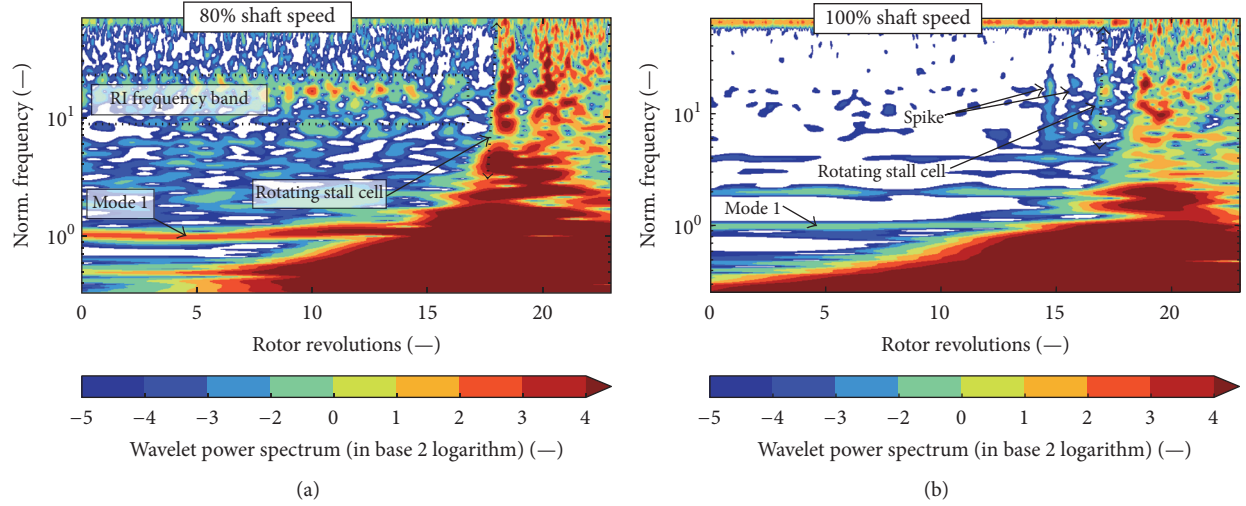


FIGURE 4: Wavelet power spectra for the green signals (2nd circ. pos. from the bottom) in Figure 3 for 80% (a) and 100% (b).

is visibly better because no instability is present in the flow field. The rotation speed of this mode corresponds to the rotation speed of the shaft. It might be therefore the signature of a geometrical default in the rotor. This default might be found in about 4–8 blades (temporal extension of pressure peaks) with a different tip gap than the surrounding blades but further tip gap measurements are necessary to support this hypothesis. It might be the geometrical trigger for the onset of the spike inception. Weichert and Day [15] found that, in 90% of the investigated stall inception events, the spike perturbation would form in the same rotor passage due to a geometrical default.

Wavelet spectra shall clarify the timeline of the formation of the instability structures during the stall inception. Figure 4 shows the wavelet power spectra computed on the green

signal (2nd signal from the bottom) in Figure 3. The wavelet spectra are obtained using the tools of Torrence and Compo [16] with a Morlet wavelet, which has been proven useful for turbomachinery applications, for example, by Lin et al. [17]. The wavelet analysis is conducted in each case with an input signal normalized by the standard deviation computed on the first half of the signal. The vertical axis traces the normalized frequency (by the shaft rotating frequency) and the horizontal axis the rotor revolutions, which correspond to the ones presented in Figure 3.

At 80% speed, the RI is seen as a wide frequency band with elevated power. The origin of these frequencies will be discussed later on in this work. The BPF is located at the upper limit of the spectrum. It corresponds to the normalized frequency 64 whereas the RI frequency band can be seen

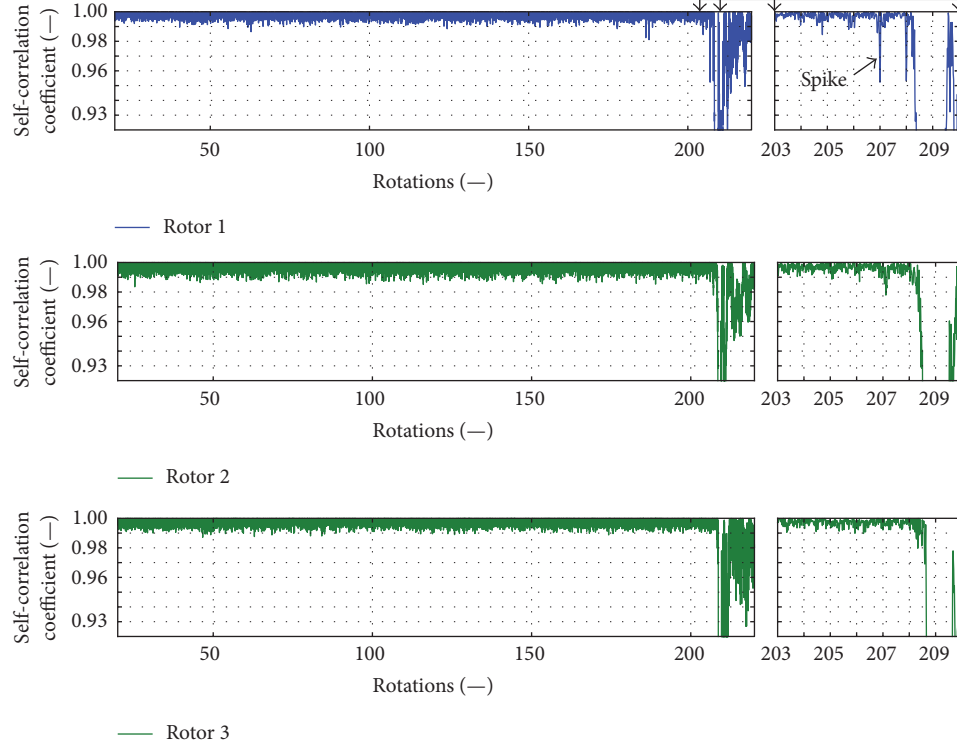


FIGURE 5: Disturbance detection by “self-correlation” of casing pressure signals at LE of rotors 1 to 3 at 100%  $\Omega$ .

around 18. The BPF is not disturbed by the rotating instability. The rotating stall cell appears as a vertical trace in the wavelet spectrum. Low frequency content related to the rotating stall and surge causes the zone of high power (red). The absence of the interblade pressure gradient due to the detached flow (rotating stall cell) is found as an interruption of the BPF trace in the wavelet spectrum. Surge is eventually seen as a chaotic spectrum without a clear frequency content starting from about rotor revolution 19.

At 100% shaft speed, mode 1 is present as well (Figure 4(b)) up to the rotating stall inception. Tracing of mode 1 is no longer possible once the low frequency content arises (large white zone) and a clear link between mode 1 and the spike is therefore not possible. The spike is seen at normalized frequency 16. That corresponds to the inverse of the temporal extension. With 64 rotor blades, the temporal extension corresponds thus to 25% of the rotor blades passing in time. Recent research work demonstrates a vortexlike structure as the initial form of the spike, for example, the work of Pullan et al. [4]. This present arrangement of measurement probes does not detect this vortexlike structure with less than one pitch extension. The spike structure might grow too rapidly circumferentially in between the measurement probe locations.

The flow perturbation is understood as a rotating stall and no longer spike or RI, when the BPF is disturbed because of the possible absence of the interblade pressure gradient. This frontier is indicated with a dashed line (with arrows at both ends) for both shaft rotation speeds.

A fine spike detection method and the origin of the RI frequency band are discussed in the following parts of this paper.

**4.2. Spike Detection Method.** The temporal and spatial locations of the stall inception are identified with an analysis of the casing pressure signals above the rotors (close to the LE) during more than 200 rotor revolutions prior to any surge inception. One example is presented for the spike type stall inception at 100% shaft speed in Figure 5. For this detection method, the signals are cut in segments representing each temporal period ( $2\pi/16\Omega$ ) and are low-pass-filtered below the blade passing frequency at 7 kHz, allowing the detection of small (compared to BPF) stall inception related disturbances. A cross-correlation is calculated between each segment and the corresponding one a revolution earlier (“self-correlation”). Normalized by the autocorrelation, a correlation coefficient of 1 represents a perfect match between two signals. The maxima of the cross-correlations per temporal period are eventually plotted and give a fine measure for meaningful changes in the flow field. This stall precursor detection method resembles the one proposed by Dhingra et al. [18]. A spike would decrease the maximum correlation coefficient. Please note that the rotor revolution numbers in Figure 5 are not related to the one seen in Figure 5 earlier.

Globally, the unsteadiness increases in flow direction. This is seen as increasing background noise or band of fluctuations between 0.99 and 1. The surge inception occurs between revolutions 208 and 209 and is found as drop of the coefficient below values of 0.925. In this example, a

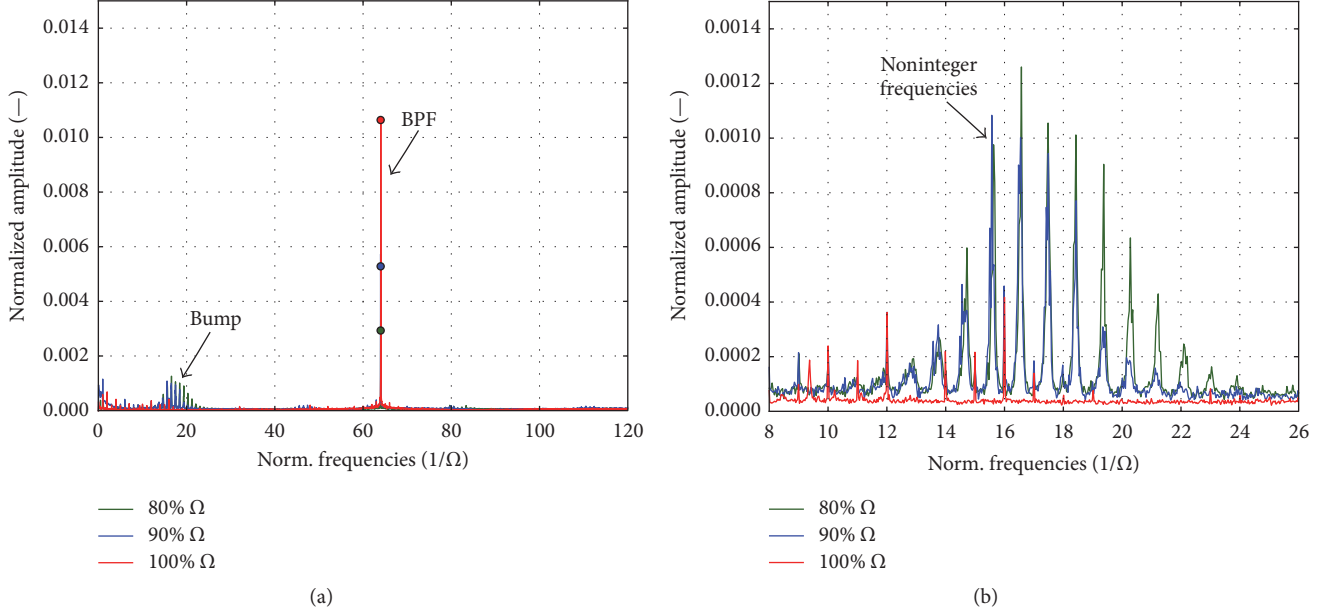


FIGURE 6: Frequency spectra of a casing pressure probe close to the rotor  $\sim 1$  LE in comparison of three shaft rotation speeds ( $80\% \Omega$ ,  $90\% \Omega$ , and  $100\% \Omega$ ), “full” spectrum (a), and zoom on frequency bump (b).

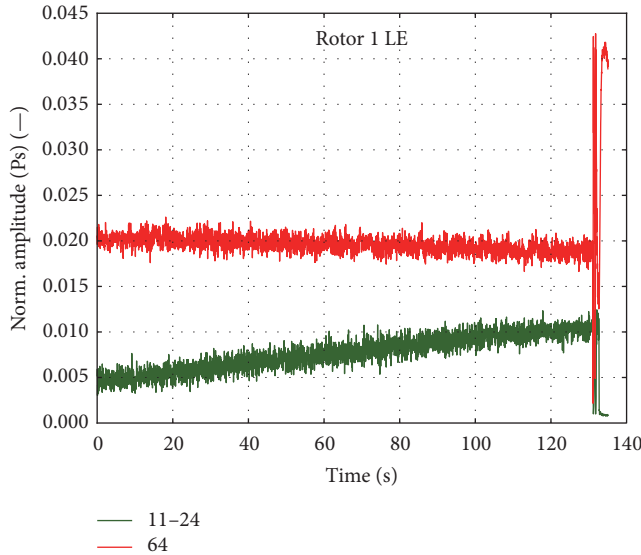


FIGURE 7: Temporal evolution of rotating instability modes (11 to 24) and rotor blade passing frequency during surge inception measurement.

disturbance appears about 20 revolutions prior to the surge inception in rotor 1 (understood as “predisturbance”). It causes the coefficient to drop to a value outside of the noise band. With the instrumentation setup, this is not always observed before surge inception in this compressor. In all surge inception measurements though, the “last” disturbance prior to surge occurs first in rotor 1. This can be seen in the zoom in Figure 5 on the right at revolution 207. During the same revolution, a disturbance is also found in rotor 2. In none of the measurements, rotor 2 shows the disturbance

prior to the one in rotor 1. Furthermore, the predisturbances occur only in rotor 1 and never in rotor 2 or 3. A disturbance arises always last in rotor 3, only as a consequence of the disturbances upstream. In conclusion, disturbances leading to the stall inception of the compressor occur in rotor 1.

This method was also applied to measurements at part shaft speed but a unique perturbation such as the spike was not detected (not shown here). The observations on the RI and the stall inception with the RI present in the flow field will be presented hereinafter.

**4.3. Rotating Instability (RI).** For an operating point close to the stall limit, frequency spectra are obtained from signals of a high-frequency casing pressure probe axially located close to rotor 1 leading edge and presented for three shaft speeds ( $80\% \Omega$ ,  $90\% \Omega$ , and  $100\% \Omega$ ) in Figure 6. The input signals have a length corresponding to about 400 rotor revolutions, and the spectra are integrated over bands of  $6 \text{ Hz}/\Omega$  to reduce the noise. Always when approaching the stall limit at part speeds ( $80\% \Omega$  and  $90\% \Omega$ ) with the CREATE compressor, an increase of several amplitudes (forming a “bump”) is observed in these frequency spectra at about 30% of the dimensionless blade passing frequency (12 to 24 compared to 64). The maximum amplitude of the bump reaches about 12% of the BPF of the rotor 1. That is also the case in the measurements for a previous version of the compressor at part speed but has not been investigated before. These frequencies do not arise at  $95\% \Omega$  in the previous compressor version. Thus the switch from spike type stall inception to a type with multiple frequencies happens probably between  $90\% \Omega$  and  $95\% \Omega$ . The available measurement data does not allow linking this switch to a change in the flow field.

The multiple peaks are characteristic of rotating instabilities as commonly reported in literature. The discrete peaks

are found at about the same normalized frequencies comparing multiple measurements for the two part shaft speeds presented in this paper. The RI peaks arise at nonintegers of the shaft speed. This is different from the 100% shaft speed, where peaks are found in the same frequency range but are harmonics of the shaft rotation speed, or correspond to harmonic 16 which is linked to the compressor periodicity. At 100% shaft speed, a noninteger exception is the normalized frequency of about 9.3. It is not related to the RI but probably related to an acoustic phenomenon in the downstream rotors, as referred to in the work of Courtade and Ottavy [6].

The frequency gap between the RI peaks is constant and is a characteristic of RI. This link between the peaks and the rotating frequency was also identified by Kameier and Neise [19]. It corresponds to the rotating frequency of the RI. In the present case, the rotating speed ( $\omega_{RI}$ ) has been calculated from the cross-correlations between signals obtained at different circumferential positions just upstream of rotor 1, applying (3). It leads to  $\omega_{RI} = 0.925 \Omega$ , which perfectly fits the frequency gaps between the peaks of the RI bump.

Rotating frequencies of  $0.5 \Omega$  to  $0.65 \Omega$  have been reported in several works on RI ([2, 20–22]) and  $0.7 \Omega$  was reported by Inoue et al. [7]. Note that among these references the works of Baumgartner et al. [20] and Vignau-Tuquet and Girardeau [22] were conducted on high-pressure compressors. Also a rotation speed of  $0.9 \Omega$  has been reported by Zhang et al. [23] in a numerical work on a turbine working locally as a compressor at low mass flow rate. In the present case,  $\omega_{RI} = 0.925 \Omega$  appears high but not out of range of what has been reported in literature. The maximum amplitude is found close to the rotor 1 LE and there is no trace of the instability in rotors 2 and 3 (not detailed here). Likewise, Mailach et al. [2] reported the maximum RI amplitude in the first 30% of rotor blade chord. Furthermore we know from their work (and others) that the RI trace is usually limited to 10% of span towards the casing.

Figure 7 presents the RI bump's amplitude evolution over hundreds of rotations towards surge inception. The temporal evolutions of the RI (integrated over the normalized frequencies from 11 to 24) and the rotor 1 BPF are presented based on the casing pressure signal from a probe positioned close to the rotor 1 LE. The temporal evolution is obtained from windowed Fourier transforms using signals with a length of three rotor revolutions per window and an overlap of 1.5 revolutions. The measurements start at a loaded stable operating point and the outlet throttle valve is closed very slowly giving quasi-steady operating conditions. The compressor falls into stall and surge after about 131 seconds from the beginning of the presented acquisition. During the valve closing, the BPF decreases in amplitude by less than 10% but the integrated amplitude of the RI doubles. The RI amplitude reaches a critical level (close to stall) when it surpasses half of the BPF amplitude in this compressor configuration. This information could be fed into a stall warning system. Eventually, the RI is evolving into rotating stall without a detectable spike type stall inception as shown in Figure 3.

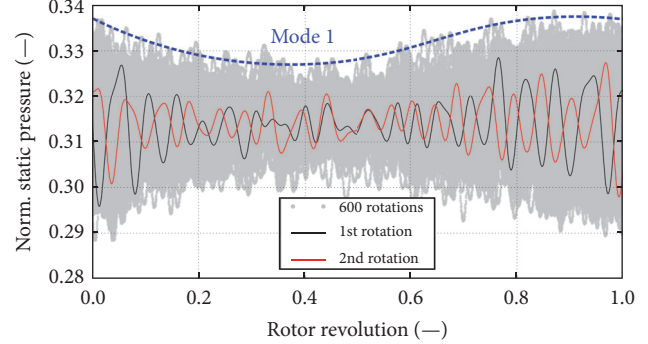


FIGURE 8: Casing pressure signal of 600 rotor revolutions stacked and superposed on two example revolutions (low-pass filtered at 5 kHz, below BPF) at a location above rotor 1 close to the LE.

The main focus in the next section is put on the periodic rotating behavior of the RI in this compressor, contrary to the unstable behavior suggested by the naming “rotating instability.”

**4.3.1. Variation of Temporal Extension of RI Disturbances.** The observations on the temporal extension variations of the RI disturbances will be presented from raw signal plots to a detailed frequency analysis in this section.

Figure 8 shows unsteady casing pressure signals acquired with a measurement probe located close to the LE of rotor 1 at the casing. The signals are low-pass-filtered below the BPF at 5 kHz. An example of two successive rotor revolutions is plotted in red and black. The oscillations in those signals correspond to RI passing in front of the probe. The grey envelope is obtained in superimposed time trace of the pressure signals over 600 rotor revolutions. It reveals temporal mode 1 over one rotor revolution. The minimum modulation is found at about 0.4 rotor revolutions and the maximum modulation at the beginning or ending of the rotor revolutions. The amplitude modulation is in the order of magnitude of the RI induced fluctuations. With the RI present, the amplitude modulation might present the influence of the compressor on the RI. One could imagine that, once per rotor revolution, rotor blades with different tip gaps than the average pass by the measurement probe and modulate the RI amplitude. This is a hypothesis but could not be verified because time-resolved tip gap measurements were not available.

Figure 9 presents also the two previous successive pressure signals, but with a time axis now equal to the RI revolution time period ( $t_{RI} = 1/\omega_{RI} = 1/0.925$  rotor rev.). Those two pressure signals are well in phase. This could be shown for any two arbitrary successive signals. It reflects the temporal periodicity of the RI (related to the rotating frequency  $\omega_{RI}$ ) over the RI revolution time period. Furthermore, a regular spaced cosine is also plotted in the figure as a reference (black dashed line). The peaks of the two pressure signals are aligned only very few times with the reference cosine. That implies a temporal extension variation of the RI disturbances out of the perspective of the fixed probe in the casing. This temporal extension variation appears periodic because of the

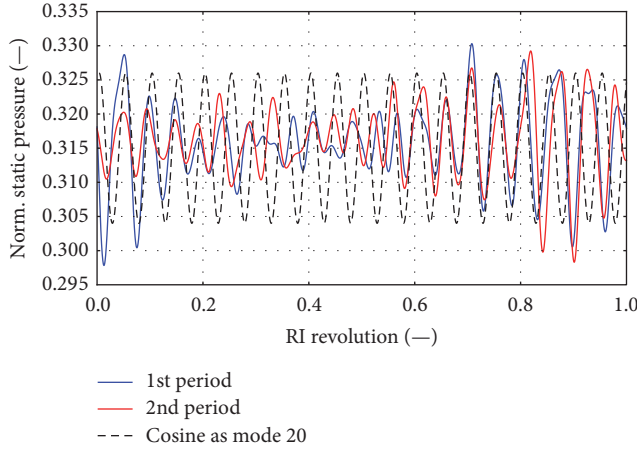


FIGURE 9: Two successive RI revolutions of the rotating instability in the casing pressure signal from above the rotor 1 LE (low-pass filtered at 5 kHz, below BPF, colored lines), and cosine as reference (black dashed line).

fairly good match between the two periods. Additionally, the effect of the previously demonstrated amplitude modulation (AM), associated with mode 1 in Figure 8, is visible here. The AM causes peaks of different amplitudes between two RI revolutions (“red” versus “blue”) at a given time point of a RI revolution. That can be explained by the fact that the AM is not periodic to a revolution of the RI but to a rotor revolution.

In conclusion, the pressure signals present fluctuations with nonconstant periods which are in phase over a time corresponding to one RI revolution, but an amplitude modulation of the RI is imposed by the rotor periodicity.

Hereafter, the variation of the temporal extension of the RI induced fluctuations is evaluated with a wavelet analysis.

Figure 10 shows the casing pressure signal (a) low-pass-filtered at 7 kHz (below BPF). Counting the RI induced peaks in the signal does not yield a constant number per rotor revolution. The short signal length of three rotor revolutions might give another impression because of the temporal periodicity being very close to one shaft rotation ( $1/\omega_R = 1/0.925 \text{ rev.} = 1.081 \text{ rev.}$ ).

At the bottom of the same figure, the wavelet power spectrum is shown with a zoom on the rotating instability frequencies. The variation of the temporal extension of one RI disturbance is seen as a modulation in the wavelet spectrum. A high frequency is related to a narrow peak (short temporal extension) in the low-pass-filtered signal, and vice versa for a low frequency. The temporal evolution of the “frequency with the maximum wavelet power” can be extracted as a signal, which is sketched with the black solid line.

This “frequency with the maximum wavelet power” signal is presented for 10 rotations in Figure 11(a). Faulty peaks can be explained by the limited temporal resolution of the wavelet spectrum. With Fourier transforms of this extracted signal, the frequency spectrum is computed and shown in Figure 11(b). The main frequencies constituting this signal are the rotating frequency of the rotating instability ( $\omega_{\text{RI}} = 0.925 \Omega$ ) and its harmonics.

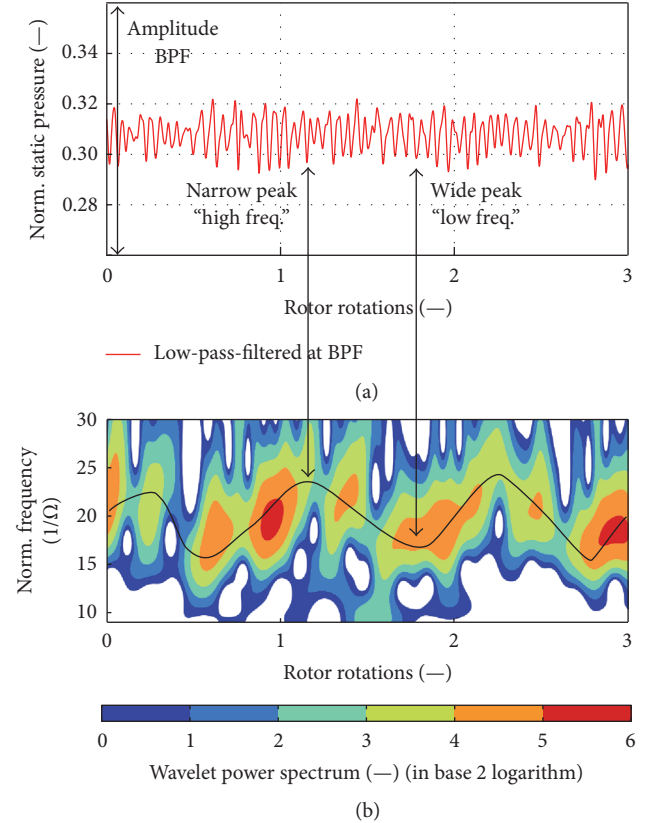


FIGURE 10: Rotating instability characterization with casing pressure signals over three rotor revolutions (a) and wavelet power spectrum (b).

This result allows the interpretation that the rotation of the disturbance relative to the blade row seems to cause the periodic modulation of the disturbance over the circumference. Consequently, the temporal period of the modulation corresponds to  $1/\omega_{\text{RI}} = 1.081$  rotor revolutions. In other words, one RI revolution corresponds to 1.081 rotor revolutions. Counting the peaks passing over 600 RI revolutions leads to a mean number of 20.097 peaks per RI revolution, with a standard deviation of 1.02 peaks. Note that RI revolutions with 21 peaks are followed immediately by RI revolutions with 19 peaks, which explains the standard deviation. This shows that there is no change in the number of peaks or rotation speed of the instability over hundreds of RI revolutions up to rotating stall inception.

**4.3.2. Discussion.** The result of a classical RSI would be a regular spaced (in time and space) lobed structure according to Tyler and Sofrin [24] and induce a single peak in the frequency spectra of a pressure signal. For a multistage compressor, Courtiade et al. [25] demonstrated that the amplitude of the mode could change with the time, but not its frequency. The RI is not a classical RSI because it is found as an irregular spaced lobed structure in time. That means its structure is not imposed by a blade row with constant blade pitches. The periodic temporal extension variations resemble the result of a classical frequency modulation (FM), which consists of a

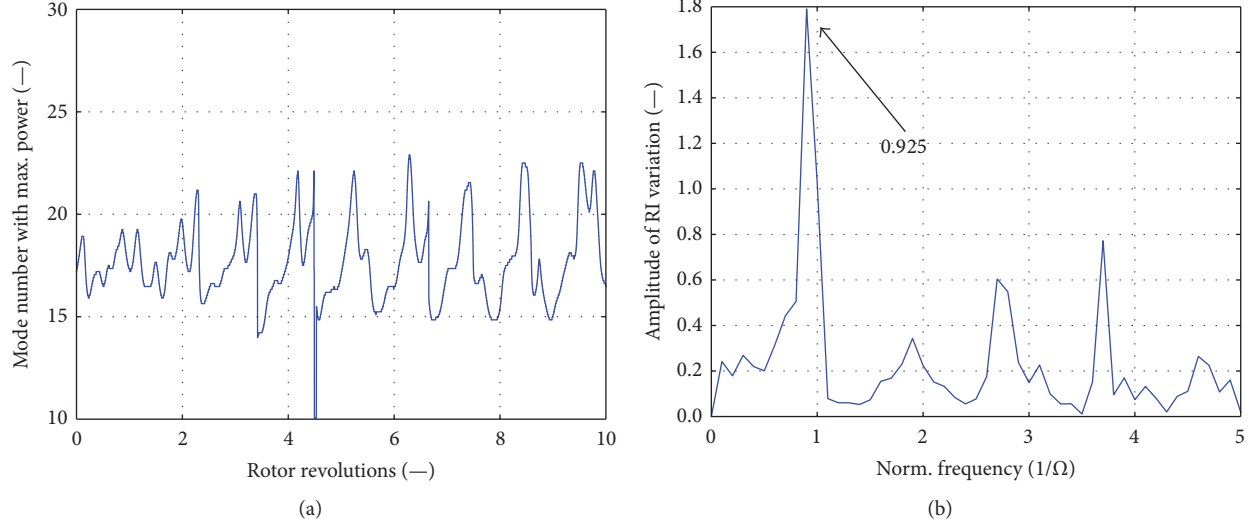


FIGURE 11: Frequency variation of rotating instability over time: temporal evolution (a); frequency spectrum (b).

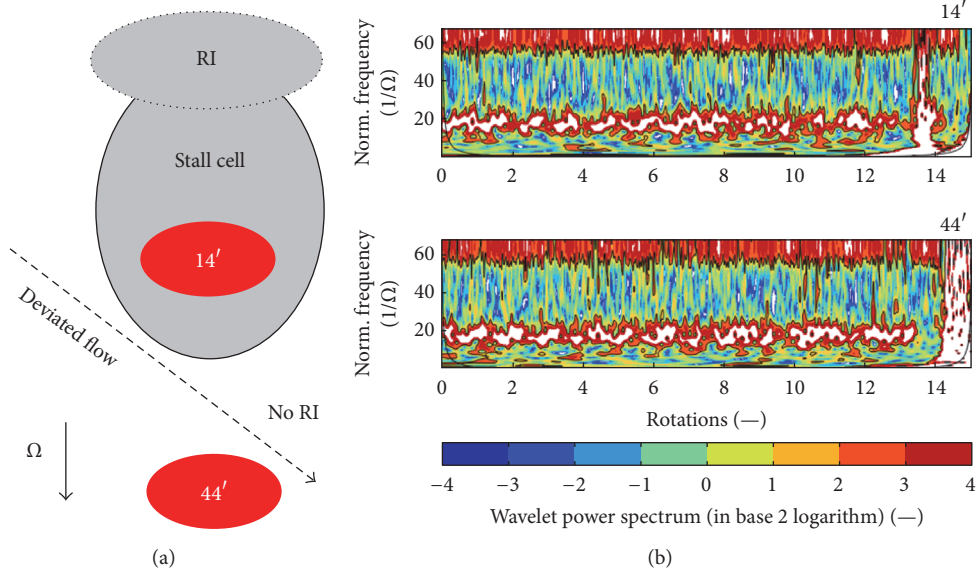


FIGURE 12: Rotating instability trace in wavelet analysis (b) and sketch (a) based on two signals positioned upstream of rotor 1 at 14' and 44' (red ellipse).

high frequency (the carrier signal) and a modulation signal. Furthermore, a FM would also be seen as multiple peaks in a frequency spectrum. In the case of the RI, the carrier frequency is a theoretical unmodulated rotating disturbance with a frequency of  $f_c = 20 \times 0.92 \Omega = 18.5 \Omega$ . The rotating disturbance might be caused by a separation vortex on the rotor blade suction surface and its interaction with the neighboring blade passages [3] but cannot be resolved with the fairly coarse measured grid (12 synchronized wall pressure probes). The modulation signal is equal to the rotating frequency of the RI with  $f_m = \omega_{RI} = 0.925 \Omega$  (as found with the wavelet analysis). A relative motion of the disturbance to the blades would be also observed in a compressor cascade, where RI can also occur as shown by Beselt et al. [9].

**4.3.3. RI at Stall Inception.** We observed in this compressor that once a rotating stall cell is detected (e.g., local vanishing of interblade pressure gradient), the frequency trace of the rotating instability disappears as shown in Figure 12. The signals of two probes (positioned at 14' and 44' upstream of rotor 1) are analyzed with wavelet transforms, and the amplitude variations of the normalized frequencies up to the rotor 1 BPF are given in the two power maps. The signals are zoomed in about 13 rotations prior to rotating stall inception. The wavelet transforms are conducted with a temporal resolution which allows the detailed analysis of the amplitude evolution. A wavelet analysis is always a trade-off between frequency and temporal resolution. Thus the frequency resolution of the BPF is not ideal here and is

found as a large horizontal band above normalized frequency 60. Again, the rotating instability is found in the band of normalized frequency of 11 to 24.

The stall inception is seen as vertical stripe of elevated power (white) at rotation 13.5 at the top (14') and rotations 14 at the bottom (44'). Note that the rotor is turning from probe 1 (14') to probe 2 (44'), and so does the rotating stall cell. Close to the probe at 14' the rotating stall cell forms, induces a blockage, and causes a diversion of the flow that decreases the loading in this part of the rotor, as introduced by Emmons et al. [26]. As a consequence, the rotating instability is no longer seen in the unloaded sector of the rotor, that is, by the probe at 44'. This behavior is summarized in the sketch in Figure 12(a). The rotating instability disappears thanks to the reorganization of the flow field. This shows the very fast response of the rotating instability to changes in the flow field. The rotating instability does not reappear once the rotating stall cell is established as can be seen after rotation 14 of the signal at 14'.

## 5. Conclusion

This work made use of high-frequency measurements for the study of rotating instability and spike type stall inception in a high-speed compressor.

Widely reported characteristics of rotating instabilities in low-speed compressors could be identified here (e.g., frequency rake and rotation speed) at part speed in this high-speed multistage compressor (CREATE). The high-speed environment and standard tip gap sizes make this an unprecedented test case.

An original new result for the rotating instability is the demonstration of a constant rotation speed ( $0.925 \Omega$ ) with a constant number of disturbances (20) over a large number of rotating instability revolutions. The variation over time of the disturbance extension was identified to resemble classical frequency modulation (FM), periodic to  $1/0.925 \Omega$ , causing the well-known frequency rake. Additionally, an amplitude modulation (AM) occurs, periodic to a rotor revolution, and marks the modulation of the rotating instability by the compressor system (e.g., geometry defaults). Finally the rotating instability characterized by a bump (frequency rake) in the spectra appears in the present case to be very stable, contrary to the controversy chosen naming.

The modulation of possible rotating separation vortices (forming the rotating instability) needs to be proven with higher spatially resolved measurements. In future collaborative works, the newly identified characteristics of the rotating instability could be verified on existing measurement databases of cases presented in literature.

For nominal compressor speed, a fine spike detection method was applied but the first spikelike perturbations appear usually only up to 5 rotor revolutions prior to surge in this compressor. That demonstrates the abrupt stall onset in the high-speed axial compressor environment. This makes a useful stall warning system impossible. Pressure measurements on the rotor blade surface close to the tip might be necessary for an earlier and finer detection of the spike inception.

## Nomenclature

BPF:	Blade passing frequency
RI:	Rotating instability
$\Omega$ :	Rotating speed of the compressor shaft
$\omega_{\text{RI}}$ :	Rotating frequency of rotating instability
PE, L, NS:	Peak efficiency, loaded, and near surge operating points
Rev.:	Revolutions
LE:	Leading edge.

## Conflicts of Interest

The authors declare that they have no conflicts of interest.

## Acknowledgments

The authors are grateful to Safran Aircraft Engines for supporting the CREATE compressor research program and for granting permission to publish these results. The funding provided via the Consortium Industrie-Recherche en Turbomachines (CIRT) is gratefully acknowledged. The analysis of the measurement data would not have been possible without the high-quality acquisition by the measurement team for the high-speed test rigs at the LMFA, formed of Sébastien Goguely, Gilbert Halter, Pierre Laucher, and Lionel Pierrard. Their help and advice for the work with the experimental data are gratefully acknowledged.

## References

- [1] I. J. Day, "Stall, surge, and 75 years of research," *Journal of Turbomachinery*, vol. 138, no. 1, Article ID 011001, 16 pages, 2015.
- [2] R. Mailach, I. Lehmann, and K. Vogeler, "Rotating instabilities in an axial compressor originating from the fluctuating blade tip vortex," *Journal of Turbomachinery*, vol. 123, no. 3, pp. 453–460, 2000.
- [3] M. Inoue, M. Kuroumaru, T. Tanino, S. Yoshida, and M. Furukawa, "Comparative studies on short and long length-scale stall cell propagating in an axial compressor rotor," *Journal of Turbomachinery*, vol. 123, no. 1, pp. 24–32, 2001.
- [4] G. Pullan, A. M. Young, I. J. Day, E. M. Greitzer, and Z. S. Spakovszky, "Origins and structure of spike-type rotating stall," *Journal of Turbomachinery*, vol. 137, no. 5, Article ID 051007, 11 pages, 2015.
- [5] I. J. Day, T. Breuer, J. Escuret, M. Cherrett, and A. Wilson, "Stall inception and the prospects for active control in four high-speed compressors," *Journal of Turbomachinery*, vol. 121, no. 1, pp. 18–27, 1999.
- [6] N. Courtiade and X. Ottavy, "Experimental study of surge precursors in a high-speed multistage compressor," *Journal of Turbomachinery*, vol. 135, no. 3, Article ID 061018, 9 pages, 2013.
- [7] M. Inoue, M. Kuroumaru, S. Yoshida, T. Minami, K. Yamada, and M. Furukawa, "Effect of tip clearance on stall evolution process in a low-speed axial compressor stage," in *Proceedings of the ASME Turbo Expo*, pp. 385–394, Vienna, Austria, June 2004.
- [8] K. Yamada, H. Kikuta, M. Furukawa, S. Gunjishima, and Y. Hara, "Effects of tip clearance on the stall inception process in

- an axial compressor rotor," in *Proceedings of the ASME Turbo Expo 2013*, San Antonio, Tex, USA, June 2013.
- [9] C. Beselt, B. Pardowitz, R. Van Rennings, and P. U. Thamsen, "Influence of the clearance size on rotating instability in an axial compressor stator," in *Proceedings of the 10th European Conference on Turbomachinery Fluid dynamics & Thermodynamicsics*, Lappeenranta, Finland, 2013.
- [10] X. Ottavy, N. Courtiade, and N. Gourdain, "Experimental and computational methods for flow investigation in high-speed multistage compressor," *Journal of Propulsion and Power*, vol. 28, no. 6, pp. 1141–1155, 2012.
- [11] N. Gourdain, F. Wlassow, and X. Ottavy, "Effect of Tip clearance dimensions and control of unsteady flows in a multi-stage high-pressure compressor," *Journal of Turbomachinery*, vol. 134, no. 5, Article ID 051005, 13 pages, 2012.
- [12] J. Schreiber, X. Ottavy, G. N. Boum, S. Aubert, and F. Sicot, "Numerical simulation of the flow field in a high speed multistage compressor-study of the time discretization sensitivity," in *Proceedings of the ASME Turbo Expo 2015*, Montreal, Canada, June 2015.
- [13] J. Schreiber, X. Ottavy, G. N. Boum, and N. Gourdain, "Influence of rotor tip flow field mis-prediction on rotating disturbance near surge in a high speed multistage compressor," in *Proceedings of the ASME Turbo Expo 2016*, Seoul, South Korea, June 2016.
- [14] N. Courtiade, *Experimental analysis of the unsteady flow and instabilities in a high-speed multistage compressor [Ph.D. thesis]*, Ecole centrale de Lyon, Ecully, France, 2012.
- [15] S. Weichert and I. Day, "Detailed measurements of spike formation in an axial compressor," *Journal of Turbomachinery*, vol. 136, no. 5, Article ID 051006, 9 pages, 2013.
- [16] C. Torrence and G. P. Compo, "A practical guide to wavelet analysis," *Bulletin of the American Meteorological Society*, vol. 79, no. 1, pp. 61–78, 1998.
- [17] F. Lin, J. Chen, and L. Meilin, "Wavelet analysis of rotor-tip disturbances in an axial-flow compressor," *Journal of Propulsion and Power*, vol. 20, no. 2, pp. 319–334, 2004.
- [18] M. Dhingra, Y. Neumeier, J. V. R. Prasad, and H.-W. Shin, "Stall and surge precursors in axial compressors," in *Proceedings of the 39th AIAA/ASME/SAE/ASEE Joint Propulsion Conference and Exhibit*, Huntsville, Ala, USA, July 2003.
- [19] F. Kameier and W. Neise, "Experimental study of tip clearance losses and noise in axial turbomachines and their reduction," *Journal of Turbomachinery*, vol. 119, no. 3, pp. 460–471, 1997.
- [20] M. Baumgartner, F. Kameier, and J. Hourmouziadis, "Non-engine order blade vibration in a high pressure compressor," in *Proceedings of the in 12th International Symposium on Airbreathing Engines*, Melbourne, Australia, 1995.
- [21] J. März, C. Hah, and W. Neise, "An experimental and numerical investigation into the mechanisms of rotating instability," *Journal of Turbomachinery*, vol. 124, no. 3, pp. 367–374, 2002.
- [22] F. Vignau-Tuquet and D. Girardeau, "Aerodynamic rotating vortex instability in a multi-stage axial compressor," in *Proceedings of the in 17th International Symposium on Airbreathing Engines*, Munich, Germany, 2005.
- [23] L. Y. Zhang, L. He, and H. Stür, "A Numerical investigation of rotating instability in steam turbine last stage," *Journal of Turbomachinery*, vol. 135, no. 1, Article ID 011009, 2012.
- [24] J. M. Tyler and T. G. Sofrin, "Axial flow compressor noise studies," *SAE Transactions*, vol. 70, pp. 309–332, 1962.
- [25] N. Courtiade, X. Ottavy, and N. Gourdain, "Modal decomposition for the analysis of the rotor-stator interactions in multistage compressors," *Journal of Thermal Science*, vol. 21, no. 3, pp. 276–285, 2012.
- [26] H. W. Emmons, C. E. Pearson, and H. P. Grant, "Compressor Surge and Stall Propagation," *Transaction of the ASME*, vol. 77, pp. 455–469, 1955.

## Research Article

# Investigation of Performance and Rotor Tip Flow Field in a Low Speed Research Compressor with Circumferential Groove Casing Treatment at Varying Tip Clearance

**Matthias Rolfes, Martin Lange, and Ronald Mailach**

*Technische Universität Dresden, Institute of Fluid Mechanics, Chair of Turbomachinery and Flight Propulsion,  
01062 Dresden, Germany*

Correspondence should be addressed to Matthias Rolfes; matthias.rolfes@tu-dresden.de

Received 16 March 2017; Accepted 1 June 2017; Published 31 July 2017

Academic Editor: Funazaki Ken-ichi

Copyright © 2017 Matthias Rolfes et al. This is an open access article distributed under the Creative Commons Attribution License, which permits unrestricted use, distribution, and reproduction in any medium, provided the original work is properly cited.

Experimental investigations in a single-stage low speed axial research compressor are presented. The influence of four different rotor tip clearances on the overall compressor performance and on the rotor tip flow field is investigated in configurations with and without circumferential groove casing treatments. Piezo-resistive pressure transducers are used to capture the unsteady flow field in the rotor tip region. The investigated casing groove is effectively working at the three largest investigated tip clearance sizes. The largest achieved operating range increase by the groove is 6.9%. The groove can delay the upstream movement of the flow interface between leakage flow and main flow and thus increase the stable operating range. Rotating instabilities are shown to exist at large tip clearance sizes in throttled operating conditions. Their amplitudes can be damped by the casing groove. No modal activities could be detected in the current single-stage compressor build.

## 1. Introduction

The relative motion between blades and casing dictates the necessity of radial clearances in an axial compressor. It is commonly known that an increase in tip clearance to chord ratios decreases pressure ratio, efficiency, and normally operating range of an axial compressor; see, for example, Wisler [1] and Cumpsty [2]. In service, the clearance ratios of a gas turbine's axial compressor are normally not constant but change due to wear, transient operations, and thermal expansions. Moreover, the minimum absolute clearance level can also be constrained by different thermal expansions of the components. As modern compressors tend to have very high pressure ratios, the last stages have very small blade heights which, together with the above-mentioned constraints, leads to larger clearance ratios here. The use of wide-chord blades is not able to totally compensate for this effect. These observations underline the fact that axial compressors at least partially run with tip clearances that are greater than favored by aerodynamic, which lead to the above-mentioned performance penalties.

One possible means to recover a loss in operating range due to a tip clearance increase is the use of circumferential groove casing treatments. Their simplicity and ease of installation put them in the focus of research for several decades. In the 1970s several experimental works [3–5] showed the general effectiveness of circumferential groove casing treatments. It is also in this early period that the potential of grooves to reduce the sensitivity towards large tip clearances has been proven. One example for a more recent investigation on circumferential groove CTs using CFD methods is the work by Shabbir and Adamczyk [6]. The authors showed that the flow of the compressor is stabilized by a momentum exchange between groove and main passage flow and furthermore that grooves reduce the aerodynamic blockage near the rotor tip. Concerning the working mechanism of casing groove some authors, for example, Lu et al. [7], Perrot et al. [8], and Rolfes et al. [9], showed that grooves work by delaying the upstream movement of the flow interface between tip leakage flow and passage flow and therefore shift the point where spill-over of leakage flow occurs towards lower mass flows. On the other hand, Houghton and Day [10] and Li et al. [11] showed

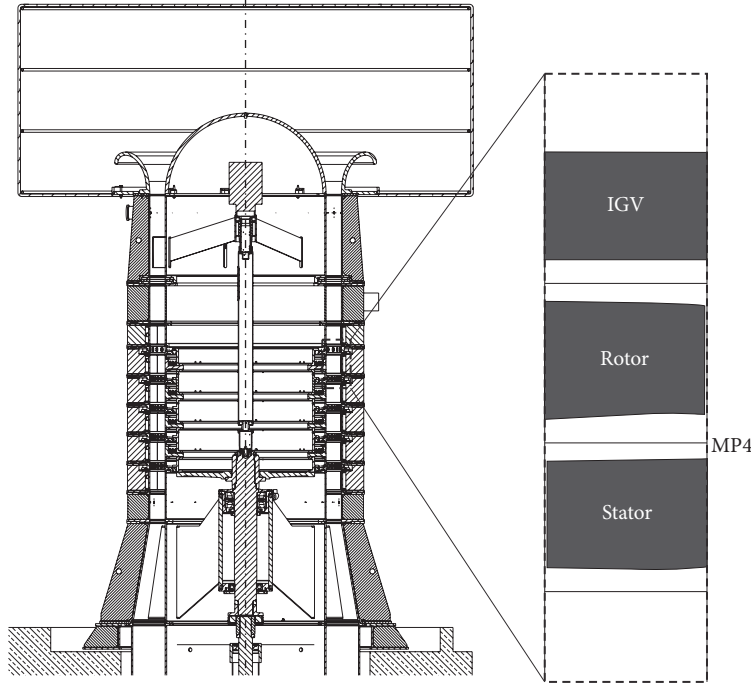


FIGURE 1: LSRC Dresden, cross section of single-stage build.

that the influence of the flow interface is not mandatory for a well working circumferential groove. This shows that the working mechanism of circumferential groove is still not universally understood and that different mechanisms might exist.

Compressor stability, the reason for surge or stall and the way towards it, is in the focus of interest since compressors in gas turbines became widely used. A very detailed overview of research in this field is given by Day [12]. Mailach et al. [13] and März et al. [14] investigated the highly controversial field of rotating instabilities (RI) within the topic of compressor stability. Mailach et al. found out that the observed disturbances are called forth by periodic fluctuations of the tip leakage vortex. Other authors, for example, Wisler et al. [15], connect the occurrence of RI in Mailach et al. to the fact that one stage of the four-stage compressor has been weakened by a tip clearance increase. Young et al. [16], however, found similar disturbances as Mailach et al. and März et al. that rotated relative to the rotor under near stall conditions in their investigated single-stage compressor with large tip clearance. According to Camp and Day [17] compressor stall can be caused by a local (mostly in the rotor tip) flow breakdown, the so called spikes, in only one or two blade passages that grow into stall cells. The authors also found modal oscillations that exist long before stall and are characterized by flow field oscillations of a wavelength of the compressor circumference or half the circumference. Modes are not directly linked with compressor stall, but can grow into a stall cell with further throttling. These authors concluded that modes appear when the compressor stalls with a positively (or zero) sloped characteristic and spikes when the characteristic is negatively sloped at stall.

In this paper a single-stage low speed axial compressor with and without casing grooves at four different rotor tip clearances is investigated. Besides overall performance, the influence of tip clearance increases and casing groove on the rotor tip flow field is shown. Their influence on rotating instabilities and modal oscillations will also be addressed to increase understanding of these phenomena.

## 2. Test Compressor and Measurement Techniques

The investigations have been performed on the Low Speed Research Compressor at Technische Universität Dresden. The reference configuration of the LSRC consists of 4 stages. One characteristic of the compressor is its vertical arrangement. The air passes 4 repeating stages from top to bottom. Different operating points are set by a throttle in the basement. The cross section of the compressor is shown in Figure 1 and reference build parameters can be found in Table 1. Boos et al. [18] and Künzelmann et al. [19] presented detailed information about the compressor installation and measurement results for the reference build. For the investigation at hand the compressor has been installed in a single-stage configuration. Different tip clearances were realized by milling the compressor blades to the desired height. Four rotor tip clearances were investigated. The smallest tip clearance (TC) is  $s/c = 1.2\%$  and has been increased to  $s/c = 2.5\%$ ,  $s/c = 3.7\%$ , and  $s/c = 5.0\%$ . Stator hub clearance has been kept constant at  $s/c = 2.1\%$ . The installed blading has been the same as in Rolfs et al. [9]. It has been designed by ALSTOM Power to model the rear stages of a high pressure compressor of a state of the art gas turbine.

TABLE 1: Data of the LSRC reference build.

Casing diameter	1500 mm
Hub-to-tip ratio	0.84
Blade count IGV	51
Blade count rotor	63
Blade count stator	83
Chord length rotor, MS	110 mm
Chord length stator, MS	89 mm
Solidity of rotor blades, tip	1.55
Mass flow, DP	$\dot{m} = 25.35 \text{ kg/s}$
Reynolds number rotor inlet, MS	$Re = 5.7 \cdot 10^5$
Mach number rotor inlet, MS	$Ma = 0.22$

DP: design point; MS: midspan.

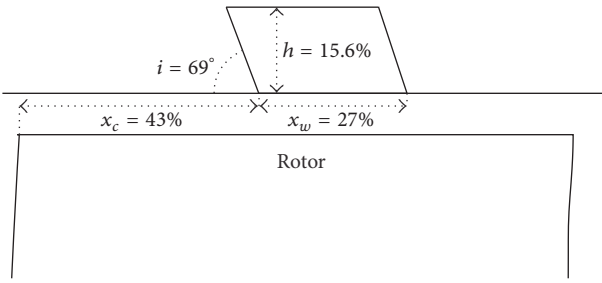


FIGURE 2: Geometry of circumferential casing groove.

The geometry of the circumferential casing groove is depicted in Figure 2. The performance of the compressor with  $s/c = 5.0\%$  and this groove has already been described in Rolfes et al. [9].

This paper presents the characteristics of the compressor and results from unsteady wall pressure measurements with piezo-resistive pressure transducers which were installed flush in the rotor casing. All measurements were performed at design speed of 1000 rpm at standard conditions.

Compressor characteristics are composed of 11 throttle positions from open throttle to stall. At each of these positions the stator vanes are traversed in 57 uniformly distributed steps over two pitches. These data are arithmetically averaged to form one point on the speed line. The overall pressure rise is determined with an accuracy of  $\pm 0.02\%$  by 12 casing static pressure taps in the exit plane and 6 casing static pressure taps in the inlet plane of the compressor. To calculate the total pressure ratio, the total pressures in the inlet and exit planes are derived by an iterative procedure from the static values by the assumption of a perfect gas. Thus, the curves of the total pressure ratio presented in this paper are derived from casing static pressure taps. To calculate the efficiency, data from a high-precision torquemeter (accuracy 0.01% full-scale at 5000 Nm) are used which results in a measuring accuracy of the efficiency of  $\pm 0.2$  percentage points (representing the 95% confidence interval). Total temperature at the inlet of the compressor is measured via 8 resistance thermometers in the filter cage. In the exit plane 6 total temperature probes equipped with

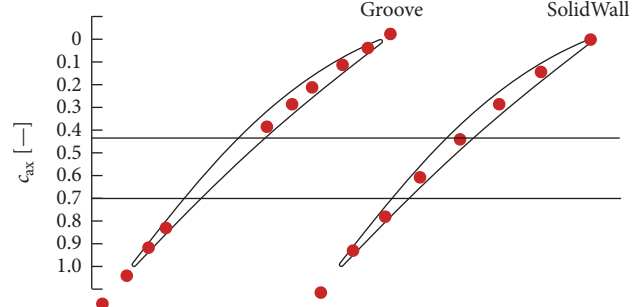


FIGURE 3: Arrangement of pressure transducers over rotor, left: Groove, right: SolidWall.

a thermocouple are equally spaced around the compressor circumference. Enthalpy is derived from the measured quantities of temperature and pressure by the assumption of a perfect gas. The stall point of the compressor has been explicitly tested for each configuration. The performance parameters of the compressor characteristics are calculated as follows:

$$\eta = \frac{\dot{m}_{in} \cdot (h_{total,is,out} - h_{total,in})}{M \cdot 2\pi n}$$

isentropic efficiency

$$\xi = \frac{\dot{m}_{in} \cdot \sqrt{T_{total,in}} / p_{total}}{\dot{m}_{in,DP} \cdot \sqrt{T_{total,in,DP}} / p_{total,DP}}$$

flow rate coefficient (1)

$$\pi_t = \frac{p_{total,out}}{p_{total,in}} \quad \text{total pressure ratio}$$

$$\Psi_{t-s} = \frac{2 \cdot (p_{out} - p_{total,in})}{u_{MS}^2 \cdot \rho}$$

total-to-static pressure coefficient

$$\phi = \frac{v_{ax}}{u} \quad \text{flow coefficient.}$$

Mounting piezo-resistive pressure sensors flush with the rotor casing allows the unsteady wall pressure over the rotor to be captured. For these measurements the stator vanes have been traversed in 21 steps over one pitch. The arrangement of the transducers along the blade chord can be found in Figure 3. The left hand side shows the sensors for the groove configuration and the right hand side that of the solid wall configuration. For clarity, the limits of the circumferential groove are plotted on both sides.

The standard deviation of the unsteady wall pressure, which is used in the presentation of the results, is defined as follows:

$$\sigma_p = \sqrt{\frac{1}{N} \sum_{i=0}^{N-1} (p_i(t) - \langle p(t) \rangle)^2}. \quad (2)$$

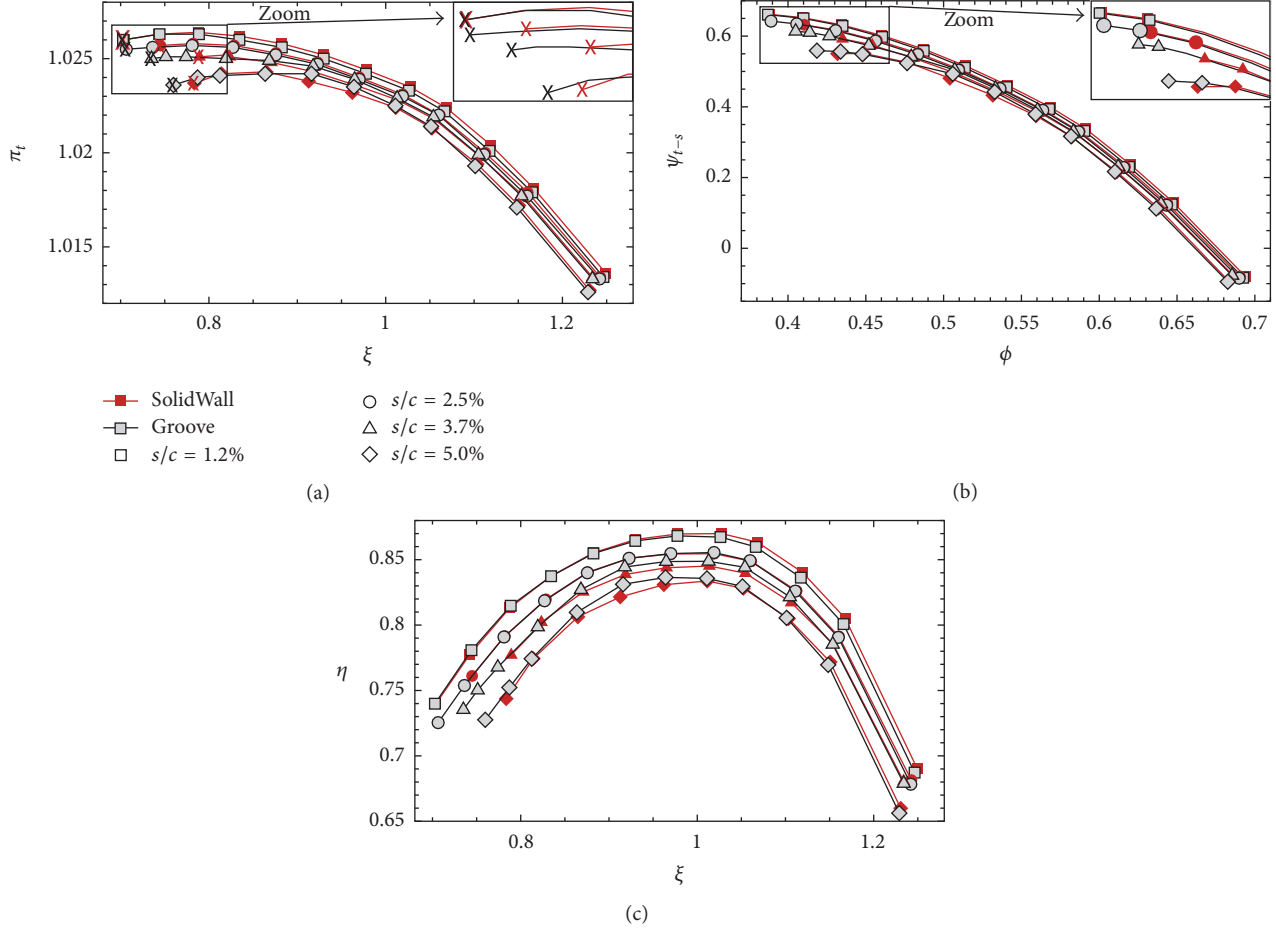


FIGURE 4: Compressor characteristics: (a) total pressure ratio, (b) total-to-static pressure coefficient, and (c) efficiency.

Here,  $p_i$  is the current pressure value,  $N$  is the number of revolutions, and  $\langle p(t) \rangle$  is the ensemble-averaged pressure value.

### 3. Results

**3.1. Compressor Characteristics.** The compressor characteristics for all four tip clearance sizes are plotted in Figure 4. The throttle settings are identical between each configuration. Figure 4(a) shows the total pressure ratio over flow rate coefficient. In this part of the figure, the last stable operating points are marked by an X to better distinguish the stall points between SolidWall and Groove. The zoomed region has the same intention. Figure 4(c) shows isentropic efficiency over flow rate coefficient and the total-to-static pressure coefficient is plotted over flow coefficient in Figure 4(b). Here, the zoomed region only shows symbols for the last two measured points on the characteristic curve to simplify the identification of the slopes of the characteristics. The flow coefficients of the stall point and the percentage reduction in stall mass flow due to the Groove can be found in Table 2 for all tested configurations.

At the smallest tip clearance of  $s/c = 1.2\%$  the compressor has the highest total pressure ratio and efficiency due to

TABLE 2: Stalling flow coefficients and percentage reduction of stall mass flow for each configuration.

$s/c$	Configuration	$\phi_{\text{Stall}}$	$\Delta m_{\text{Stall}}$
1.2%	SolidWall	0.388	0%
	Groove	0.387	
2.5%	SolidWall	0.410	
	Groove	0.389	5.1%
3.7%	SolidWall	0.435	
	Groove	0.405	6.9%
5.0%	SolidWall	0.432	
	Groove	0.419	3.0%

the lowest tip leakage flow loss. The Groove is not able to positively influence either total pressure ratio, efficiency, or stall mass flow (see Table 2) at this tip clearance size. At flow rate coefficients close to stall Groove and SolidWall show nearly identical total pressure ratios and efficiencies whereas at flow rates higher than design ( $\xi \geq 1.0$ ) both are slightly reduced by Groove. One reason for the lack of operating range increase can be that the rotor is not tip-critical in this configuration.

As expected, an increase of tip clearance to  $s/c = 2.5\%$  leads to a loss in total pressure ratio and efficiency and an increase in stall mass flow. The casing treatment obviously starts working at this size of tip clearance. With the casing treatment the stall mass flow is reduced by 5.1% (Table 2). The compressor is now able to run at a flow rate coefficient as low as that of SolidWall of the smallest tested tip clearance size  $s/c = 1.2\%$ . The Groove configuration still shows a small reduction in total pressure ratio which, however, is smaller than at  $s/c = 1.2\%$ . Isentropic efficiency is not decreased by the Groove at this size of tip clearance.

With further increased tip clearance to  $s/c = 3.7\%$  total pressure ratio, efficiency, and operating range decrease. The Groove remains effective and decreases the minimum flow rate coefficient by 6.9% compared to SolidWall at the same clearance level, which can be seen in Table 2. Groove at this tip clearance size now even reaches a slightly lower minimum mass flow than SolidWall of  $s/c = 2.5\%$ . The highest decrease of flow rate coefficient leads to the assumption that the Groove is most effective at this clearance configuration. Another distinctive feature in this configuration is the increase in total pressure ratio and efficiency in regions  $0.85 < \xi < 1.1$ .

The last tip clearance increase to  $s/c = 5.0\%$  leads to a stronger decreasing total pressure rise and efficiency of SolidWall near stall than in the steps of tip clearance increase before. Furthermore, the stall mass flow of SolidWall has not been increased in contrast to  $s/c = 3.7\%$  but has been slightly reduced. This behavior is reproducible and has been measured several times. The Groove, however, is still able to decrease the minimum stall mass flow by 3% (Table 2). The Groove increases efficiency in the region from  $\xi = 1.1$  to stall by a maximum of 1%.

According to Camp and Day [17] and Day [12] the total-to-static characteristics are helpful to identify the type of stall inception. With a negatively sloped total-to-static characteristic stall is likely to occur by spikes whereas a zero slope indicates modal stall inception. The total-to-static pressure coefficient clearly shows negative slopes at tip clearance sizes of  $s/c = 1.2\%$ ,  $s/c = 2.5\%$ , and  $s/c = 3.7\%$  for both SolidWall and Groove, which can be seen in the zoomed region in Figure 4(b). Here, stall is likely to occur via spikes. The largest tip clearance configuration however shows a zero slope near stall for SolidWall and thus, according to Camp and Day, possible modal activities. The Groove configuration of  $s/c = 5.0\%$ , however, shows again a negative slope.

It is noteworthy that the zero slope of the total-to-static characteristics occurs at the tip clearance size that showed no increase in stall mass flow compared to the next smaller tip clearance.

The following is an addition to a comparison of different investigations in open literature that has been presented by Berdanier and Key [20]. They plotted the percentage increase in stall flow coefficient relative to the smallest tested tip clearance size  $\Delta\phi_{\text{Stall}}$  over tip clearance size for results from Wisler [1], McDougall [21], and their own test results. In Figure 5, which is based on Berdanier and Key, the data from the present paper are added as well as data of both compressors A and B from Wisler et al. [15]. The clearance

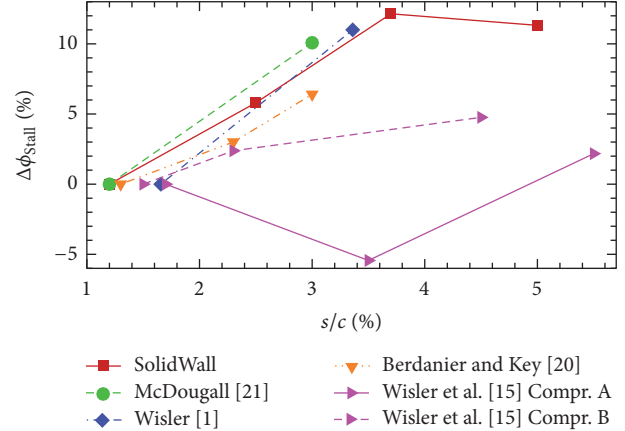


FIGURE 5: Stalling flow coefficient at different tip clearance sizes.

TABLE 3: Clearance derivatives of different investigations.

Investigation	Clearance derivative $\delta$
Wisler [1]	6.5
McDougall [21]	5.6
Berdanier and Key [20] TC1-2	3.0
Berdanier and Key [20] TC2-3	4.8
Wisler et al. [15] Compr. A TC1-2	-3.0
Wisler et al. [15] Compr. A TC2-3	3.8
Wisler et al. [15] Compr. B TC1-2	3.0
Wisler et al. [15] Compr. B TC2-3	1.1
Present Paper TC1-2	4.5
Present Paper TC2-3	5.3
Present Paper TC3-4	-0.6

derivative  $\delta$  (the increase in stall flow coefficient per 1% clearance increase) that has also been discussed by Berdanier and Key is shown in Table 3 for the same test cases as in Figure 5. Some of the investigations tested more than two tip clearance sizes, so the derivatives for each step of tip clearance increase are listed (TC1-2, e.g., is the first step of tip clearance increase of the particular investigation).

The increase in stall mass flow that resulted from a tip clearance increase from  $s/c = 1.2\%$  to  $2.5\%$  (TC1-2) and from  $s/c = 2.5\%$  to  $3.7\%$  (TC2-3) in the present paper fits well into the data presented by Berdanier and Key. The clearance derivatives of 4.5 and 5.3, respectively, are within the range of 3 to 6 that the other investigations show. This increase in clearance derivative from TC1-2 to TC2-3 has also been shown by Berdanier and Key for their compressor. The last tested tip clearance increase from  $s/c = 3.7\%$  to  $5.0\%$  (TC3-4) in this paper, however, shows a remarkably different behavior because the stall mass flow is not increased but decreased and hence the derivative is -0.6. This behavior has not been detected by [1, 20, 21] because their largest tip clearance size is notably lower than the largest tested tip clearance size in this paper. Wisler et al. [15] tested two compressors A and B with largest tip clearance sizes of  $s/c = 5.5\%$  and  $s/c = 4.5\%$ ,

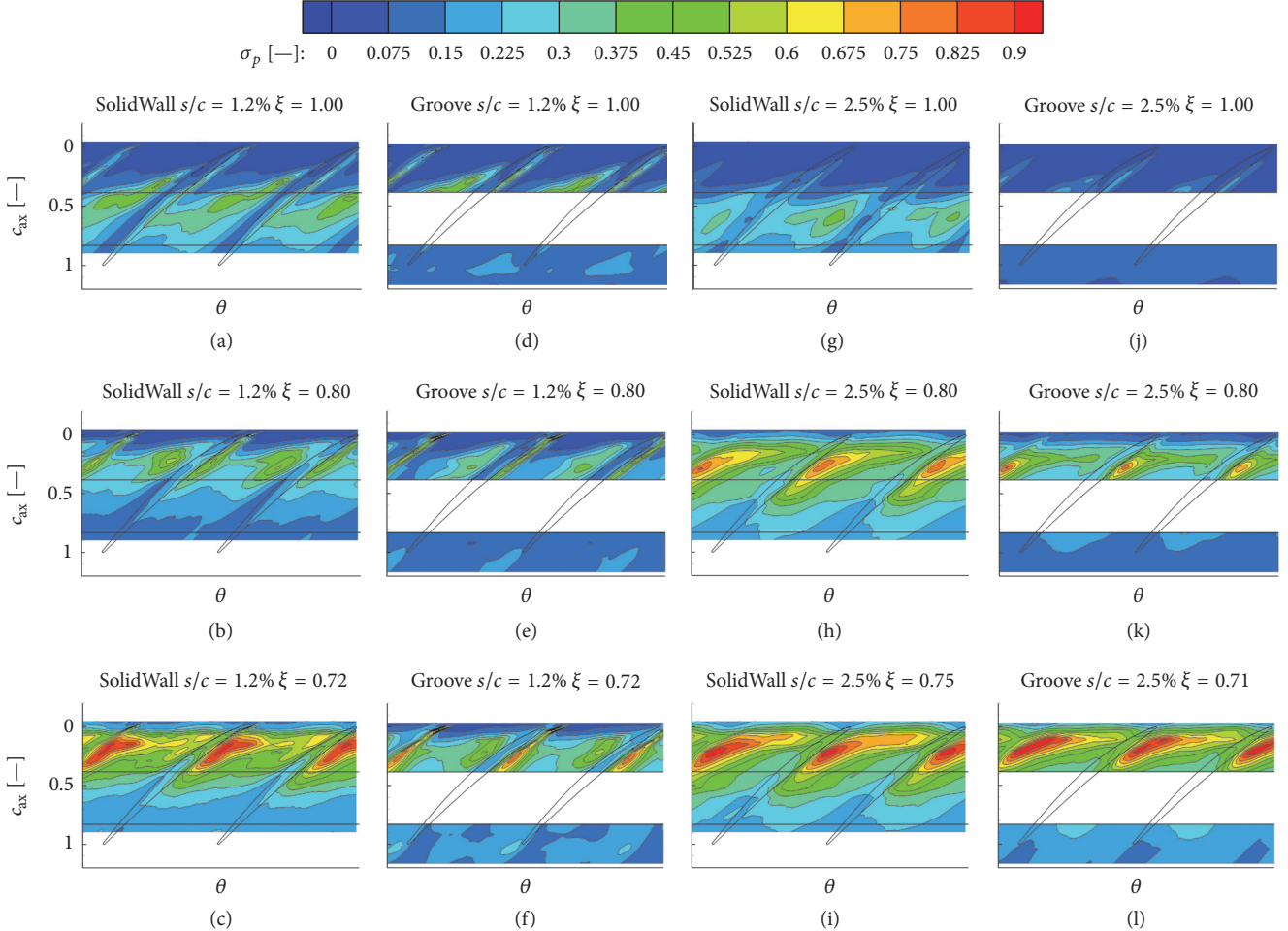


FIGURE 6: Standard deviation of casing static pressure over rotor for SolidWall and Groove at  $s/c = 1.2\%$  and  $s/c = 2.5\%$  at three different operating points ((a, d, g, j): design point, (b, e, h, k): throttled operating point, and (c, f, i, l): near stall of current configuration).

respectively. Both compressors show a different behavior than the results presented before. Compressor A shows at TC1-2 a decrease in stall mass flow which results in a clearance derivative of  $-3$ . According to Wisler et al. stability in compressor A is limited by tip and hub blockage whereas compressor B is more sensitive to tip blockage and therefore has a derivative of  $3$  at TC1-2. These results show that the clearance derivative is strongly dependent on the investigated compressor and that effects like a shift of the stall mechanism (either from hub to tip or possibly from rotor to stator) with tip clearance can also play a dominant role. The second tip clearance increase of compressor B in [15] shows a derivative of only  $1.1$ . One could speculate that this reduced derivative of TC2-3 compared to TC1-2 hints to a similar behavior as in the present paper, a negative derivative at larger tip clearances. It is however not visible due to the limited number of investigated tip clearance sizes in [15] that result in an almost doubling of tip clearance size from TC1-2 to TC2-3. Thus, the fact that other investigations do not show a negative clearance derivative at larger tip clearances might be also due to a relatively low resolution between tightest and largest clearance.

The information from the present investigation is a valuable addition to data in open literature. It confirms the findings of Berdanier and Key [20] and add new information for tip clearances larger than  $s/c = 4\%$ .

**3.2. Wall Pressure over Rotor.** The following section deals with the results of the unsteady wall pressure measurements over the rotor.

The standard deviation of the static wall pressure ( $\sigma_p$ ) is plotted over two rotor pitches in Figure 6 for  $s/c = 1.2\%$  and  $s/c = 2.5\%$  and in Figure 7 for  $s/c = 3.7\%$  and  $s/c = 5.0\%$ . Results for SolidWall and Groove are shown at three different operating points, the design point ( $\xi = 1.00$ ), a throttled operating point ( $\xi = 0.80$ ), and a near stall operating point of the respective configuration. Due to brevity, at  $s/c = 5.0\%$  the operating points that are shown for the SolidWall configuration are only the design point and  $\xi = 0.80$ . Because it is not possible to place sensors in the Groove region on the casing radius, the Groove results show a blank space. This region is also indicated by horizontal black lines in the SolidWall results. In the presented plots, high values of

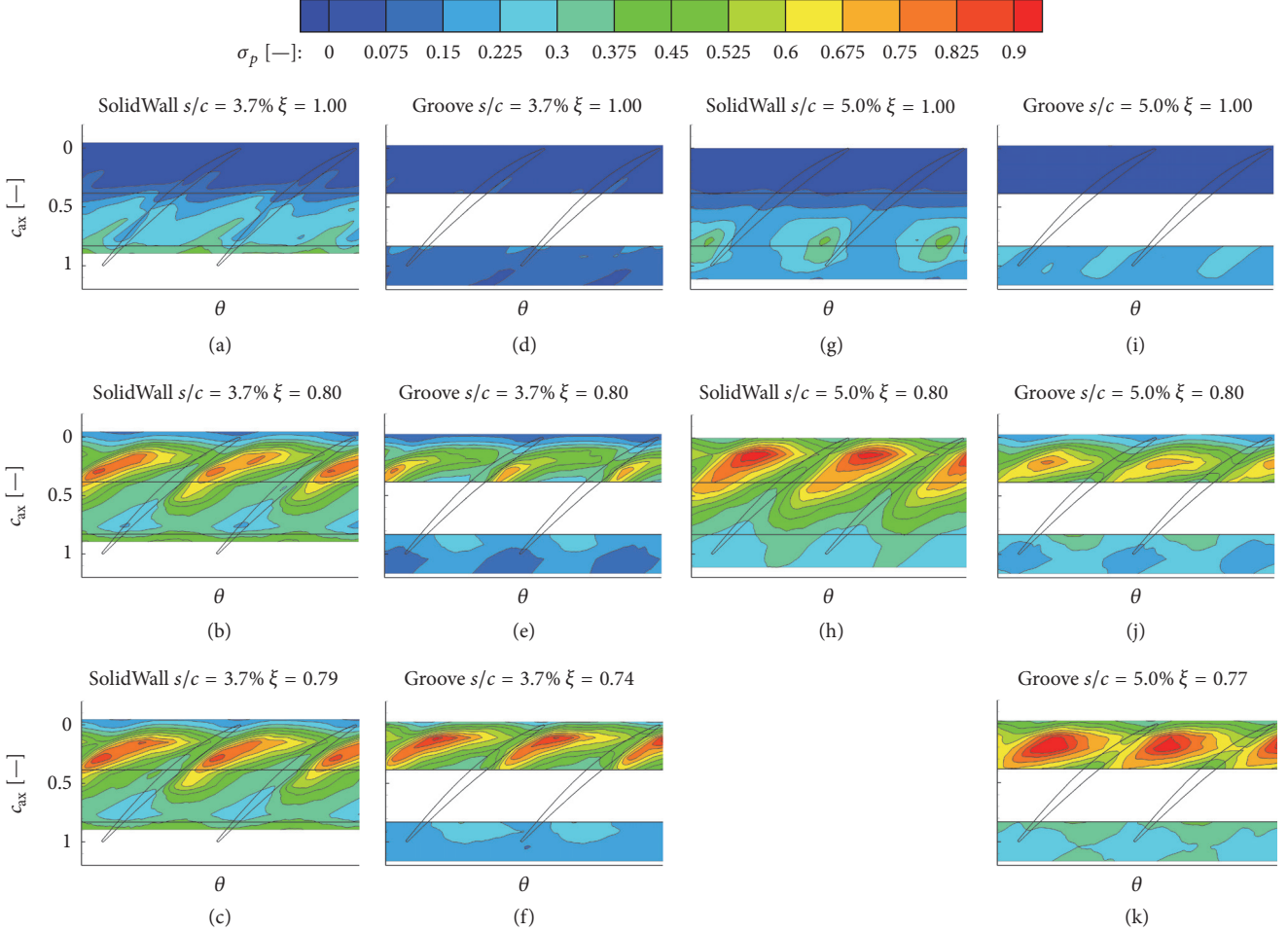


FIGURE 7: Standard deviation of casing static pressure over rotor for SolidWall and Groove at  $s/c = 3.7\%$  and  $s/c = 5.0\%$  at three different operating points ((a, d, g, i): design point, (b, e, h, j): throttled operating point, and (c, f, k): near stall of current configuration).

standard deviation can be found in regions where the tip leakage vortex interacts with the main flow.

**3.2.1.  $s/c = 1.2\%$ .** At the design point of SolidWall (Figure 6(a)) high standard deviations (and thus the tip leakage vortex) start near the suction side of the blade around  $c_{ax} = 0.2$ . The vortex expands into the passage and in a region around  $c_{ax} = 0.6$  it reaches the pressure side of the opposite blade. With increased throttling (Figure 6(b)) the region of high standard deviation moves upstream towards the leading edge. The vortex now travels towards the pressure side of the opposite blade in the front half of the blade and reaches it at approximately  $c_{ax} = 0.25$ . This means that also the vortex inclination against axial direction is increased. At the last stable operating point (Figure 6(c)) the upstream boundary of the tip leakage vortex is nearly vertical. The highest standard deviations can be found near the pressure side of the opposite blade, indicating a strong vortex fluctuation in this area. The increase in standard deviation from design point to near stall can be attributed to an increase in vortex strength with throttling.

At the design point of Groove (Figure 6(d)) vortex size and position are in the same region as in the SolidWall

configuration. A manipulation of the vortex by the Groove cannot be detected under these operating conditions. At  $\xi = 0.80$  (Figure 6(e)) differences between SolidWall and Groove occur. The values of high standard deviation near the blade pressure side are reduced in contrast to the SolidWall and the values of  $\sigma_p$  are lower in the passage. At the near stall operating point, the Groove's influence is enhanced. The standard deviations in the whole region upstream the Groove are lower than in the SolidWall configuration. The inclination of the upstream boundary of the tip leakage vortex has also been lowered. Despite the fact that the Groove influences the near casing flow field at the smallest tip clearance configuration, the Groove is not able to reduce the stall mass flow; see Figure 4. This underlines the previous assumption that stall at  $s/c = 1.2\%$  is not triggered by the near casing flow in the rotor.

**3.2.2.  $s/c = 2.5\%$ .** With increasing tip clearance to  $s/c = 2.5\%$  the tip leakage vortex at the design point (Figure 6(g)) now starts more downstream around  $c_{ax} = 0.3$ . The region where the vortex reaches the pressure side is nearly unchanged in comparison with the next smaller tested tip clearance size. The Groove (Figure 6(j)) does not influence the starting point

of the vortex at  $\xi = 1.00$ . At throttled operation in Figure 6(h) the vortex inclination has increased notably, as before. High values of  $\sigma_p$  can be found near the pressure side of the opposite blade around  $c_{ax} = 0.3$ . At the near stall operating point (Figure 6(i)) these values are further increased and the upper boundary of the tip leakage vortex is nearly vertical and blocks the whole near casing passage. This is in good agreement with one of Vo et al.'s [22] criteria for rotating stall onset, the spill-over of leakage fluid into the neighboring passage. The influence of the Groove can again be seen at the two last operating points (Figures 6(k) and 6(l)). The upper boundary of the tip leakage vortex at  $\xi = 0.80$  is more downstream than in the SolidWall case and the standard deviations have been reduced. At the near stall operating point of Groove (which is 4 percentage points lower than that of SolidWall) a similar near casing flow pattern as in the SolidWall case (Figure 6(i)) exists. Thus, the Groove has been able to delay the upstream movement of the tip leakage vortex with throttling. The compressor can be throttled more intensely before the interface between the incoming flow and the tip leakage flow reaches the leading edge and causes a spill-over of leakage flow into the neighboring passage.

**3.2.3.  $s/c = 3.7\%$ .** The next tip clearance increase results at the design point (Figure 7(a)) in a further downstream movement of the point of vortex formation to approximately  $c_{ax} = 0.4$ . In contrast to the two smaller tested tip clearance sizes, high standard deviations can be found in the passage over the whole circumference and the exact point of the interaction of the vortex with the opposite blade cannot be detected. It can be seen that the Groove lies directly in the region of vortex formation and is expected to influence it. Directly downstream the Groove the standard deviation is notably smaller than in the SolidWall configuration. This underlines the above-stated assumption of a Groove's influence on the vortex formation. The lower values of standard deviation upstream the Groove in Figure 7(d) compared to the SolidWall are also attributed to the Groove's influence on the vortex. A reduction of vortex related blockage by the Groove is likely to have a positive upstream influence on the flow field. The throttled operating point of SolidWall in Figure 7(b) is at this clearance size already quite close to the near stall operating point. Thus the upper boundary of the tip leakage vortex is already placed near the blade leading edge. A similar pattern of standard deviation as in  $s/c = 2.5\%$  (Figure 6(h)) is observed. A little further throttling to  $\xi = 0.79$ , shown in Figure 7(c), moves the upper boundary of the tip leakage vortex further upstream and is expected to cause spill-over of leakage fluid and thus to limit the stable operation. The Groove influence (Figures 7(e) and 7(f)) is also similar to the next smaller tested  $s/c$ -configuration. The delay of the upstream movement of the above-mentioned interface, which can be seen at  $\xi = 0.8$  makes the compressor more stable in the rotor tip region and allows in this case an operation at flow rate coefficients that are lower by 5 percentage points in contrast to the SolidWall.

**3.2.4.  $s/c = 5.0\%$ .** At the largest tested tip clearance, the tip leakage vortex of SolidWall at the design point (Figure 7(g)) starts again more downstream than at  $s/c = 3.7\%$ . The starting

point now approximately lies at  $c_{ax} = 0.5$ . This far downstream position of the starting point prevents an impingement of the vortex on the pressure side of the next blade. The Groove configuration at the design point (Figure 7(i)) shows a reduction of standard deviations downstream the Groove. The region of enhanced  $\sigma_p$  shows, in addition, a reduced spread in circumferential direction due to the Groove. This again shows the influence of the Groove on the near casing flow field. Due to the small difference between  $\xi = 0.79$  and  $\xi = 0.80$  (Figures 7(c) and 7(b)) at  $s/c = 3.7\%$ , here only the operating point  $\xi = 0.80$  is shown in Figure 7(h). As in the configurations before, the upper boundary of tip leakage flow reaches the leading edge and causes stall at a slightly higher throttling. The mechanism of operating range improvement of Groove is also identical to the tip clearance sizes before. At  $\xi = 0.80$ , Figure 7(j), the vortex is less intensely inclined than at the SolidWall. At the near stall operating point, Figure 7(k), the upper vortex boundary reaches the leading edge, as in the near stall point of SolidWall.

**3.3. Frequency Analysis.** In this section a frequency analysis of wall pressure sensors is performed in order to find hints for rotating instabilities that have been found by Mailach et al. [13] in a different build of the same compressor that is investigated in this paper. Mailach et al. weakened the third stage of a four-stage build by locally increasing the tip clearance of the third rotor. At a tip clearance of  $s/c = 4.3\%$  their frequency spectra showed typical humps at one-third of blade passing frequency that have been attributed to a fluctuating tip leakage vortex. It is now interesting to find out if these fluctuations also happen in a single-stage compressor with enlarged tip clearance or only in a weakened stage of a multistage compressor, where the weakened stage is stabilized by the surrounding stages and can therefore be operated at lower flow rate coefficients than the similar single-stage.

Frequency spectra of wall pressure sensors at  $c_{ax} \approx 0.125$  are shown in Figure 8 for all tested tip clearance sizes at the throttled operating point. At  $\xi = 1.00$  none of the four tested clearance sizes shows any activities at frequencies lower than BPF; therefore these results are omitted. For the smallest tested clearance this can also be observed at the throttled operating point. This is in good agreement with Mailach et al., who showed that RI only occur in the throttled operating region of a compressor with relatively large tip clearance size. At  $s/c = 2.5\%$ , however, a rise of amplitudes in the region  $0.4\text{--}0.5 \cdot \text{BPF}$  can be seen at  $\xi = 0.80$  for the SolidWall. This is a first sign that rotating instabilities, as Mailach et al. called the fluctuations of the tip leakage vortex, occur in this compressor build. The rise in amplitudes is also visible for Groove but in a lower extent. It seems that the Groove is able to damp the observed fluctuations.

The throttled operating points of the two largest clearances again show increasing amplitudes below BPF. At  $s/c = 3.7\%$  the SolidWall shows amplitudes below BPF that are nearly twice as high as in the next smaller tip clearance configuration. The frequencies, where the high amplitudes occur, are shifted towards lower values, compared with  $s/c = 2.5\%$ , and are now in the region of  $0.35\text{--}0.45 \cdot \text{BPF}$ . Here, it is now very obvious that the Groove is able to damp the high

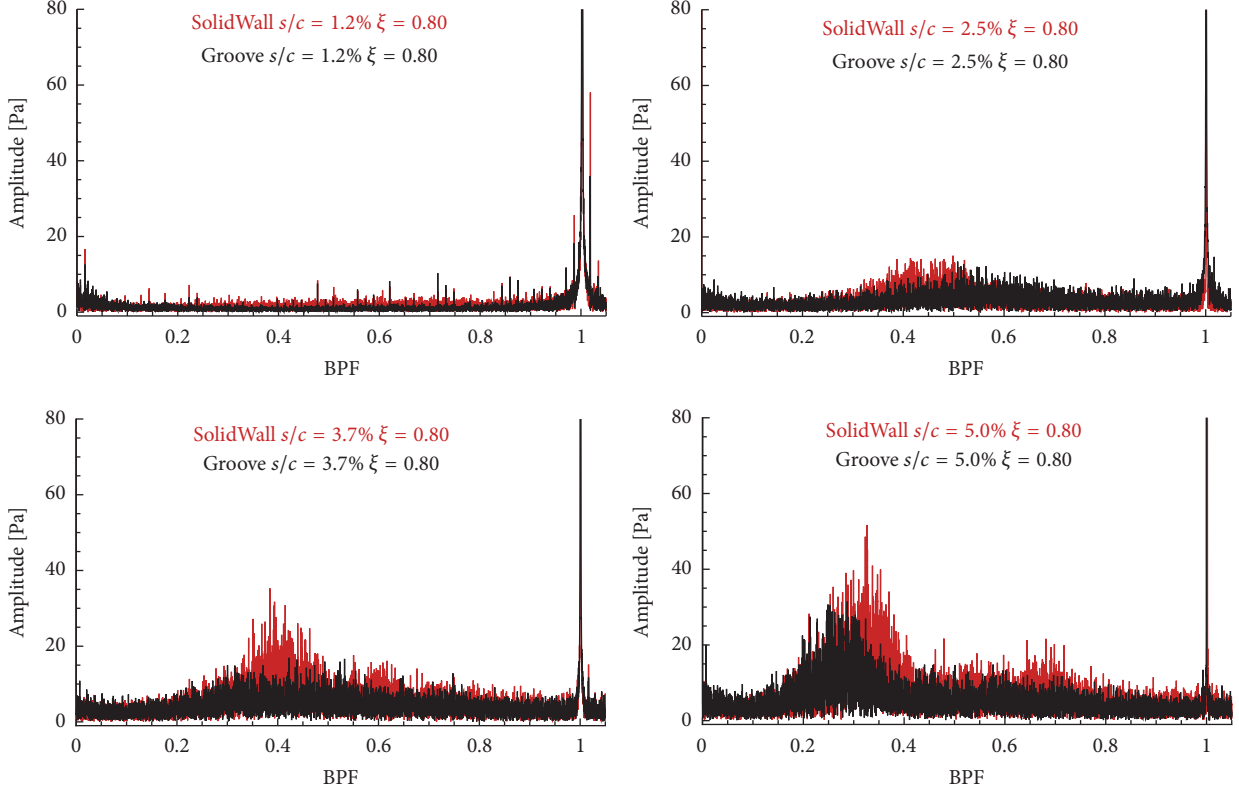


FIGURE 8: Frequency spectra of wall pressure sensor at  $c_{ax} \approx 0.125$  for SolidWall and Groove at the throttled operating point for  $s/c = 1.2\%$ ,  $2.5\%$ ,  $3.7\%$ , and  $5.0\%$ .

amplitudes. The largest clearance shows a further increase in low frequency amplitudes and a further shift of these frequencies that now lie in a region of  $0.3\text{--}0.4 \cdot \text{BPF}$ . In this operating point a second hump is visible at around  $0.7 \cdot \text{BPF}$  which is probably a modulation of the hump around  $0.3\text{--}0.4 \cdot \text{BPF}$  and the BPF itself. Looking at the Groove configuration, the damping of the low frequency hump can be seen again.

In the frequency spectra, that are presented in Figure 8, the RI show amplitudes that are relatively small with up to 60 Pa. This can be attributed to the low periodicity of the disturbances and to the fact that the frequency spectra are derived from a dataset with approximately 5300 blade passings. In the raw data, the disturbance is much more pronounced and has amplitudes of more than 1000 Pa. This has also been addressed in [13].

The following conclusions can be drawn from this paragraph. No rotating instabilities occur at the tightest clearance. The other three investigated clearance sizes showed a rise in frequencies around one-half to one-third of BPF. Thus, the occurrence of RI is not limited to a weakened stage in a multistage compressor but is also detected in a single-stage compressor. The amplitudes of the above-mentioned frequencies rise with increased rotor tip clearance together with a shift towards lower frequencies. Furthermore, it has been shown that the investigated casing grooves are able to influence the rotating instabilities as they reduce their amplitudes in the frequency spectra.

**3.4. Time-Resolved Casing Static Pressure.** This section discusses time-resolved casing static pressures for all clearance configurations in order to detect a flow pattern that can be linked to the occurrence of rotating instabilities that have been identified in the previous section.

The time-resolved casing static pressures for all clearance configurations are shown in Figures 9 and 10. The data are derived from one sensor array (see Figure 3) at a fixed position on the compressor circumference. It is known from Mailach et al. [13] that RI rotate relative to the rotor with approximately 50% of rotor speed. The plotted results show snapshots of 10 rotor passages that have passed the measurement position. Snapshots at other instants of time show results that are analogous to the plotted results. Static pressure is depicted by the pressure coefficient which is defined as  $c_p = (p - p_\infty)/(p_{in} - p_\infty)$  where  $p_{in}$  is the static pressure at rotor inlet and  $p_\infty = 101325$  Pa. The operating point of the SolidWall configurations for the respective clearances is the near stall operating point; the operating point of Groove is identical to SolidWall. The dashed white lines connect the low pressure regions in each plot. These are traditionally linked with the trajectory of the tip leakage vortex. From other investigations (e.g., [23, 24]) it is known that this is a simplification and that, under certain operating conditions, the near casing flow field shows multiple vortical structures and not one clearly defined tip leakage vortex. This becomes obvious in our results at the largest tested tip clearance that is presented later.

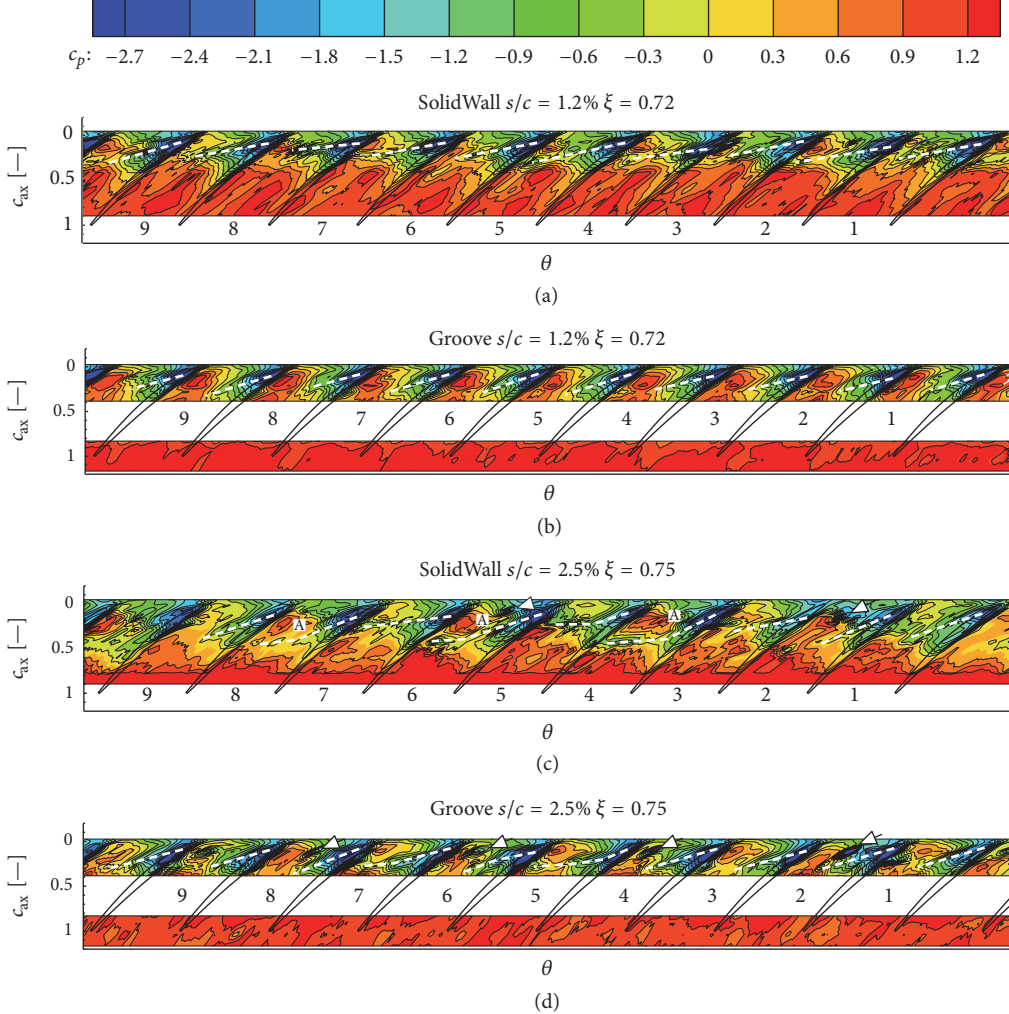


FIGURE 9: Time-resolved casing static pressure over rotor for SolidWall and Groove at  $s/c = 1.2\%$  (a, b) and  $s/c = 2.5\%$  (c, d). SolidWall operating points are near stall, Groove operating points identical to SolidWall.

At the smallest tested tip clearance size (Figures 9(a) and 9(b)) the tip leakage vortices start near the leading edge in the region  $c_{ax} \approx 0.1$  at both SolidWall and Groove. The plotted tip leakage vortices of SolidWall slightly differ from passage to passage. In passages 5 and 7 the region of high  $c_p$  on the blade pressure side is interrupted by a low pressure spot which seems to stem from the tip leakage vortex. In passages 6 and 8, however, these low pressure spots do not appear. These differences are responsible for the increase of standard deviations in Figure 6(c). The Groove configuration of the same clearance size (Figure 9(b)) shows nearly the same flow pattern in each passage. A variation of tip leakage vortex trajectory cannot be detected. The above-mentioned low pressure spots on the blade pressure side vanished. Consequently the standard deviations (see Figure 6(f)) are lower than in SolidWall. It can be concluded that for  $s/c = 1.2\%$  tip leakage vortex fluctuations are either small (SolidWall) or not present (Groove), which means that the Groove has a small influence on the near casing flow

field that does not lead to an increase in operating range though.

With an increase of tip clearance to  $s/c = 2.5\%$  the flow field in SolidWall (Figure 9(c)) is getting more irregular. The differences in vortex trajectory from passage to passage are now easy to detect. Moreover, the region of low  $c_p$  near the leading edge of the blade now differs strongly in every passage. Although only ten passages are shown in the figures, a repeating pattern can already be detected. Passages 4, 6, and 8 (and partially passage 2) all show a high pressure spot around  $c_{ax} = 0.25$  on the blade pressure side (see region A) and have very similar vortex trajectories. Passages 3, 5, and 7 however show a higher inclination (against axial direction) of the tip leakage vortex trajectory. This change of flow pattern in every other passage that passes the measurement position leads to an increase of amplitudes in the frequency spectra around  $0.5 \cdot \text{BPF}$  (the frequency spectra for  $\xi = 0.75$  are not shown here, for brevity, but show an amplitude increase at the same frequencies as the operating point  $\xi = 0.80$  in Figure 8).

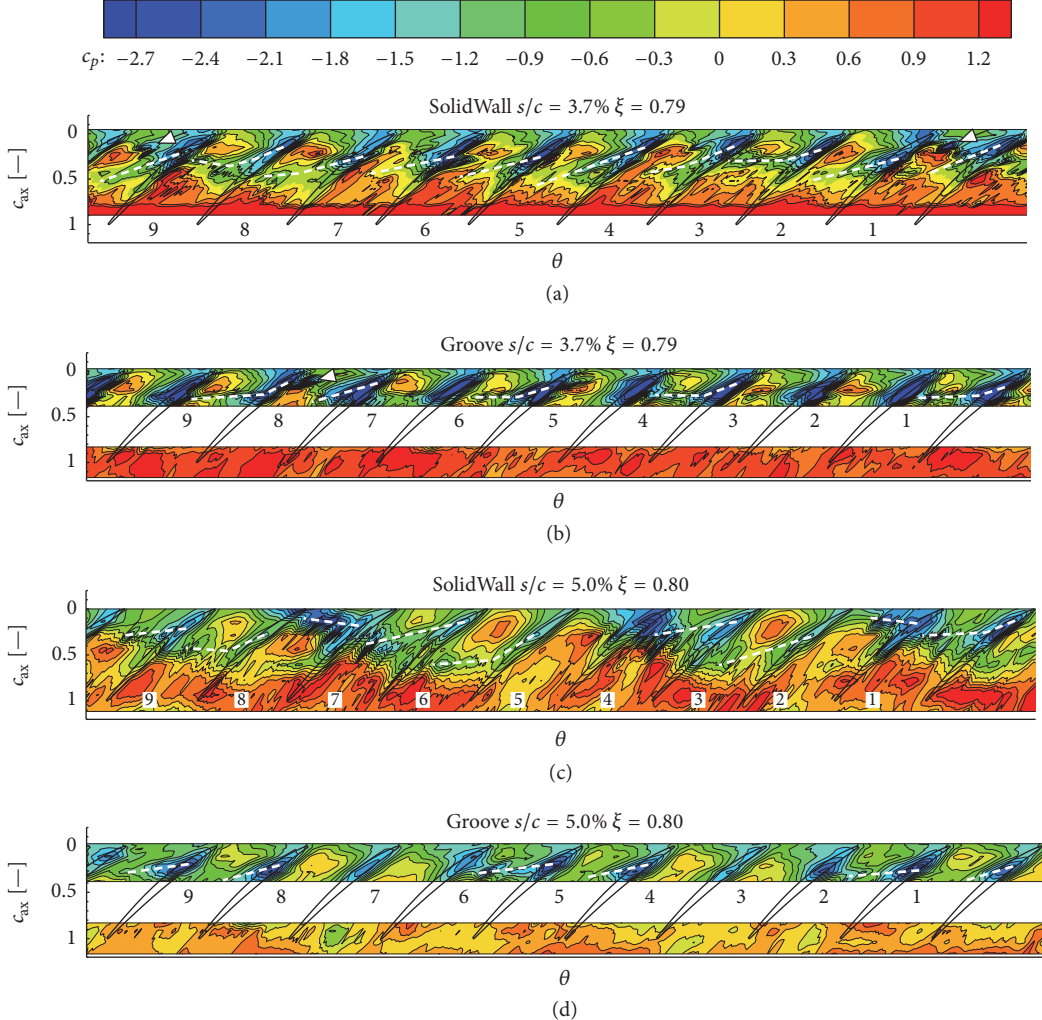


FIGURE 10: Time-resolved casing static pressure over rotor for SolidWall and Groove at  $s/c = 3.7\%$  (a, b) and  $s/c = 5.0\%$  (c, d). SolidWall operating points are near stall, Groove operating points identical to SolidWall.

The fact that the peak in the frequency spectra around  $0.5 \cdot \text{BPF}$  is not sharp but blurred is due to the fact that the above-mentioned pattern is not repeating strictly every other passage but slightly changes.

The black-and-white arrows in passages 2 and 6 mark a low pressure spot which is positioned in the passage between suction side and pressure side of the blade. The source that causes this low pressure spot is not clear. It could be the radial vortex that Hah [25] identified in his investigation which is part of the tip leakage vortex. Inoue et al. [26] and Pullan et al. [27] also identified a radial vortex which stems from blade separation and also produces a low pressure spot in the instantaneous casing pressure. Weichert et al. [28] also linked their observed low pressure spot in the passage near the leading edge with a radial vortex as in [26, 27].

The flow field of Groove at  $s/c = 2.5\%$  is shown in Figure 9(d). Here, different tip leakage vortex trajectories between the passages can also be observed. The pattern, however, is not as regular as in the SolidWall. In passages 2 and 8, for example, the trajectories are pretty similar and

in both passages a distinct high pressure region near the pressure side exists. The vortex trajectories in passages 7 and 5 seem to reach the pressure side of the blade and thus the above-mentioned area of high pressure is interrupted. The low pressure spots that have been found in SolidWall are also present in Groove. They are again marked by black-and-white arrows. In this case, they appear in passages 2, 4, 6, and 8. This regular appearance, however, is not visible throughout the whole dataset. The authors in [26–28] all linked the appearance of their radial vortices to the formation of a spike that initiated compressor stall. The fact that Figure 9(d) shows the appearance of the low pressure spots at an operating point which is not near stall makes the same mechanism for its appearance as in [26, 27] less likely.

At the tip clearance of  $s/c = 3.7\%$  the tip leakage vortex fluctuations increase; see Figure 10(a). In passages 3 and 9 the vortex stands nearly vertical in the passage whereas in the other passages it shows a notably lower inclination. Like in  $s/c = 2.5\%$ , a strong variation of the minimum pressure spot over the blade is present. The blades on the right hand sides

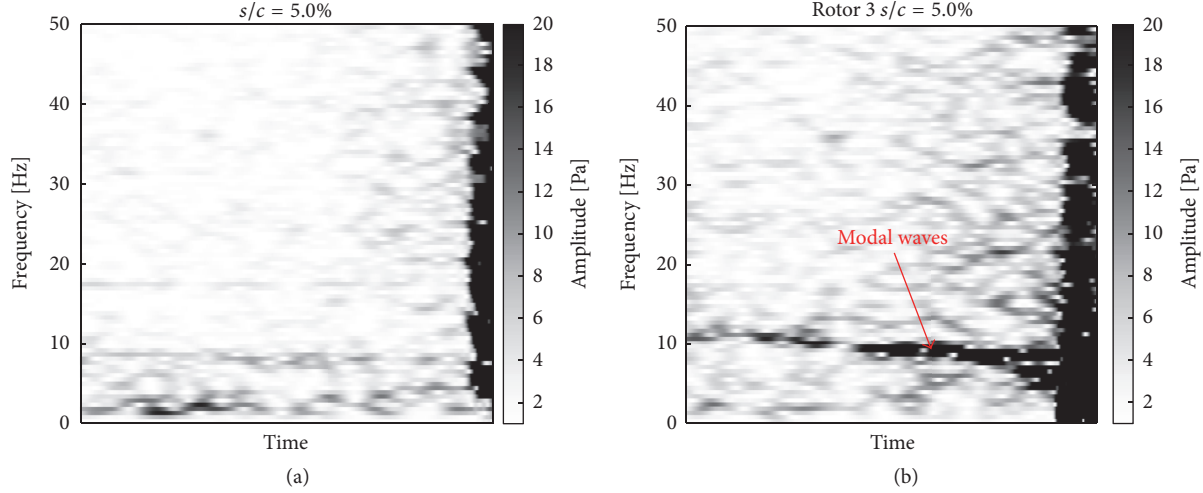


FIGURE 11: Spectrogram of microphone at  $c_{ax} = -0.2$  (upstream rotor leading edge). (a)  $s/c = 5.0\%$  of single-stage test. (b)  $s/c = 5.0\%$  only in Rotor 3 of four-stage test.

of passages 2 and 8 both have a position of minimum over-blade pressure that is far more downstream than in the other passages. The low pressure spots marked by the arrow again show the potential existence of radial vortices near the blade leading edge. In the Groove configuration (Figure 10(b)) the position of minimum over-blade pressure is identical in each passage, which results in similar starting points of the tip leakage vortex. The position of the Groove makes it difficult to track the vortices in this configuration. It is, however, obvious that vortex fluctuations are still present. The spectral analysis in Figure 8 revealed that the dominant peak has been damped by the Groove. This means that the periodicity of appearance of the vortex fluctuations is unchanged compared to SolidWall, but its amplitudes have been damped.

The increase of rotor tip clearance to  $s/c = 5.0\%$  drastically alters the near casing flow field. As mentioned earlier, especially at this tip clearance size, the dashed white lines are a strong simplification of the tip leakage vortex path. The figure suggests that multiple vortical structures are present. The SolidWall (Figure 10(c)) now exhibits very strong tip leakage vortex fluctuations. A periodic pattern can be identified. Starting in passage 3, the vortex starts around  $c_{ax} = 0.3$  and proceeds within the passage. In passage 4, the starting point of the vortex moved upstream to  $c_{ax} = 0.15$ . The vortex trajectory is steeper than in passage 3 and the vortex interacts with the pressure side of the adjacent blade around  $c_{ax} = 0.3$ . Passage 5 then shows a very pronounced low pressure spot near the leading edge and from the measured pressure field the vortex trajectory cannot be estimated anymore. The following passage 6 is similar to passage 3 and the pattern of vortex fluctuation starts again. This pattern is responsible for the increase of amplitudes at frequencies around 0.3· BPF that were identified in Figure 8. In Figure 10(d), Groove configuration, the vortex fluctuations are not as pronounced as in SolidWall. Again, the Groove positions hinder the tracking of the vortex path. In some passages, for example, passages 2 and 6, the vortex is highly inclined against axial direction so that it is proceeding in the passage upstream the

Groove. Passages 8 and 4 and passages 7 and 3 also show very similar patterns upstream the Groove which leads to the assumption that a similar pattern as in SolidWall is present. In both SolidWall and Groove of  $s/c = 5.0\%$  the low pressure spots in the passage near the leading edge cannot be identified anymore, or are overlaid by the tip leakage vortex.

**3.5. Modal Activities.** The total-to-static characteristics in Figure 4 showed a zero slope near stall for SolidWall of  $s/c = 5.0\%$  and according to general opinion hint to an existence of modal activities. Therefore in this section the occurrence of modal waves is investigated.

The spectrogram of a single microphone positioned 16 mm upstream the rotor leading edge is shown in Figure 11 during a slow closing of the throttle into stall. Figure 11(a) shows results of the SolidWall of  $s/c = 5.0\%$  whereas Figure 11(b) shows results from third rotor of a four-stage test, where only rotor 3 runs with an increased clearance of  $s/c = 5.0\%$ . In the case of the weakened stage a distinct disturbance is visible throughout the whole time line which starts at frequencies slightly above 10 Hz that decrease with further throttling. Mailach [29] showed that these amplitudes are evoked by modal waves in the compressor. In the present single-stage test these disturbances cannot be detected neither at the largest tip clearance (see Figure 11(a)) nor at any other tip clearance size. Furthermore, no influence of the Groove on modal activities could be detected.

The results presented above reveal that the slope of the total-to-static characteristics does not seem to be a sufficient criterion to predict modal waves in an axial compressor.

#### 4. Conclusions

In this paper, detailed measurements in a single-stage build of the Low Speed Research Compressor at Technische Universität Dresden have been presented. Four different tip clearance sizes of  $s/c = 1.2\%, 2.5\%, 3.7\%$ , and  $5.0\%$  have been

investigated with and without a circumferential groove casing treatment. The overall compressor performance as well as the rotor tip flow field have been evaluated. The main conclusions of the paper are as follows:

- (i) The present casing groove works well at the three largest tested tip clearance sizes ( $s/c = 2.5\%, 3.7\%$ , and  $5.0\%$ ). Here, it increases the compressor's operating range and partially the efficiency. At the smallest tested tip clearance size of  $s/c = 1.2\%$  the grooves do not exhibit a negative influence on efficiency between design point and stall.
- (ii) Results from unsteady wall pressure measurements show that the groove is able to delay the upstream movement of the flow interface between tip leakage and main flow and thereby increases compressor stability.
- (iii) The peaks in the frequency spectra in regions around  $0.3\text{--}0.5\cdot$  BPF could clearly be linked to rotating instabilities.
- (iv) The rotating instabilities increase in amplitude with tip clearance size. At the same time the frequency of appearance in the frequency spectra is decreased because the periodic pattern of RI increases from every other to every third blade passage.
- (v) Low pressure spots near the leading edge in the passage have been observed that could be evoked by radial vortices either of the Inoue et al. [26] and Pullan et al. [27] type or by a mechanism described by Hah [25].
- (vi) Although the total-to-static characteristics at Solid-Wall of  $s/c = 5.0\%$  show a zero slope near stall, no modal activities could be detected.

## Nomenclature

### Greek Symbols

$\eta$ :	Isentropic efficiency
$\theta$ :	Circumferential coordinate
$\xi$ :	Flow rate coefficient
$\pi_t$ :	Total pressure ratio
$\phi$ :	Flow coefficient
$\Delta\phi_{\text{Stall}}$ :	Percentage reduction in stall flow coefficient relative to smallest tip clearance size
$\Psi_{t-s}$ :	Total-to-static pressure coefficient
$\rho$ :	Density [ $\text{kg}/\text{m}^3$ ]
$\sigma_p$ :	Standard deviation of casing wall pressure
$\delta$ :	Clearance derivative.

### Latin Symbols and Abbreviations

BPF:	Blade passing frequency
$c$ :	Chord length [m]
$c_{\text{ax}}$ :	Nondimensional axial chord length
DP:	Design point
$h$ :	Depth of casing groove in % axial chord

$h_{\text{total}}$ :	Total enthalpy [ $\text{m}^2/\text{s}^2$ ]
$i$ :	Inclination angle of casing groove [ $^\circ$ ]
is:	Isentropic
IGV:	Inlet guide vane
LSRC:	Low Speed Research Compressor
$\Delta\dot{m}_{\text{Stall}}$ :	Percentage reduction of stall mass flow
$\dot{m}$ :	Mass flow [ $\text{kg}/\text{s}$ ]
$M$ :	Torque [Nm]
MP:	Measuring plane
MS:	Midspan
$n$ :	Shaft speed [1/min]
$p$ :	Static pressure [Pa]
$P_{\text{total}}$ :	Total pressure [Pa]
RI:	Rotating instabilities
$s$ :	Tip clearance size [m]
SW:	SolidWall
$T_{\text{total}}$ :	Total temperature [K]
TC:	Tip clearance
$u$ :	Blade speed [m/s]
$v_{\text{ax}}$ :	Axial component of absolute velocity [m/s]
$x_w$ :	Width of casing groove in % axial chord
$x_c$ :	Axial location of casing groove in % axial chord.

## Disclosure

The responsibility for the content lies solely with its authors.

## Conflicts of Interest

The authors declare that there are no conflicts of interest regarding the publication of this article.

## Acknowledgments

The authors gratefully acknowledge the industrial partner ALSTOM Power for their permission to publish this paper.

## References

- [1] D. C. Wisler, "Loss reduction in axial-flow compressors through low-speed model testing," *Journal of Engineering for Gas Turbines and Power*, vol. 107, no. 2, pp. 354–363, 1985.
- [2] N. A. Cumpsty, *Compressor Aerodynamics*, Krieger Publishing, 2004.
- [3] W. M. Osborn, G. W. Lewis, and L. J. Heidelberg, "Effect of Several Porous Casing Treatments on Stall Limit and on Overall Performance of an Axial Flow Compressor Rotor, NASA Technical Note D-6537," Tech. Rep., 1971.
- [4] D. C. Prince, D. C. Wisler, and D. E. Hilvers, "Study of Casing Treatment Stall Margin Improvement Phenomena, NASA Report CR 134552," Tech. Rep., 1974.
- [5] H. Takata and Y. Tsukuda, "Stall margin improvement by casing treatment - its mechanism and effectiveness," *Journal of Engineering for Power*, vol. 99, no. 1, pp. 121–133, 1977.
- [6] A. Shabbir and J. J. Adamczyk, "Flow mechanism for stall margin improvement due to circumferential casing grooves on axial compressors," *Journal of Turbomachinery*, vol. 127, no. 4, pp. 708–717, 2005.

- [7] X. Lu, W. Chu, J. Zhu, and Y. Wu, "Mechanism of the interaction between casing treatment and tip leakage flow in a subsonic axial compressor," in *Proceedings of the 2006 ASME 51st Turbo Expo, GT2006-90077*, pp. 79–90, Barcelona, Spain, May 2006.
- [8] V. Perrot, A. Touyeras, and G. Lucien, "Detailed CFD analysis of a grooved casing treatment on an axial subsonic compressor," in *Proceedings of the 7th European Conference on Turbomachinery: Fluid Dynamics and Thermodynamics, ETC7-016*, March 2007.
- [9] M. Rolfs, M. Lange, and K. Vogeler, "Experimental investigation of circumferential groove casing treatments for large tip clearances in a low speed axial research compressor," in *Proceedings of the ASME Turbo Expo 2015: Turbine Technical Conference and Exposition, GT2015-42646*, Montreal, Quebec, Canada, June 2015.
- [10] T. Houghton and I. Day, "Enhancing the stability of subsonic compressors using casing grooves," *Journal of Turbomachinery*, vol. 133, no. 2, Article ID 021007, 2011.
- [11] J. Li, F. Lin, S. Wang, J. Du, C. Nie, and J. Chen, "Extensive experimental study of circumferential single groove in an axial flow compressor," in *Proceedings of the Proceeding of the ASME Turbo Expo 2014: Turbine Technical Conference and Exposition, GT2014-26859*, Düsseldorf, Germany, June 2014.
- [12] I. J. Day, "Stall, surge, and 75 years of research," *Journal of Turbomachinery*, vol. 138, no. 1, Article ID 2478223, 2015.
- [13] R. Mailach, I. Lehmann, and K. Vogeler, "Rotating instabilities in an axial compressor originating from the fluctuating blade tip vortex," *Journal of Turbomachinery*, vol. 123, no. 3, pp. 453–460, 2001.
- [14] J. März, C. Hah, and W. Neise, "An experimental and numerical investigation into the mechanisms of rotating instability," *Journal of Turbomachinery*, vol. 124, no. 3, pp. 367–375, 2002.
- [15] D. Wisler, B. F. Beacher, and H.-W. Shin, "Effects of loading and clearance variation on tip vortex and endwall blockage," in *Proceedings of the 9th International Symposium on Transport Phenomena and Dynamics of Rotating Machinery, 10–14 February 2002*.
- [16] A. Young, I. Day, and G. Pullan, "Stall warning by blade pressure signature analysis," *Journal of Turbomachinery*, vol. 135, no. 1, Article ID 011033, 2012.
- [17] T. R. Camp and I. J. Day, "A study of spike and modal stall phenomena in a low-speed axial compressor," *Journal of Turbomachinery*, vol. 120, no. 3, pp. 393–401, 1998.
- [18] P. Boos, H. Möckel, J. M. Henne, and R. Seimeler, "Flow measurement in a multistage large scale low speed axial flow research compressor," in *Proceedings of the ASME 1998 International Gas Turbine and Aeroengine Congress and Exhibition, 98-GT-432*, Stockholm, Sweden.
- [19] M. Künzelmann, R. Müller, R. Mailach, and K. Vogeler, "Steady and unsteady flow field in a multistage low-speed axial compressor - A test case," in *Proceedings of the 2008 ASME Turbo Expo, GT2008-50793*, pp. 447–455, Berlin, Germany, June 2008.
- [20] R. A. Berdanier and N. L. Key, "The effects of tip leakage flow on the performance of multistage compressors used in small core engine applications," *Journal of Engineering for Gas Turbines and Power*, vol. 138, no. 5, Article ID 052605, 2016.
- [21] N. M. McDougall, "A comparison between the design point and near stall performance of an axial compressor," *Journal of Turbomachinery*, vol. 112, no. 1, pp. 109–115, 1989.
- [22] H. D. Vo, C. S. Tan, and E. M. Greitzer, "Criteria for spike initiated rotating stall," *Journal of Turbomachinery*, vol. 130, no. 1, Article ID 011023, 2008.
- [23] D. Tan, Y. Li, H. Chen, I. Wilkes, and J. Katz, "The three dimensional flow structure and turbulence in the tip region of an axial flow compressor," in *Proceedings of the ASME Turbo Expo 2015: Turbine Technical Conference and Exposition, GT2015-43385*, Montreal, Quebec, Canada, June 2015.
- [24] D. Tan, Y. Li, I. Wilkes, R. L. Miorini, and J. Katz, "Visualization and time-resolved particle image velocimetry measurements of the flow in the tip region of a subsonic compressor rotor," *Journal of Turbomachinery*, vol. 137, no. 4, Article ID 041007, 2015.
- [25] C. Hah, "Effects of double-leakage tip clearance flow on the performance of a compressor stage with a large rotor tip gap," *Journal of Turbomachinery*, vol. 139, no. 6, Article ID 061006, 2017.
- [26] M. Inoue, M. Kuroumaru, T. Tanino, and M. Furukawa, "Propagation of multiple short-length-scale stall cells in an axial compressor rotor," *Journal of Turbomachinery*, vol. 122, no. 1, pp. 45–54, 2000.
- [27] G. Pullan, A. M. Young, I. J. Day, E. M. Greitzer, and Z. S. Spakovszky, "Origins and structure of spike-type rotating stall," *Journal of Turbomachinery*, vol. 137, no. 5, Article ID 051007, 2015.
- [28] S. Weichert and I. Day, "Detailed measurements of spike formation in an axial compressor," *Journal of Turbomachinery*, vol. 136, no. 5, Article ID 051006, 2013.
- [29] R. Mailach, *Experimentelle Untersuchung von Strömungsinstabilitäten im Betriebsbereich zwischen Auslegungspunkt und Stabilitätsgrenze eines vierstufigen Niedergeschwindigkeits-Axialverdichters* [Doctoral thesis], Technische Universität Dresden, 2001.

## Research Article

# Transition Process from Diffuser Stall to Stage Stall in a Centrifugal Compressor with a Vaned Diffuser

Nobumichi Fujisawa and Yutaka Ohta

Department of Applied Mechanics and Aerospace Engineering, Waseda University, 3-4-1 Okubo, Shinjuku-ku, Tokyo 169-8555, Japan

Correspondence should be addressed to Yutaka Ohta; [yutaka@waseda.jp](mailto:yutaka@waseda.jp)

Received 1 February 2017; Accepted 3 May 2017; Published 31 May 2017

Academic Editor: Gerard Bois

Copyright © 2017 Nobumichi Fujisawa and Yutaka Ohta. This is an open access article distributed under the Creative Commons Attribution License, which permits unrestricted use, distribution, and reproduction in any medium, provided the original work is properly cited.

The transition process from a diffuser rotating stall to a stage stall in a centrifugal compressor with a vaned diffuser was investigated by experimental and numerical analyses. From the velocity measurements, it was found that the rotating stall existed on the shroud side of the diffuser passage in the off-design flow condition. The numerical results revealed the typical vortical structure of the diffuser stall. The diffuser stall cell was caused by the systematic vortical structure which consisted of the tornado-type vortex, the longitudinal vortex at the shroud/suction surface corner (i.e., leading edge vortex (LEV)), and the vortex in the throat area of the diffuser passages. Furthermore, the stage stall, which rotated within both the impeller and diffuser passages, occurred instead of the diffuser stall as the mass flow rate was decreased. According to the velocity measurements at the diffuser inlet, the diffuser stall which rotated on the shroud side was shifted to the hub side. Then, the diffuser stall moved into the impeller passages and formed the stage stall. Therefore, the stage stall was caused by the development of the diffuser stall, which transferred from the shroud side to the hub side in the vaneless space and expanded to the impeller passages.

## 1. Introduction

Centrifugal compressors equipped with vaned diffusers are widely used in industry because of their high pressure-rise characteristics. However, they are likely to result in unsteady phenomena, such as surges and rotating stalls, as compared with vaneless diffusers. The unstable operating range is enlarged by surges and rotating stalls that have the potential to cause serious accidents. Turbochargers are generally used for a wide operating range, including off-design conditions. However, centrifugal compressors are not subjected to similar operating conditions. Therefore, understanding the flow physics behind rotating stalls is important for improving high pressure compressor performance and for safe operation in off-design flow condition.

Many researchers have focused on rotating stalls in axial compressors [1–4]. In addition, several articles have also been devoted to the study of rotating stalls in centrifugal compressors [5–8]. In recent years, there has been a renewed interest in diffuser rotating stalls that occur in centrifugal compressors with vaned diffusers. For example, Spakovszky

reported that four-cell backward travelling modal waves occur in the vaneless space prior to the surge [9]. Everitt et al. reported the generation mechanism of spike stall inception by numerical analysis [10]. The short wavelength stall inception in centrifugal compressors with vaned diffusers was caused by the separation on the shroud side of the diffuser leading edge and radial flow reversal throughout the vaneless space. As Bousquet et al. accurately pointed out, the growth of the amplitude of a modal wave rotating in the vaneless space led to occurrence of the diffuser rotating stall; this was evident from the numerical analysis [11]. The authors also have reported that the unsteady behavior of the diffuser stall was influenced by the unsteady vortices at the leading edge of the diffuser vane during the off-design operation [12, 13].

Furthermore, several researchers have reported that the rotating stall changed its scale and behavior in accordance with the decrement of mass flow rate in turbomachinery. In axial machines, Outa et al. showed that the flow blockages, which were generated and developed separately in the respective cascades of the rotor and stator, get coupled with each other and propagate as a stage stall cell with

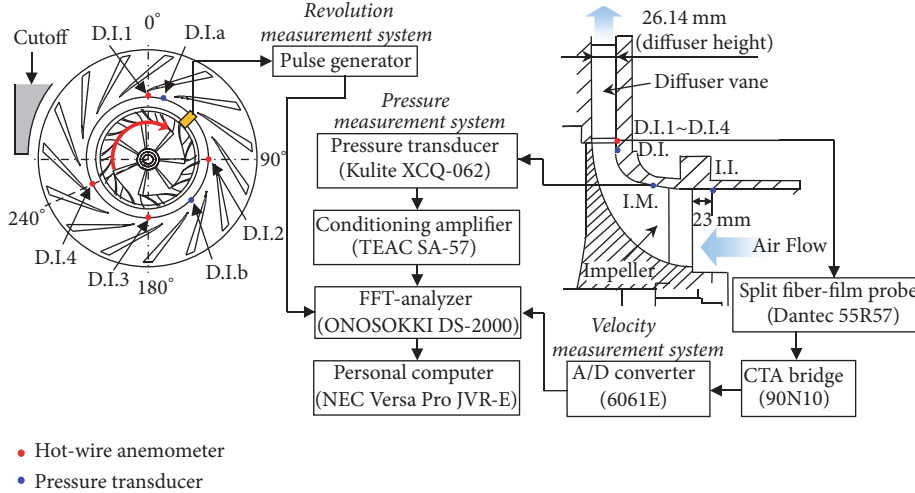


FIGURE 1: Experimental apparatus and measuring system.

decreasing mass flow rate [14]. Yoshida et al. investigated the rotating stalls that occur in the impeller and diffuser passages [15]. The behavior of the rotating stall was found to be dependent on the impeller-diffuser radial gap. Mizuki and Oosawa experimentally reported unsteady flow patterns in a centrifugal compressor with a vaneless diffuser during rotating stall and surge [16]. The part-span stall at the leading edge of the impeller changed to a full-span stall, as the flow rate decreased. Moreover, the strong influence of the full-span stall at the impeller inlet appeared during the surge. Zheng and Liu also examined the flow physics of rotating stalls and surge through their experiments [17]. The behavior of rotating stalls and surge was found to be dependent on the rotor speed and mass flow rate. However, very few researchers have reported on the transition process of the rotating stall via a detailed investigation of the internal flow field.

This study investigated the transition from the diffuser rotating stall to the stage stall in the vaned diffuser of a centrifugal compressor during the off-design operation. First, we focused on the generation mechanism of the diffuser stall by the both experimental and numerical analysis. The detached eddy simulation (DES) analysis was carried out to investigate the vortical structure of the diffuser stall. Secondly, we also investigated the transition characteristics of rotating stalls by the experiments.

## 2. Experimental Apparatus and Procedure

**2.1. Experimental Apparatus.** The compressor being tested had a centrifugal design based on that of a turbocharger used for marine diesel engines. The dimensions of the compressor are listed in Table 1 and the geometric configuration of the compressor and the main measurement system is illustrated in Figure 1. During the experiments, the rotational speed,  $N$ , of the compressor was set to  $6000 \text{ min}^{-1}$ . The test impeller was an open-shroud type with seven main and splitter blades, and its inlet and outlet diameters were 248 and 328 mm, respectively. The shroud clearance of the impeller

TABLE 1: Dimensions of tested compressor.

Tested centrifugal compressor		
Rotational speed	$N$	$6000 \text{ min}^{-1}$
Mass flow rate	$G$	$1.64 \text{ kg/s}$
Pressure ratio	$p_{t5}/p_{t1}$	1.1
Impeller		
Number of blades (main + splitter)	$Z$	14 (7 + 7)
Inlet diameter	$D_1$	248 mm
Outlet diameter	$D_2$	328 mm
Exit blade width	$B_2$	26.14 mm
Diffuser		
Blade shape	Wedge	
Number of vanes	$V$	15
Leading edge Diameter	$D_3$	360 mm
Trailing edge Diameter	$D_4$	559 mm
Diffuser width	$B_4$	26.14 mm

was approximately 1.0% of the impeller inlet blade width,  $B_1 = 105.6 \text{ mm}$ .

The vaned diffuser was employed in the experiments. The vaned diffuser had 15 wedge-type diffuser vanes located between two parallel diffuser walls of height,  $B_4$ , of 26.14 mm. The distance between the impeller exit and diffuser leading edge,  $L_{id}$ , was set to 16 mm. The original wedge-type diffuser vane (ODV) was employed in the experiments. The vanes were attached to the shroud surface of the channel diffuser.

The volute was designed to give the circumferential uniform pressure at the design operation. Near to the stall point ( $\phi = 0.14$ ), the flow is decelerated in the circumferential direction and the pressure rises around the volute. However, the fluctuation of circumferential pressure in vaneless space at the off-design point is  $\pm 50 \text{ Pa}$  at most, from the pressure measurements. Therefore, the unsteady behavior of diffuser stall was not highly affected by the volute design.

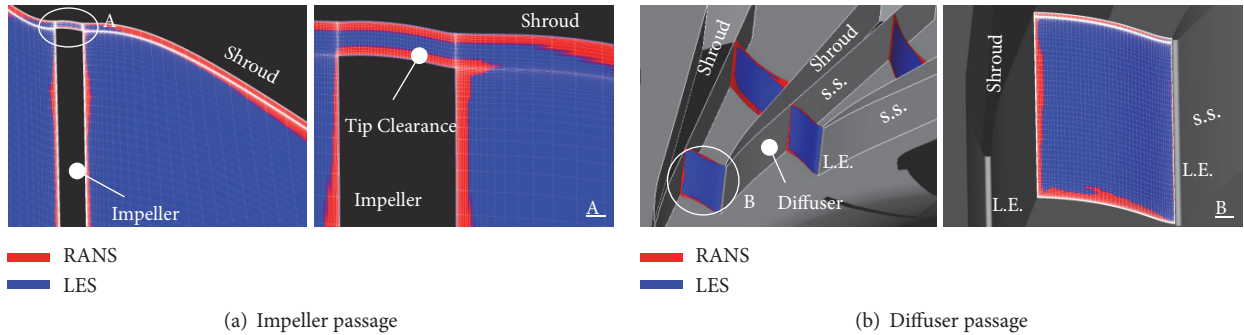


FIGURE 2: RANS/LES region within impeller and diffuser passages.

**2.2. Measuring Methods.** The operation point of the compressor was set using a butterfly valve installed at the outlet duct. The mass flow rates were calculated using an orifice flow meter and a thermocouple installed at the outlet duct end. The pressure-rise characteristics were measured using a differential pressure transducer (Yamatake JTD920A) installed at the exit of the compressor scroll. The error of differential pressure probe was less than  $\pm 0.1\%$ . The measuring bandwidth is from 2.0 kPa to 14 MPa. The total pressure rise at the compressor exit was calculated by the pressure rise at the exit of the compressor scroll and the meridional velocity which was calculated by mass flow rate.

The pressure and velocity measuring systems for investigating unsteady phenomena are also illustrated in Figure 1. The pressure transducers (Kulite, XCQ-062-25A) with an error within  $\pm 0.1\%$  were mounted flush with the shroud surface of the compressor. The diameter of pressure probe head was 1.7 mm. The pressure was measured at the following points along the impeller passage: impeller inlet (I.I.), impeller midsection (I.M.), and diffuser inlet (D.I.a and D.I.b). The diameter of above three points is  $0.757D_2$ ,  $0.758D_2$ , and  $1.024D_2$ , respectively. Furthermore, the spanwise distribution of the impeller-discharge flow was measured in the diffuser circumferential direction (D.I.1–D.I.4), using by a split-film probe (DANTEC, 55R57) with a constant-temperature anemometer (DANTEC, Streamline 90N10). The length of split-film probe was 8 mm and the film length was 1.25 mm. The measurement location  $D = 339$  mm was located between the impeller exit and the diffuser leading edge. The four measurement points are placed at 0 deg, 90 deg, 180 deg, and 240 deg. The impeller-discharge flow measurement was traversed from the hub to the shroud side every 5% of the diffuser width (20 points). The unsteady pressure and velocity traces were measured at a sampling frequency of 25.6 kHz. The temporal resolution is about 20 samples per blade passing period.

### 3. Computational Procedure

**3.1. Governing Equations.** The present simulations were conducted using the in-house computational fluid dynamics (CFD) code, which had been validated for various turbomachinery flows. The code solved the governing equation of continuity, a three-dimensional compressible Navier-Stokes

equation, an energy equation, and an equation for the state of an ideal gas. The convective flux was evaluated by the flux difference splitting (FDS) [18], which is extended to the third order using the monotonic upwind scheme for conservative laws (MUSCL) interpolation [19]. The viscous flux was determined as a second-order central difference using Gauss' theorem. The matrix free Gauss-Seidel (MFGS) implicit algorithm was employed for the time integration [20]. The DES approach, which is a hybrid scheme involving large eddy simulation (LES) and RANS [21], was employed in the turbulent modelling. The DES was based on the shear stress transport (SST)  $k-\omega$  turbulence model [22]. This model incorporates a dependency on the local turbulence length scale. The model constant  $C_{DES}$  was set to the value recommended by Strelets et al. Both Coriolis and centrifugal forces were considered to be inertial force terms in the relative coordinate system. The RANS and LES regions of both the impeller and diffuser passages are illustrated in Figure 2. This DES simulation code could transform the RANS-mode in regions near the wall into the LES-mode inside the fluid volume.

**3.2. Computational Domains.** The computational domains employed in the numerical simulations are illustrated in Figure 3. The grid system included all the flow passages (14 impeller and 15 diffuser passages). The computational domain was divided into three regions: the moving impeller, stationary diffuser, and the moving tip clearance regions. The volute region was not included in this simulation. For the whole domain including the tip clearance region, the mesh was generated with the multiblock structured grid using AutoGrid5 ver9.1 (NUMECA International). In the full annulus analysis, the impeller (including the clearance region) and diffuser system had 26.2 and 24.8 million cells, respectively. The computational grid incorporated seven main and splitter blades and 15 diffuser vanes and had 51.0 million cells. The cell width at the walls was  $0.1 \mu\text{m}$ , which corresponded to a  $y+$  parameter that was approximately equal to one along all solid surfaces. From the grid dependency test in partial annulus analysis, the grid density was sufficient in order to capture the unsteady behavior of vortices near the diffuser vane.

*3.3. Boundary Conditions.* At the inflow boundary, the total pressure and temperature were fixed. At the outflow boundary, a throttle resistance with a load coefficient was assumed

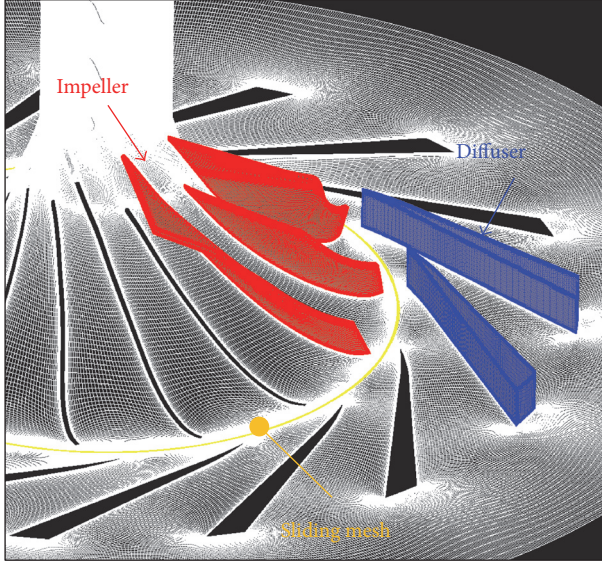


FIGURE 3: Overview of computational grid.

to exist between the boundary and the external atmosphere. The mass flow rate was not fixed at the outlet boundary because we assumed the throttle resistance with a load coefficient in order to simulate the velocity and pressure fluctuation caused by stall. We already observed the mass flow fluctuation at the exit of the compressor in both experiments and numerical simulations. Therefore, the static pressure at the outlet boundary was related to the mass flow rate through the boundary. Across the sliding boundary separating the moving impeller and stationary diffuser frames, the most recent data on one side was interpolated to obtain the data for the opposite side by using a sliding mesh for unsteady simulation. Nonslip and adiabatic conditions were adopted for the wall conditions.

## 4. Results and Discussion

**4.1. Stall Characteristics of Tested Compressor.** The experimental and numerical results of compressor performance are exhibited in Figure 4. The numerical total pressure-rise characteristics were obtained from DES unsteady analysis. The flow and total pressure-rise coefficients are defined as follows:

$$\phi = \frac{60Q}{\pi^2 D_2^2 B_2 N}, \quad (1)$$

$$\Psi_t = \frac{60^2 \Delta p_t}{\rho \pi^2 D_2^2 N^2 / 2}.$$

The ODV experimental results were denoted by the black circles in the figure. The simulations were conducted at seven operating points from the design point ( $\phi_{opt} = 0.24$ ) to the deep stall point ( $\phi = 0.10$ ). The time-averaged results of the unsteady DES analysis were in good agreement with the measured results obtained using the ODV, with the

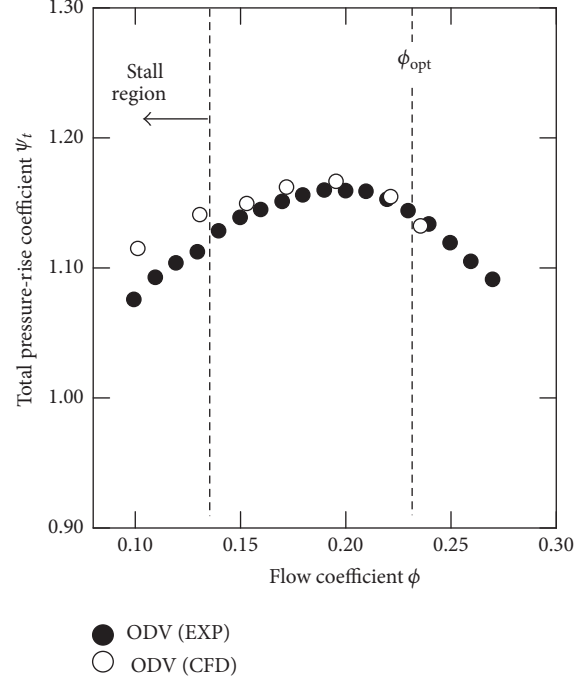


FIGURE 4: Compressor performance.

exception of results at stall point ( $\phi = 0.14$  and  $0.10$ ). One reason for this is that the additional loss from the volute was not concluded in this numerical simulation. Particularly at deep stall point ( $\phi = 0.10$ ), the compressor performance data obtained numerically, using CFD, was higher in value than that obtained experimentally. The resulting question about the performance remarkably mismatch at  $\phi = 0.10$  is considered later in detail.

To investigate the unsteady characteristics of rotating stall, the impeller-discharge flow was measured with a split-film anemometer at  $\phi = 0.14$  and  $0.10$ . The spatial distribution of the FFT (Fast Fourier Transformation) results in the spanwise direction is shown in Figure 5. The vertical axis represents the intensity of radial velocity fluctuation. The measurement of flow coefficient,  $\phi = 0.14$ , shows that the large intensity of velocity fluctuations occurred at 25 Hz near the shroud side. We have already reported that these unsteady phenomena at 25 Hz, which were equivalent to 25% of the impeller rotational speed, were caused by the rotating stall within the diffuser passages [12]. Therefore, this disturbance, as illustrated in Figure 5(a), was considered to result from the diffuser stall fluctuations. When the mass flow decreased ( $\phi = 0.10$ ), the diffuser stall fluctuation was not found and a large intensity velocity fluctuation occurred at 22 Hz in Figure 5(b). From a previous study [23], we found that the large intensity fluctuations, called “stage stall,” rotated within the impeller and diffuser passages. In comparison with the diffuser stall, the stage stall cell had a much larger intensity of velocity fluctuation over the entire span, especially near the hub side. In addition, from the pressure experiments, the number of diffuser and stage stall cell was found to be one. Thus, the rotating stall behavior of the tested compressor varied with the decreasing mass flow rate.

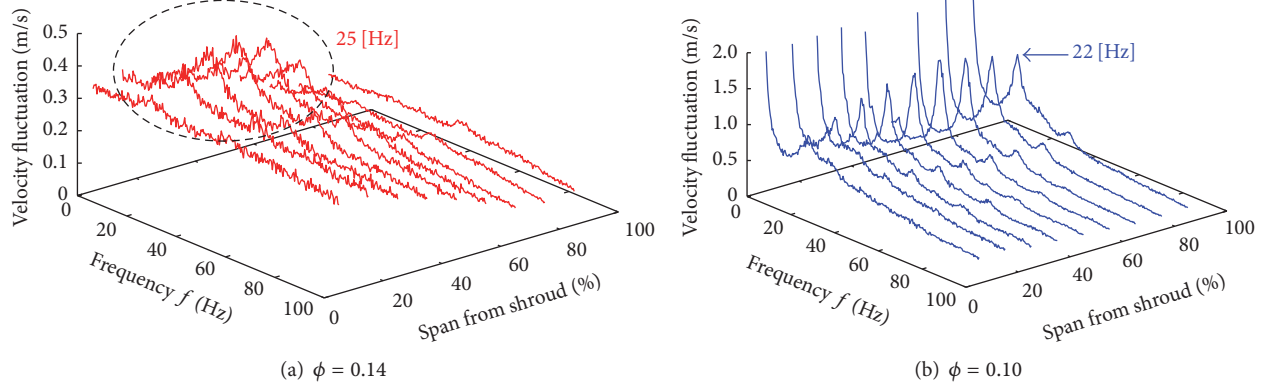


FIGURE 5: Distribution of velocity fluctuation in spanwise direction (ODV).

**4.2. Structure of Diffuser Stall Cell.** First, the rotational structure of the diffuser stall cell at flow coefficient  $\phi = 0.14$  was investigated using numerical analysis. To investigate the unsteady characteristics of rotating stall, the casing wall static pressure fluctuation was measured at two positions (D.I.a and D.I.b). The experimental and numerical casing pressure traces are presented in Figure 6. The red lines represent the low-pass filtered traces and the low-pass filter frequencies were set to 30 Hz. From the both experimental and numerical traces, the disturbance that was propagated in vaneless space can be observed. The rotational speed of this disturbance was approximately 25% of impeller speed. The unsteady phenomena at 25 Hz, which were equivalent to 25% of impeller rotational speed, were caused by the diffuser rotating stall. In addition, the influence of impeller stall fluctuation could be excluded because the scale of disturbances caused by the impeller stall were much smaller than that of the diffuser stall at diffuser inlet from Figure 5. Therefore, the numerical results for diffuser stall were in good agreement with the results obtained by the experiments.

Furthermore, the instantaneous casing pressure fluctuations in the vaneless space at nondimensional times  $t^* = 0.0-31.5$  are illustrated in Figure 7. The vertical axis is each diffuser vane, which was labelled with numbers from one to fifteen. The low casing static pressure region, which is represented by a black dashed circle, propagated to the next diffuser passage as time passed. The rotational speed of this region was approximately 25% of the impeller rotational speed. Thus, it may be concluded that this low static pressure region was caused by the diffuser rotating stall cell. Furthermore, the radial velocity fluctuation measured at the diffuser inlet is illustrated in Figure 8. The red and blue lines represent the diffuser passages numbers 1-2 and 7-8, respectively. The red dashed line, as illustrated in Figure 8, indicates the average of radial velocities calculated for all diffuser passages. As shown in this figure, the radial velocity of the diffuser passage numbers 7-8 was lower than the average radial velocity, because the diffuser rotating stall cell was approaching the diffuser passage numbers 7-8 from the nondimensional time,  $t_{\text{a}}^* = 0.0$ , as illustrated in Figure 7. At the nondimensional time,  $t_c^* = 4.5$ , the radial velocity of

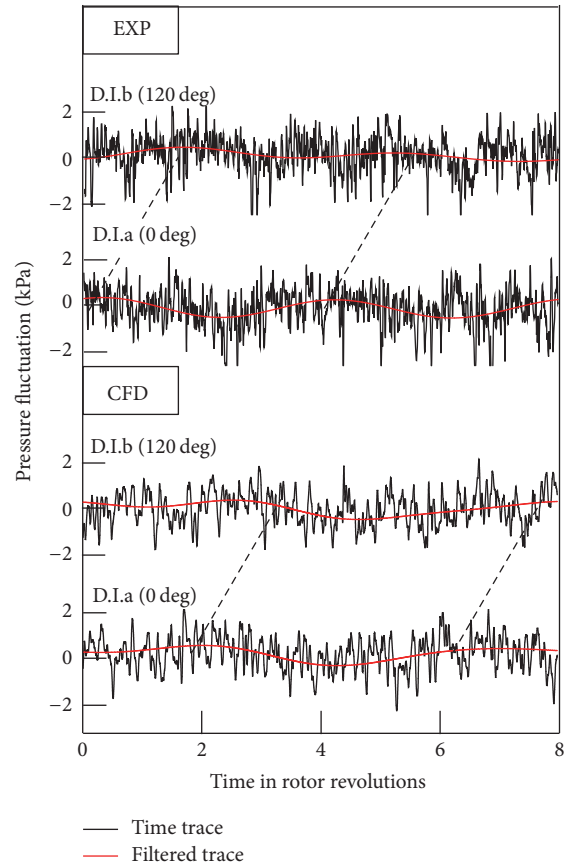


FIGURE 6: Casing wall pressure traces measured at diffuser inlet circumferential direction (D.I.a and D.I.b).

the diffuser passage numbers 7-8 was significantly decreased. Therefore, these results suggested that the flow within the diffuser passage was stalled by the blockage effect of the diffuser stall cell formation.

Then, the instantaneous vortical structure of the low static pressure region at the nondimensional time,  $t_c^* = 4.5$ , is illustrated in Figure 9. The vortex structure within several stalled diffuser passages numbers 7-11, as illustrated

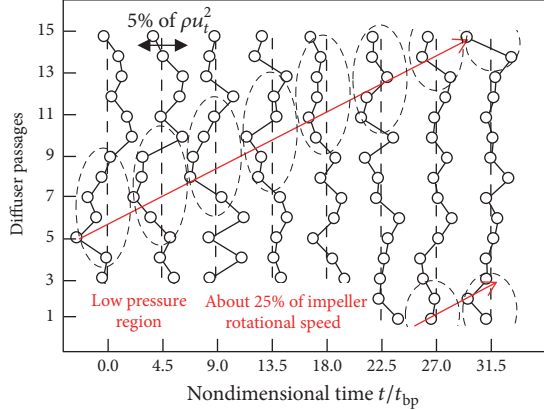


FIGURE 7: Casing static pressure fluctuations at diffuser inlet from nondimensional time  $t^* = 0.0$  to  $t^* = 31.5$  (CFD).

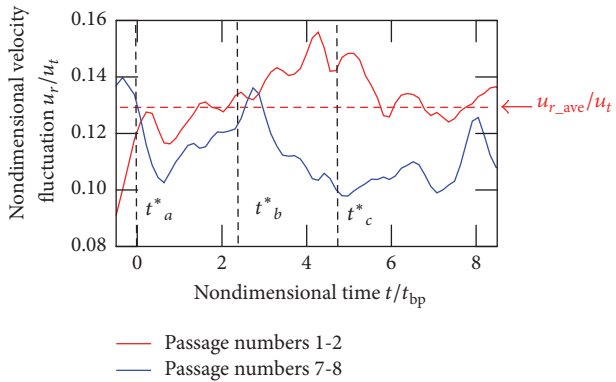


FIGURE 8: Radial velocity fluctuation measured at diffuser inlet (CFD).

in Figure 7, is visualized by Q-definition [24] and colored by nondimensional helicity. In the flow fields at the nondimensional time,  $t^*_c = 4.5$ , the tornado-type vortex connecting the shroud wall and diffuser suction surface was observed on the suction surface of diffuser vanes numbers 7 and 9. Longitudinal vortex was also developed on the suction surface of diffuser vanes numbers 8 and 10. This vortex is called the LEV. The LEV was developed and it formed a substantial blockage within the diffuser passages at off-design points. Furthermore, the other vortical structure was found near the pressure surface of diffuser vanes numbers 8 and 10. This vortex formed a blockage in the throat area, which induced a strong reversal flow near the shroud side. Therefore, it was determined that the developed vortical structure was formed within the stall cell.

To understand the unsteady behavior of the diffuser stall cell, the instantaneous vortical structure within diffuser passages numbers 7-8 at nondimensional times  $t^*_a$ ,  $t^*_b$ , and  $t^*_c$  was visualized. The vortex core colored by nondimensional helicity within diffuser passages numbers 7-8 is illustrated in Figure 10. First, the tornado-type vortex on the suction surface of the diffuser vane was generated at the nondimensional time  $t^*_a = 0.0$ . The tornado-type separation was caused by the positive incidence angle to

the diffuser vane near the shroud side, which had resulted from the stall cell approaching diffuser passages numbers 7-8. Then, the tornado-type vortex was developed and the LEV was observed at the shroud/suction surface corner at the nondimensional time  $t^*_b = 2.1$ . The developed LEV was extended to the next diffuser vane (number 8) because of the high adverse pressure gradient within the diffuser passage. Additionally, the LEV leg was observed on the suction surface of the diffuser vane number 7. The LEV was caused by the secondary flow effect on the suction surface of the diffuser vane. The flow near the suction surface rolled up to the shroud side because of the vertical pressure gradient and formed the longitudinal vortex at the shroud/suction surface corner. At the nondimensional time,  $t^*_c = 4.5$ , the LEV interacted with the next diffuser leading edge and formed the throat area blockage, which induced the strong reversal flow near the shroud side. Accordingly, the separation vortex was considered as having been generated on the suction surface of diffuser vane number 8 with the passage of time, because the incidence angle to diffuser vane number 8 was highly positive. The newly formed tornado-type vortex and LEV were also observed near the leading edge of diffuser vane number 7.

For an improved understanding of the generation mechanism of the vortices near the diffuser vane, the time-averaged distribution and isolines of the static pressure on the diffuser suction surface and casing wall are shown in Figure 11. The vectors on the suction surface and casing wall represent the pressure gradient vectors. Furthermore, the limiting streamlines on the diffuser suction surface are illustrated in Figure 12. Near the diffuser leading edge, the strength of vertical pressure gradient on the suction surface gradually increased from the hub to midspan because the tornado-type vortex resulted in the low-pressure region near the shroud side. From the limiting streamlines of the suction surface, the focus point of the tornado-type vortex leg was to be observed at the diffuser leading edge. In addition to this, the suction surface streamlines rolled up from the hub side to the shroud side because of the high vertical pressure gradient near the diffuser leading edge. As illustrated in Figure 11(b), the direction of circumferential pressure gradient vector on the shroud wall was strongly adverse near the suction surface of the diffuser leading edge, which was the origin of the tornado-type separation vortex. The pressure gradient vectors in the throat area were directed to the impeller exit and leading edge of the succeeding diffuser vane. This is because of the static pressure recovery within the diffuser passage.

To summarize, the structure of the diffuser stall is illustrated in Figure 13. Initially, the tornado-type vortex connecting the shroud wall and diffuser suction surface was generated on the suction surface of the diffuser vane. The LEV developed with the growth of the tornado-type vortex and it approached the succeeding diffuser vane because of the high adverse pressure gradient near the shroud side. Then, the developed LEV interacted with the succeeding diffuser leading edge and formed the throat area blockage with the passage of time. The blockage in the throat area induced the radial reversal flow of high magnitude near the shroud side, and the next separation vortex was formed because of the back flow. Finally, the throat area blockage

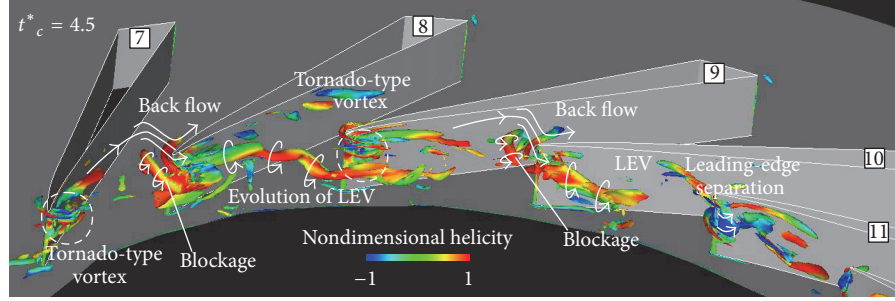


FIGURE 9: Instantaneous vortical structure of diffuser stall within diffuser passages number 7 to number 11.

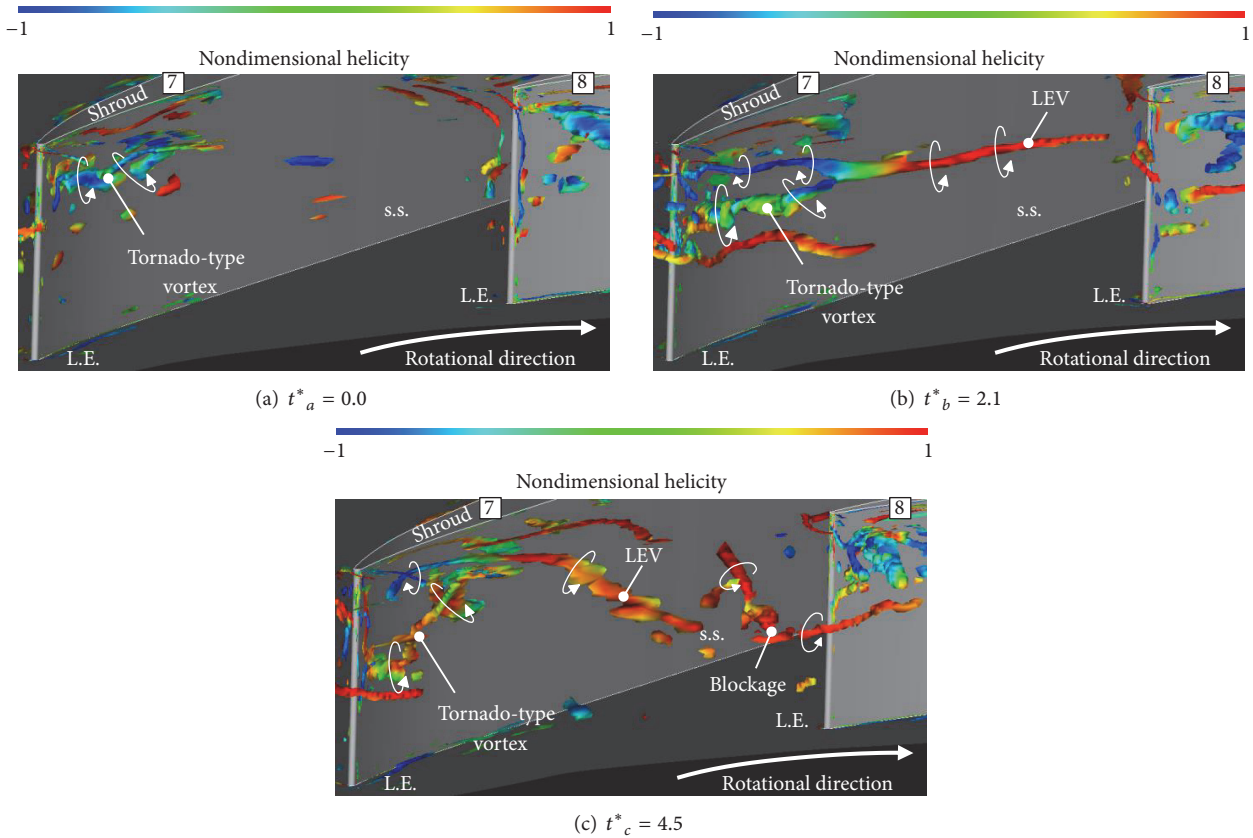
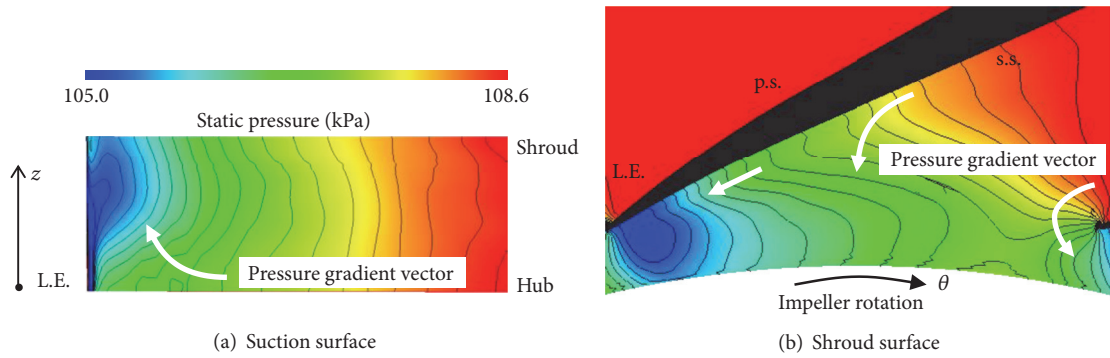
FIGURE 10: Instantaneous vortical structure within diffuser passage numbers 7-8 at nondimensional time  $t^*_a$ ,  $t^*_b$ , and  $t^*_c$ .

FIGURE 11: Distribution of static pressure on diffuser suction surface and casing wall.

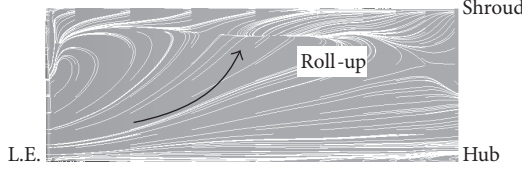


FIGURE 12: Limiting streamlines on diffuser suction surface.

resulted in the tornado-type vortex and LEV. The diffuser stall cell, which was formed by the systematic vortical structure and which consisted of the tornado-type vortex, LEV, and throat blockage, propagated to the succeeding diffuser vane. Therefore, the evolution of the tornado-type vortex and LEV was the cause of the diffuser rotating stall in the centrifugal compressor with a vaned diffuser.

The tested compressor is the low-pressure ratio centrifugal compressor; however the results of vortical structure of diffuser stall cell can be generalized not only low-pressure fluid machinery but also high pressure compressors. For example, Everitt et al. [10] reported the similar unsteady vortices at the diffuser leading edge in a high speed centrifugal compressor, as with the case of our paper. Furthermore, we confirmed that the LEV had the same form at high speed and the size of the LEV was increased at low mass flow rate by CFD analysis, as we have mentioned in our previous paper [12]. Therefore, we may say that the knowledge obtained by this paper about the vortical structure of diffuser stall was also applied to the high pressure ratio centrifugal compressor.

**4.3. Transition to the Stage Stall.** Next, the generation mechanism of the stage stall cell was investigated by experimental analysis at  $\phi = 0.10$ . The velocity and pressure measurements were conducted to reveal the detailed flow fields, when the stage stall occurred. Figure 14 shows the measurement results of radial velocity and casing wall pressure traces (30 Hz low-pass filter) at the diffuser inlet. The low-pass filter was conducted by the inverse Fourier transformation to the measured spectra which cut the high frequency range. The top left and right figures represent the radial velocity traces on the hub side and shroud side, respectively. The left two traces and the right one are measured simultaneously. These figures indicate that the radial reversed flow basically occurred on the shroud side and that the intensity of pressure fluctuation was small in the vaneless space (blue background color: condition (a)). However, the radial velocity was abruptly accelerated on the shroud side and decelerated on the hub side (red background color: condition (b)). Then, there was also a large intensity of pressure and velocity fluctuations (green background color: condition (c)). The cut-off frequency (30 Hz) is closer to the observed rotating stalls frequency (25 Hz and 22 Hz). However, the cut-off frequency was appropriate, because we focused on the whole intermittent process (conditions (a)–(c)) in this study. In addition, the spanwise radial velocity distributions of the impeller-discharge flow on the conditions (a) and (b) are measured at D.I.1–D.I.4 using by two split-film probes, as shown in Figure 15. One probe was set on the hub side in order to capture the stall conditions (a) to (c). Another velocity probe was set to measure the velocity

distribution on each condition. On the flow condition (a), the flow on the shroud side was reversed at all measuring points. Furthermore, the reversed flow at D.I.1–D.I.4 moved from the shroud side to the hub side on condition (b). Thus, it was assumed that the flow condition in vaneless space at  $\phi = 0.10$  was divided into three behaviors and switched unsteadily.

The power spectra of the velocity fluctuations on each condition in the vaneless space are shown in Figure 16. The velocity fluctuations (measured at 25 Hz) caused by the diffuser stall were found near the shroud side on condition (a). Then, the diffuser rotating fluctuations transferred to the hub side on condition (b). Finally, the large intensity of the velocity fluctuation caused by the stage stall was found over the entire span, especially near the hub side. In addition, the low-pass filtered velocity traces were analyzed by wavelet transforms in order to estimate the unsteady behavior of the rotating stalls appearing in the compressor. The wavelet transform of a velocity signal,  $u(t)$ , is defined as follows:

$$W(a, b) = \frac{1}{\sqrt{a}} \int \psi^*(T) u(t) dt, \quad (2)$$

where  $t$  is the time,  $\psi^*(T)$  is a mother wavelet,  $a$  is a scaling factor,  $b$  is a time transformation factor, and  $T = (t - b)/a$ . In this work, the Gabor mother wavelet of

$$\psi^*(T) = \frac{1}{\sqrt{2\pi a}} e^{-T^2/2a^2} e^{-iT} \quad (3)$$

was applied for capturing rotating stall disturbances. Here, the constant parameter,  $\sigma$ , is defined as  $\sigma = 32$  in this work. Figure 17 shows the contour of the wavelet transform  $W(a, b)$  for the low-pass filtered radial velocity traces on the hub side. The vertical axis indicated the frequency,  $f$ . When the radial velocity was decelerated, the diffuser stall fluctuation was appeared. Then, the unsteady disturbances at 25 Hz disappeared, and the stage stall fluctuation was found on condition (c). Finally, the stage stall fluctuation was not found on condition (a). Therefore, it was considered that the diffuser stall which rotated on the shroud side suddenly moved to hub side and evolved into stage stall.

Figure 18 shows the results of simultaneous measurement of radial velocity in vaneless space and casing wall pressure traces (30 Hz low-pass filter) within impeller passages. The top figure is the radial velocity trace on the hub side. The bottom three figures represent the casing pressure traces in the meridional direction, I.I., I.M., and D.I.a. From the results at I.I. and I.M., the scale of pressure fluctuation in condition (b) was larger than condition (a), because the diffuser stall was considered to be expanded to impeller passages. In addition, the stage stall fluctuation was also found in the impeller passages. Figure 19 shows the power spectra of each flow condition measured on the impeller shroud wall in the meridional direction. The red, green, and blue lines indicate the pressure fluctuation level of I.I., I.M., and D.I.a. From these results, the diffuser stall cell was not found within the impeller passages on the flow condition (a). However, the pressure fluctuation of the diffuser stall occurred within the impeller passages on condition (b). Thus, the diffuser stall was considered to expand into the impeller passages

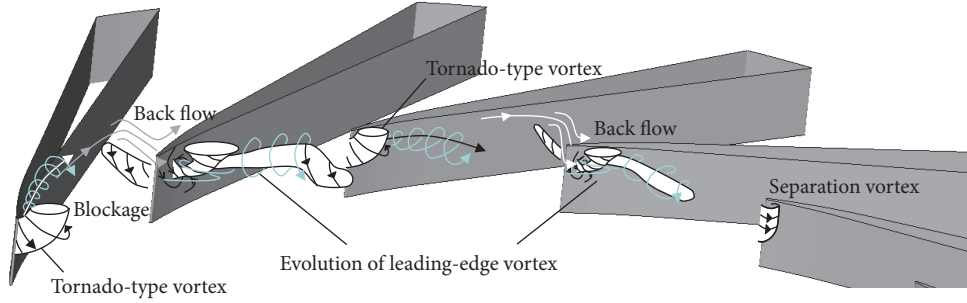


FIGURE 13: Illustration of rotating mechanism of diffuser stall cell.

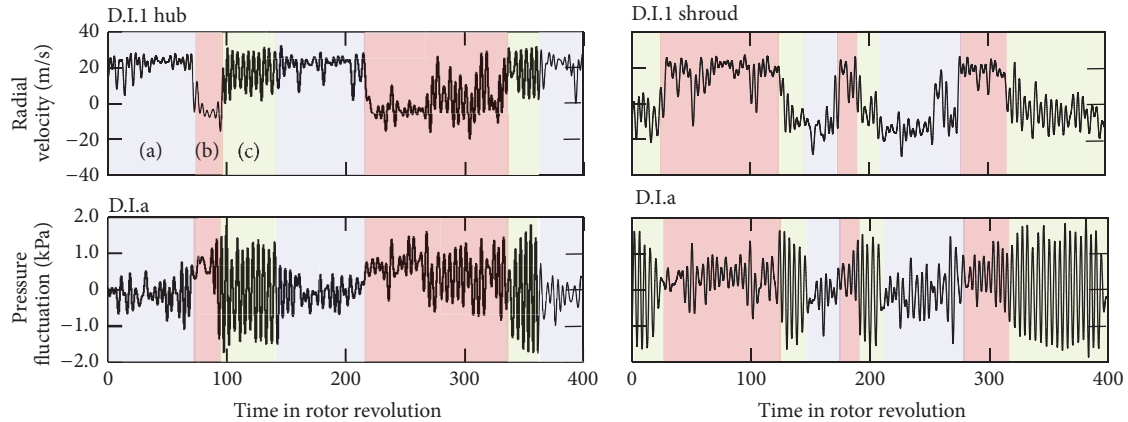
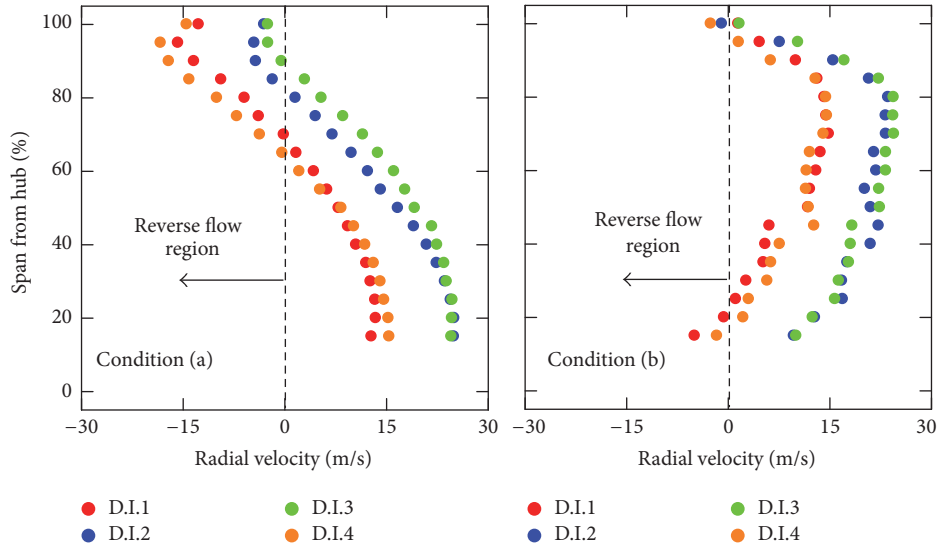
FIGURE 14: Radial velocity and pressure fluctuation traces at diffuser inlet ( $\phi = 0.10$ , 30 Hz low-pass filter).

FIGURE 15: Spanwise radial velocity distributions of the impeller-discharge flow on conditions (a) and (b).

before the stage stall occurred. Finally, the stage stall cell was formed by the expansion of the diffuser stall on condition (c). Furthermore, the pressure fluctuations measured at 55 Hz were found from the power spectra of LI. on conditions (a) and (b). Based on the previous report [12, 13], this 55 Hz pressure fluctuation was caused by the impeller rotating stall.

In the axial compressor, it was reported that the stall cells, which consisted of multiple vortices, merged into a single vortex cell. The single vortex cell blocked the flow in the rotor and stator passages as the mass flow rate decreased [14]. The suggested stall cell structure at the early stage in the axial compressors was similar to the diffuser stall cell observed

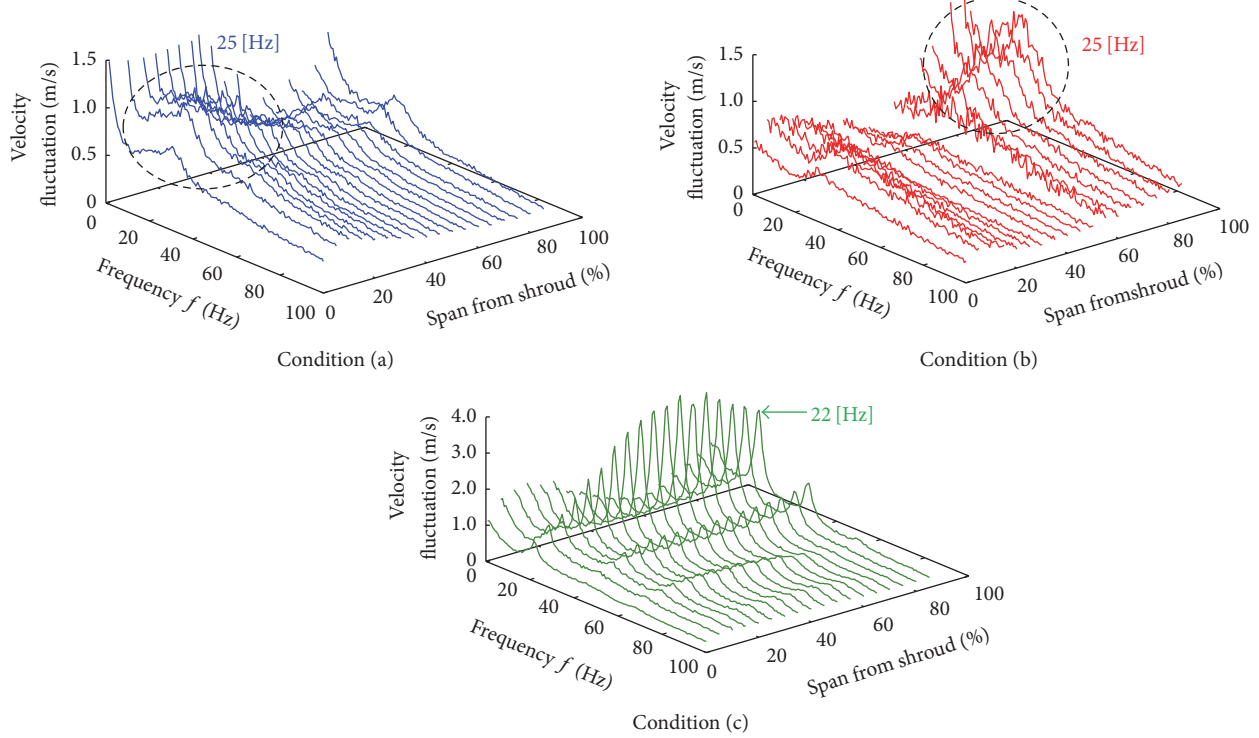


FIGURE 16: Distribution of velocity fluctuation in spanwise direction on three conditions (a)~(c).

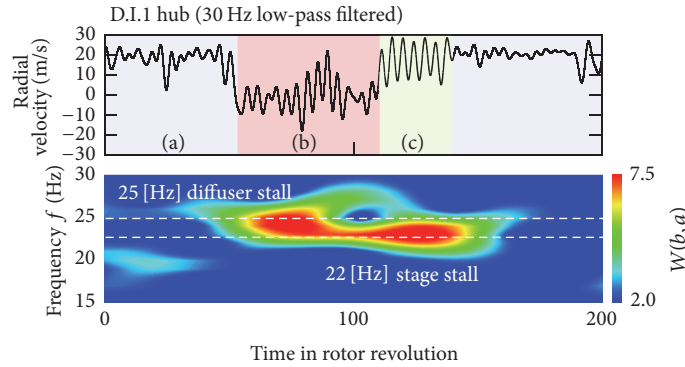


FIGURE 17: Contour map of the wavelet transform  $W(a, b)$  for the low-pass filtered radial velocity traces on the hub side.

above. The CFD analysis was able to capture the impeller and diffuser stall cell; however the development from the diffuser stall to stage stall was not found at the flow coefficient  $\phi = 0.10$ . Therefore, the performance mismatch between experimental and CFD results occurred at  $\phi = 0.10$  because the stage stall deteriorated the compressor performance. The detailed experimental and CFD analysis will be conducted in future studies to examine the relationship between the impeller and diffuser/stage stall cell.

In summary, the stage stall, which rotated within both impeller and diffuser passages, occurred instead of the diffuser stall as the mass flow rate was decreased ( $\phi = 0.10$ ). The diffuser stall, which rotated on the shroud side, was suddenly shifted to the hub side. Then, the diffuser stall moved into the impeller passages and formed the stage stall. Therefore, the

stage stall was caused by the development of the diffuser stall, which transferred from the shroud side to the hub side in the vaneless space and expanded to the impeller passages. In fact, the change in vertical structure from shifting the diffuser stall position was the key to understand the inception mechanism of stage stall. In future work, we will focus on the unsteady structure of diffuser stall before the occurrence of the stage stall by CFD analysis. In addition, we will reveal the clues of the stage stall getting back process to diffuser stall (conditions (c) to (a)).

## 5. Conclusions

The vortical structure of diffuser stall and the transition from diffuser stall to stage stall in a centrifugal compressor with

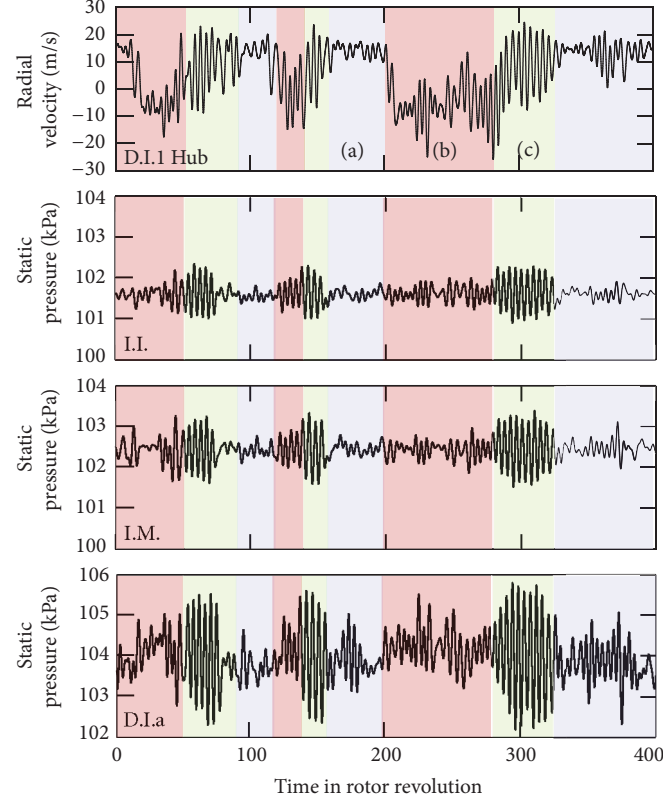


FIGURE 18: Radial velocity at diffuser inlet and static pressure traces at meridional direction ( $\phi = 0.10$ , 30 Hz low-pass filter).

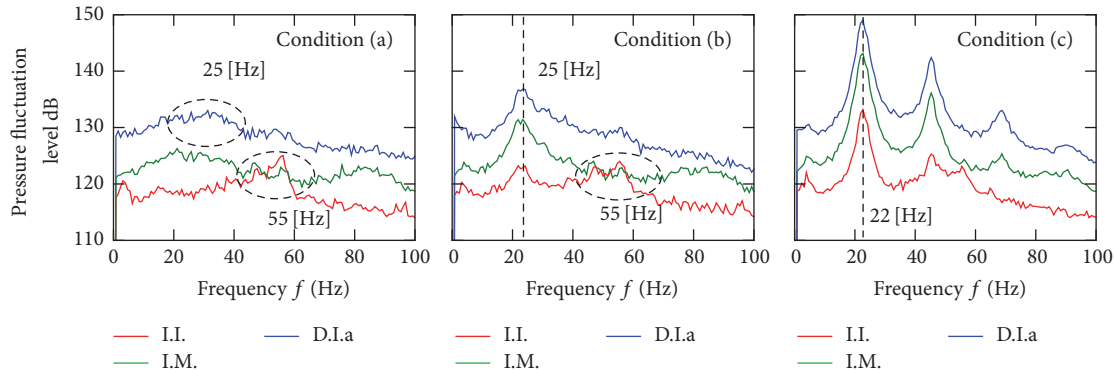


FIGURE 19: Power spectra of pressure fluctuations in impeller passage ( $\phi = 0.10$ ).

a vaned diffuser were investigated by experimentation and through CFD analysis.

The results can be summarized as follows:

- In the tested compressor, the diffuser stall rotated at 25% of the impeller rotational speed during off-design flow operation. Both the experimental and numerical results revealed the rotation of the diffuser stall cell in the vaneless space on the shroud side of the flow passage. In addition, large fluctuations occurred at 22 Hz, and were caused by stage stall when the mass flow rate decreased. The stage stall expanded over the entire span in the vaneless space.

- The vortical structure of the diffuser stall cell consisted of the tornado-type vortex, LEV, and throat blockage. The stall cell's typical vortical structure propagated to the succeeding diffuser passages.
- The tornado-type separation was caused by the positive incidence angle to the diffuser vane near the shroud side. The LEV developed with the growth of the tornado-type vortex and extended to the succeeding diffuser vane. The developed LEV subsequently interacted with the succeeding diffuser leading edge and formed the throat area blockage. Finally, the tornado-type vortex and LEV were developed by the throat area blockage. The diffuser rotating stall was

caused by the evolution of the tornado-type vortex and LEV.

- (iv) The diffuser stall which rotated on the shroud side was suddenly shifted to the hub side as the mass flow rate decreased. The diffuser stall then moved into the impeller passages and formed into the stage stall. The stage stall was caused by the development of the diffuser stall, which transferred from the shroud side to the hub side in the vaneless space and expanded to the impeller passages.

## Nomenclature

- B*: Diffuser passage height (m)  
*D*: Diameter (m)  
*G*: Mass flow rate (kg/s)  
*L<sub>id</sub>*: Distance between impeller exit and diffuser leading edge (m)  
*N*: Rotational speed (min<sup>-1</sup>)  
*Q*: Volume flow rate (m<sup>3</sup>/s)  
*W*: Wavelet coefficient  
*V*: Number of diffuser vanes  
*Z*: Number of impeller blades  
*f*: Frequency (Hz)  
*t*: Time (s)  
*t<sub>bp</sub>*: Blade passing time (s)  
*t\**: Nondimensional time ( $= t/t_{bp}$ )  
*p*: Static pressure (Pa)  
*p<sub>t</sub>*: Total pressure (Pa)  
*u*: Velocity (m/s)  
*u<sub>r</sub>*: Radial velocity (m/s)  
*u<sub>t</sub>*: Circumferential velocity at impeller exit (m/s).

### Greek Letters

- $\rho$ : Air density (kg/m<sup>3</sup>)  
 $\phi$ : Flow coefficient  
 $\psi_t$ : Total pressure-rise coefficient  
 $\psi^*$ : Mother wavelet function.

### Subscripts

- 1: Impeller inlet  
2: Impeller outlet  
3: Diffuser leading edge  
4: Diffuser trailing edge.

### Abbreviations

- D.E.: Diffuser exit  
D.I.: Diffuser inlet  
I.I.: Impeller inlet  
I.M.: Impeller midsection  
LEV: Leading edge vortex  
ODV: Original wedge-type diffuser vane.

## Conflicts of Interest

The authors declare that they have no conflicts of interest.

## Acknowledgments

This work was supported by Grant-in-Aid for Research Activity Start-Up no. 16H07293 from Japan Society for the Promotion of Science.

## References

- [1] F. K. Moore and E. M. Greitzer, "A theory of post-stall transient in axial compressor systems: part 1 development of equations," *ASME Journal of Engineering for Gas Turbines Power*, vol. 108, pp. 69–76, 1986.
- [2] E. M. Greitzer and F. K. Moore, "A theory of post-stall transient in axial compressor systems: part 2 application," *ASME Journal of Engineering for Gas Turbines and Power*, vol. 108, no. 2, pp. 231–239, 1986.
- [3] I. J. Day, "Stall inception in axial flow compressors," *ASME Journal of Turbomachinery*, vol. 115, pp. 1–9, 1993.
- [4] M. Inoue, M. Kuroamaru, T. Tanino, and M. Furukawa, "Propagation of multiple short-length-scale stall cells in an axial compressor rotor," *Journal of Turbomachinery*, vol. 122, no. 1, pp. 45–54, 2000.
- [5] U. Haupt, M. Rautenberg, and A. N. Abdel-Hamid, "Blade excitation by broad-band pressure fluctuations in a centrifugal compressor," *ASME Journal of Turbomachinery*, vol. 110, no. 1, pp. 129–137, 1988.
- [6] U. Haupt, U. Seidel, A. N. Abdel-Hamid, and M. Rautenberg, "Unsteady flow in a centrifugal compressor with different types of vaned diffusers," *ASME Journal of Turbomachinery*, vol. 110, no. 3, pp. 293–302, 1988.
- [7] I. Tomita, S. Ibaraki, M. Furukawa, and K. Yamada, "The effect of tip leakage vortex for operating range enhancement of centrifugal compressor," *Journal of Turbomachinery*, vol. 135, no. 3, Article ID 051020, 2013.
- [8] Y. Fukuda, Y. Takeyama, and Y. Ohta, "Characteristics of rotating instability in a centrifugal blower with shrouded impeller," *Transactions of the JSME*, vol. 80, no. 809, pp. 1–11, 2014 (Japanese).
- [9] Z. S. Spakovszky, "Backward traveling rotating stall waves in centrifugal compressors," *Journal of Turbomachinery*, vol. 126, no. 1, pp. 1–12, 2004.
- [10] J. N. Everitt and Z. S. Spakovszky, "An Investigation of Stall Inception in Centrifugal Compressor Vaned Diffuser," *Journal of Turbomachinery*, vol. 135, no. 1, Article ID 011025, 2012.
- [11] Y. Bousquet, N. Binder, G. Dufour, X. Carboneau, M. Roumeas, and I. Trebinjac, "Numerical simulation of stall inception mechanisms in a centrifugal compressor with vaned diffuser," *Journal of Turbomachinery*, vol. 138, no. 12, Article ID 121005, 2016.
- [12] N. Fujisawa, S. Hara, Y. Ohta, and T. Goto, "Unsteady behavior of leading edge vortex and diffuser stall inception in a centrifugal compressor with vaned diffuser," in *Proceedings of the ASME FEDSM 2014*, 2014.
- [13] N. Fujisawa, S. Ikezu, and Y. Ohta, "Structure of Diffuser Stall and Unsteady Vortices in a Centrifugal Compressor," in *Proceedings of the ASME Turbo Expo 2016*, 2016.
- [14] E. Outa, Y. Ohta, D. Kato, and K. Chiba, "Two-dimensional study on evolution of deep rotating stall under uniform inlet conditions in an axial compressor cascades," in *Proceedings of the 14th International Society for Air Breathing Engines*, pp. 1–11, 1999.

- [15] Y. Yoshida, H. Tsurusaki, Y. Murakami, and Y. Tsujimoto, “Rotating stalls in centrifugal impeller/vaned diffuser systems (1st Report),” *Transactions of the JSME*, vol. 56, no. 530, pp. 2991–2998, 1990 (Japanese).
- [16] S. Mizuki and Y. Oosawa, “Unsteady flow within centrifugal compressor channels under rotating stall and surge,” *Journal of Turbomachinery*, vol. 114, no. 2, pp. 312–320, 1992.
- [17] X. Zheng and A. Liu, “Phenomenon and mechanism of two-regime-surge in a centrifugal compressor,” *Journal of Turbomachinery*, vol. 137, no. 8, Article ID 081007, 2015.
- [18] J. L. Steger and R. F. Warming, “Flux vector splitting of the inviscid gasdynamic equations with application to finite-difference methods,” *Journal of Computational Physics*, vol. 40, no. 2, pp. 263–293, 1981.
- [19] B. van Leer, “Towards the ultimate conservative difference scheme. V. A second-order sequel to Godunov’s method,” *Journal of Computational Physics*, vol. 32, no. 1, pp. 101–136, 1979.
- [20] E. Shima, “A simple implicit scheme for structured/unstructured cfd,” in *Proceedings of 29th Fluid Dynamic Conference*, pp. 325–328, 1997.
- [21] P. R. Spalart, M.-H. Jou, M. Strelets, and S. R. Allmaras, “Comments on the feasibility of les for wings and on the hybrid rans/les approach, advances in DNS/LES,” in *Proceedings of the First AFOSR International Conference on DNS/LES*, 1997.
- [22] M. Strelets, “Detached Eddy simulation of massively separated flows,” *AIAA Paper*, Article ID 2001-0879, 2001.
- [23] S. Ikezu, N. Fujisawa, and Y. Ohta, “Characteristics of a Centrifugal Compressor with Vaned Diffuser,” in *Proceedings of the 6th Asian Joint Workshop on Thermophysics and Fluid Science*, 2016.
- [24] J. Jeong and F. Hussain, “On the identification of a vortex,” *Journal of Fluid Mechanics*, vol. 285, pp. 69–94, 1995.

## Research Article

# Experimental and Numerical Investigations of Surge Extension on a Centrifugal Compressor with Vaned Diffuser Using Steam Injection

**Chuang Gao,<sup>1</sup> Weiguang Huang,<sup>1</sup> Tianhua Zheng,<sup>2</sup> Kang Yang,<sup>2</sup> Haosen Yang,<sup>2</sup> and Yun Cao<sup>2</sup>**

<sup>1</sup>*Shanghai Advanced Research Institute, Chinese Academy of Sciences, Shanghai, China*

<sup>2</sup>*Division of Aerodynamics, Department of R&D, Helan Turbines, Co., Ltd., China*

Correspondence should be addressed to Chuang Gao; [gaoc@sari.ac.cn](mailto:gaoc@sari.ac.cn)

Received 7 February 2017; Revised 6 April 2017; Accepted 13 April 2017; Published 29 May 2017

Academic Editor: Ryoichi Samuel Amano

Copyright © 2017 Chuang Gao et al. This is an open access article distributed under the Creative Commons Attribution License, which permits unrestricted use, distribution, and reproduction in any medium, provided the original work is properly cited.

This paper presents the first report on surge extension with steam injection through both experimental and numerical simulation. The experimental section covers the test facility, instrumentation, and prestall modes comparison with and without steam injection. It is found that surge extension is not in proportion to injected steam. There exists an upper bound above which deteriorates the margin. Injection of less than 1% of the designed mass flow can bring about over 10% margin improvement. Test results also indicated that steam injection not only damps out prestall waves, but also changes prestall modes and traveling direction. At 90% speed, injection changed the prestall mode from spike to modal, while at 80% speed line, it made the forward traveling wave become backward. Through numerical simulation, location and number of injectors, molecular weight, and temperature of injected gas are modified to explore their influences on surge margin. Similar to the test results, there exists an upper bound for the amount of steam injected. The flow field investigation indicates that this bound is caused by the early trigger of flow collapse due to the injected steam which is similar to the tip leakage flow spillage caused spike stall in axial compressors.

## 1. Introduction

Compressor flow instabilities may occur if the fluid flow decreases below a certain limit. Rotating stall and surge are such aerodynamic instabilities that occur in both axial and centrifugal compressors [1–24]. Surge, however, can result both in severe vibration and damage to compressor units and in reduced efficiency. Although many researches were published in the open literature on these two phenomena, the prediction and control of surge are still far away from the requirement of industrial application. In most cases, this can only be done case by case as it depends on the design.

For impellers with a vaned diffuser, most of the researches attribute rotating stall and surge to the increase of incidence angle at low flow rate; however, Spakovszky [2] pointed out that vaned space just in front of the vaned diffuser is the root cause of rotating stall in the NASA CC3 compressor. Schleer et al. [3] measured the trajectories of tip clearance

vortex at different flow rates and concluded that the tip clearance vortex caused the surge incipience. More recently, researchers from the von Karman Institute and University of Hannover [4] noticed the influences of volute on both performance and instability.

To control rotating stall and surge in a centrifugal compressor, various design features have been investigated: self-circulation device [13], variable inlet guide vanes (VIGV), adjustable vaned diffuser vanes, ported shroud [15], grooved diffuser [16], air injection, or bleeding [8].

The analyses for the prestall, stall inception, and the generation of fully developed stall were to explore the interrelationship among them and were then applied in the design of prewarning and stall control systems. Experimental exploration of compressor prestall or stall inception usually involves several transducers for unsteady pressure recording distributed circumferentially in one or more axial locations. The pressure transducer settings for axial compressors were

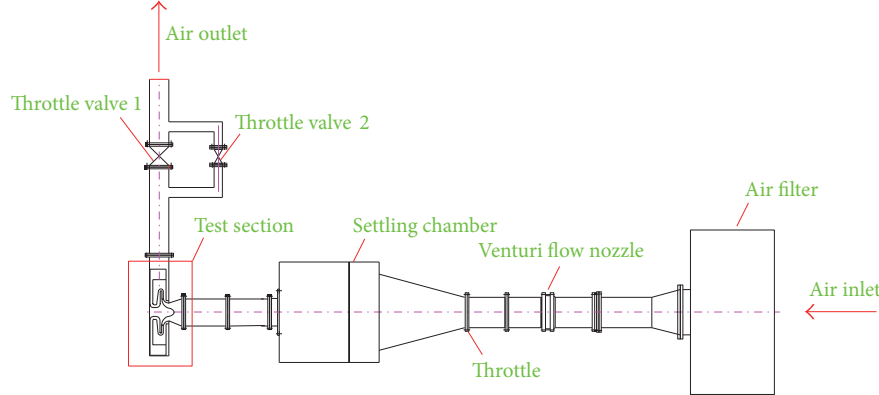


FIGURE 1: Schematic layout of the test facility.

often on the casing above the rotor [20] while the setup for centrifugal compressors sometimes may be considered on both the rotor and the diffuser to tell the stall inception location [24]. Pressure signals should be traced when compressors are throttled to stall. The definitions of prestall, stall inception, and fully developed stall (surge in some cases) were clearly described in [20] and can be understood according to the magnitude of pressure perturbation from relatively calm to large. Tryfonidis et al. [20] also indicated that the rotating stall influences the surge inception mechanism.

The stall wave was typically reported to travel in positive rotor direction as most of the axial compressor did, but in centrifugal compressors, negative traveling stall wave was also reported. Besides, two types of stall, modal stall and spike-like stall, were defined according to the stall length scale. With the theoretical background of this length scale study, various control methods were developed against different length scale stalls. Several methods have been conducted to analyze the circumferentially traveling pressure perturbation. Tryfonidis et al. [20] developed the spatial Fourier decomposition for stall inception area with the PSD analysis for traveling wave energy. In the past decades, the wavelet method was also quickly developed for further understanding of the physical mechanisms which lead to stall, but the result is sensitive to the parameter selection.

To sum up, researches on centrifugal compressor flow instabilities are still not enough for fully understanding and controlling rotating and surge.

Recently, with the stringent requirements on pollutant emissions, the Chinese government encourages distributed energy systems, especially combined cooling, heating, and power (CCHP) systems, in which the key component is a gas turbine. Considering the population of residential areas in most Chinese cities, it has been found that a gas turbine of 2 MW output level is best suited for CCHP systems. At this power level, the gas turbine efficiency is much lower than those used in power plants. Generally, small gas turbines are always used together with a HRSG (heat recovery steam generator) which could provide heating in winter and cooling in summer with absorption refrigerating machine.

In most parts of China, however, there are almost no requirements on both cooling and heating in transitional

seasons, which means that the gas turbine has to be shut down due to its low simple cycle efficiency.

With such background, the authors intend to boost the power output and efficiency through reinjecting the steam from the HRSG. However, to fulfill this aim, the compressor surge line has to be moved to the left due to the increased back pressure caused by the steam injected. Then, a question arises: can we use part of the power boost steam to increase the surge margin without using an external air supply?

The current paper reports related experimental results about impeller and vaned diffuser. The structure of the paper could be summarized as follows. A brief introduction is provided in Section 1. Test facility, experimental procedure, and data acquisition are illustrated in Section 2. The influences of steam injection characteristics at different rotational speeds on stage performance and surge range are discussed in Section 3. Prestall modes are analyzed and compared between a solid casing and one with steam injection in Section 5. Numerical models, compressor performance, surge margin, and diffuser inlet flow angle variation with steam mass flow are investigated using the same configuration as test facility. Flow physics for surge enhancement are then discussed in Section 6. Section 7 covers influences of injected gas properties, injector configuration, and so forth in detail. Conclusion and acknowledgment are given in the last two sections.

## 2. Test Facilities and Instrumentation

**2.1. Test Facilities.** The experiments were conducted on the 500 kW DC motor driven test rig at the Product Laboratory in Shaanxi Blower Company. Figure 1 shows the schematic layout of the test facility.

Ambient air is drawn into the pipe through an air filter and through a flow nozzle to measure the flow rate. The settling chamber is used to lower the gas velocity and make the impeller incoming flow more uniform. After the test section, the compressed air is discharged into the atmosphere. The mass flow rate can be adjusted by two valves. The cross section of the test section is shown in Figure 2.

The test impeller is scaled down by a factor of 0.5 to reduce the power consumption so that it can be driven by the motor

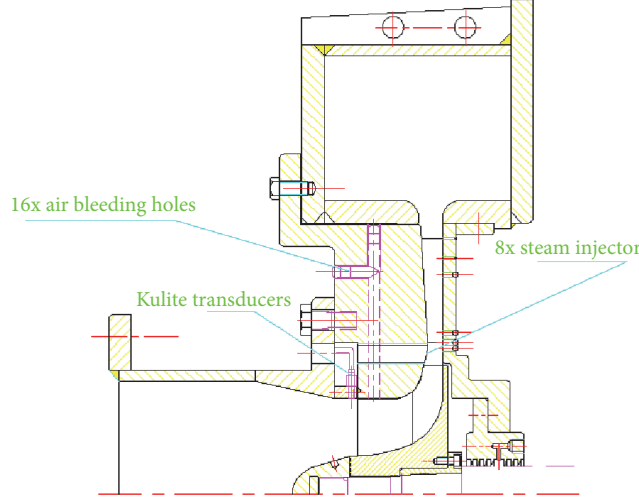


FIGURE 2: Cross-sectional view of the test section.

TABLE 1: Typical design parameters.

Total pressure ratio	—	3.55
Designed mass flow rate	kg/s	3.2
Impeller tip speed	m/s	433
Blade number	—	16 + 16
Impeller tip radius	m	0.115
Average blade exit angle	Deg	90
Impeller blade inlet angle	Deg	52
$n_s$ (dimensionless)	—	0.83
Diffuser inlet angle	Deg	1.6
Diffuser vane number	—	23
Diffuser area ratio	—	2.1

on site. For the scaled version, the primary design parameters are given in Table 1.

In the present test, the compressor was operated at 60%, 70%, 80%, and 90% of the design speed to reduce the risk of potential surge damage at 100% speed. Eight steam injectors were installed midway between the impeller tip and the diffuser leading edge. Sixteen air bleeding holes formed by radial channel and axial channel were used for impeller throat air bleeding, the results of which are not covered in the current paper.

The collector after the diffuser has a constant cross-sectional area which is chosen to be 4 times the vaned diffuser outlet throat area to eliminate the asymmetric influences on upstream components.

**2.2. Instrumentation.** Compressor performance was evaluated by measuring the static pressure and temperature at the inlet of the impeller and the exit of the collector using a pressure transducer from Rosemount Engineering Co. A flow nozzle (shown in Figure 1) was used to measure the mass flow rate based on the pressure and temperature of the surroundings. A five-hole cobra probe with a thermocouple

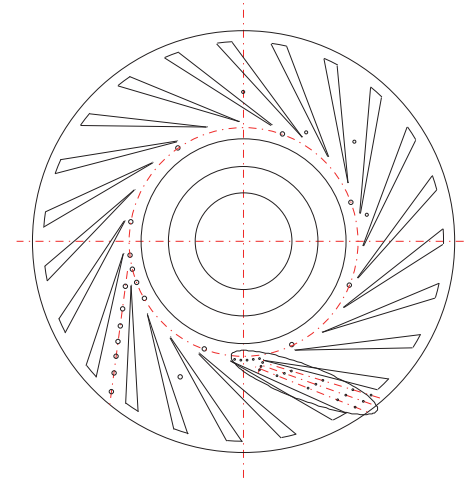


FIGURE 3: Steady and unsteady pressure taps in the diffuser.

was used to measure the total pressure and temperature at the impeller outlet ( $r/r_2 = 1.04$ ).

For the unsteady pressure measurements, 31 Kulite transducers were used. Six of them were uniformly installed 5 mm ahead of the impeller leading edge as shown in Figure 2. 23 of them were installed at the diffuser leading edge, in the diffuser throat, and inside the diffuser channel to record pressure data variation while throttling. The left two were installed in the exhaust collector. Besides the 23 unsteady transducers, 20 steady pressure taps circled by the ellipse shown in Figure 3 were in one channel to find pressure contour variation with reduction of flow rate.

The other two transducers are installed on the collector casing to study the flow behavior inside the collector. A photo of the test rig without shroud is shown in Figure 4 to show the location of the Kulite transducers in the diffuser.

During the test, two throttling valves were fully opened for steady operation at each speed line. Then, they are



FIGURE 4: A photo of the test impeller and transducers.

gradually throttled until the compressor surges. For each speed line, at least six operating points are measured. At each point, all the unsteady pressure data were acquired and stored for at least 20 seconds. After all six performance data measurements are taken, two valves are opened a little to make the compressor operate at the nearest stable point; then, the valves are throttled gradually to push the compressor into surge; after several surge cycles, the valves are quickly opened to 100% in order to pull the compressor out of surge. Unsteady pressure data were acquired all through this process in order to analyze stall/surge precursor and pathology. Sampling frequency of all the 31 transducers was chosen to be 50 kHz in order to avoid frequency alias and to provide enough time resolution.

### 3. Effects of Steam Injection on Performance and Surge Extension

Based on the analysis of component stability [24], accumulated shroud side separation due to centrifugal and Coriolis force, and positive results from Skoch [8], eight injectors are uniformly installed on the shroud side located in the middle of the impeller exit and diffuser leading edge to minimize impeller and diffuser mutual interaction. The position and

tip segment of the injector are designed to take advantage of Coanda flow effects [18] as shown in Figure 5.

For the compressor test alone facility, the injected steam is generated from an electric boiler. The maximum steam mass flow rate is 200 kg/h. In the current experiment, the steam pressure is kept as 6 bar limited by the used electrical boiler and this number should be higher with HRSG used on site.

At constant impeller rotational speed, the injected steam mass flow is increased and kept at several different flow rates to investigate its influences on surge margin. At each steam flow rate, valves are gradually throttled to find the surge flow rate. In this paper, surge margin improvement (SMI) is defined as  $(m_{so} - m_s)/m_{so} \times 100\%$ , in which  $m_s$  and  $m_{so}$  are surge flow rates with and without steam injection, respectively.

Variations of SMI under 80% and 90% of the designed rotational speed for six different steam flow rates (I: 0.521 g/s, II: 1.042 g/s, III: 2.083 g/s, IV: 3.125 g/s, V: 4.167 g/s, and VI: 5.208 g/s) are shown in Figure 6.

In Figure 6, it is obviously observed that the trends for these two different rotational speeds are different especially at high steam flow rate. For the line with  $\text{Mu} = 0.96$ , there is an optimum steam flow for which the surge extension is maximized. This trend is kept the same for  $\text{Mu} = 1.08$  except for the first point. For this point only, 0.15% designed mass flow rate can increase surge margin by over 11%. This effect is the same as the fifth point of which the mass flow rate is seven times as large as that of the first point. The strange phenomenon is that the surge margin extension decreased with increasing injected steam mass flow rate. This implies that the traditional explanation based on flow angle might not be correct for the surge inception of centrifugal compressor or at least for this compressor. Detailed explanation was given in Section 4 from the point of different stall mode about the different trends shown by 80% and 90% speed line.

After reviewing the test data, it is found that steam injection brings about loss to both pressure ratio and efficiency as shown in Figure 7. Stage efficiency is defined by the following equation:

$$\eta_{\text{stage}} = \frac{T_{t1} \left[ (P_{3,\text{st}}/P_{t1})^{(n-1)/n} - 1 \right] m_1 + T_{t1,\text{inject}} \left[ (P_{3,\text{st}}/P_{t1,\text{hole}})^{(n-1)/n} - 1 \right] m_{\text{inject}}}{m_1 (T_{3,\text{st}} - T_{t1}) + m_{\text{inject}} (T_{3,\text{st}} - T_{t1,\text{hole}})}. \quad (1)$$

Even with the same steam flow rate, the loss deviates greatly. For example, for the index equal to 5 (flow rate: 4.167 g/s), the loss at  $\text{Mu} = 0.96$  is almost 8 times that of  $\text{Mu} = 1.08$ . Another interesting phenomenon is that good SMI points always coincide with good loss ones. The above phenomena shown by Figures 6 and 7 are repeatable at different ambient conditions from three test days.

### 4. Prestall Modes and Surge Characteristics

*4.1. Unsteady Pressure Traces.* Pressure traces at 80% and 90% with and without steam injection located at different

streamwise locations (impeller inlet, semivaneless diffuser, diffuser throat, and diffuser midpassage) during stall ramp just before surge are presented in Figures 8(a)–8(d).

In Figure 8, it is observed that the prestall waves are pronounced at the diffuser throat which means that the dominant modes here are the diffuser modes. Thus, the following studies are focused on diffusers. The magnitude of pressure perturbations with injection is on the same level as the case without injection. Additionally, one interesting finding is that the prestall mode even changed from spike to be of modal type as shown in Figure 8(b) on 90% rotational speed with the existence of steam. It can be explained that

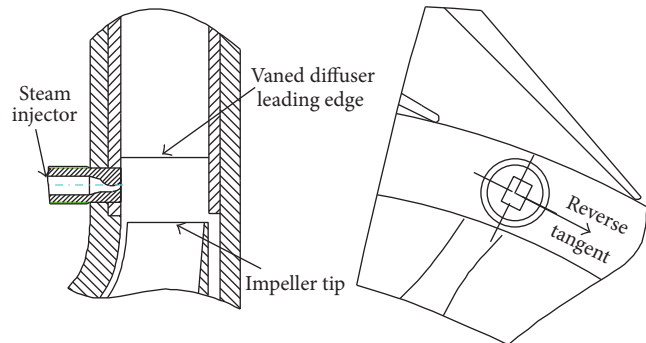


FIGURE 5: Steam injector.

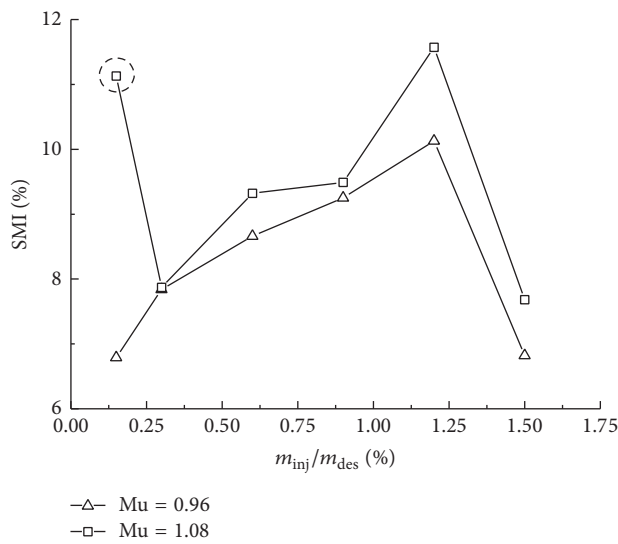


FIGURE 6: Steam injection percentages on surge extension.

the injected flow at shroud increases system damping which caused the prestall mode's variation from short wave (spike) to long wave (modal). Instead of flow injection in the current paper, endwall flow bleeding on the hub side can also generate similar effects as shown by Spakovszky and Roduner [5] in a turbocharger compressor.

With a closer view, it can also be seen that the steam injection damped out the pressure oscillation after surge ( $t = 0$ ) occurred through comparison of the wave segment in the black circle with the same segment with injection. It is worth noting that, after surge, the pressure traces at the impeller inlet behave much less violently than those in other locations or in the same location with steam injection on. This also indicates that surge root comes from the diffuser area. Damping that pressure perturbation amplitude can reduce the surge intensity.

This can also explain the strange phenomenon shown by Figure 6 in which the largest surge margin improvement is at the smallest injection flow at 90% speed line while the surge margin improvement at 80% speed line is gradually increased with the amount of steam flow. This means that, at 90% speed line, the prestall wave is a spike which is nonlinear. With the increase of steam injection, the prestall wave changes from

spike to be modal which is linear long wave. And at 80% speed line, the prestall wave is always linear modal wave.

**4.2. Traveling Wave Energy Analysis of Prestall Behavior.** Traveling wave energy method was used to analyze the prestall wave traveling frequency and direction. The  $x$ - and  $y$ -axis of the TWE spectra depicted in Figure 9 were normalized by rotor revolution and rotor frequency ( $N$  means one rotor  $1x$  frequency in later description), respectively. To further analyze this prestall activity, the pressure signals are decomposed into spatial Fourier harmonics. For each harmonic, the evolution of power spectrum is then computed. The plotted spectrum is the difference between the positive and the negative frequency spectra of the complex spatial Fourier coefficient. Peaks and valleys therefore stand for the forward (with the rotor revolution direction) and backward (against the rotor revolution direction) traveling waves as described by Tryfonidis et al. [20]. In Figures 9 and 10, the time index equal to zero is assigned for fully developed stall (surge).

Figure 9 shows the 90% TWE results without steam injection. The impeller rotating frequency which is  $1N$  was clearly shown. The  $0.3N$  frequency was the first stall frequency emerging at relatively high mass flow rate compared with that of surge point, and  $0.13N$  that appeared in the 3rd harmonic just before surge is the second stall frequency. The  $0.3N$  frequency in the 1st harmonic is clearly the dominant frequency and mode before surge, and  $0.13N$  frequency is the dominated stall precursor in the 3rd mode. Both stall precursors traveled in the forward direction.

However, with  $120\text{ kg/h}$  steam injection, the  $0.3N$  frequency was suppressed and almost invisible. The  $0.13N$  frequency dominated all the other harmonics as shown in Figures 10 and 11. In Figure 11, due to the in-phase or unchanged phase features of the 4 pressure traces at different circumferential angles, the authors claim that these circumferential areas are covered by one stall cell. This means that, after steam injection, there exists one big stall cell that moves in the impeller rotation direction in the speed ratio of 13%.

For the 80% TWE results with/without steam injection, the results are similar. The  $0.22N$  frequency was the first stall wave emerging at relatively high mass flow rate and the  $0.13N$  appeared in the 2nd harmonic just before surge. The only difference and strange thing is that the prestall modal wave traveling direction of  $0.13N$  shifts from forward (rotation direction) to be backward (against rotation direction). This phenomenon can be observed by listing all circumferential unsteady pressure traces in circumferential direction as shown in Figure 12. This further complicates surge scenario and was also never been reported before in public references. Similarly, as shown in Figure 11, Figure 12 also indicates a stall cell moving slowly against impeller rotation direction with injected steam but with larger size than the case of 90%.

Detailed influences of the amount of steam injection ( $0\text{ kg/h}$ ,  $30\text{ kg/h}$ ,  $60\text{ kg/h}$ , and  $120\text{ kg/h}$ ) on prestall mode activity at two different rotational speeds (80% and 90%) in a semivaneless space are summarized in Figure 13. At 80% speed, the  $0.22N$  content only existed at  $0\text{ kg/h}$  and was suppressed in other cases. With the increase of injection flow,

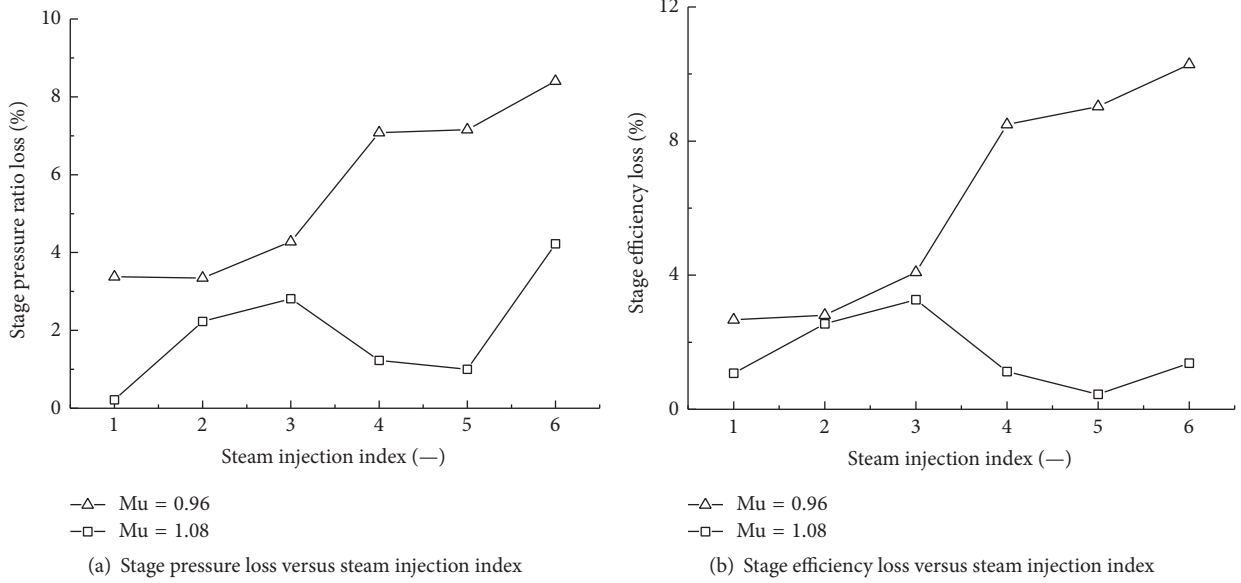


FIGURE 7

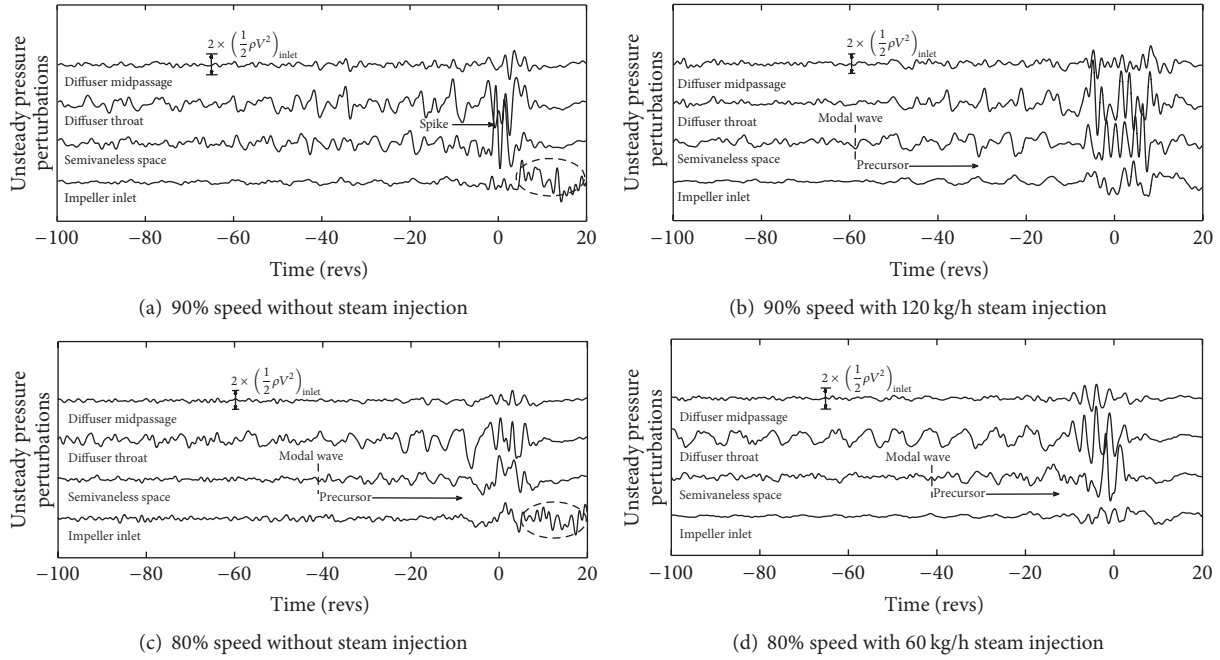


FIGURE 8: Pressure perturbation analysis for streamwise locations.

the amplitude of prestall waves was gradually attenuated. At 90% speed, the frequency of the original 0.3 N prestall wave decreased from 0.3 N to be 0.23 N with 120 kg/h. With 150 kg/h injection flow (not shown in the figure), this content is completely suppressed. From the figure, nonlinear coupling between different modes can be easily found which means one mode always has contributions from other harmonics by seeing that the same frequency exists in different modes. It can be observed that 30 kg/h injection damps out almost all the prestall modes compared to other amounts of injections. If, further, more steam is injected, some higher modes can be

damped further, but not that obviously. These observations agree well with test results shown in Figure 6.

**4.3. Discussion on Experimental Results.** Depending upon steam quality (superheated/saturated), nozzle parameter (position/number/angle), and other factors, there are several things that happen with steam injection into the flow path. These things are as follows:

- (a) The injection of steam into the flow path has an effect on the properties of the flow, especially in changes

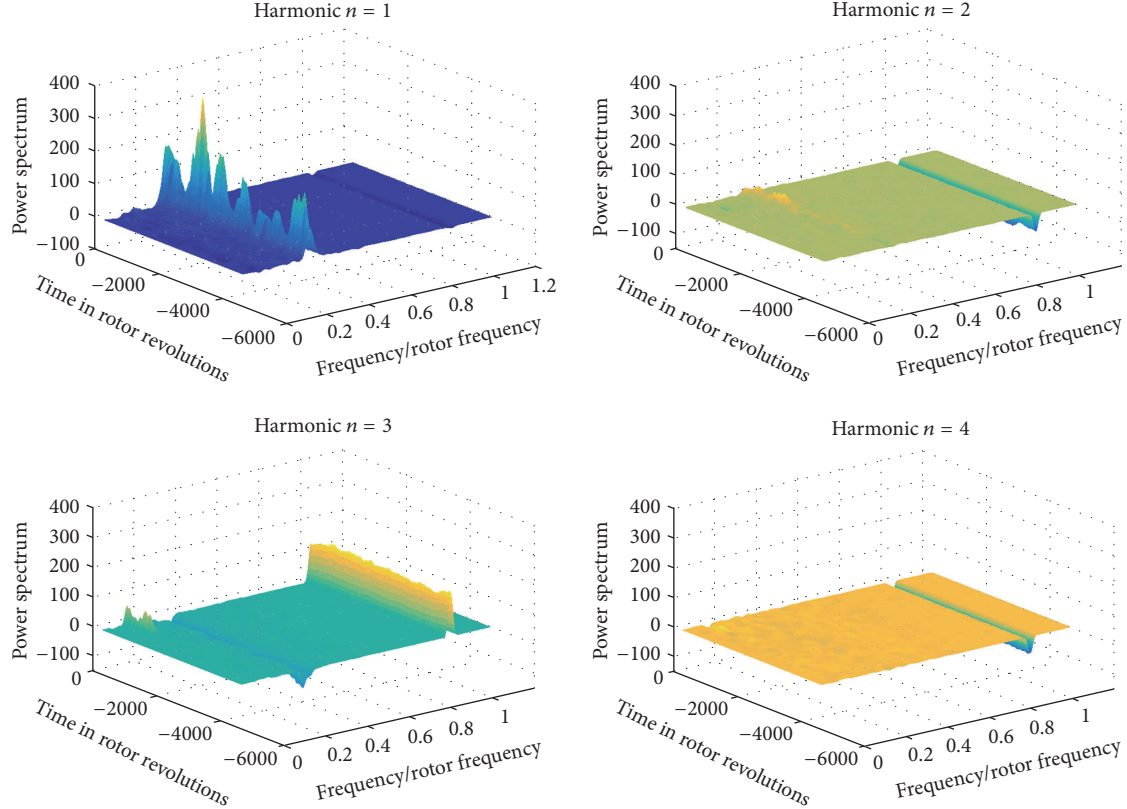


FIGURE 9: Spectrograms of the 1st, 2nd, 3rd, and 4th spatial harmonic pressure perturbations during stall ramp at 90% design speed without steam injection.

- to the gas constant, theta, and gamma. This finally changes the operating characteristics of the diffuser.
- (b) Depending upon temperature difference between steam and air, the heat transfer effect between the two fluids influences the incidence angle of the diffuser through changes in velocity vectors.
  - (c) The different nonuniform temperature in both circumferential and axial directions changes the local corrected speed and local corrected flow which makes different parts of the diffuser work under different inlet flow conditions.
  - (d) The steam injection can enhance the flow momentum of the flow near the shroud where wake and separation always exist and delay the flow separation which improves diffuser stability.
  - (e) At subsonic diffuser inlet conditions, steam injection can also have certain influences on the impeller performance which might also be beneficial for the stability.

To answer the above questions, numerical simulations and detailed flow field analysis were performed.

## 5. Numerical Procedures

Full annulus numerical grids are meshed with impeller, injector, vaned diffuser, and volute. The grids are blade centered

TABLE 2: Mesh densities of CFD domains.

Domain	Numbers of grids
Rotor	2328384
Diffuser	2435424
Injector	180168
Collector	289856
Total	5233832

multiblocks with hexahedral structure. The stator and rotor grids had ATM optimized topology which was a proprietary blocking strategy for obtaining good quality grids. The grids were made finer at the regions where high gradients were expected in the flow passage. The 3D computational grids used in the analysis are shown in Figure 14. The mesh in the boundary layers was refined to ensure  $Y+$  ranged from 30 to 40, the total grids number was about 5.2 million, and mesh densities after grid independency check for each component are given in Table 2.

The  $k-\epsilon$  turbulence model with a scalable wall function was chosen. A total pressure and total temperature inlet boundary condition were used at the rotor inlet, a mass flow outlet boundary condition was set at the diffuser outlet, and a second mass flow inlet was defined at the injectors inlet. The rotor domain was solved in rotational coordinate frame with rotational speed of 30780 rpm. The rotor domain and

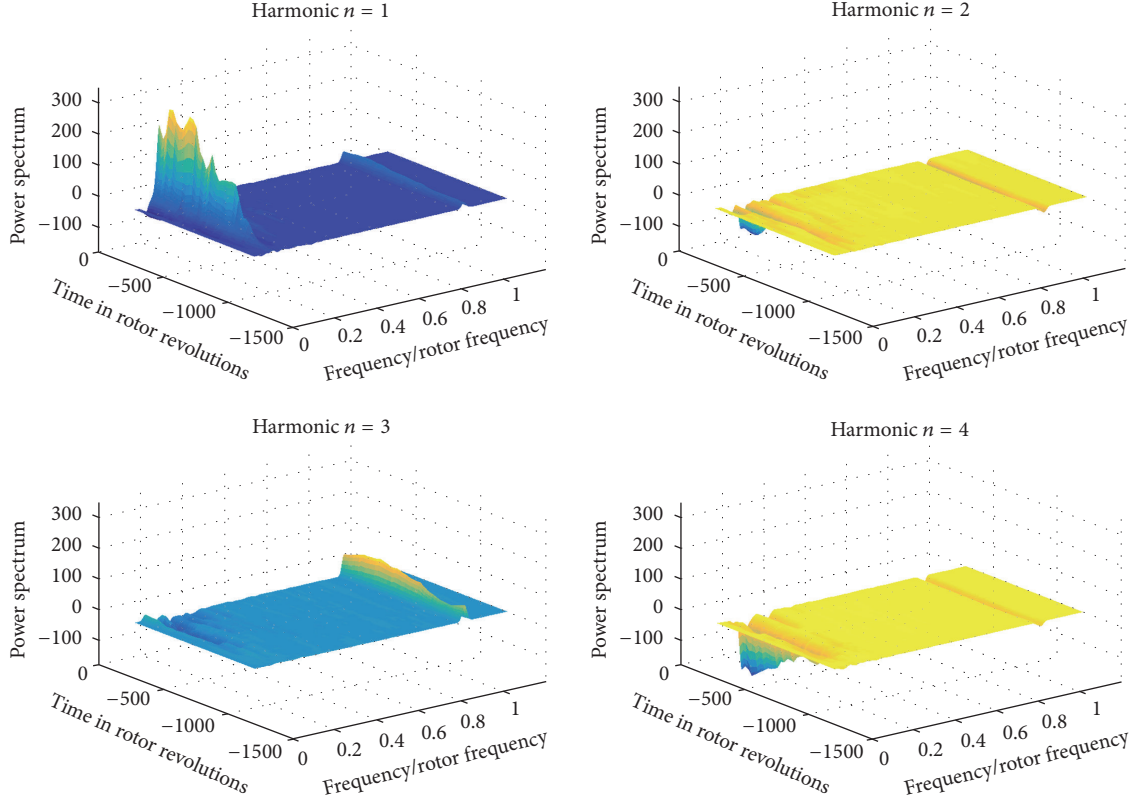


FIGURE 10: Spectrograms of the 1st, 2nd, 3rd, and 4th spatial harmonic pressure perturbations during stall ramp at 90% design speed with 120 kg/h steam injection.

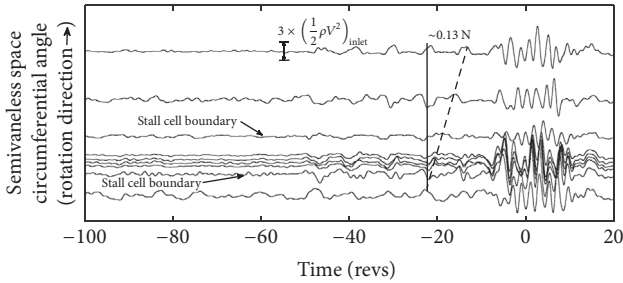


FIGURE 11: Unsteady pressure traces at 90% speed with 120 kg/h steam injection (Kulite transducers all located in a semivaneless space).

injection domain exchanged boundary conditions across the mixing plane interface. The downstream side was treated as an inlet face with the boundary conditions defined by averaged flow properties at the impeller exit. The upstream impeller side could be seen as an outlet face with the exit flow condition being provided by the diffuser inlet flow. The case was considered to be converged when the RMS was below  $1e - 5$  and the variation of the TTE (total-to-total efficiency) was within 3%.

Compressor performance was evaluated by measuring the static pressure and temperature at the inlet of the impeller and exit of the gas collector using a pressure transducer from Rosemount Engineering Co., Ltd. A flow nozzle was used

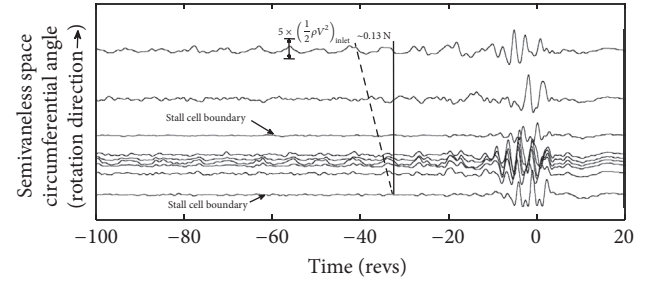


FIGURE 12: Unsteady pressure traces at 80% speed with 60 kg/h steam injection (Kulite transducers all located in a semivaneless space).

to measure the mass flow rate based on the pressure and temperature of the surroundings. A five-hole cobra probe with a thermoresistor was used to measure the total pressure and temperature just at the impeller outlet.

Figure 15 presents the comparisons between computed and measured compressor characteristics with 120 kg/h steam injection and without steam injection at 90% speed, which plotted both the TTPR and the TTE as a function of diffuser exit mass flow corrected to sea level total pressure and temperature; the choke limit and the surge limit frame the operating range on both ends of the abscissa. Both the CFD predictions and the experimental datum with steam injection extended the stable flow range, while around 5% drops in

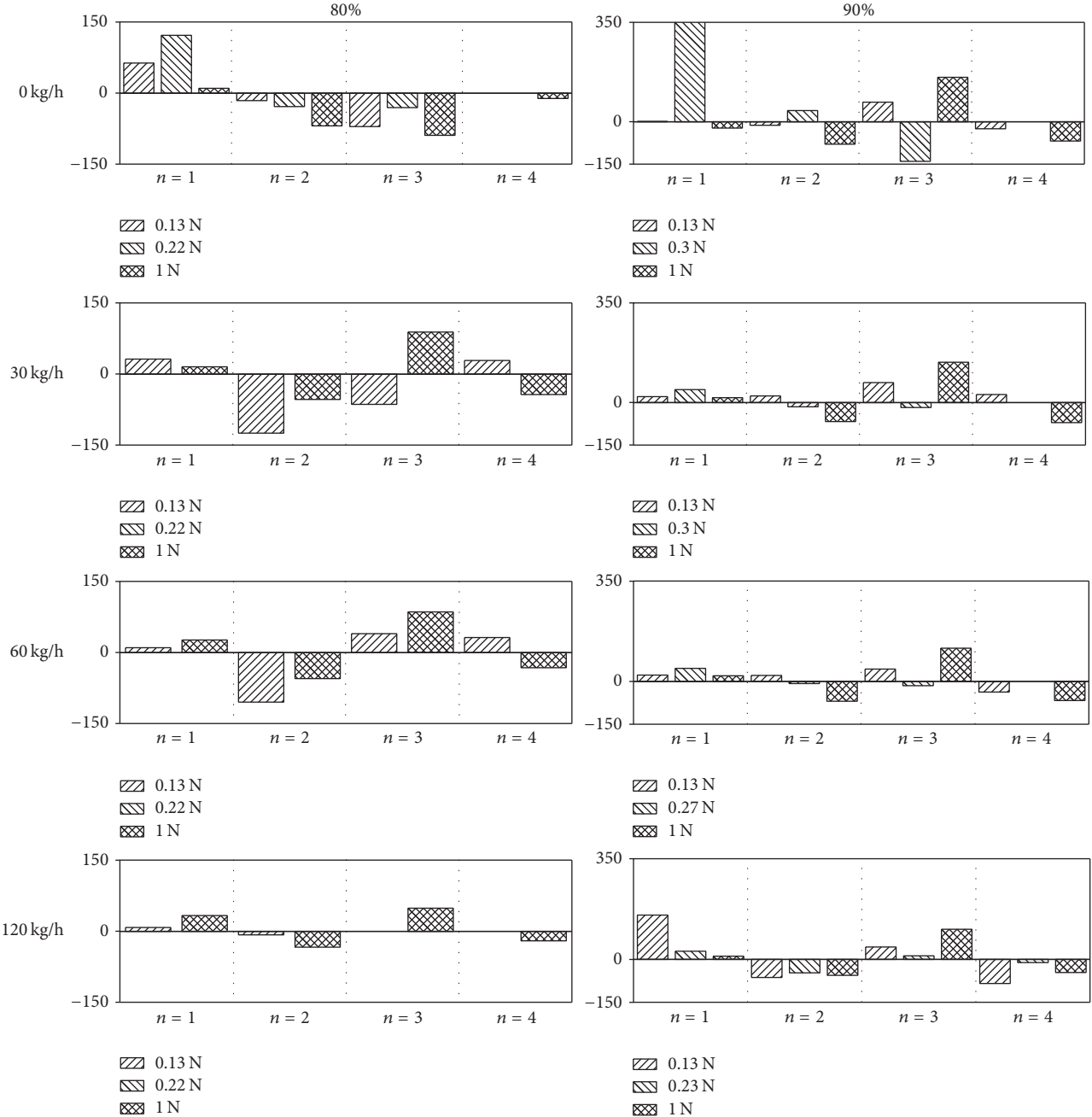


FIGURE 13: Harmonic content of traveling energy of the first four prestall modes at the diffuser inlet.

pressure ratio and efficiency were observed in steam injected technology compressors.

The overall agreement between experiments and computational data was reasonable. The simulation characteristics indicated a higher pressure rise and higher efficiency than that observed in experiment. The difference in pressure ratio and efficiency between the measurements and CFD calculations could possibly be attributed to the turbulence model. As the full flow passage model cases were simulated,  $\kappa$ - $e$  turbulence model was selected in order to procure convergence in the calculations. However, some loss may be ignored and the compressor performance was improved.

## 6. Mechanisms of Surge Enhancement with Steam Injection

In order to clearly identify the effect of steam injection on impeller and vaned diffuser, the individual components of the stage were studied separately. Impeller total efficiency and pressure recovery coefficient ( $C_p$ ) of the vaned diffuser based on the CFD results are used to depict the performance of the impeller and the diffuser. Calculated results with different steam flow rates at the same operating point are shown in Figure 16. Each curve is composed of 20 different span stations from hub to shroud, that is, from 0.0 to 1.0. Thus, the

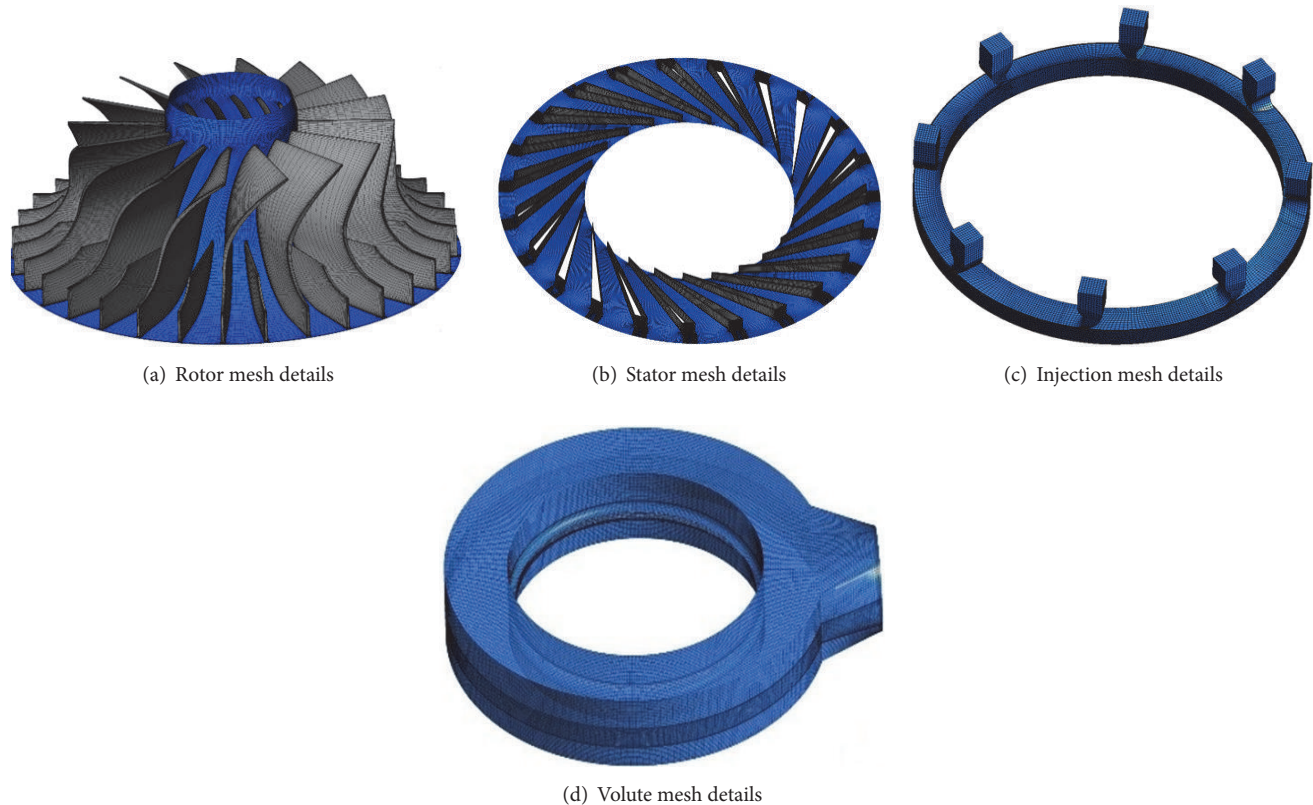


FIGURE 14: CFD computational grids.

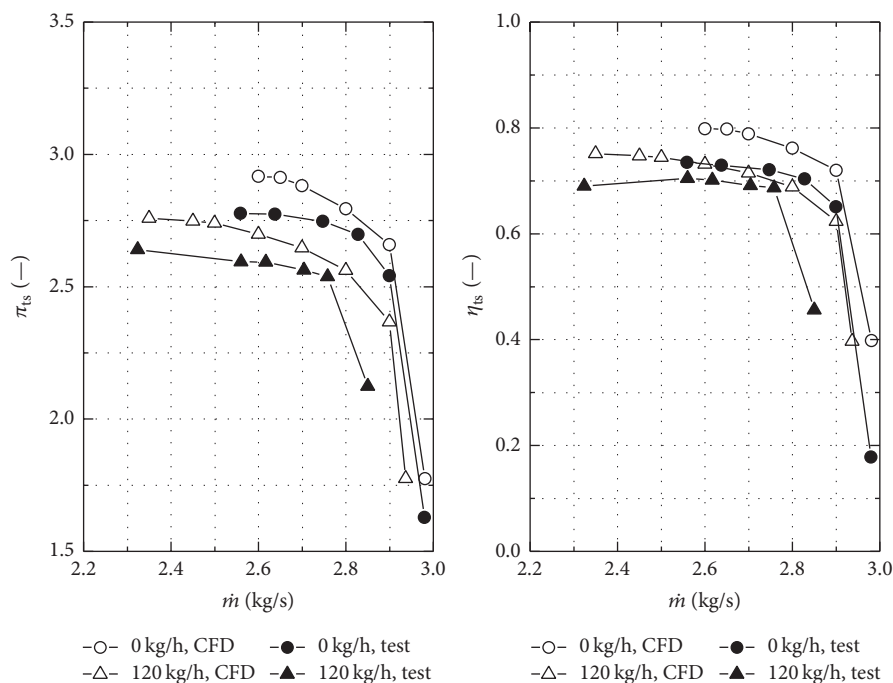


FIGURE 15: Performance comparison between numerical simulation and test results.

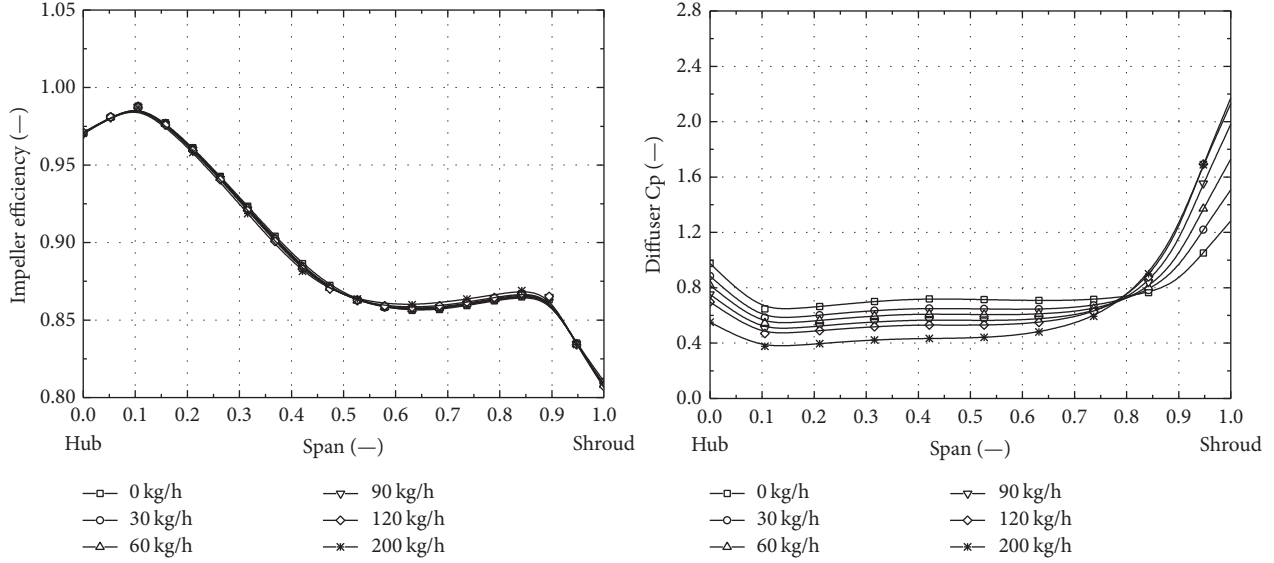


FIGURE 16: Characteristics of the impeller and the diffuser.

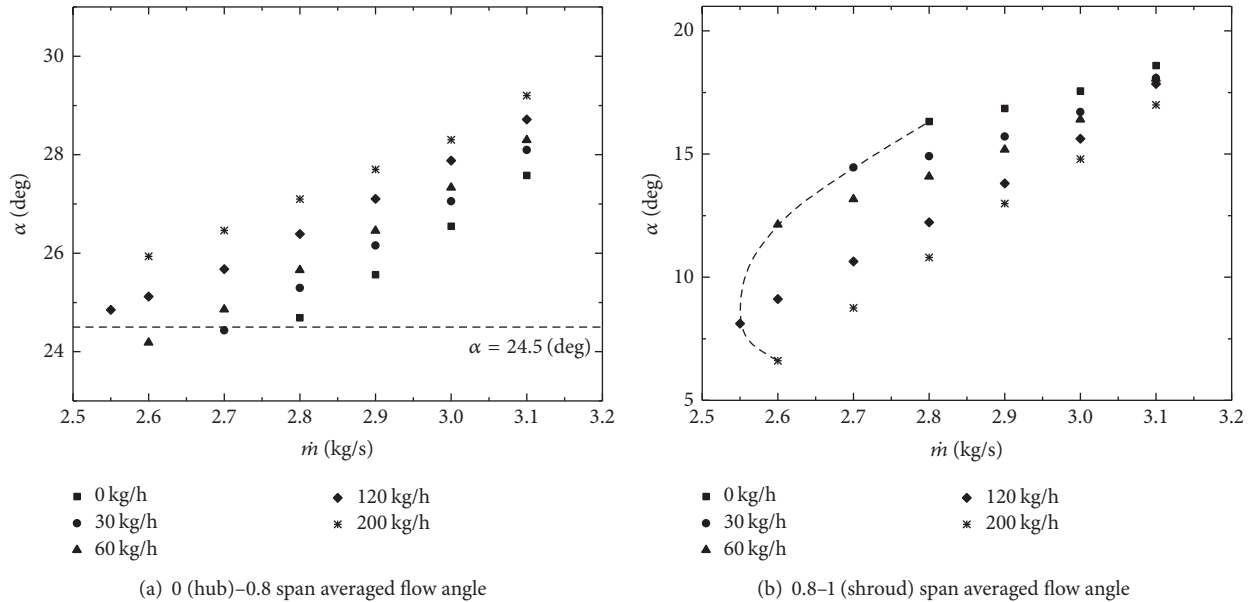


FIGURE 17: Flow angle at diffuser inlet of different span ranges.

diffuser can be decomposed to 20 small diffuser segments and each of them operates at its own working condition. Results show that the impeller efficiency stays constant at different steam injected flow rates, which means that the injected steam hardly affects the performance of the impeller.

However, the diffuser Cp near the shroud side shows a large increase with injected steam, while the change of Cp from hub to 80% blade height is much smaller. The diffuser Cp value varies obviously as the steam flow rate increases from 30 kg/h to 120 kg/h.

From the above observed trends, a conjecture can be reached that the vaned diffuser is the dominant component that affects the stage stability.

The trends of diffuser inlet absolute velocity flow angle at different operating conditions and different flow rate steam injection are plotted in Figure 17. In the 0–0.8 span analysis, as the mass flow rate through the compressor decreases from choke to surge, the average absolute flow angle at the diffuser inlet reduces. At the same operating condition, the flow angle increases after steam is injected. It could also increase velocity flow angle at the same operating condition and improve surge margin. Compressor surge occurred when the flow angle reached about 24.5 under all different steam injection flow rate conditions except 200 kg/h, at which the compressor surge occurred at larger flow rate. Therefore, the surge margin improvement was not in proportion to the steam flow rate.

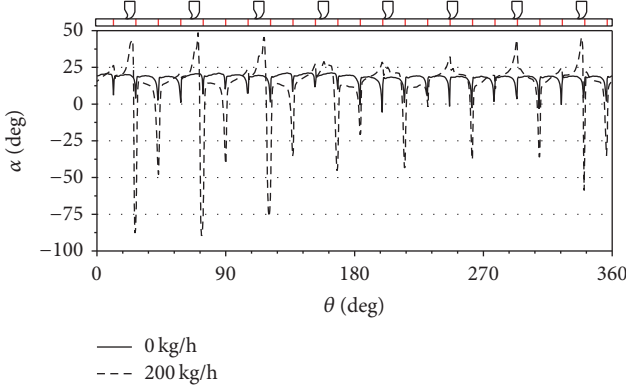


FIGURE 18: Absolute velocity flow angle at 0.9 span at the diffuser inlet.

In certain cases, the large steam injection rate has a smaller surge margin improvement than small steam injection. This phenomenon could be explained in the 0.8–1 span analysis. Steam injection could decrease the velocity flow angle at the same operating conditions and deteriorate the flow structure in this area. The velocity flow angle reached the critical value under 200 kg/h steam injection condition. Therefore, surge occurred earlier when steam flow rate was 200 kg/h. This could be attributed to the excessively small velocity flow angle in 0.8–1 span and will be explained in the following section.

The absolute velocity flow angle at 0.9 span at the diffuser inlet with different steam injection rates was plotted relative to the peripheral direction in Figure 18. Eight steam injectors were uniformly installed upstream of 23 diffuser blades. Their relative positions in the peripheral direction are also shown in the figure. In the current case, the steam is injected in the reverse direction of impeller rotation. Therefore, the direct impact of steam injection was to decrease the circumferential velocity at high span regions and increase the flow angle at the 8 injectors' locations. However, Figure 18 also indicated that flow angle was decreased suddenly as fluid passed through an injector adjacent downstream blade.

If the steam injector is located just between two adjacent diffuser vanes in peripheral direction, flow angle suddenly increased just after the steam injector and flow angle decreased excessively at the neighboring diffuser vane behind this injector. And if the steam injector is located close to a diffuser vane or coincided with a blade in theta direction due to odd number of diffuser vanes, flow angle increased unintelligibly at the steam injection locations, while flow angle decreased slightly at the neighboring diffuser vane behind this injector. In general, as the steam injection flow rate increased from 0 kg/h to 200 kg/h, the flow angle at the steam injector location increased greatly while the flow angle at the neighboring diffuser vane behind this injector decreased excessively.

Detailed flow structures and flow mechanism were studied to explain the feature of the flow angle discussed above. Figure 19 presents the velocity vector field comparison at 90% span around the diffuser inlet area including two certain steam injectors and their downstream neighboring

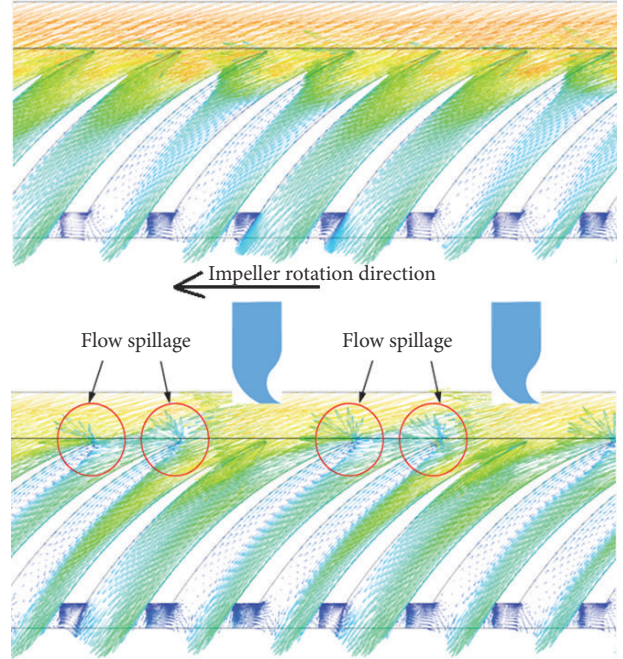


FIGURE 19: Surface streamline at 0.9 span around the diffuser inlet.

diffuser vanes with 0 kg/h at numerical surge point and 200 kg/h steam injection. As indicated in red circles, with injected steam against the direction of impeller rotation, the circumferential velocity decreased, and thus the diffuser inlet flow angle at high span regions increased. Steam injection causes streamline to turn toward the blade passage, and the flow will spill over adjacent blade leading edge, thus triggering system instability. However, the streamline flowed into the next downstream blade passage instead of the current one affected by the neighboring diffuser vane. This was the main reason that flow angle decreased excessively at the neighboring diffuser vane behind an injector, and separation or blockage in injector positioned diffuser passage may be responsible for the observed behavior. This is quite similar to those found in axial compressor.

To figure out how the steam injection affected the flow angle, the circumferential velocity and the radial velocity versus the normalized span location at the diffuser inlet with a main flow rate of 2.8 kg/s are shown in Figure 20, respectively. In general, large injection mass flow generated a stronger influence on the velocity. But the influence was not linear with respect to the span location. The variation of  $V_\theta$  was limited to the high span space due to the Coanda effect, and a uniform  $V_\theta$  is obtained for different injection flow rate below 0.5 span, while  $V_r$  decreased near the shroud side and increased near the hub side. This was because the main flow rate, which is directly associated with  $V_r$ , was set to be a constant value. If the mass through the high span space was reduced, the mass through the low span space must increase to maintain a constant mass flow. The coupled influence by  $V_\theta$  and  $V_r$  increased the flow angle in the low span and decreased it in the high span.

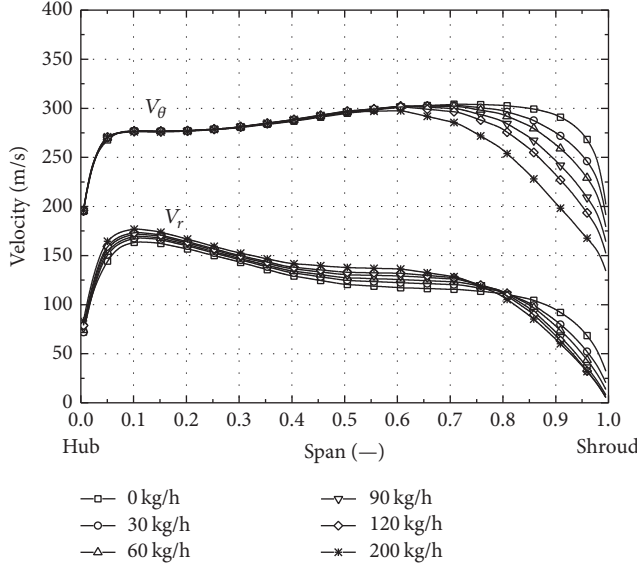


FIGURE 20:  $V_\theta$  and  $V_r$  with different steam injection at the diffuser inlet.

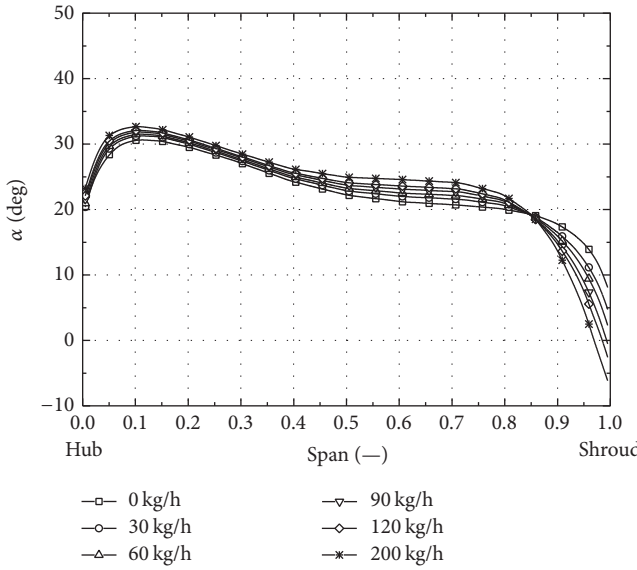


FIGURE 21: Flow angle with different steam injection at the diffuser inlet.

However, this could not explain why there was a cross point of the flow angles versus the normalized span location at the diffuser inlet at different steam injection rate conditions, as illustrated in Figure 21. The authors believe that it should be caused by the Coanda effect which means the radial attached span will remain unchanged regardless of the change in the injected mass flow.

## 7. Influences of Thermal Physics Properties

**7.1. Molecular Weight.** To study the material influence, three ideal gases were chosen: steam ( $M < 29$ ),  $N_2$  ( $M \approx 29$ ), and  $CO_2$  ( $M > 29$ ). To eliminate the influences of other factors

TABLE 3: Boundary conditions of different materials.

Gas	Compressor mass flow (kg/s)	Injected gas static temperature (K)	Injected gas mass flow (kg/s)
Steam ideal gas	2.80	438	0.0333
$N_2$ ideal gas	2.80	438	0.0416
$CO_2$ ideal gas	2.80	438	0.0521

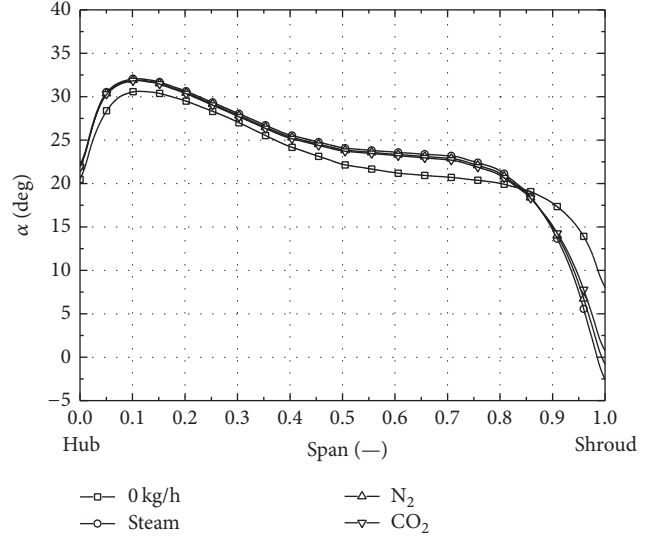


FIGURE 22: Flow angle in span direction.

TABLE 4: Boundary conditions of different temperatures.

Injected gas static temperature (K)	Compressor mass flow (kg/s)	Gas injected	Injected gas mass flow (kg/s)
573	2.80	$N_2$	0.0364
438	2.80	$N_2$	0.0416
293	2.80	$N_2$	0.0508
223	2.80	$N_2$	0.0583
173	2.80	$N_2$	0.0662

involved, the authors keep the momentum of injected gas constant. The related injected gas properties are given in Table 3.

Figure 22 compares the flow angle from hub to shroud. Slight discrepancies can be observed. The results show that the diffuser inlet flow angle decreases from hub to shroud. The light gas can reduce 0.87–1 span flow angle and enhance it at 0–0.87 span and increase span averaged flow angle.

Figure 23 illustrates the volume fraction from hub to shroud obtained from the meridional surface at the same radius of the injectors. Mass flow in Table 4 and volume fraction in Figure 23 indicate that the larger the mass flow is, the larger the volume fraction injected is.

**7.2. Temperature and Heat Transfer.** Figure 24 compares the flow angle from hub to shroud. The results show that the

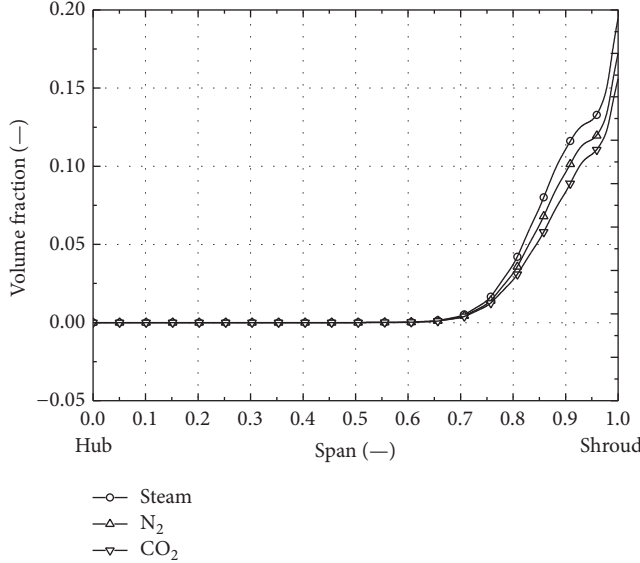


FIGURE 23: Volume fraction obtained from the meridional surface at the same radius of the injectors.

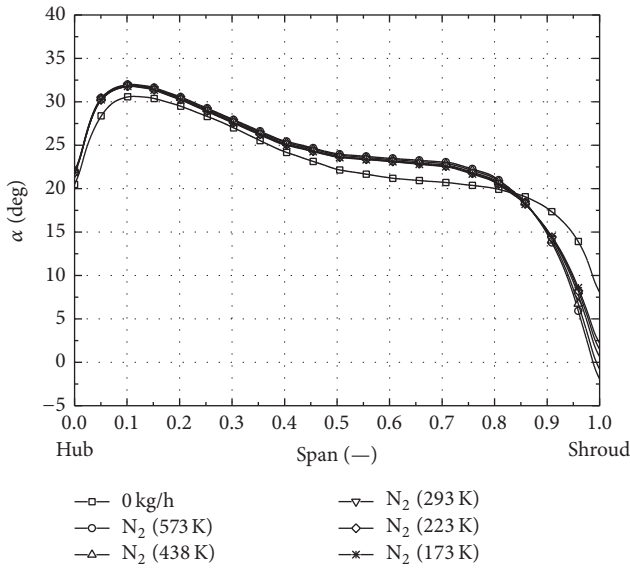


FIGURE 24: Flow angle in span direction of different temperatures.

diffuser inlet flow angle decreases from hub to shroud. The higher gas temperature can reduce 0.87–1 span flow angle and enhance it at 0–0.87 span and thus increase span averaged flow angle.

Figure 25 depicts the volume fraction from hub to shroud obtained from the meridional surface at the same radius of the injectors. It shows that the larger the mass flow is, the smaller the volume fraction is.

The volume flow as the dominant factor that changes the flow angle can be concluded by the comparisons of mass and volume flow influence above. Therefore, with the same momentum injection, higher temperature or smaller molecular weight gas can both increase the diffuser inlet flow

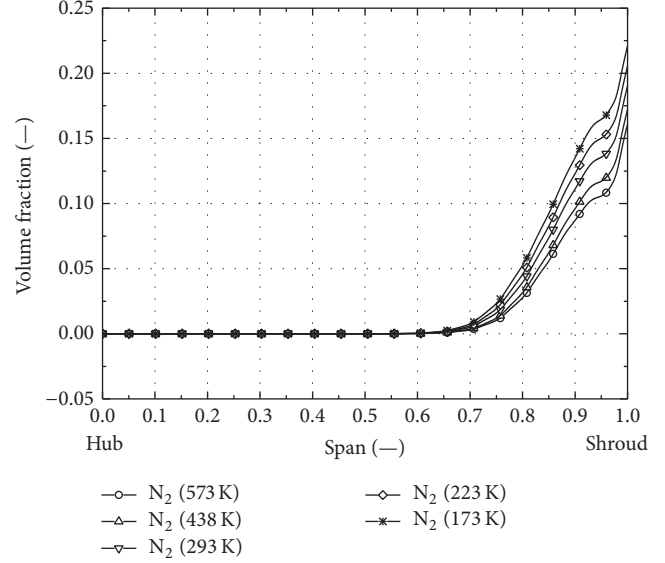


FIGURE 25: Volume fraction obtained from the meridional surface of different temperatures.

angle and extend the compressor stable operation range. For example, if the injected gas temperature is higher than the air temperature, then it will heat up the air, cause it to expand, and thus increase radial velocity near the shroud side.

**7.3. Asymmetric and Symmetric Injector, Air Bleeding, and Air Recirculation.** As discussed above, the injector position would affect the flow pattern downstream of that injector significantly. In order to figure out the influence on the enhancement, cases of 8 asymmetrically distributed injectors and 23 uniformly distributed injectors were simulated here.  $\eta\Delta$  and  $\alpha\Delta$  represent the efficiency variation rate under the surge limit and the change rate of the mean flow angle at the inlet of the diffuser vane space compared to those of cases without injection, respectively. The results demonstrate that the change of the injector position does not improve the enhancement compared with the former cases, and a distinct decrease of efficiency was captured for the case of 23 injectors.

At last, the air bleeding and air recirculation were tested, as shown in Figure 26. Air bleeding out from the pipes installed at each vane passage throat was discharged to the environment or reinjected to the diffuser vaneless space. The total air bleeding mass flow was set to be 30 kg/h. The air recirculation flow was driven by the differential pressure between the vane throat and vaneless space, measured as about 135 kg/h. But SMI is only about 1/3 of the case of steam injection. It shows that the air bleeding configuration enhances the stability with an increase of efficiency, while the injection configurations decrease it. But it is confused that the air recirculation, which can be regarded as a combination of bleeding out and injection, reduces the surge margin distinctly. A positive influence on the flow angle, which the air recirculation had, always indicates an increase of the surge margin; however, it failed in this case. The reason may be the complex flow in the bleeding tubes that affects the convergence of the simulations.

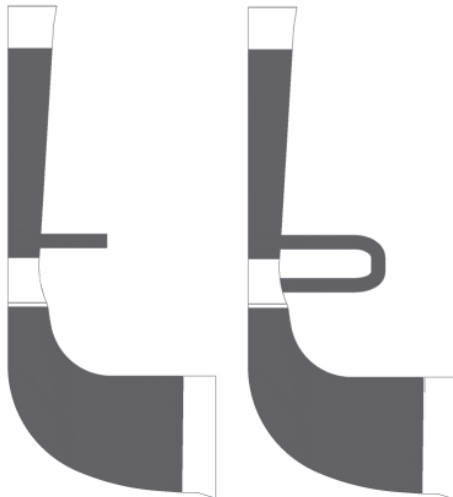


FIGURE 26: Air bleeding and air recirculation configuration.

## 8. Conclusions

A centrifugal compressor with vaned diffuser was analyzed in detail through both experimental and numerical methods. After comparing the steady CFD results and unsteady test data, some conclusions could be made as follows:

- (a) Steam injection is shown to be an effective method to improve stage stability. 0.3% of compressor designed mass flow rate steam can increase the surge margin by over 9.0% at  $\text{Mu} = 1.08$ . At each speed line, there is an optimum steam flow rate.
- (b) Steam injection changes the type of stall precursor from spike to modal waves at 90% speed line. In addition, it changes the stall cell traveling direction from forward to backward at 80% speed.
- (c) Both efficiency and pressure ratio drop with steam injection.
- (d) The root cause of the compressor surge is the flow angle at the diffuser inlet, and the surge margin could be improved by decreasing the incidence angle at the diffuser inlet.
- (e) At the same momentum injection, higher temperature or lighter gas can increase the diffuser inlet flow angle and extend the compressor stable operation range.
- (f) The 8 asymmetrical injectors and the 23 circumferentially symmetrical injectors performed less and equal enhancement compared with the normal configuration, respectively. A distinct decrease of efficiency occurred for the 23-injector case, which demonstrated a more pressure loss. The air bleeding increased the stability and the efficiency. But the air reinjection had a negative effect on the surge margin.
- (g) Traditional flow instability theory based on incidence caused flow separation can still be applied for vaned diffuser by viewing its spanwise distribution.

(h) Symmetric injector is better than asymmetric case from the point of SMI.

(i) Steam injection is more effective than simple bleeding at throat area or recirculation in SMI but will result in a drop of efficiency.

## Nomenclature

$p$ :	Pressure (kPa)
$b$ :	Axial width (mm)
$r$ :	Radius (mm)
$f_s$ :	Sampling frequency (kHz)
$Q$ :	Volumetric flow rate ( $\text{m}^3/\text{s}$ )
$T$ :	Temperature (K)
$V$ :	Absolute velocity (m/s)
$W$ :	Relative velocity (m/s)
$U$ :	Impeller circumferential velocity (m/s)
$n$ :	Impeller rotational speed (rpm)
$N$ :	Number of blades (—)
TWE:	Traveling wave energy.

## Greek Symbols

$\alpha$ :	Absolute flow angle from tangential direction (°)
$\beta$ :	Blade angle from tangential direction (°)
$\phi$ :	Flow coefficient defined as $Q/\pi r_2^2 u_2$
$\psi$ :	Pressure rise coefficient defined as $\Delta P/(1/2)\rho_\infty u_2^2$
$\rho$ :	Density.

## Subscripts

0:	Stage inlet
1:	Impeller inlet
2:	Impeller outlet/vaned diffuser inlet
3:	Vaned diffuser outlet
4:	Collector outlet
$r$ :	Radius direction
$\theta$ :	Tangential direction
$\infty$ :	Atmospheric condition.

## Conflicts of Interest

The authors declare that they have no conflicts of interest.

## Acknowledgments

This project is supported by the National Natural Science Foundation of China under Grants nos. 51306199 and 51405130. The authors would like to acknowledge the kind comments and discussions on the design of the test facility by Colin Rodgers.

## References

- [1] E. Greitzer, "The stability of pumping systems," *ASME Journal of Fluids Engineering*, vol. 103, no. 11, pp. 193–242, 1981.
- [2] Z. S. Spakovszky, "Backward traveling rotating stall waves in centrifugal compressors," *Journal of Turbomachinery*, vol. 126, no. 1, pp. 1–12, 2004.

- [3] M. Schleer, S. J. Song, and R. S. Abhari, "Clearance effects on the onset of instability in a centrifugal compressor," *Journal of Turbomachinery*, vol. 130, no. 3, Article ID 031002, 11 pages, 2008.
- [4] D. Hagelstein, K. Hillewaert, R. A. Van Den Braembussche, A. Engeda, R. Keiper, and M. Rautenberg, "Experimental and numerical investigation of the flow in a centrifugal compressor volute," *Journal of Turbomachinery*, vol. 122, no. 1, pp. 22–31, 2000.
- [5] Z. S. Spakovszky and C. H. Roduner, "Spike and modal stall inception in an advanced turbocharger centrifugal compressor," *Journal of Turbomachinery*, vol. 131, no. 3, Article ID 031012, 2009.
- [6] H. Tsurusaki and T. Kinoshita, "Flow control of rotating stall in a radial vaneless diffuser," *Journal of Fluids Engineering, Transactions of the ASME*, vol. 123, no. 2, pp. 281–286, 2001.
- [7] W. Huang, S. Geng, J. Zhu, and H. Zhang, "Numerical simulation of rotating stall in a centrifugal compressor with vaned diffuser," *Journal of Thermal Science*, vol. 16, no. 2, pp. 115–120, 2007.
- [8] G. J. Skoch, "Experimental investigation of diffuser hub injection to improve centrifugal compressor stability," *Journal of Turbomachinery*, vol. 127, no. 1, pp. 107–117, 2005.
- [9] T. Hirano, T. Uchida, and H. Tsujita, "Control of surge in centrifugal compressor by using a nozzle injection system: universality in optimal position of injection nozzle," *International Journal of Rotating Machinery*, vol. 2012, Article ID 259293, 8 pages, 2012.
- [10] C. Gao, C. Gu, T. Wang, and B. Yang, "Analysis of geometries' effects on rotating stall in vaneless diffuser with wavelet neural networks," *International Journal of Rotating Machinery*, vol. 2007, Article ID 76476, 2007.
- [11] K. B. Abidogun, "Effects of vaneless diffuser geometries on rotating stall," *Journal of Propulsion and Power*, vol. 22, no. 3, pp. 542–549, 2006.
- [12] X. Sun, D. Sun, and W. Yu, "A model to predict stall inception of transonic axial flow fan/compressors," *Chinese Journal of Aeronautics*, vol. 24, no. 6, pp. 687–700, 2011.
- [13] F. B. Fisher, "Application of map width enhancement devices to turbocharger compressor stages," SAE255 Paper No. 8809794. Power boost: light, medium and heavy duty engines. SP-780, 1989.
- [14] M. Werner, R. Baar, P. Haluska et al., "Bidirectional flow measurement based on the differential pressure method for surge analysis on a small centrifugal compressor", proceedings of the institute of mechanical engineers, part A," *Journal of Power and Energy, Turbocharger and Turbocharging Special Issue*, 2016.
- [15] A. Stein, S. Niazi, and L. N. Sankar, "Computational analysis of stall and separation control in centrifugal compressors," *Journal of Propulsion and Power*, vol. 16, no. 1, pp. 65–71, 2000.
- [16] C. Gao, C. Gu, T. Wang, and B. Yang, "Passive control of rotating stall in vaneless diffuser with radial grooves: detailed numerical study," in *Proceedings of the 2009 ASME Turbo Expo*, pp. 1225–1232, Orlando, Fla, USA, June 2009.
- [17] R. Taghavi-Zenouz, E. Solki, and H. Afshari, "Stall margin improvement of a centrifugal compressor utilizing various stepped tip gap configurations," *Proceedings of the Institution of Mechanical Engineers, Part A: Journal of Power and Energy*, vol. 228, no. 7, pp. 772–781, 2014.
- [18] G. W. Felsing and Moller P. S., "Coanda flow over circular cylinder with injection normal to surface," *AIAA Journal*, vol. 7, no. 5, pp. 842–846, 1969.
- [19] R. L. Davis and J. Yao, "Computational approach for predicting stall inception in multistage axial compressors," *Journal of Propulsion and Power*, vol. 23, no. 2, pp. 257–265, 2007.
- [20] M. Tryfonidis, O. Etchevers, J. D. Paduano, A. H. Epstein, and G. J. Hendricks, "Pre-stall behavior of several high-speed compressors," *Journal of Turbomachinery*, vol. 117, no. 1, pp. 62–80, 1995.
- [21] C. S. Tan, I. Day, S. Morris, and A. Wadia, "Spike-type compressor stall inception, detection, and control," *Annual Review of Fluid Mechanics*, vol. 42, pp. 275–300, 2010.
- [22] Y.-S. Yoon and S. J. Song, "Analysis and measurement of the impact of diffuser width on rotating stall in centrifugal compressors," *Journal of Mechanical Science and Technology*, vol. 28, no. 3, pp. 895–905, 2014.
- [23] Y. Bousquet, X. Carbonneau, G. Dufour, N. Binder, and I. Trebinjac, "Analysis of the unsteady flow field in a centrifugal compressor from peak efficiency to near stall with full-annulus simulations," *International Journal of Rotating Machinery*, vol. 2014, Article ID 729629, 11 pages, 2014.
- [24] C. Gao, W. G. Huang, H. W. Zhang, Y. L. Yao, and J. C. Duan, "Surge characteristics and range extension with steam injection in a centrifugal compressor with vaned diffuser," in *Proceedings of the ASME, 2013, International Mechanical Engineering Congress & Exposition (IMECE '13)*, San Diego, Calif, USA, November 2013.

## Research Article

# Active Flow Control in a Radial Vaned Diffuser for Surge Margin Improvement: A Multislot Suction Strategy

Aurélien Marsan,<sup>1</sup> Isabelle Trébinjac,<sup>2</sup> Stéphane Moreau,<sup>1</sup> and Sylvain Coste<sup>3</sup>

<sup>1</sup>Department of Mechanical Engineering, Université de Sherbrooke, Sherbrooke, QC, Canada J1K 2R1

<sup>2</sup>LMFA, Ecole Centrale de Lyon, 36 Avenue Guy de Collongue, 69134 Ecully, France

<sup>3</sup>Safran Helicopter Engines, Avenue Joseph Szydlowski, 64510 Bordes, France

Correspondence should be addressed to Aurélien Marsan; aurelien.marsan@usherbrooke.ca

Received 31 January 2017; Accepted 9 April 2017; Published 9 May 2017

Academic Editor: Yutaka Ohta

Copyright © 2017 Aurélien Marsan et al. This is an open access article distributed under the Creative Commons Attribution License, which permits unrestricted use, distribution, and reproduction in any medium, provided the original work is properly cited.

This work is the final step of a research project that aims at evaluating the possibility of delaying the surge of a centrifugal compressor stage using a boundary-layer suction technique. It is based on Reynolds-Averaged Navier-Stokes numerical simulations. Boundary-layer suction is applied within the radial vaned diffuser. Previous work has shown the necessity to take into account the unsteady behavior of the flow when designing the active flow control technique. In this paper, a multislot strategy is designed according to the characteristics of the unsteady pressure field. Its implementation results in a significant increase of the stable operating range predicted by the unsteady RANS numerical model. A hub-corner separation still exists further downstream in the diffuser passage but does not compromise the stability of the compressor stage.

## 1. Introduction

The stable operating range of centrifugal compressors is limited toward low mass flow rate by the onset of flow instabilities, either rotating stall or surge. This limitation is detrimental to the acceleration rate of the compressor that is a key performance parameter in particular for turboshaft engines and can also prevent operation at maximum efficiency which may lay at or close to the surge line. It is then of primary concern for turboshaft designers to better understand the surge inception process in centrifugal compressors and to develop design or control techniques in order to delay the surge.

In this context, the radial vaned diffuser appears to be a key component for surge inception in centrifugal compressors operating at high rotational speed. This was already pointed out by Came [1] in 1976 and has been confirmed by several studies since, but at this time the impeller was the most critical element of the stage from a performance point-of-view and the improvement efforts have then mostly focused on it.

In 1975 for a centrifugal compressor for automotive engine, Amann et al. [2] attributed the occurrence of rotating stall and surge to the radial vaned diffuser.

In 1994, Hunziker and Gyarmathy [3] have worked on a single-stage centrifugal compressor equipped with a radial vaned diffuser made of circular-arc vanes whose stagger angle could be adjusted. Maximum rotational speed is 22,000 rpm and maximum pressure ratio is about 2,0. By analyzing the stability in various operating conditions and configurations using the criteria about the slope of the characteristics proposed by Greitzer in [4], the authors have concluded that the diffuser has a destabilizing influence at high rotational speed and for low mass flow rate which may explain the onset of surge. In particular, the diffuser entry zone is expected to play a major role since it has a stabilizing effect over the whole operating line but switches to a destabilizing effect at low mass flow rate.

In 2001, Wernet et al. [5] investigated the surge inception in the NASA-CC3 centrifugal compressor equipped with the wedge vane diffuser using digital particle imaging velocimetry. The design rotational speed is 21,789 rpm for a design

pressure ratio of about 4. They have shown that the flow reversal at surge starts within the diffuser and then propagates upstream until forward flow is reestablished.

More recently, in 2010, Everitt and Spakovszky [6, 7] studied the onset of instabilities in a high-speed preproduction centrifugal compressor stage used for large diesel engines. The design pressure ratio is 5 and the impeller tip Mach number is greater than one at design speed. The radial vaned diffuser is made of airfoil vanes. Using the strategy first investigated by Hill IV [8] based on an isolated diffuser numerical model, the authors identify the growth of a flow separation at the leading-edge of the radial vaned diffuser as one of the necessary conditions for the formation of short-wavelength spike stall precursors.

In 2014, Bousquet et al. [9] studied a 2.5 pressure ratio subsonic centrifugal compressor stage designed by Liebherr-Aerospace Toulouse SAS and integrated it in an air-conditioning system. It is composed of a backswept splitted unshrouded impeller and a radial vaned diffuser made of wedge blades. Design rotational speed is 38000 rpm. Based on the results of full-annulus 3D unsteady RANS simulations, the authors observed the growth of a flow separation at the leading-edge of the diffuser vane when moving the operating point toward the surge limit, in a similar manner to that previously reported by Everitt and Spakovszky [6, 7]. For that particular test case, however, this flow separation does not lead to an accumulation of vortical structure in the vaneless diffuser and the operating point remains stable until the flow separates at the leading-edge of the impeller blades [10].

Then, Buffaz et al. [11, 12] studied the onset of instabilities in a supersonic centrifugal compressor stage designed and built by Safran Helicopter Engines (SHE), both experimentally and numerically. The compressor was mounted on a 1 MW test rig at the LMFA, École Centrale de Lyon, France, and detailed unsteady pressure measurements in the diffuser entry zone were performed. A full-annulus simulation of the surge inception was also conducted. The growth of a boundary-layer separation on the suction side of the diffuser vanes when moving the operating point toward the surge limit was again observed. This separation degenerates into a rotating stall finally leading to surge.

Other numerical investigations were conducted by Benichou and Trébinjac [13, 14] on another transonic centrifugal compressor designed and built by Safran Helicopter Engines (SHE). The test case is composed of a backswept unshrouded impeller and a splitted vaned diffuser. Pressure ratio is about 4 at a rotational speed of 40,000 rpm. The analysis of the flow field predicted by URANS simulations for an operating point near surge suggested that a boundary-layer separation on the suction side of the diffuser vanes was responsible for the surge inception.

Finally, the surge inception scheme proposed by Everitt and Spakovszky and based on the growth of a separation at the leading-edge of the diffuser vanes was found by Fujisawa et al. [15] in a centrifugal compressor of a turbocharger for marine diesel engines operating at low-speed. The study also showed the interaction between the diffuser leading-edge separation vortex and the tip leakage flow from the impeller.

Given the importance of the flow separation in the surge inception process for centrifugal compressor stages enlightened by these studies, the use of an active control technique aiming at controlling the flow separation within the diffuser is expected to be an effective way for delaying the surge. In particular, the boundary-layer suction technique has proven its effectiveness in case of axial compressors in order to either delay the surge or increase the blade loading [16–20].

In the next section, previous control strategies are reviewed.

## 2. Previous Control Strategies

Came [1] already mentioned in 1976 the possibility of designing efficient diffusers of smaller radial extent using boundary-layer suction. Still, there is no evidence yet in the literature of the interest of the boundary-layer suction in case of centrifugal compressors. The following aims at giving an overview of the other flow control techniques that have been applied to centrifugal compressors equipped with a radial vaned diffuser.

Botros and Henderson [21] give an extensive technology assessment of the surge control techniques for centrifugal compressors developed until 1993. The authors report the common use of 1D control technique based on the opening of a recycle valve when the surge is detected or on active control of the throttling element. Design methods are also given, as, for example, the use of a backswept impeller. The reduction of the diffuser exit width or specific designs of the diffuser inlet are also mentioned as means to influence the surge flow rate. Finally, a pioneering casing treatment developed by Amann et al. [2] in 1975 is reported. This treatment is applied to a centrifugal compressor whose surge is triggered by the occurrence of rotating stall within the radial vaned diffuser. It consists in a circumferential slot put at the impeller trailing edge and connected to an annular chamber. A significant decrease of the surge flow rate is reported. The effectiveness of the control is attributed to the uniformization of the pressure distribution over the circumference. Another technique relying on the same principle was proposed by Raw [22] in 1986. The so-called “porous throat diffuser” technique is based on the linking of the diffuser throats through slots connected to an azimuthal chamber. Again, the stabilizing effect is explained by the uniformization of the flow between all the diffuser passages, which may prevent the stall of any one diffuser vane before another one and then avoid the occurrence of rotating stall.

Later, Nelson et al. [23] managed to experimentally reduce the surge mass flow rate of an axicentrifugal stage by 1% using air injection into the throats of the diffuser passages.

Skoch also investigated the effectiveness of the air injection technique applied to the NASA CC3 compressor [24, 25] on the basis of the work of Spakovszky [26]. Injector nozzles were inserted first at the shroud of the vaneless diffuser space. It was found that the mere obstruction created by the injector nozzles at the shroud was sufficient to significantly decrease the surge mass flow rate and concluded that the benefit in diffuser stability came from the reduction of the incidence on the diffuser vanes. This conclusion was supported by hub-side

injection experiments, whose conclusions were similar. The effects of the air injection technique in the NASA CC3 test case have been recently investigated numerically by Halawa et al. [27].

Other publications can be found in patents. A device is suggested by Schönenborn [28] based on boundary-layer suction on the suction face of the diffuser vanes. He also suggests that the bled flow could be used for the cooling of the turbine blades, for example. Another is proposed by Leblanc [29], the fluid being bled from the suction face of the diffuser vanes and then reinjected upstream in the vaneless diffuser space.

No detailed assessment of the potential of the boundary-layer suction technique applied to centrifugal compressor has been done yet. This is the objective of the present study.

### 3. Test Case

The test case is a centrifugal compressor stage designed and built by Safran Helicopter Engines (SHE), composed of a backswept splitted unshrouded impeller and a radial vaned diffuser. It is used as a rear compression stage in a helicopter engine. The flow at the impeller outlet is transonic. This compressor is installed in a 400 kW test rig of the DAEP Laboratory at the Institut Supérieur de l'Aéronautique et de l'Espace (ISAE), Toulouse, France. A complete description of the experimental test rig is available in [30].

For the compressor operating at its nominal rotational speed, previous work based on steady-state numerical calculations has shown the growth of corner stall within the semivaneless space of the diffuser when moving the operating point of the compressor toward the low mass flow rate [31]. This corner stall was supposed to limit the stability of the compressor stage and was also predicted by unsteady numerical simulations [32]. A boundary-layer suction technique had been foreseen and then studied in order to control the corner stall. According to steady-state numerical calculations relying on the mixing-plane approach, the suction led to a significant increase of the stable operating range of the compressor. But these promising results were challenged by unsteady numerical simulations [30]. The detailed analysis of the flow in the diffuser with suction has shown that the hub-corner separation was not completely removed by the suction, contrary to the prediction of the steady-state numerical model: a corner separation still existed in the diffuser downstream of the location of the initial boundary-layer separation, and the stable operating range was not extended. This result confirms the high influence of the unsteadiness on the flow in the diffuser entry zone, especially in centrifugal compressors with small radial gap between the impeller and the vaned diffuser [33]. The scrolling of the impeller blades in front of the diffuser vanes generates intense high pressure waves, in the same manner as already observed in another transonic Safran Helicopter Engines centrifugal compressor [34]. These high pressure waves are reinforced when crossing the diffuser throat. This generates intense instantaneous adverse pressure gradients that cannot be predicted by the steady-state numerical model and are supposed to provoke the boundary-layer separation. Figure 1

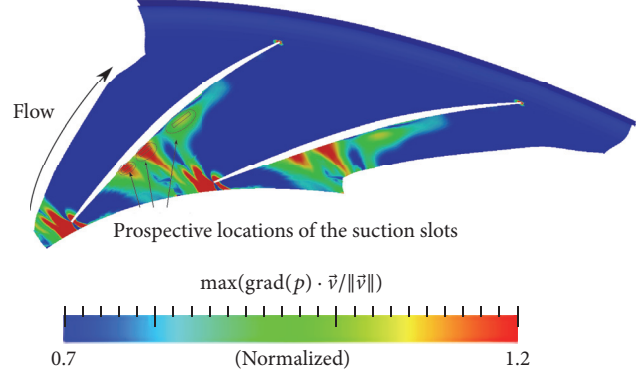


FIGURE 1: Maxima of instantaneous adverse pressure gradient, without control. Prospective locations of the suction slots.

shows the map of the maxima of the instantaneous adverse pressure gradient in the diffuser over one period.

Given that conclusion, the control strategy was adapted in order to take into account the unsteadiness. A multislots suction strategy was proposed but not evaluated. This strategy relies on three suction slots distributed along the diffuser suction side on the hub surface, at the locations of the maxima of the instantaneous adverse pressure gradient, as shown in Figure 1. The paper presents the results obtained by this multislots suction strategy.

### 4. Numerical Setup

Numerical simulations have been performed with the elsA software, developed by ONERA, the French aerospace laboratory [35]. This code solves the Reynolds-Averaged Navier-Stokes equations with a cell-centered finite volume method applied on multiblock-structured meshes [31, 32]. The flow is considered fully turbulent and the effect of turbulence on the mean flow field is modeled thanks to the two variables ( $k-l$ ) turbulence model of Smith. The time integration is performed with a backward Euler scheme with implicit operators. Spatial discretization is achieved with Roe's second-order scheme and Harten's correction.

The mesh is the same as for the previous studies. It has been generated using the commercial meshing software Autogrid from Numeca. It counts 6,07 million points for one impeller-diffuser passage. The first cell height on the walls is 1 micrometer, which corresponds to a dimensionless wall distance  $y^+$  approximately equal to 1 along all solid surfaces. The impeller tip clearance is included in the numerical model and is meshed with a C-H topology. Filets between the endwalls and the blades are included neither in the impeller nor in the radial vaned diffuser. Previous studies have shown that mesh independence in the diffuser is reached.

Unsteady numerical simulations of the flow within the compressor stage have been performed using the phase-lagged assumption which is based on the Tyler and Sofrin relation and is also known as the chorochronic approach [36–38].

In a previous publication [32], experimental unsteady pressure signals available in the diffuser entry zone have

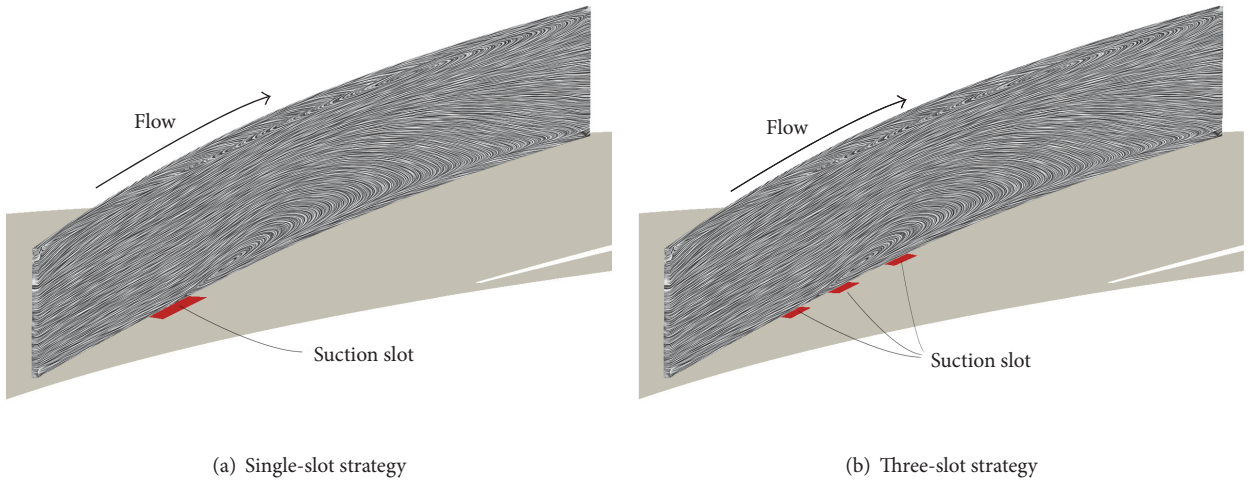


FIGURE 2: Suction strategies.

been compared with the unsteady numerical results (without suction). The comparison has ensured the capability of the numerical model at describing the flow in this compressor, even at near surge operating points.

For the present study, the numerical parameters have been kept the same except for the time step which is defined as

$$\delta t = \frac{2\pi}{\omega N_R N_S N_{qo}}, \quad (1)$$

where  $N_R$  and  $N_S$  are the numbers of rotor and stator blades and  $\omega$  is the rotational speed and  $N_{qo}$  is a parameter. For the base case, the  $N_{qo}$  parameter has been progressively doubled in order to check the time step convergence, starting from  $N_{qo} = 20$  and ending at  $N_{qo} = 160$ . Regarding the convergence,  $N_{qo}$  was set to 60 for the single-slot suction case, as a compromise between the time step convergence and the computational time, and 80 for the multislots suction case.

The exit static pressure was set by prescribing a ratio between the value of the static pressure and the mass flow rate at the mesh exit plane. This allows computing the flow at a mass flow rate lower than the peak of the performance curve, which is necessary in order to reach the stability limit.

The boundary-layer suction was modeled by a surface mass-flux boundary-condition. The results obtained with this simplified model had been previously compared with those obtained by including the entire slot within the numerical model, using the chimera technique [39]. The relevance of the boundary-condition approach for analyzing the suction effect on the diffuser flow has been demonstrated: the boundary limit condition technique cannot describe the possible recirculation zone within the suction slot, but its effect on the main flow is consistent with the effect predicted using the chimera technique [31] and is more appropriate for the present study that does not deal with the important issue of designing an optimal suction slot.

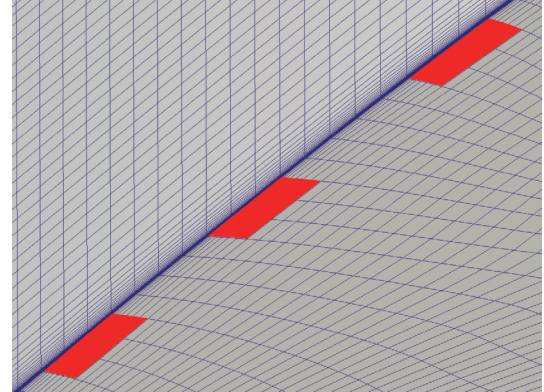


FIGURE 3: Numerical model of the three-slot suction effect by a boundary limit condition.

## 5. Control Strategy

Figure 2 shows the two suction strategies that are compared here. The single-slot strategy is the one that has already been studied and did not reach any improvement of the surge margin according to the time-dependent numerical simulations [30]. The three-slot strategy is the one which is under the scope of the present paper, the slots being located at the maxima of the instantaneous adverse pressure gradient.

Mass flow rate removed through the suction slots was chosen equal to 1 percent of the surge mass flow rate of the compressor without suction, which is consistent with the previous study, and the surface mass-flux was prescribed homogeneous all over the aspiration surface. In the case of the three-slot suction strategy, the surfaces of the three suction slots are slightly different from each other. The effect of suction is indeed modeled by a boundary limit condition and the possible area of the slots is constrained by the areas of the faces of the wall mesh (Figure 3). 0.32 percent of the surge mass flow rate is then removed through the first upstream slot, 0.33 percent through the second one, and 0.35 percent

through the last downstream (the total being still equal to 1 percent of the surge mass flow rate).

## 6. Results

Given the strong unsteady interaction between the impeller and the diffuser for lowest mass flow rate operating points, the phase-lagged numerical calculation has required more than 25 impeller revolutions in order to reach the convergence for the last converged operating point with the three-slot suction strategy.

The limit of stability was searched by progressively increasing the prescribed ratio between the pressure and the mass flow rate at the outlet. It is important to notice that the limit of stability of the numerical model toward low mass flow rates has been reached for the base and the single-slot cases, but not for the three-slot case. Numerically stable operating points with the three-slot suction strategy could then exist at mass flow rate lower than the last plotted operating point.

## 7. Performance

Figure 4(a) shows the total-to-static pressure ratio of the compressor stage, plotted as a function of the standard mass flow rate at the impeller inlet. As indicated in the figure, no stable operating point has been found for the base case and the single-slot case below  $\dot{m}_R^{\text{std}} \approx 0.97$ . On the contrary, it has been possible to reach the convergence for a much lower mass flow rate with the three-slot suction strategy. Both suction techniques result in an increase of the total-to-static pressure ratio of the compressor stage.

In order to analyze more precisely the effect of the suction on the performance of the compressor stage, Figures 4(b) and 4(c) show the main performance coefficients for the impeller and the radial vaned diffuser. Figure 4(b) shows the total-to-static pressure ratio of the impeller plotted as a function of the diffuser inlet standard mass flow rate. Figure 4(c) shows the static pressure recovery coefficient in the different parts of the diffuser, also plotted as a function of the standard mass flow rate at the diffuser inlet. All contributions are calculated with respect to the kinetic energy at the vaneless diffuser inlet, that is, the impeller trailing edge, so that they can be added in order to find the static pressure recovery coefficient of the whole vaned diffuser.

The total-to-static pressure ratio of the impeller reaches a maximum at a mass flow rate which is close to the stability limit of the base case and the single-slot suction case. The three-slot suction strategy allows reaching a stable operating point for a mass flow rate lower than that of the total-to-static pressure ratio maximum. Indeed, the control should stabilize the operation of the diffuser.

The origin of the saturation of the total-to-static pressure rise of the impeller is not yet identified. It could be caused by a flow separation within the impeller or by a particular behavior of the tip leakage vortex, for example. Some future study should aim at clarifying the flow pattern within the impeller. Given the fact that the limit of stability of the base case is reached at the peak of the total-to-static pressure ratio of

the impeller, the surge inception could be possibly explained by an interaction with a particular flow structure within the impeller which leads to the destabilizing of the diffuser hub-corner separation. Such an interaction between boundary-layer separation in the diffuser and the flow structure at the impeller outlet has already been observed [40].

The effect of the suction on the diffuser static pressure recovery process is visible in Figure 4(c). The  $C_p$  of the semivaneless diffuser space is greatly increased by the control, with both the single-slot and the three-slot suction strategies. According to previous works which have identified the entry zone of the diffuser as a critical zone for the onset of instabilities [3, 41], the fact that the slope is steeper (negative slope) should have a stabilizing effect on the diffuser work. But the single-slot suction strategy does not improve the overall operating range despite the increase of  $C_p$  in the semivaneless space. The only observation of the slopes to check a stability is thus proved to be insufficient.

Figure 5 shows the blockage coefficients calculated at the impeller trailing edge, the diffuser leading-edge, the diffuser throat and the diffuser trailing edge, near hub (between 0% and 30% of span-height), Figure 5(a), in the mid-span region (between 30% and 70% of span-height), Figure 5(b), and near shroud (between 70% and 100% of span-height), Figure 5(c). Blockage coefficient in a section S is defined as

$$B_S = 1 - \frac{\int_S \rho \mathbf{v} \cdot \mathbf{n} dS}{|\rho \mathbf{v} \cdot \mathbf{n}|_{\max}}. \quad (2)$$

These coefficient are plotted for several operating points, as a function of the standard mass flow rate at the diffuser inlet.

In all sections except at the diffuser trailing edge, the blockage coefficients are very similar between the single-slot and the three-slot suction cases. In particular, there is no difference between the blockage curves at the diffuser throat. Finally, the only difference between the single-slot and the three-slot strategies is visible on the blockage coefficient at the diffuser trailing edge. The blockage decreases in the near hub region with the three-slot suction strategy. On the contrary, it increases in the near shroud region. This balance between the near hub and the near shroud blockage has been previously explained by the growth of a shroud-corner separation on the suction side of the diffuser vanes when the hub-corner separation is controlled [30].

## 8. Flow Structure

Figure 6 compares the skin-friction pattern on the suction side of the diffuser vanes for the three test cases. The compared operating points are those labeled in Figure 4(c) and have similar diffuser inlet standard mass flow rates, that is, similar diffuser inlet flow field conditions. The location of the suction slots are also shown. A hub-corner separation still exists with the three-slot strategy downstream of the last suction slot. Compared with the single-slot case, it is however translated downstream, and the control of the hub-corner separation is more effective. It now takes place far downstream of the diffuser throat, which could explain the

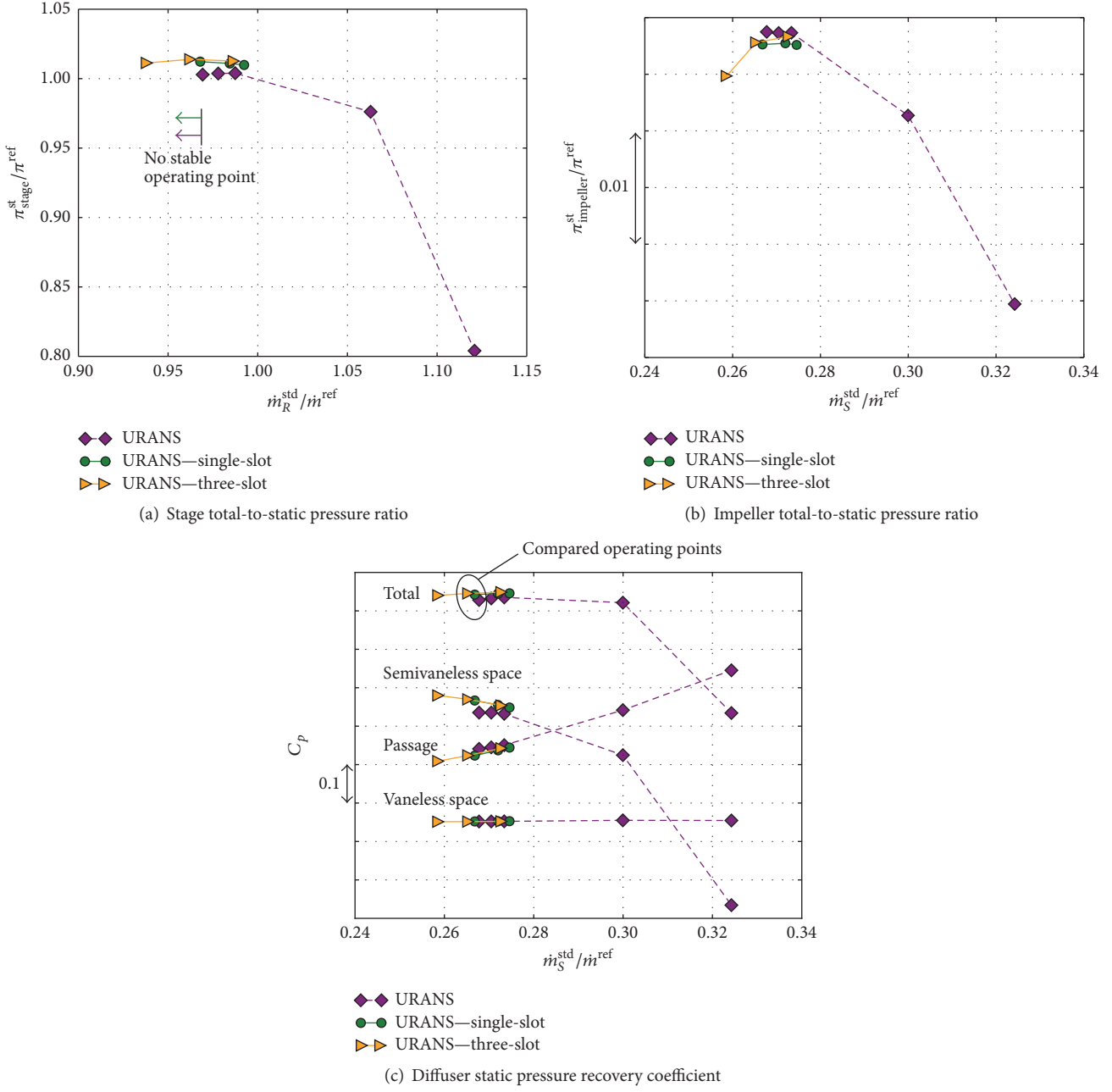


FIGURE 4: Performance of the compressor.

stabilizing effect of the three-slot suction case. As a consequence, the shroud-corner separation develops more. This explains the increase of the blockage near shroud previously mentioned, seen in Figure 5(c).

With the single-slot suction, the new location of the hub-corner separation downstream of the suction slot had been explained by the existence of intense instantaneous adverse pressure gradients [30]. In order to challenge that criterion for boundary-layer separation, Figure 7 shows the fields of the maximum of the instantaneous adverse pressure gradient in a plane located at 10 percent of span-height for the three-slot suction case. The location of the main saddle point of the skin-friction pattern in the corner is indicated by a black

square. Here, the field of the maximum of instantaneous adverse pressure gradient is not modified by the three-slot suction effect, and the maxima are still located at the suction slots. The separation yet occurs downstream of the third maximum limit. A perspective of the present study could be to extend the third suction slot in order to cover the entire third maximum of instantaneous adverse pressure gradient, and verify if it could lead to a complete removal of the hub-corner separation.

Figure 8 shows a general overview of the flow structure in the radial vaned diffuser with three-dimensional streamlines calculated from time-averaged flow field. The three-dimensional streamlines are colored by the value of the Mach

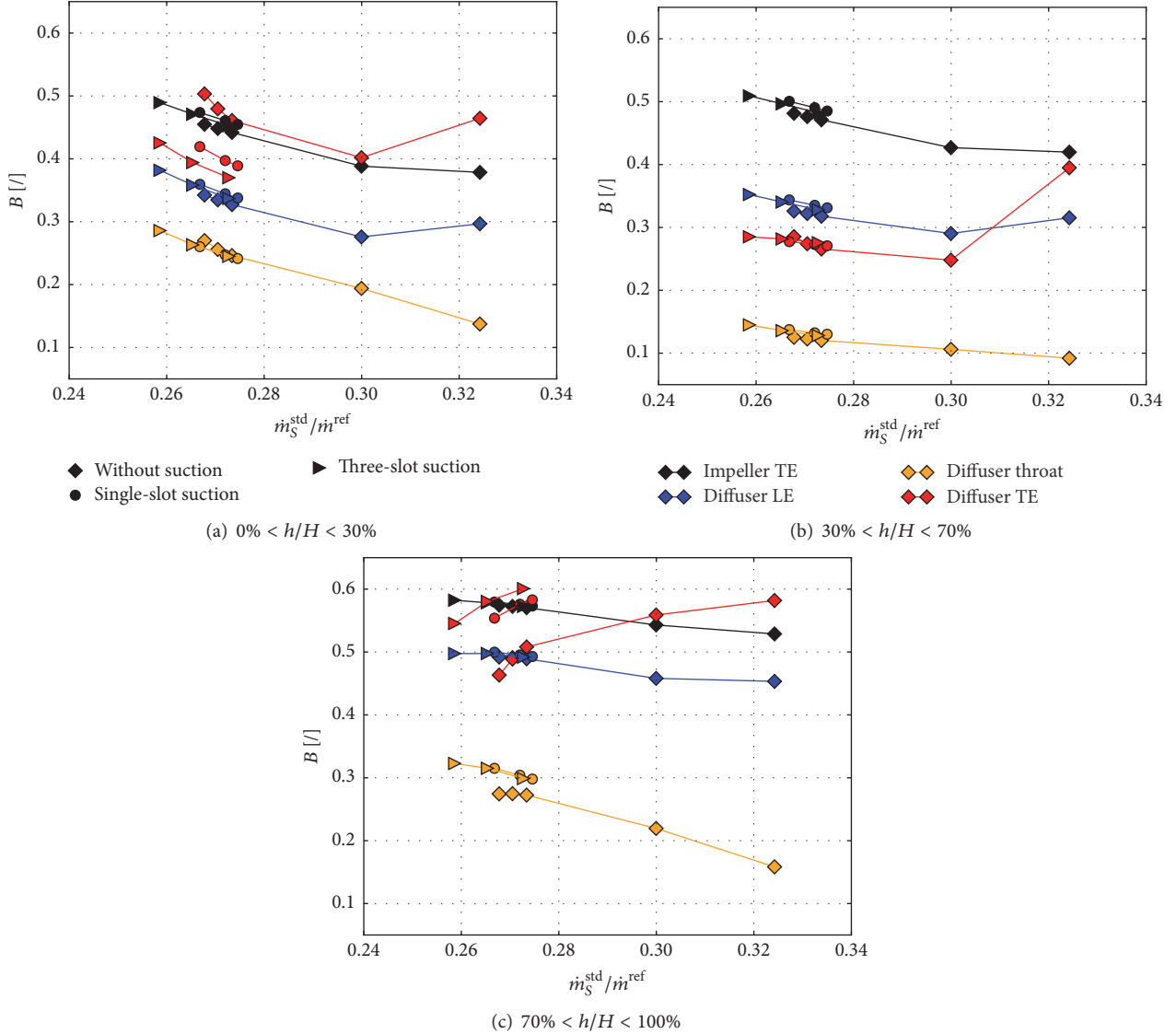


FIGURE 5: Blockage coefficients in the diffuser.

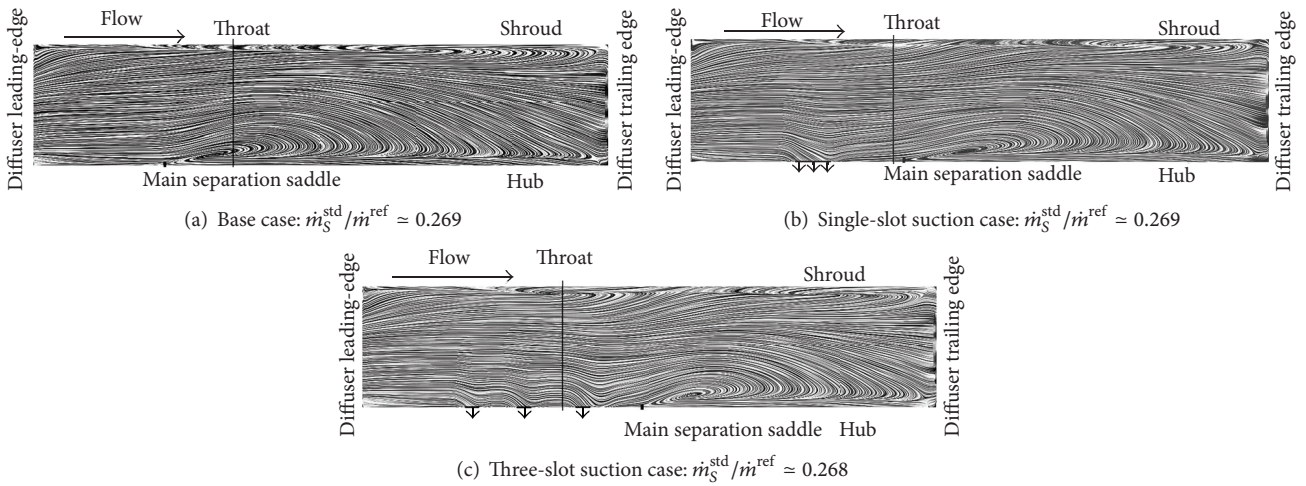


FIGURE 6: Skin-friction on the diffuser suction side.

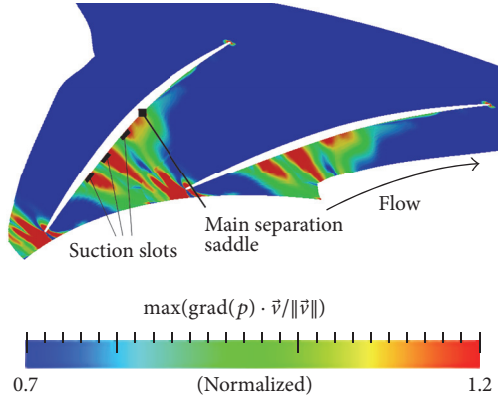


FIGURE 7: Maximum of instantaneous adverse pressure gradient—three-slot suction case.

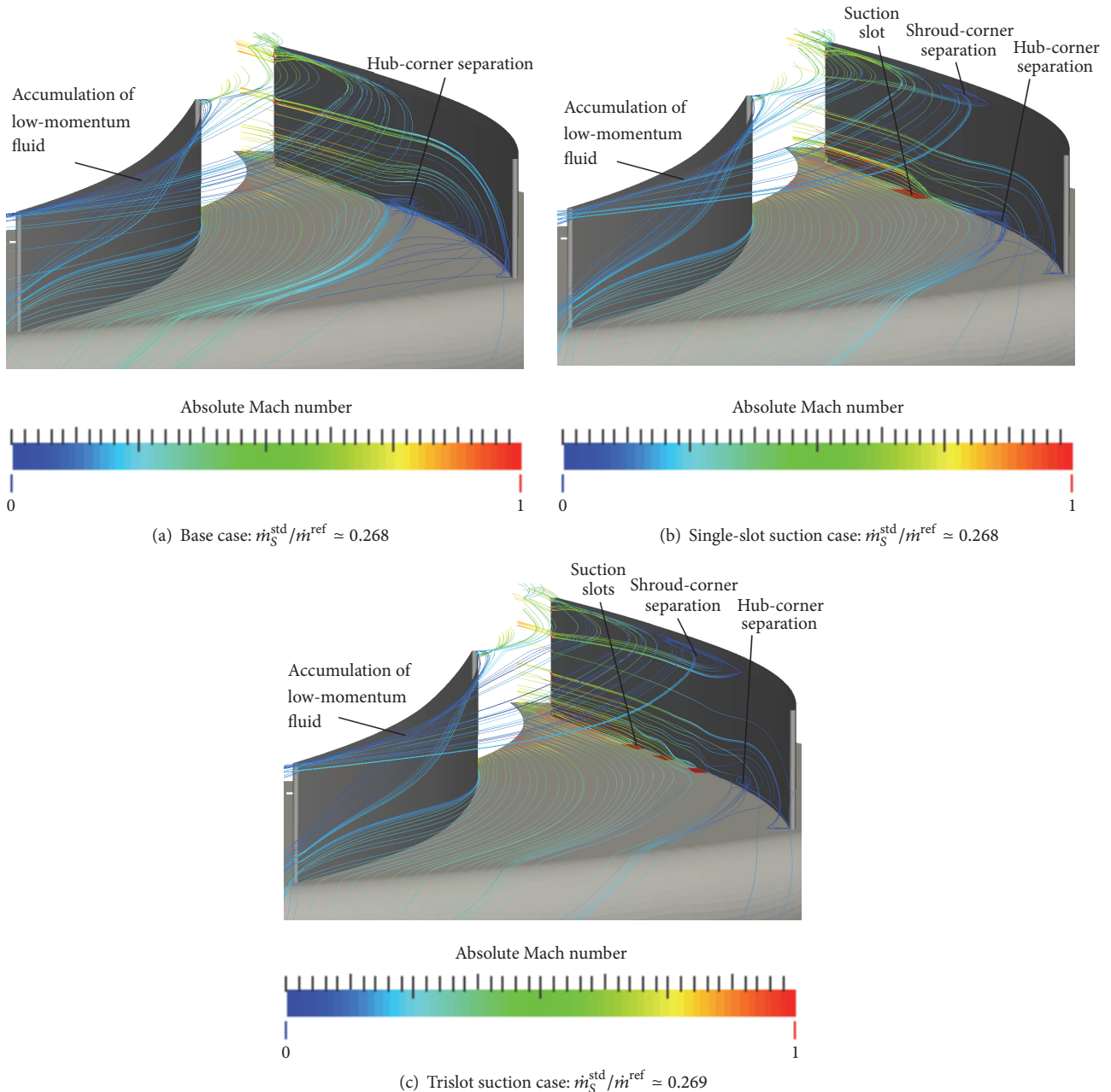
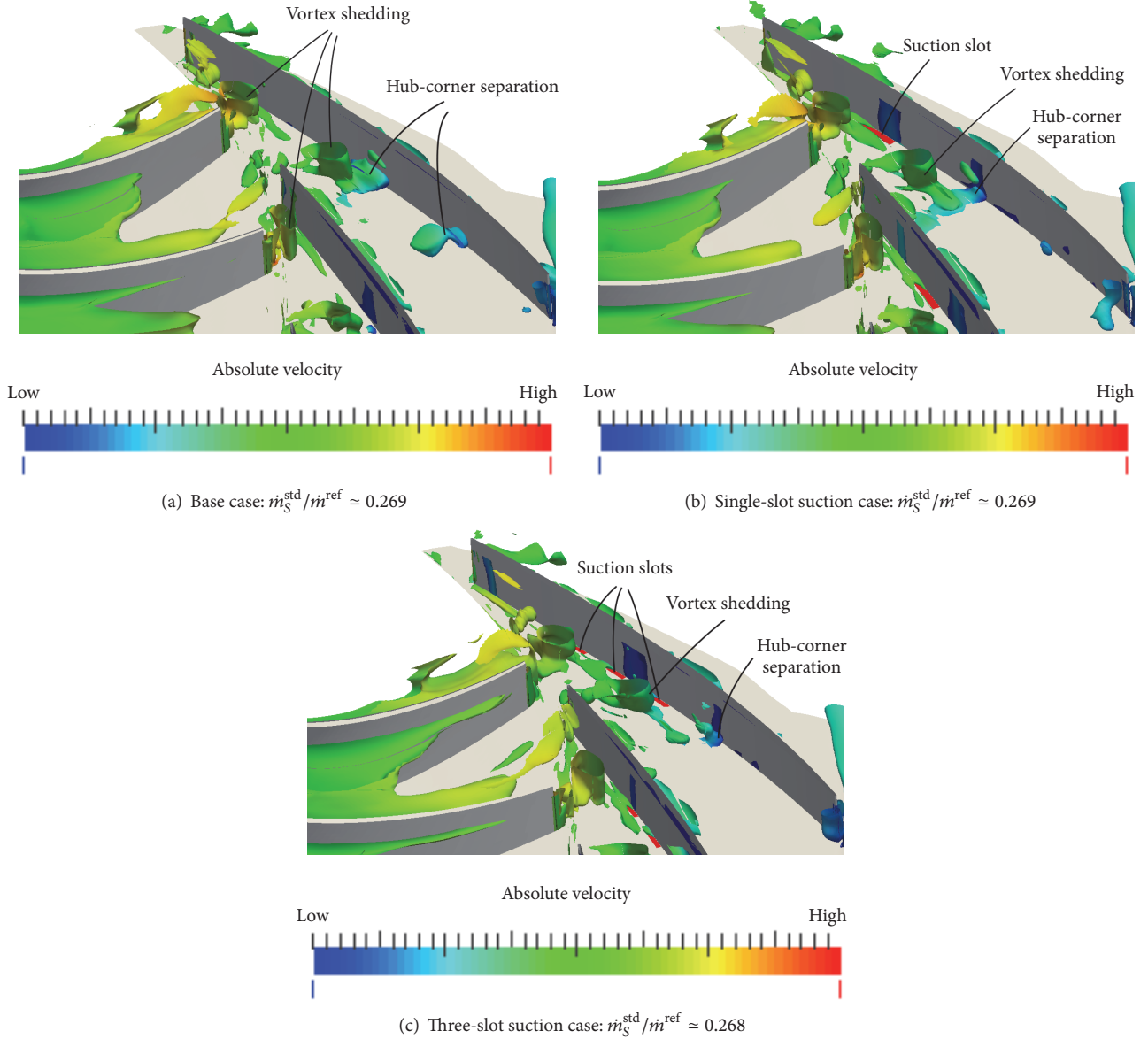


FIGURE 8: Three-dimensional streamlines.

FIGURE 9: Isocontours of Q-criterion in the diffuser colored by velocity:  $Q = 30$ .

number along the streamlines. It stresses the translation of the hub-corner separation downstream under the effect of the suction and the growth of the shroud-corner separation, as previously mentioned.

In order to give more insight on the effect of suction, Figure 9 shows isocontours of Q-criterion in the diffuser computed from instantaneous flow fields for the three cases without and with control. The Q-criterion is a local measure of the excess of rotation rate relative to the strain rate [42]. It allows identifying the vortices as flow regions with positive second invariant of the velocity gradient tensor [43]. For clarity, isocontours are not plotted in the near-tip region, above  $h/H = 80\%$ .

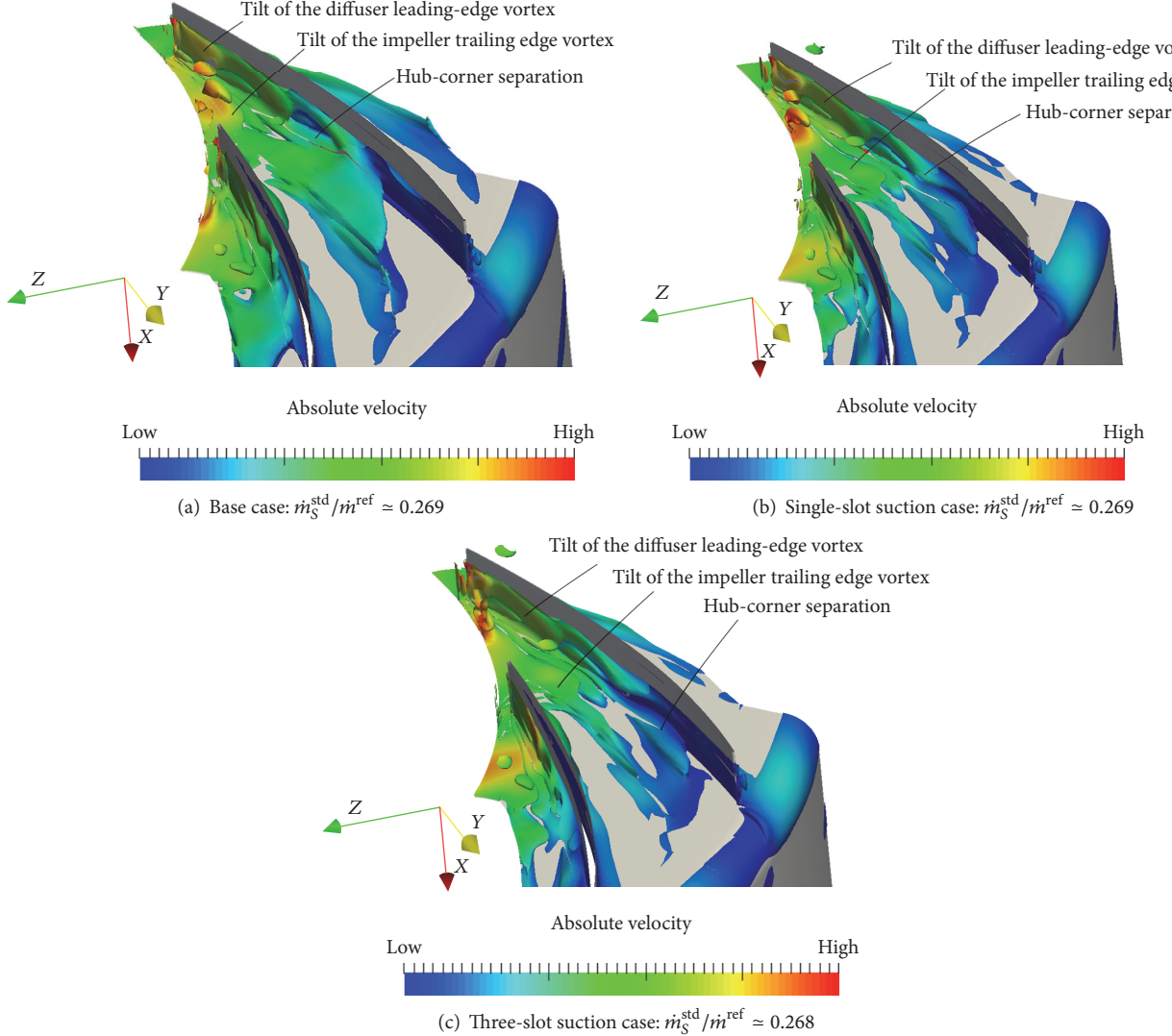
The impeller vortex shedding and the hub-corner separation vortex are both visible in the three figures. For the base case, Figure 9(a), these two vortices merge together,

which is expected to notably increase the size of the hub-corner separation vortex. With the single-slot control strategy, Figure 9(b), they still merge together but their interaction is decreased as the hub-corner separation is deflected. With the three-slot suction strategy, the interaction is barely visible given the chosen value for the isocontour.

This analysis stresses that the hub-corner separation development does not only result from the growth of the boundary-layers in the diffuser. It is also promoted by the interaction between the hub-corner separation vortex and other vortices like the impeller trailing edge vortex.

The vorticity transport equation that simplifies as

$$\frac{\partial \Omega_i}{\partial t} + U_j \frac{\partial \Omega_i}{\partial x_j} = \underbrace{\Omega_j \frac{\partial U_i}{\partial x_j}}_A + \nu \frac{\partial^2 \Omega_i}{\partial x_j^2} \quad (3)$$

FIGURE 10: Isocontours of tilt of the  $\Omega_x$  vorticity component.

for incompressible and isotropic fluids subject to conservative body forces gives more understanding about the feeding of the hub-corner vortex by other vortices. In this equation, the term  $A$  stands for the increase of the vorticity due to the tilt of vortices under velocity gradients. In case of a radial diffuser, the spanwise component of the vorticity can then feed the blade-to-blade vorticity under the effect of the spanwise velocity gradient. The impeller trailing edge vortex can then tilt and feed the hub-corner separation vortex thanks to the terms  $\Omega_x(\partial U_y / \partial x)$  and  $\Omega_x(\partial U_z / \partial x)$ ,  $x$  being the spanwise axis. In order to illustrate this phenomenon and to highlight the interaction between the impeller trailing edge vortex and the hub-corner separation vortex, Figure 10 shows isocontours of  $\sqrt{(\Omega_x(\partial U_y / \partial x))^2 + (\Omega_x(\partial U_z / \partial x))^2}$  for the three cases.

In Figure 10(a), a large structure is indeed visible near the hub surface and in the middle of the diffuser passage. It corresponds to the tilt of the foot of the impeller trailing

edge vortex that flows into the hub-corner separation and contributes to its growth. The hub-corner separation is also clearly visible in the figure, since the hub-corner separation vortex captures the boundary-layer on the diffuser suction side. It then redirects the  $\Omega_x$  vorticity component of the boundary-layer toward the blade-to-blade direction.

Another structure is also visible on the suction side of the diffuser vane. It corresponds to the tilt of the  $\Omega_x$  vorticity generated at the diffuser leading-edge due to the high incidence on the diffuser vanes at near surge operating point. Then, the diffuser leading-edge vortex also contributes to the growth of the hub-corner separation.

Under the effect of the suction, the hub-corner separation growth is slowed down and the interaction with the impeller vortex shedding is decreased. In Figure 10(b), the tilt of the impeller trailing edge vortex is less than for the base case. With the three-slot suction case, in Figure 10(c), the interaction is further decreased, and this may be the explanation of

the increase of stable operating range when the hub-corner separation is pushed downstream.

However, the role played by the diffuser leading-edge vortex is unchanged under the effect of the suction, and it now appears to be the main visible interaction that feeds the hub-corner separation. Further work should aim at gaining more understanding of the role played by this diffuser leading-edge vortex and its consequences for the surge inception. Controlling the development or the trajectory of this vortex could lead to a complete removal of the hub-corner separation.

## 9. Conclusions and Outlooks

According to the URANS numerical model, and at the nominal rotational speed, the three-slot suction strategy allows a significant increase of the centrifugal compressor operating range toward low mass flow rate. This demonstrates the interest of the boundary-layer suction technique in order to improve the performance of centrifugal compressor stages. It also confirms that the hub-corner separation in the diffuser is involved in the surge inception for the present test case.

The single-slot suction strategy allows delaying the hub-corner separation growth, and the three-slot strategy delays it further. As a consequence, the interaction between the hub-corner separation vortex and the impeller trailing edge vortex shedding is reduced, which is expected to be the key feature of the control of the surge. With the three-slot strategy, this interaction is almost cancelled, and this may explain the increase of the stable operating range.

The analysis has also revealed the interaction between the hub-corner separation and the diffuser leading-edge separation vortex, which should be taken into consideration in order to achieve a complete removal of the hub-corner separation. The leading-edge separation may be controlled by suction applied to the diffuser suction side, or by other control techniques as vortex generator, for example.

Finally, the interest of the multislots control strategy should also be challenged at other rotational speeds, and the issue of the optimal shapes of the suction slots should be addressed, prior to conducting experiments.

## Conflicts of Interest

The authors declare that there are no conflicts of interest regarding the publication of this paper.

## Acknowledgments

The authors would like to thank Turbomeca, Safran group, for providing the test case and supporting the present study. Thanks also are due to the ISAE laboratory at Université de Toulouse, where the experimental test rig is set up. Thanks are due to ONERA, which develops the elsA software and provides support regarding the numerical simulations.

## References

- [1] P. Came, "The current state of research and design in high pressure ratio centrifugal compressors," DTIC Document, 1976.
- [2] C. Amann, G. Nordenson, and G. Skellenger, "Casing modification for increasing the surge margin of a centrifugal compressor in an automotive turbine engine," *ASME*, vol. 97, no. 3, pp. 329–335, 1975.
- [3] R. Hunziker and G. Gyarmathy, "Operational stability of a centrifugal compressor and its dependence on the characteristics of the subcomponents," *Journal of Turbomachinery*, vol. 116, no. 2, pp. 250–259, 1994.
- [4] E. Greitzer, "The stability of pumping systems," *Journal of Fluids Engineering*, vol. 103, pp. 193–242, 1981.
- [5] M. P. Wernet, M. M. Bright, and G. J. Skoch, "An investigation of surge in a high-speed centrifugal compressor using digital PIV," *Journal of Turbomachinery*, vol. 123, no. 2, pp. 418–428, 2001.
- [6] J. N. Everitt, *Investigation of stall inception in centrifugal compressors using isolated diffuser simulations [M.S. thesis]*, MIT Dept. Aero/Astro, 2010.
- [7] J. N. Everitt and Z. S. Spakovszky, "An investigation of stall inception in centrifugal compressor vaned diffuser," *Journal of Turbomachinery*, vol. 135, Article ID 011025, 2012.
- [8] R. A. Hill IV, *Simulation of spike stall inception in a radial vanted diffuser [M.S. thesis]*, Massachusetts Institute of Technology, 2007.
- [9] Y. Bousquet, X. Carboneau, G. Dufour, N. Binder, and I. Trébinjac, "Analysis of the unsteady flow field in a centrifugal compressor from peak efficiency to near stall with full-annulus simulations," *International Journal of Rotating Machinery*, vol. 2014, Article ID 729629, 11 pages, 2014.
- [10] Y. Bousquet, N. Binder, G. Dufour, X. Carboneau, M. Roumeas, and I. Trébinjac, "Numerical simulation of stall inception mechanisms in a centrifugal compressor with vanted diffuser," *Journal of Turbomachinery*, vol. 138, no. 12, Article ID 121005, 2016.
- [11] N. Buffaz and I. Trébinjac, "Aerodynamic instabilities in transonic centrifugal compressor," *Mechanics and Industry*, vol. 15, no. 3, pp. 191–196, 2014.
- [12] I. Trébinjac, E. Benichou, and N. Buffaz, "Full-annulus simulation of the surge inception in a transonic centrifugal compressor," *Journal of Thermal Science*, vol. 24, no. 5, pp. 442–451, 2015.
- [13] E. Benichou and I. Trébinjac, "Comparison of steady and unsteady flows in a transonic radial vanted diffuser," *Journal of Turbomachinery*, vol. 138, no. 12, Article ID 121002, 2016.
- [14] E. Benichou and I. Trébinjac, "Numerical analysis of an alternate stall in a radial vanted diffuser," in *ASME Turbo Expo 2016: Turbomachinery Technical Conference and Exposition*, American Society of Mechanical Engineers, 2016.
- [15] N. Fujisawa, S. Ikezu, and Y. Ohta, "Structure of diffuser stall and unsteady vortices in a centrifugal compressor with vanted diffuser," in *ASME Turbo Expo 2016: Turbomachinery Technical Conference and Exposition*, American Society of Mechanical Engineers, 2016.
- [16] A. Merchant, J. L. Kerrebrock, J. J. Adamczyk, and E. Braunsheidel, "Experimental investigation of a high pressure ratio aspirated fan stage," *American Society of Mechanical Engineers*, pp. 493–502, 2004.
- [17] B. J. Schuler, J. L. Kerrebrock, and A. Merchant, "Experimental investigation of a transonic aspirated compressor," *Journal of Turbomachinery*, vol. 127, no. 2, pp. 340–348, 2005.

- [18] S. A. Gbadebo, N. A. Cumpsty, and T. P. Hynes, "Control of three-dimensional separations in axial compressors by tailored boundary layer suction," *Journal of Turbomachinery*, vol. 130, no. 1, Article ID 011004, 2008.
- [19] J. L. Kerrebrock, A. H. Epstein, A. A. Merchant et al., "Design and test of an aspirated counter-rotating fan," *Journal of Turbomachinery*, vol. 130, no. 2, Article ID 021004, 2008.
- [20] A. Godard, F. Bario, S. Burguburu, and F. Lebuf, "Experimental and numerical study of a subsonic aspirated cascade," in *ASME Turbo Expo 2012: Turbine Technical Conference and Exposition*, pp. 253–267, American Society of Mechanical Engineers, 2012.
- [21] K. K. Botros and J. F. Henderson, "Developments in centrifugal compressor surge control - a technology assessment," *Journal of Turbomachinery*, vol. 116, no. 2, pp. 240–249, 1994.
- [22] J. Raw, "Surge margin enhancement by a porous throat diffuser," *Canadian Aeronautics and Space Journal*, vol. 32, no. 1, pp. 54–61, 1986.
- [23] E. B. Nelson, J. D. Paduano, and A. H. Epstein, "Active stabilization of surge in an axialcentrifugal turboshaft engine," *Journal of Turbomachinery*, vol. 122, no. 3, pp. 485–493, 2000.
- [24] G. J. Skoch, "Experimental investigation of centrifugal compressor stabilization techniques," *Journal of Turbomachinery*, vol. 125, no. 4, pp. 704–713, 2003.
- [25] G. J. Skoch, "Experimental investigation of diffuser hub injection to improve centrifugal compressor stability," *Journal of Turbomachinery*, vol. 127, no. 1, pp. 107–117, 2005.
- [26] Z. S. Spakovszky, "Backward traveling rotating stall waves in centrifugal compressors," *Journal of Turbomachinery*, vol. 126, no. 1, pp. 1–12, 2004.
- [27] T. Halawa, M. S. Gadala, M. Alqaradawi, and O. Badr, "Optimization of the efficiency of stall control using air injection for centrifugal compressors," *Journal of Engineering for Gas Turbines and Power*, vol. 137, no. 7, Article ID 072604, 2015.
- [28] H. Schönenborn, "Removal of cooling air on the suction side of a diffuser vane of a radial compressor stage of gas turbines," US Patent 6,210,104, April 2001.
- [29] A. Leblanc, "Diffuser with enhanced surge margin," US Patent 8,556,573, October 2013.
- [30] A. Marsan, I. Trébinjac, S. Coste, and G. Leroy, "Influence of unsteadiness on the control of a hub-corner separation within a radial vaned diffuser," *Journal of Turbomachinery*, vol. 137, no. 2, 12 pages, 2015.
- [31] A. Marsan, I. Trébinjac, S. Coste, and G. Leroy, "Study and control of a radial vaned diffuser stall," *International Journal of Rotating Machinery*, vol. 2012, Article ID 549048, 12 pages, 2012.
- [32] A. Marsan, I. Trébinjac, S. Coste, and G. Leroy, "Temporal behaviour of a corner separation in a radial vaned diffuser of a centrifugal compressor operating near surge," *Journal of Thermal Science*, vol. 22, no. 6, pp. 555–564, 2013.
- [33] I. Trébinjac, P. Kulisa, N. Bulot, and N. Rochuon, "Effect of unsteadiness on the performance of a transonic centrifugal compressor stage," *Journal of Turbomachinery*, vol. 131, no. 4, Article ID 041011, 9 pages, 2009.
- [34] N. Bulot and I. Trébinjac, "Effect of the unsteadiness on the diffuser flow in a transonic centrifugal compressor stage," *International Journal of Rotating Machinery*, vol. 2009, Article ID 932593, 11 pages, 2009.
- [35] L. Cambier and J. P. Veuillot, "Status of the elsA CFD software for flow simulation and multidisciplinary applications," in *Proceedings of the 46th AIAA Aerospace Science Meeting and Exhibit*, vol. 664, Reno, Nev, USA, 2008.
- [36] J. I. Erdos, E. Alzner, and W. McNally, "Numerical solution of periodic transonic flow through a fan stage," *AIAA Journal*, vol. 15, no. 11, pp. 1559–1568, 1977.
- [37] J. M. Tyler and T. G. Sofrin, "Axial flow compressor noise studies," *SAE International*, vol. 70, Article ID 620532, 24 pages, 1962.
- [38] G. A. Gerolymos, G. J. Michon, and J. Neubauer, "Analysis and application of chorochronic periodicity in turbomachinery rotor/stator interaction computations," *Journal of Propulsion and Power*, vol. 18, no. 6, pp. 1139–1152, 2002.
- [39] L. Castillon, G. Billonnet, S. Péron, and C. Benoit, "Numerical simulations of technological effects encountered on turbomachinery configurations with the chimera technique," in *Proceedings of 27th International Congress of the Aeronautical Sciences*, Nice, France, September 2010.
- [40] Y. Bousquet, X. Carbonneau, G. Dufour, N. Binder, and I. Trébinjac, "Analysis of the unsteady flow field in a centrifugal compressor from peak efficiency to near stall with full-annulus simulations," *International Journal of Rotating Machinery*, vol. 2014, Article ID e729629, 11 pages, 2014.
- [41] Z. S. Spakovszky and C. H. Roduner, "Spike and modal stall inception in an advanced turbocharger centrifugal compressor," *Journal of Turbomachinery*, vol. 131, no. 3, Article ID 031012, 2009.
- [42] P. Chakraborty, S. Balachandar, and R. J. Adrian, "On the relationships between local vortex identification schemes," *Journal of Fluid Mechanics*, vol. 535, pp. 189–214, 2005.
- [43] J. C. Hunt, A. Wray, and P. Moin, "Eddies, streams, and convergence zones in turbulent flows," Tech. Rep. CTR-S88, Center for Turbulence Research, 1988.

## Research Article

# Application of System Identification for Modeling the Dynamic Behavior of Axial Flow Compressor Dynamics

Marco P. Schoen<sup>1</sup> and Ji-Chao Lee<sup>2</sup>

<sup>1</sup>Department of Mechanical Engineering, Idaho State University, Mail Stop 8060, Pocatello, ID 83209, USA

<sup>2</sup>Institute of Engineering Thermophysics, CAS, 11 Beisihuanxi Road, Beijing 100190, China

Correspondence should be addressed to Marco P. Schoen; schomarc@isu.edu

Received 1 February 2017; Accepted 11 April 2017; Published 7 May 2017

Academic Editor: Pietro Zunino

Copyright © 2017 Marco P. Schoen and Ji-Chao Lee. This is an open access article distributed under the Creative Commons Attribution License, which permits unrestricted use, distribution, and reproduction in any medium, provided the original work is properly cited.

Identification of a one-stage axial compressor system is addressed. In particular, we investigate the underlying dynamics of tip air injection and throttle activation to the overall compressor dynamics and the dynamics around the tip of the compressor blades. A proposed subspace system identification algorithm is used to extract three mathematical models: relating the tip air injection to the overall dynamics of the compressor and to the flow dynamics at the tip of the compressor blade and relating the movement of the throttle to the overall compressor dynamics. As the system identification relies on experimental data, concerns about the noise level and unmodeled system dynamics are addressed by experimenting with two model structures. The identification algorithm entails a heuristic optimization that allows for inspection of the results with respect to unmodeled system dynamics. The results of the proposed system identification algorithm show that the assumed model structure for the system identification algorithm takes on an important role in defining the coupling characteristics. A new measure for the flow state in the blade passage is proposed and used in characterizing the dynamics at the tip of the compressor blade, which allows for the inspection of the limits for the utilized actuation.

## 1. Introduction

Operation of axial compressor systems, as found in a number of aerospace applications, faces difficulties due to instabilities at the peak of its performance curves. To mitigate these instabilities, a number of different control mechanisms have been introduced. Among them are air injection into the tip of the blade passage [1–3] and the use of grooved casings [4–6]. Modeling of the overall compressor dynamics has been a challenging undertaking, resulting in the well-known Moore-Greitzer model. However, there does not exist a model relating the influence of air injection to the overall system dynamics. One of the aims of this work is to present a system identification based approach to characterize the influence of the air injection—commonly used to control the compressor—to the overall compressor dynamics.

As the system identification relies on experimental data, concerns about the noise level need to be addressed as well as unmodeled system dynamics. The unmodeled system

dynamics can become an important issue when the experimental data do not include all system modes during the system identification experiment or the assumed model structure does not allow for accommodating one or more particular dynamic characteristics. We propose to utilize two different model structures to investigate the unmodeled system dynamics and the effects of the proposed optimization. These structures are the autoregressive moving average with exogenous input (ARMAX) model and the autoregressive with exogenous input (ARX) model. An innovation sequence is extracted by using an estimated parameter sequence. The ARMAX model and ARX model parameters are then utilized to construct a Hankel matrix, representing the sampled impulse response of the system relating tip air injection to pressure rise coefficient. A singular value decomposition of the Hankel matrix is performed for an eigensystem realization (ERA, [7, 8]) resulting in a state-space description of the coupling dynamics. However, prior to performing the state-space realization, a heuristic optimization algorithm is

introduced to optimize the singular values with respect to the measured output data. This allows for minimization of the noise influence to the extracted state-space model as well as the effect the assumed model structure has on fitting to the recorded characteristics from the system identification experiment. The proposed system identification is used for data collected on an isolated rotor axial compressor system whose blade geometry allows for spike stall inception. The tip air injection is applied in a random fashion in order to allow for sufficient system mode excitation. The resulting pressure rise and associated flow coefficient are computed using a set of pressure sensors. The optimization of the Hankel matrix is accomplished by using a Tabu Search (TS) algorithm [9]. The TS searches the vicinity around each singular value defined by a percentage of the largest singular value. The eigensystem realization is done using a balanced realization, an input-normal form, and an output normal form realization in order to assess the impact of the optimized singular values. Another aim of this work is to characterize the dynamics within the blade passage at the tip of the rotor blade due to air injection at the leading edge of the rotor blade. Finally, the proposed hybrid system identification algorithm using TS is used to model the compressor dynamics excited by movements of the throttle and the resulting pressure rise changes.

In the following, the details of the system identification scheme as well as the proposed realization and optimization are introduced.

## 2. System Identification Algorithm

Consider a linear, time-invariant, discrete time system:

$$\dot{x}(k+1) = Ax(k) + Bu(k) + w(k) \quad (1)$$

$$y(k) = Cx(k) + Du(k) + v(k), \quad (2)$$

where  $A, B, C$ , and  $D$  are the system matrices and  $\{y\} \in \mathbb{R}^{n_y \times L}$ ,  $\{u\} \in \mathbb{R}^{n_u \times L}$ , are the output and input data sequences recorded during a system experiment with some sample frequency  $f_s$ , resulting in  $L$  discrete data points for each of the two sequences.  $n_y$  is the number of outputs, and  $n_u$  is the number of inputs;  $\{w\} \in \mathbb{R}^{n \times L}$  is the process noise and  $\{v\} \in \mathbb{R}^{n_y \times L}$  is the measurement noise, while  $\{x\} \in \mathbb{R}^{n \times L}$  is the state vector.

In order to estimate the state variable  $x$ , a Kalman filter  $K$  is used, provided the states are observable [10]. Hence, the system given by (1) and (2) can be reformulated. Defining the Kalman filter gain  $K$  as

$$K = P_F C^T [R_F + C P_F C^T]^{-1} \in \mathbb{R}^{n \times n_y}, \quad (3)$$

where  $P_F \in \mathbb{R}^{n \times n}$  is the solution of the steady-state algebraic Riccati equation. Hence,

$$\hat{x}(k+1) = A\hat{x}(k) + Bu(k) + Ke(k), \quad (4)$$

$$\hat{y}(k) = C\hat{x}(k) + Du(k) + \varepsilon(k), \quad (5)$$

where

$$\varepsilon(k) = y(k) - C\hat{x}(k) - Du(k). \quad (6)$$

The system in (1) is in the process form, while the system in (4) is in the innovation form. Using (6) in (4) results and defining  $\bar{A} = [A - KC]$  and  $\bar{B} = [B - KD]$ , we arrive at the predictor form of the given system:

$$\hat{x}(k+1) = \bar{A}\hat{x}(k) + \bar{B}u(k) + Ky(k), \quad (7)$$

$$\hat{y}(k) = C\hat{x}(k) + Du(k) + \varepsilon(k). \quad (8)$$

The predictor form of (8) can be used to derive an AutoRegressive with eXogenous input (ARX) model:

$$\begin{aligned} \hat{y}(k) &= \bar{C}\bar{A}^{p_1} \hat{x}(k-p_1) + \bar{C}\bar{A}^{p_1-1} \bar{B}u(k-p_1) \\ &\quad + \bar{C}\bar{A}^{p_1-2} \bar{B}u(k-p_1-1) + \cdots + \bar{C}\bar{B}u(k-1) \\ &\quad + Du(k) + \bar{C}\bar{A}^{p_1-1} Ky(k-p_1) \\ &\quad + \bar{C}\bar{A}^{p_1-2} Ky(k-p_1-1) + \cdots \\ &\quad + \bar{C}\bar{A}^2 Ky(k-3) + \bar{C}\bar{A} Ky(k-2) \\ &\quad + CKy(k-1) + \varepsilon(k). \end{aligned} \quad (9)$$

Note,  $\bar{A} = [A - KC]$  is an asymptotically stable square matrix; hence if  $p_1$  is sufficiently large, we have

$$\bar{A}^{p_1} \approx 0. \quad (10)$$

Equation (9) becomes

$$\begin{aligned} \hat{y}(k) &= \bar{C}\bar{A}^{p_1-1} \bar{B}u(k-p_1) + \bar{C}\bar{A}^{p_1-2} \bar{B}u(k-p_1-1) \\ &\quad + \cdots + \bar{C}\bar{B}u(k-1) + Du(k) \\ &\quad + \bar{C}\bar{A}^{p_1-1} Ky(k-p_1) \\ &\quad + \bar{C}\bar{A}^{p_1-2} Ky(k-p_1-1) + \cdots \\ &\quad + \bar{C}\bar{A}^2 Ky(k-3) + \bar{C}\bar{A} Ky(k-2) \\ &\quad + CKy(k-1) + \varepsilon(k). \end{aligned} \quad (11)$$

Note that  $\bar{C}\bar{A}^{i-1}\bar{B}$  are the system Markov parameters and  $\bar{C}\bar{A}^{i-1}K$  are the Kalman filter Markov parameters. Also, the existence of  $K$  is guaranteed if the system is detectable and  $(A, Q^{1/2})$  is stabilizable [7].

Equation (11) is of the form

$$y(k) = \sum_{i=1}^{p_1} a_i y(k-i) + \sum_{i=1}^{p_1} b_i u(k-i) + \varepsilon(k), \quad (12)$$

where  $a_i = \bar{C}\bar{A}^{i-1}K$  and  $b_i = \bar{C}\bar{A}^{i-1}\bar{B}$ . Assuming the system is observable and controllable, the following output vector can

be created (for simplicity, we assume  $D = 0$  or the first input = 0):

$$\begin{aligned} y(0) &= Cx(0), \\ y(1) &= Cx(1) = \bar{C}\bar{A}x(0), \\ y(2) &= Cx(2) = \bar{C}\bar{A}x(1) = \bar{C}\bar{A}^2x(0), \\ &\vdots \\ y(n-1) &= \bar{C}\bar{A}^{n-1}x(0). \end{aligned} \quad (13)$$

Hence

$$P_o = \begin{Bmatrix} C \\ \bar{C}\bar{A} \\ \bar{C}\bar{A}^2 \\ \vdots \\ \bar{C}\bar{A}^{n-1} \end{Bmatrix} \quad (14)$$

is the observability matrix. The system is observable if  $P_o$  is of rank( $P_o$ ) =  $n$ . To test for controllability, one can create a state vector:

$$\begin{aligned} x(1) &= \bar{A}x(0) + \bar{B}u(0), \\ x(2) &= \bar{A}[\bar{A}x(0) + \bar{B}u(0)] + \bar{B}u(1) = \bar{A}^2x(0) \\ &\quad + \bar{A}\bar{B}u(0) + \bar{B}u(1), \\ &\vdots \\ x(n) &= \bar{A}^nx(0) + \bar{A}^{n-1}\bar{B}u(0) + \cdots + \bar{B}u(n-1), \\ x(n) - \bar{A}^nx(0) & \end{aligned} \quad (15)$$

$$= [\bar{B} \ \bar{A}\bar{B} \ \bar{A}^2\bar{B} \ \cdots \ \bar{A}^{n-1}\bar{B}] \begin{Bmatrix} u(n-1) \\ u(n-2) \\ u(n-3) \\ \vdots \\ u(0) \end{Bmatrix}.$$

Here

$$P_c = [\bar{B} \ \bar{A}\bar{B} \ \bar{A}^2\bar{B} \ \cdots \ \bar{A}^{n-1}\bar{B}] \quad (16)$$

is a square matrix. The discrete time system is controllable if and only if  $\text{rank}(P_c) = n$ . Suppose the system of (4) and (5) is controllable and observable with rank  $n$ ; then

$$H = P_o P_c,$$

$$H = \begin{Bmatrix} C \\ \bar{C}\bar{A} \\ \bar{C}\bar{A}^2 \\ \vdots \\ \bar{C}\bar{A}^{n-1} \end{Bmatrix} [\bar{B} \ \bar{A}\bar{B} \ \bar{A}^2\bar{B} \ \cdots \ \bar{A}^{n-1}\bar{B}],$$

$$H = \begin{bmatrix} \bar{C}\bar{B} & \bar{C}\bar{A}\bar{B} & \bar{C}\bar{A}^2\bar{B} & \cdots & \bar{C}\bar{A}^{c-1}\bar{B} \\ \bar{C}\bar{A}\bar{B} & \bar{C}\bar{A}^2\bar{B} & \bar{C}\bar{A}^3\bar{B} & \cdots & \bar{C}\bar{A}^c\bar{B} \\ \bar{C}\bar{A}^2\bar{B} & \bar{C}\bar{A}^3\bar{B} & \bar{C}\bar{A}^4\bar{B} & \cdots & \bar{C}\bar{A}^{c+1}\bar{B} \\ \vdots & \vdots & \vdots & \ddots & \vdots \\ \bar{C}\bar{A}^{o-1}\bar{B} & \bar{C}\bar{A}^o\bar{B} & \bar{C}\bar{A}^{o+1}\bar{B} & \cdots & \bar{C}\bar{A}^{o+p-2}\bar{B} \end{bmatrix}$$

$$= \mathbb{R}^{(o \times n_y) \times (c * n_o)}. \quad (17)$$

One notices that the Hankel matrix  $H$  is composed of the system Markov parameters. Using the ARX model parameters  $b_i$ ,  $H$  can be given as

$$H = \begin{bmatrix} b_1 & b_2 & b_3 & \cdots & b_c \\ b_2 & b_3 & b_4 & \cdots & b_{c+1} \\ b_3 & b_4 & b_5 & \cdots & b_{c+2} \\ \vdots & \vdots & \vdots & \ddots & \vdots \\ b_o & b_{o+1} & b_{o+2} & \cdots & b_{o+c} \end{bmatrix}. \quad (18)$$

Defining the system Markov parameters as

$$\begin{aligned} \bar{Y}_o &= D = b_0, \\ \bar{Y}_1 &= \bar{C}\bar{B} = b_1, \\ \bar{Y}_2 &= \bar{C}\bar{A}\bar{B} = b_2, \\ &\vdots \\ \end{aligned} \quad (19)$$

then  $H$  can be written as

$$H(0) = \begin{bmatrix} \bar{Y}_1 & \bar{Y}_2 & \bar{Y}_3 & \cdots & \bar{Y}_c \\ \bar{Y}_2 & \bar{Y}_3 & \bar{Y}_4 & \cdots & \bar{Y}_{c+1} \\ \bar{Y}_3 & \bar{Y}_4 & \bar{Y}_5 & \cdots & \bar{Y}_{c+2} \\ \vdots & \vdots & \vdots & \ddots & \vdots \\ \bar{Y}_o & \bar{Y}_{o+1} & \bar{Y}_{o+2} & \cdots & \bar{Y}_{o+c} \end{bmatrix}. \quad (20)$$

To realize a state-space system of the form  $[\bar{A}, \bar{B}, C, D]$  a minimum realization is utilized (see [7, 10]). The minimum

realization allows for investigating the primary or dominant modes of the system to be identified.

Perform a SVD on  $H(0) : H(0) = R\Sigma^T$ , where

$$\Sigma = \begin{bmatrix} \Sigma_n & 0 \\ 0 & 0 \end{bmatrix} \quad \text{with } \Sigma_n = \text{diag} [\sigma_1 \ \sigma_2 \ \dots \ \sigma_n] \quad (21)$$

and the singular values are ordered as

$$\sigma_1 \geq \sigma_2 \geq \dots \geq \sigma_n > 0. \quad (22)$$

Truncate  $R$  and  $S$  to have  $n$  columns, which results into  $R_n$  and  $S_n$ . Hence the following equality exists:

$$H(0) = [R_n \Sigma^{1/2}] [\Sigma^{1/2} S_n^T] \cong P_o P_c. \quad (23)$$

Hence, the Hankel singular values are the square roots of the eigenvalues of  $P_o P_c$ :

$$\sigma_i = \sqrt{\lambda_i(P_o P_c)}. \quad (24)$$

Now there are different ways to interpret the realization. They are organized by what combination and association is being taken:

(i) input-normal form:

$$\begin{aligned} P_o &= R_n \Sigma_n, \\ P_c &= S_n^T, \end{aligned} \quad (25)$$

(ii) balanced form:

$$\begin{aligned} P_o &= R_n \Sigma_n^{1/2}, \\ P_c &= \Sigma_n^{1/2} S_n^T \end{aligned} \quad (26)$$

(iii) output normal form:

$$\begin{aligned} P_o &= R_n, \\ P_c &= \Sigma_n S_n^T. \end{aligned} \quad (27)$$

Choosing the balanced form, we have

$$\begin{aligned} P_o^T P_o &= \Sigma_n^{1/2} R_n^T R_n \Sigma_n^{1/2} = \Sigma_n, \\ P_c P_c^T &= \Sigma_n^{1/2} S_n^T S_n \Sigma_n^{1/2} = \Sigma_n. \end{aligned} \quad (28)$$

Having realized  $P_c$  and  $P_o$ , we can utilize their original definition

$$P_o = \begin{Bmatrix} C \\ C\bar{A} \\ C\bar{A}^2 \\ \vdots \\ C\bar{A}^{n-1} \end{Bmatrix}, \quad (29)$$

$$P_c = [\bar{B} \ \bar{A}\bar{B} \ \bar{A}^2\bar{B} \ \dots \ \bar{A}^{n-1}\bar{B}].$$

Hence,  $\bar{B}$  is first  $n_u$  columns of  $P_c$  or of  $\Sigma_n^{1/2} S_n^T$ ;  $C$  is first  $n_o$  rows of  $P_o$  or of  $R_n \Sigma_n^{1/2}$ ,  $D = \bar{Y}(0)$ . To compute  $\bar{A}$ , one forms

$$H(1) = \begin{bmatrix} \bar{Y}_2 & \bar{Y}_3 & \bar{Y}_4 & \dots & \bar{Y}_{c+1} \\ \bar{Y}_3 & \bar{Y}_4 & \bar{Y}_5 & \dots & \bar{Y}_{c+2} \\ \bar{Y}_4 & \bar{Y}_5 & \bar{Y}_6 & \dots & \bar{Y}_{c+3} \\ \vdots & \vdots & \vdots & \ddots & \vdots \\ \bar{Y}_{o+1} & \bar{Y}_{o+2} & \bar{Y}_{o+3} & \dots & \bar{Y}_{o+c} \end{bmatrix}. \quad (30)$$

Expressing  $H(1)$  in terms of  $[\bar{A}, \bar{B}, C, D]$ :

$$\begin{aligned} H(1) &= \begin{bmatrix} C\bar{A}\bar{B} & C\bar{A}^2\bar{B} & C\bar{A}^3\bar{B} & \dots & C\bar{A}^c\bar{B} \\ C\bar{A}^2\bar{B} & C\bar{A}^3\bar{B} & C\bar{A}^4\bar{B} & \dots & C\bar{A}^{c+1}\bar{B} \\ C\bar{A}^3\bar{B} & C\bar{A}^4\bar{B} & C\bar{A}^5\bar{B} & \dots & C\bar{A}^{c+2}\bar{B} \\ \vdots & \vdots & \vdots & \ddots & \vdots \\ C\bar{A}^o\bar{B} & C\bar{A}^{o+1}\bar{B} & C\bar{A}^{o+2}\bar{B} & \dots & C\bar{A}^{o+p-1}\bar{B} \end{bmatrix} \\ &= P_o \bar{A} P_c. \end{aligned} \quad (31)$$

Using SVD on the last equation yields

$$H(1) = P_o \bar{A} P_c = R_n \Sigma_n^{1/2} \bar{A} \Sigma_n^{1/2} S_n^T. \quad (32)$$

From this, one can compute  $\bar{A}$ :

$$\bar{A} = \Sigma_n^{-1/2} R_n^T H(1) S_n \Sigma_n^{-1/2}. \quad (33)$$

### 3. Estimation of ARMAX Model

Equation (12) is an ARX model. To incorporate a moving average term into (12), a third convolution term is added,

$$\begin{aligned} y(k) &= \sum_{i=1}^{p_1} \tilde{a}_i y(k-i) + \sum_{i=1}^{p_1} \tilde{b}_i u(k-i) + \sum_{i=1}^{p_1} \tilde{c}_i \varepsilon(k-i) \\ &\quad + \varepsilon(k), \end{aligned} \quad (34)$$

where  $a_i$ ,  $b_i$ , and  $c_i$  are the model parameter matrices. The idea of using an ARMAX model is to accommodate the innovation and noise influence. The parameters of the ARX model can be estimated using standard least-squares techniques. For the ARMAX model, the following approach is adapted.

Define

$$\begin{aligned} \bar{\Phi}(k, h_{n_1}) &= [y_k^T \ y_{k+1}^T \ \dots \ y_{k-h_{n_1}+1}^T \ u_k^T \ \dots \ u_{k-h_{n_1}+1}^T]^T, \end{aligned} \quad (35)$$

for  $0 \leq k \leq n_1$ , where the subscript is used for denoting the time index. The innovation sequence can be estimated by using

$$\hat{\varepsilon}(k, n_1) = y(k) - \hat{\alpha}^T(k, n_1) \bar{\Phi}(k-1, h_{n_1}), \quad (36)$$

where

$$\begin{aligned}\hat{\alpha}(k+1, n_1) &= \hat{\alpha}(k, n_1) + \beta(k, n_1) \tilde{\Phi}^T(k, h_{n_1}) \\ &\cdot \tilde{P}(k, n_1) \times [y(k+1) - \tilde{\Phi}^T(k, h_{n_1}) \hat{\alpha}(k, n_1)], \\ \tilde{P}(k+1, n_1) &= \tilde{P}(k, n_1) - \beta(k, n_1) \tilde{P}(k, n_1) \tilde{\Phi}(k, h_{n_1}) \quad (37) \\ &\cdot \tilde{\Phi}^T(k, h_{n_1}) \tilde{P}(k, n_1), \\ \beta(k, n_1) &= \{1 + \tilde{\Phi}^T(k, h_{n_1}) \tilde{P}(k, n_1) \tilde{\Phi}(k, h_{n_1})\}^{-1}.\end{aligned}$$

Using  $\hat{\alpha}(0, n_1) = 0$  and  $\tilde{P}(0, n_1) = \eta I$  with  $\eta > 0$ , and defining

$$\begin{aligned}\tilde{\Theta} &= [a_1 \ a_2 \ \dots \ a_{p_1} \ b_1 \ \dots \ b_{p_1} \ c_1 \ c_2 \ \dots \ c_{p_1}]^T, \\ X_{n_1} &= [\phi_0 \ \phi_1 \ \dots \ \phi_{n_1-1}]^T, \\ \Gamma_{n_1} &= [y_1 \ y_2 \ \dots \ y_{n_1}]^T, \quad (38) \\ \phi_i &= [y_i^T \ y_{i-1}^T \ \dots \ y_{i-p_1+1}^T \ u_i^T \ \dots \ u_{i-p_1+1}^T \ \varepsilon_1 \ \dots \ \varepsilon_{i-p_1+1}^T]^T,\end{aligned}$$

where the subscript is used for the time index, the estimated ARMAX parameters are given by

$$\widehat{\Theta} = [X^T(n_1) X(n_1)]^{-1} X^T(n_1) \Gamma(n_1). \quad (39)$$

To obtain a realization of the form of (39), the estimated model parameters of the ARX or ARMAX model are used to compute the system Markov parameters (see [11]) and construct a block Hankel matrix of the form given by (20) or (30). The realization then can be established by any of the three options given by (25), (26), or (27).

#### 4. Tabu Search Optimization

The Hankel matrix in (20) is composed of the sampled impulse response of the system. In addition to the system's response, there is noise, unmodeled system dynamics, and responses from auxiliary systems that are coupled with the system to be identified. As there is no method to separate the given impulse response from coupled noise, unmodeled dynamics, and auxiliary system responses, we propose to imbed an optimization into the eigensystem realization (ERA) algorithm given by [8]. The optimization is done using an Enhanced Tabu Search (ETS) algorithm. The ETS employs a two-stage process, where during the first stage a list of promising areas in the search field is established. During the second stage, the promising areas are further searched by a regular TS algorithm. Details on the employed ETS and TS are found in [9]. The ERA is updated such that after selecting the number of states of the system—based on the magnitude of the singular values in  $\Sigma$ —the entries of the selected singular values are searched within a close vicinity of their nominal value established by the SVD. The search areas are defined as

TABLE 1: Test compressor design parameters.

	Quantity
Design speed (rpm)	2400
Rotor blade number	60
Outer diameter (mm)	500
Mass flow rate (kg/s)	2.9
Rotor tip chord (mm)	36.3
Rotor tip stagger angle (deg.)	39.2
Hub-tip ratio	0.75

a percentage of the largest singular value. The cost function for the ETS and TS is given by

$$J_1 = \frac{\lambda_1}{2} \sum_{i=1}^N \{y(i) - \hat{y}(i)\}^2, \quad (40)$$

where  $\hat{y}$  is the estimated output from the resulting realized system. An easy extension to the given cost function is to incorporate a priori information of the system. For example, if the fundamental natural frequency of the system to be identified is known, (40) can be extended to

$$J_2 = \frac{\lambda_1}{2} \left( \sum_{i=1}^N \{y(i) - \hat{y}(i)\}^2 \right) + \frac{\lambda_2}{2} (\omega_n - \hat{\omega}_n)^2, \quad (41)$$

where  $\lambda_i$  are weighting factors and  $\hat{\omega}$  is the resulting estimated natural frequency.

#### 5. Experimental Setup

In this work, we utilize a one-stage compressor system with a blade geometry that allows for spike inception. The proposed identification scheme is used to identify the dynamics at different flow conditions, including near stall conditions. The dynamics of the compressor is given by the changes within the blade passage area as well as the changes in the pressure rise coefficient computed by the input and output pressures. Hence, we extract three separate models, one for the dynamics within the blade passage due to air injection, one for the input/output relationship of the compressor due to throttle movements, and one that characterizes the dynamics due to air injection pressure as the input of the system and the pressure rise coefficient as the output of the system. The compressor employed for this research is a low-speed rotor with characteristic parameters as given in Table 1. The compressor exhibits stall at 40–50% of its rotating frequency. The operating range of this compressor is given by a flow coefficient between 0.58 and 0.49, where the latter bound represents the vicinity of the stall point. The experiments were carried out using a smooth casing; that is, there are no grooves within the tip clearance casings. The average tip clearance for the setup is 1 mm. A number of pressure sensors are used, as shown in Figure 1.

Sensors 1 and 8 are utilized to compute the flow coefficient and pressure rise. A separate sensor is mounted at the injection port to measure the injection pressure. The pressure

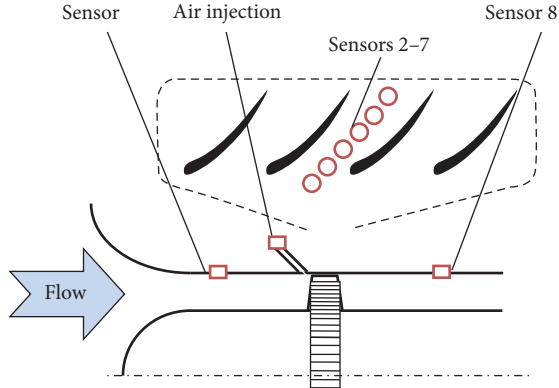


FIGURE 1: Sensor location for experimental setup. The dashed breakout view is rotated 90° and depicts the six sensors for capturing the dynamics of the blade passage.

sensors measure at a sampling rate of 20,000 Hz. There are eight air injectors, equally distributed over the circumference, injecting air at an angle of 15 degrees with a steady pressure. Sensors 2 to 7 are dedicated to the dynamics within the blade passage.

For the actuation, there are two inputs. One input is given by the movement of the throttle valve, which is used to set the operating point. The other input is accomplished via high-pressure air injection using the eight injectors equally distributed around the circumference of the compressor annulus. The setup of the measurement and injectors is shown in Figure 2(a) while the throttle valve cone movement setup is shown in Figure 2(b).

## 6. Results and Discussion

**6.1. Identification Results for Overall Dynamics due to Injection.** We first present the results for inferring the compressor dynamics modeling the dynamics related to the air injection and overall output of the compressor as measured by flow coefficient and pressure rise coefficient. Considering Figure 3, the system identification results for a flow coefficient of 0.55 are shown by the extracted Bode plots of the various realized systems. The original ARX and ARMAX model, using a balanced realization and no optimization of their singular values, indicates that both have captured very similar characteristics.

The first fundamental frequency is at around 557 Hz. Once optimization is used as well as different realization forms (input (IN), output (ON), or balanced (BN) normal), the Bode plots of the two models (ARX and ARMAX) start to diverge from each other. For the ARX based model set, the frequency responses converge to a very defined Bode plot, with a fundamental frequency of 477 Hz. For the ARMAX based model set, the resulting frequency responses are reduced in their emphasis to the fundamental frequency. The ARX based model set also shows a much improved magnitude for the first fundamental frequency. Regardless of the realization (balanced, input, or output normal), all of the optimized ARX based models seem to agree with the

first fundamental frequency and its amplitude. The phase plot does not show much change from unoptimized to optimized system identification results, for both model structures and all realizations.

At a flow coefficient of 0.55, the compressor operates sufficiently far away from the stall inception. The optimization of the singular values for the system identification algorithm is based on minimizing the error between the simulated model output and the measured overall system output, as given by (40). To gain some understanding of what these system identification results mean, we shall consider the difference of the two model structures, that is, ARX and ARMAX. The ARX model can be given in system block formulation as shown in Figure 4.

The corresponding system equation is given by

$$y(k) = \frac{B(q)}{A(q)} u(k) + \frac{1}{A(q)} v(k), \quad (42)$$

where  $q$  is the backshift operator and  $A$  and  $B$  are polynomials of the numerator and denominator. The ARMAX model is given in Figure 5.

The corresponding system equation is given by

$$y(k) = \frac{B(q)}{A(q)} u(k) + \frac{C(q)}{A(q)} v(k), \quad (43)$$

where  $C$  is the corresponding polynomial responsible for modulating the noise sequence  $v(k)$ . Comparing (42) with (43), we notice that the ARMAX model has a built-in capacity to model the unobservable noise term  $v(k)$ . However, in this case, we not only have an unobservable noise term, but also the overall system dynamics, apart from the injection induced dynamics. When using the TS optimization, the incorporated cost function entails the overall output, that is, the system dynamics output, unobservable dynamics, and the dynamics resulting from the noise sequence. As the system identification algorithm has no means to separate the different dynamics and the noise influence, it models all of it with the help of the Moving Average (MA) portion of the model structure. This is corresponding to the  $C$  polynomial in (43). As the input/output energy of the collected data is the same for all experiments, the modeling of the MA portion drains some of this energy away from the coupling dynamics and results into lower magnitude plots in the Bode diagram for the ARMAX models. The measured data is filtered prior to the application of the proposed optimization, using a notch filter to reduce the influence of the blade passing frequency (BPF). The sampling time of the data collection is set to 20 kHz, making the resulting Bode plot span over a large bandwidth. However, the overall dynamics of the compressor is found to be at much lower frequencies. This is given by the stall frequency of this compressor to be 17 Hz. Hence, the discussed frequencies in the Bode plot likely do not represent the coupling dynamics. From measurements at various locations through the compressor ducting, it was noticed that the 477 Hz frequency exists everywhere (sensors 1 and 8 in Figure 1). The true meaning of this frequency is not understood at this time. However, observations from

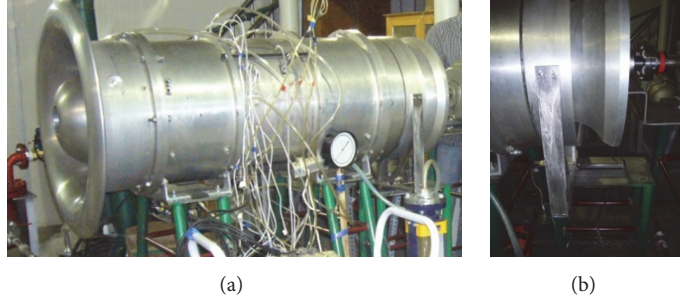


FIGURE 2: Picture of (a) side view of the one-stage axial compressor system and (b) view of the throttle using a cone movement system for controlling the flow coefficient and pressure rise.

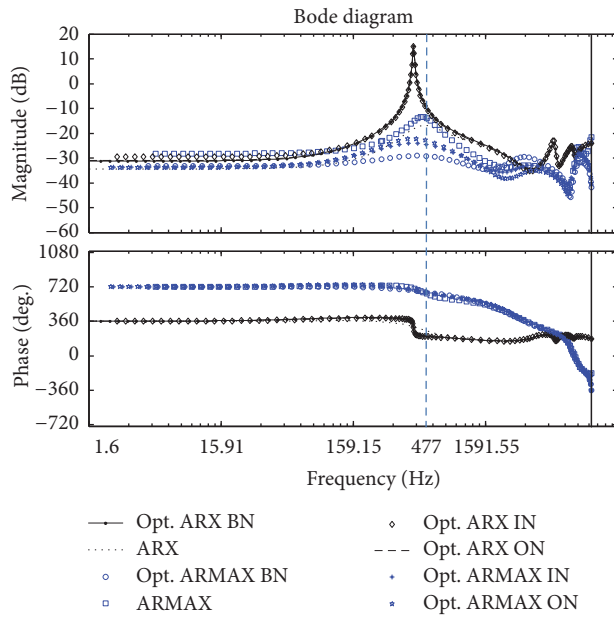


FIGURE 3: Bode plot for ARX (black) and ARMAX (blue) realization; flow coefficient = 0.55.

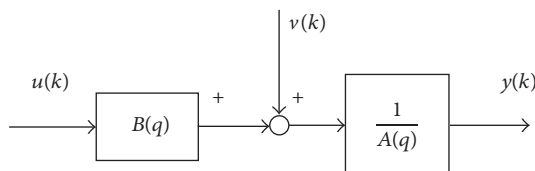


FIGURE 4: ARX model in block diagram form.

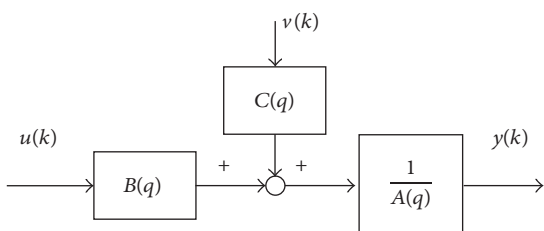


FIGURE 5: ARMAX model in block diagram form.

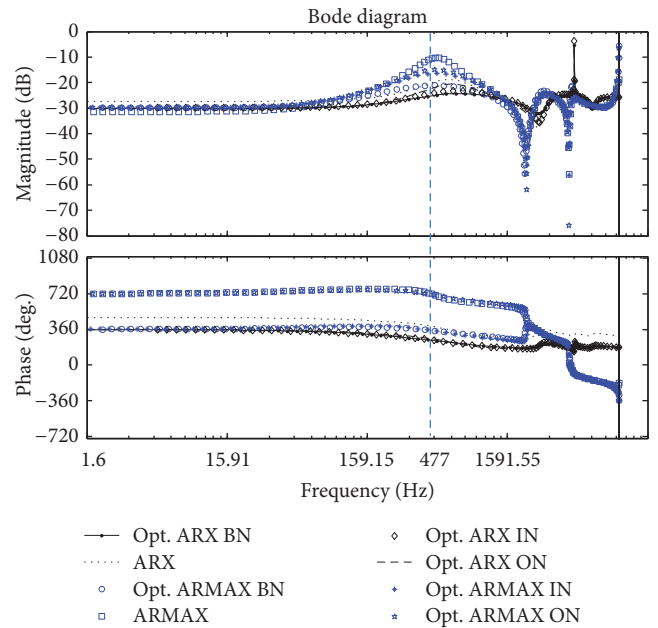


FIGURE 6: Bode plot for ARX (black) and ARMAX (blue) realization; flow coefficient = 0.51.

experiments indicate that the amplitude of this frequency decreases as the throttling increases. This observation fits the characteristics of the two Bode plots given by Figures 3 and 6.

Without any current theory explaining the observation of the mode at 477 Hz, our focus will be directed towards the low frequency behavior of the system. Doing so, we assume that the coupling dynamics are found closer to the slow dynamics frequency region. Utilizing air injection as a control input breaks up the flow structure at the blade level. The overall dynamics is given by the flow coefficient and pressure rise coefficient. These two measures seem to reside in the low frequency area of the data. Hence, a second filter is proposed to be used to prepare the collected data. In particular, a low pass filter with a cutoff frequency of 150 Hz is utilized. The filter employs 20 filter weights and a Kaiser window. In addition, the data is downsampled from 20 kHz to 400 Hz. The filtering and downsampling are used to ensure that the system

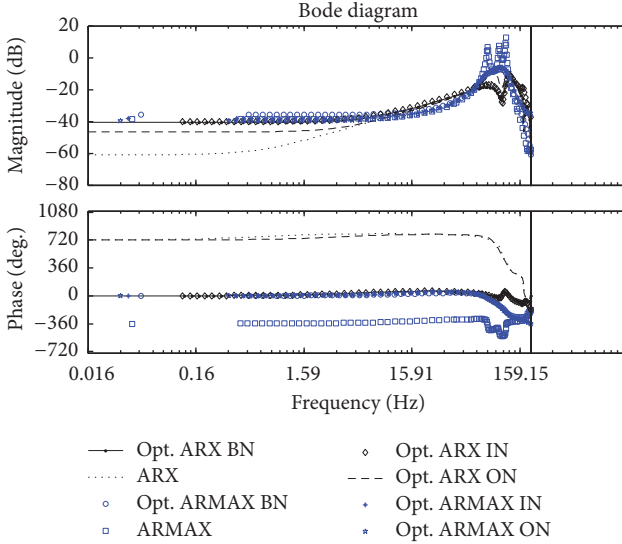


FIGURE 7: Bode plot for ARX (black) and ARMAX (blue) realization; flow coefficient = 0.58. Data is filtered and resampled prior to system identification.

identification and its optimization focus on frequencies below 150 Hz. The proposed optimal identification algorithm is employed to extract dynamic relationships between the input (injection) and the output (flow coefficient). For system identification, the data is also prepared by subtracting the dc offset; that is, the data has a zero mean. For the results, this implies that the output of the models expresses the change in flow coefficient, rather than the flow coefficient itself.

In the following, Bode plots of the various identified models are given, using the proposed filtering and resampling. Figure 7 depicts the models for a flow coefficient of 0.58 (far away from stall). From Figure 7, one can recognize two peak frequencies for the ARMAX model based systems. The first fundamental frequency is at 79.6 Hz; the second is at 114.6 Hz. For the ARX model based systems, the first fundamental frequency is at 81 Hz; the second is at 125.7 Hz. Figure 8 depicts the results for a flow coefficient of 0.55. The identification resulted in some unstable models for the ARMAX based systems; hence the results for these (blue lines) are disregarded for this flow coefficient. For the ARX based systems, the first fundamental frequency is found at 77.9 Hz, and the second at 122.5 Hz. Finally, Figure 9 depicts the outcome of the identification experiments for a flow coefficient of 0.51 (close to stall). For the ARMAX based models, the first fundamental frequency is found at 79.6 Hz and the second at 113 Hz. It is interesting to note that, for the ARX based models, three fundamental frequencies are found. In particular, for the ARX based models, the first fundamental frequency is found at 44.6 Hz, the second frequency at 81 Hz, and the third at 114 Hz. These values seem to be close to the rotor frequency and its harmonics. However, the rotor frequency and BPF are filtered out using notch filters. At a flow coefficient of 0.51, the simulated output from the identified model and the actual output (change of flow coefficient) are plotted in Figure 10.

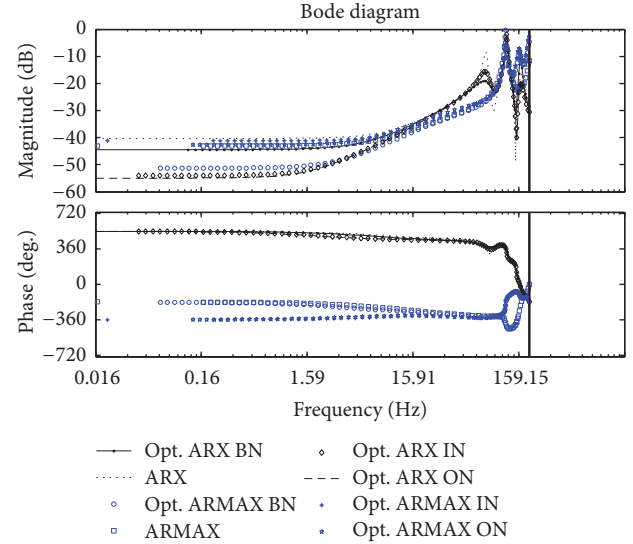


FIGURE 8: Bode plot for ARX (black) and ARMAX (blue) realization; flow coefficient = 0.55. Data is filtered and resampled prior to system identification.

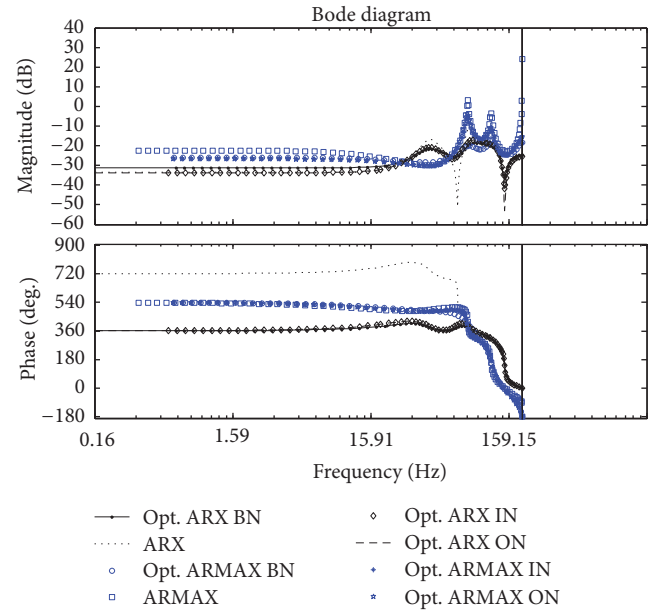


FIGURE 9: Bode plot for ARX (black) and ARMAX (blue) realization; flow coefficient = 0.51. Data is filtered and resampled prior to system identification.

A test to see if the extracted models can predict the output should provide indication if these frequencies are based on residuals of the rotor frequency or if they actually model the coupling dynamics between the injection and the pressure rise coefficient. Comparing Figures 10 and 11, the effect of the optimization is shown by the smoother output of the simulated model due to optimizing the singular values, and hence reducing the noise influence.

A similar observation can be made for the ARMAX models shown in Figures 12 and 13. Here, the ARMAX model

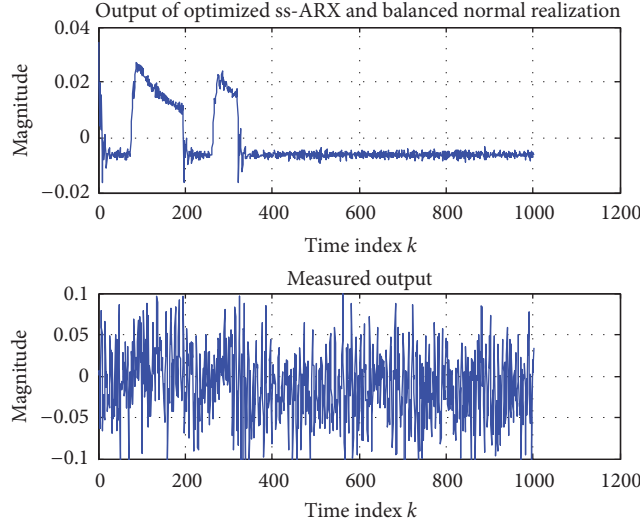


FIGURE 10: Simulated and measured output using optimized ARX (balanced realization) model at flow coefficient 0.51.

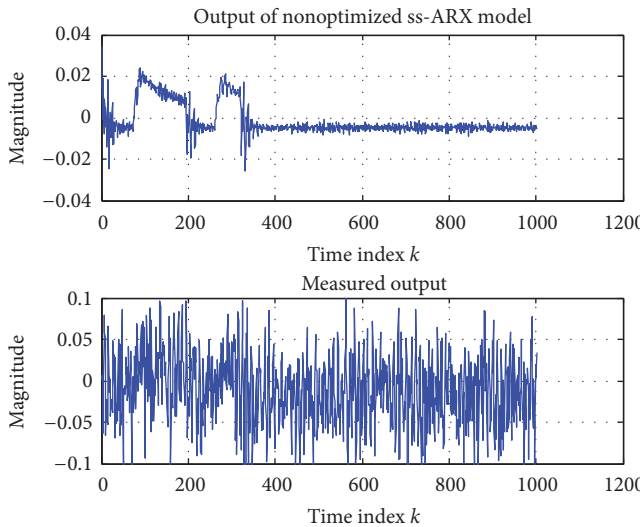


FIGURE 11: Simulated and measured output using no optimized ARX (balanced realization) model at flow coefficient 0.51.

using no optimization for the realization shows marginal stability properties (Figure 13). The performance of the ARMAX model is much improved and yields a stable system, shown in Figure 12. When overlaying the injection pressure measurements, as shown in Figure 14, the correlation between the injection pressure and the ARX model outputs is evident. The ARMAX model does capture this behavior too; however the output is inverted. Comparing the simulated output (Figure 10) with the injection pressure (Figure 14) one could conclude that the model picks up the input as a direct transmission term, representing the coupling in a static fashion. Noticing the scale of the simulated and measured response, the extracted dynamics is about half of the measured output in terms of magnitude. The optimization of the singular

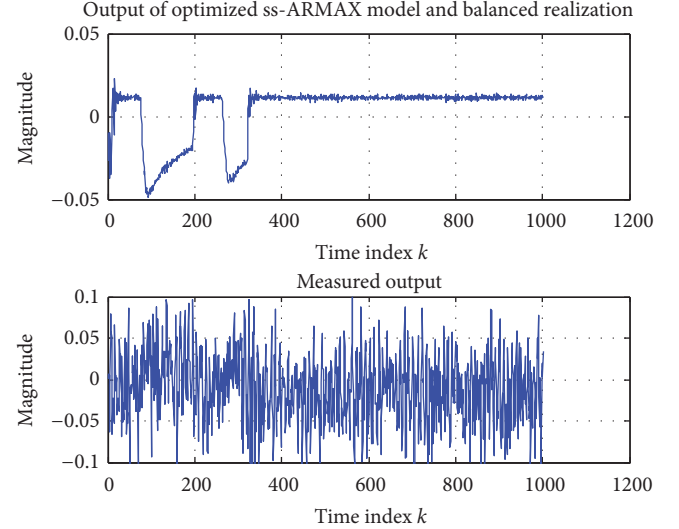


FIGURE 12: Simulated and measured output using optimized ARMAX (balanced realization) model at flow coef. 0.51.

values seems to improve the performance of the extracted models (i.e., more smooth and clean signals):

$$A = \begin{bmatrix} 0.2298 & -0.7303 & 0.0530 & 0.0037 & -0.0662 & 0.0807 \\ 0.7445 & 0.1449 & -0.1724 & -0.0107 & 0.0978 & -0.0975 \\ -0.0301 & -0.1426 & 0.3629 & 0.6134 & 0.2566 & -0.3255 \\ 0.0151 & 0.1066 & -0.3969 & 0.6055 & -0.2325 & 0.2749 \\ -0.0484 & -0.1086 & -0.3493 & -0.0472 & -0.7094 & -0.5789 \\ -0.0567 & -0.1118 & -0.4465 & -0.0500 & 0.5872 & 0.3185 \end{bmatrix}, \quad (44)$$

$$B = [0.1557 \quad -0.0893 \quad -0.1342 \quad 0.1043 \quad -0.0726 \quad -0.0549]^T,$$

$$C = [-0.1407 \quad -0.1113 \quad -0.1719 \quad -0.0065 \quad 0.0698 \quad -0.0553],$$

$$D = [0.0504].$$

The system given by the optimized ARX model (balanced realization) can be given in state-space form (see (1) and (2)) as shown above. Looking at the  $D$  term, the direct transmission term, the magnitude is comparable to the elements in the other state-space matrices. Hence the system is not static; that is, the output is a combination of the dynamic part (the  $A$ ,  $B$ , and  $C$  matrices) and the direct transmission matrix  $D$ .

The ARX/ARMAX model order is set to  $p_1 = 12$ . As these singular values are optimized using a TS algorithm, the magnitude of the cost function—as defined by (40)—is plotted versus the number of iterations. This is shown in Figure 15.

For the simulations, a total of 45 Markov parameters were used to construct the block Hankel matrix given in (20) and (30). The computation of the ARMAX model used  $n_1 = 2$ , and the TS algorithm is run for 200 iterations. A Tabu list and promising list of length 10 is used, that is, allowing 10 regions to be included in the intensification portion of the ETS algorithm, while keeping the last 10 steps of the search as forbidden moves.

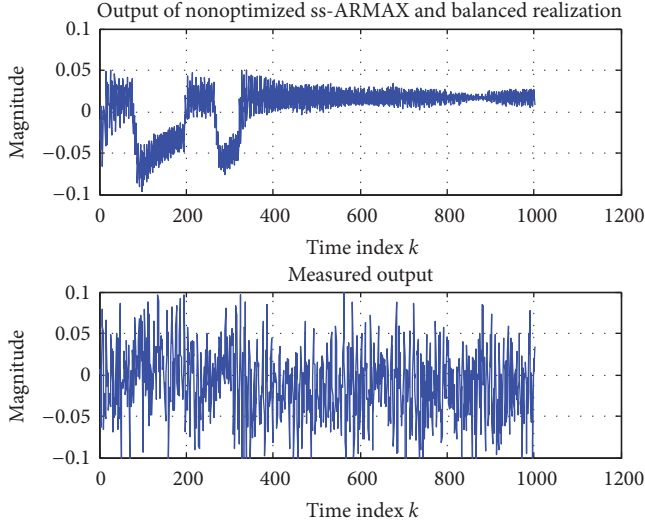


FIGURE 13: Simulated and measured output using (no optimized) ARMAX (balanced realization) model at flow coefficient 0.51.

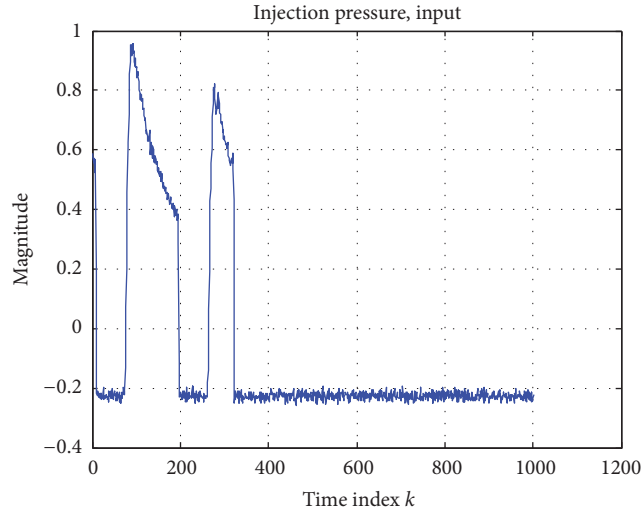


FIGURE 14: Injection pressure plot for flow coefficient 0.51, validation data.

**6.2. Identification Results for Throttle Movement and Overall Dynamics.** The proposed optimization embedded in the identification algorithm and the different cost functions are first tested using simulations. A simple second-order system with a natural frequency of 17 Hz is utilized. The simulations are carried out using different process and measurement noise levels. For each case, 20 simulations are used to statistically characterize and compare the performance of the proposed identification routines. The ETS algorithm uses 200 iterations for each simulation; the model order of the ARX and ARMAX models is  $p_1 = 15$ . For the construction of the Hankel matrix (30), 75 Markov parameters are used. The search area around the singular values is set to be  $\pm 10\%$  of the nominal value of the largest singular value. The computation of the residual sequence for the ARMAX model uses two steps; that is,  $h_{n_1} = 2$ . Table 2 lists the results of the simulation

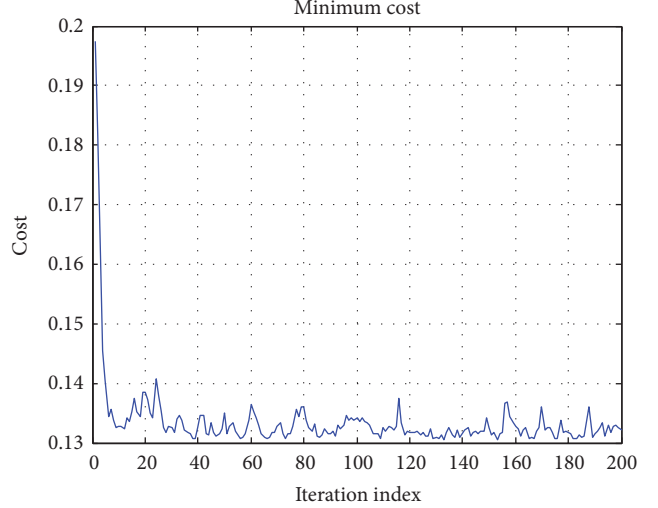


FIGURE 15: Cost during TS optimization.

using noise values of 1% and 5% standard deviation. For each approach, the nominal value (nom.), the optimized value using (40) (opt.), and (41) (opt.  $\omega$ ) are provided as the mean value and the standard deviation. For both cost functions, the weighting coefficient is set as  $\lambda_i = 2$ .

The error squared and correlation coefficients are computed based on 1000 validation data points. In Table 2, the two best performing algorithms' results are highlighted. It is evident from Table 2 that the error of the ARMAX model is greatly reduced using the proposed optimization. The results of the ARMAX model and ARX using prior knowledge of the natural frequency indicate having more consistent results based on their lower standard deviation values compared to the standard ARX model. Note also that the error and correlation incorporate the noise as part of the signal. Hence, using the methods which do not incorporate the knowledge of the natural frequency may be prone to model the noise by overfitting. Using a higher noise level, Table 3 presents the simulation results with 10% and 15% noise level.

From the inspection of these results, we conclude that the ARX and ARMAX based model identification with optimization either with or without prior knowledge of the natural frequency works sufficiently well for use of identifying the overall system dynamics of the compressor system. Considering the overall dynamics of the compressor system between the input (throttle movements) and the corresponding pressure rise coefficient, the proposed system identification algorithm with prior information of the natural frequency is used. The identified model fits well for the three different flow coefficients of 0.51, 0.55, and 0.58, indicating that the overall dynamics does not change noticeably during change of operating point. It is expected that this may change, as the operating point gets closer to stall. For the identification, the same parameters are used as given in the simulation section. The resulting natural frequency of the extracted model is 17.1 Hz using the ARMAX base model with optimum  $\omega$  and 16.8 Hz for the ARX base model with optimum  $\omega$ , that is, using (41).

TABLE 2: Simulation results with 1% and 5% noise std.

	Error squared	Correl. coef. [—]	Natural freq. [Hz]	Natural freq. error [%]
ARX-nom. 1%	1.5154	0.9338	<b>16.9958</b>	<b>0.0247</b>
Mean 5%	1.5159	0.9311	17.0211	<b>0.1241</b>
ARX-nom. 1%	0.0456	0.0078	0.0126	0.0388
Stand. dev. 5%	0.0428	0.0057	0.0993	0.3552
ARX-opt. 1%	<b>1.4606</b>	0.9337	16.5024	2.9272
Mean 5%	<b>1.4408</b>	<b>0.9383</b>	16.5826	2.4553
ARX-opt. 1%	0.0633	0.0073	0.4595	2.7031
Sta. Dev. 5%	0.0544	0.0058	0.4590	2.3990
ARX-opt $\omega$ 1%	1.4837	0.9321	16.9763	0.1394
Mean 5%	1.4828	0.9317	<b>16.9946</b>	<b>0.0317</b>
ARX-opt $\omega$ 1%	0.0369	0.0086	0.0909	0.3359
Stand. dev. 5%	0.0494	0.0051	0.0561	0.1756
ARMAX- 1%	23.4750	0.9200	17.1773	1.0429
nom. Mean 5%	36.4212	0.7272	15.1183	11.069
ARMAX- 1%	24.6217	0.0721	4.4278	12.1042
nom. Std. 5%	66.8224	0.3197	9.6057	26.5340
ARMAX- 1%	<b>1.4761</b>	<b>0.9359</b>	16.4052	3.4997
opt. Mean 5%	<b>1.4676</b>	<b>0.9364</b>	16.5794	2.4741
ARMAX- 1%	0.0710	0.0070	0.4461	2.6227
opt. Std. 5%	0.0580	0.0054	0.3955	2.1698
ARMAX- $\omega$ 1%	1.5249	<b>0.9343</b>	<b>16.9840</b>	<b>0.0941</b>
opt. Mean 5%	1.4866	0.9317	<b>17.0024</b>	<b>0.0141</b>
ARMAX- $\omega$ 1%	0.0607	0.0054	0.0445	0.1716
opt. Std. 5%	0.0619	0.0045	0.0952	0.3731

The identified model in discrete time is given in the Appendix. Comparing the results of the nonoptimum methods with the resulting identified model, the natural frequencies are well off the known frequency of 17 Hz. For example, the ARX based system identification yields a natural frequency of 2,191 Hz. The incorporation of the a priori information also helped the correlation of the estimated output to improve considerably compared to the nonoptimum identification method treated in this work.

**6.3. Identification Results for Injection and Blade Tip Flow Dynamics.** For the identification of the dynamics within the blade passage, sensors 2 to 7 are used to capture the resulting dynamics at the blade tip area. As the sensors measure the pressures at all times, the data does not correspond to a single blade passage (the compressor runs at 2400 rpm). A hall effect sensor is used to phase lock the data and computes the pressure distribution within the blade passage. A sample pressure distribution is given in Figure 16 for a flow coefficient of 0.58. The computation of the pressure distribution as shown in Figure 16 requires averaging signals over hundreds of rotations.

For the system identification of the dynamics within the blade passage, the phase locking approach will not provide

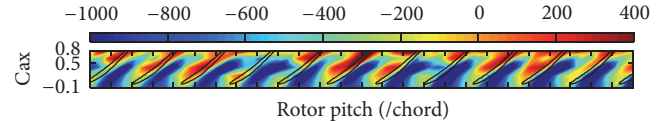


FIGURE 16: Pressure distribution within the blade passage for a section of the compressor. The units for the pressure are in [Pa], Cad is the axial tip chord, and the rotor pitch is a normalized parameter relative to blade chord.

sufficient information, as only approximately 2% of the data can be associated with one rotation of the blade passage. We assume that the measured data of one blade passage corresponds to the state of a set of blade passages at that time. This is not to say that all blade passages have the same flow distribution at a given time. We rather state that the condition of the flow is similar. By using this assumption, we propose to use an information based entropy measure for the state of the dynamics within the blade passage. Recent work utilizes the correlation coefficient between the pressure data of the blade passage and the pressure data corresponding to the same blade passage one revolution prior. The correlation coefficient is used to characterize the state of flow in a blade passage. The lower the correlation coefficient, the more unsteady the flow.

TABLE 3: Simulation results with 10% and 15% noise standard deviation.

	Error sqr.	Correlat. coef. [—]	Natural freq. [Hz]	Nat. freq. error [%]
ARX-nom. 10%	1.4850	<b>0.9351</b>	<b>17.0370</b>	<b>0.2176</b>
Mean 15%	1.5144	0.9306	17.1098	0.6459
ARX-nom. 10%	0.0780	0.0050	0.0937	0.3668
Stand. dev. 15%	0.1067	0.0066	0.2080	1.0023
ARX-opt. 10%	<b>1.4723</b>	0.9329	16.3853	3.6159
Mean 15%	<b>1.4866</b>	<b>0.9390</b>	16.3792	3.6518
ARX-opt. 10%	0.0568	0.0042	0.2628	1.5461
Sta. Dev. 15%	0.0782	0.0044	0.5484	3.1678
ARX-opt. $\omega$ 10%	1.5583	0.9313	16.9356	0.3788
Mean 15%	1.5069	0.9342	<b>16.9560</b>	<b>0.2588</b>
ARX-opt. $\omega$ 10%	0.0545	0.0063	0.0673	0.3596
Stand. dev. 15%	0.0814	0.0067	0.0687	0.2473
ARMAX- 10%	26.223	0.8083	11.9832	29.510
nom. Mean 15%	93.074	0.5015	24.5364	44.332
ARMAX- 10%	34.234	0.1483	8.9178	30.975
nom. Std. 15%	108.29	0.5021	26.108	137.97
ARMAX- 10%	<b>1.4847</b>	<b>0.9365</b>	16.6365	2.1382
opt. Mean 15%	<b>1.4377</b>	<b>0.9364</b>	16.4029	3.5123
ARMAX- 10%	0.0573	0.0070	0.4485	2.1277
opt. Std. 15%	0.0910	0.0071	0.3980	2.3409
ARMAX $\omega$ 10%	1.5181	0.9297	<b>17.0026</b>	<b>0.0153</b>
opt Mean 15%	1.5093	0.9320	<b>16.9523</b>	<b>0.2806</b>
ARMAX $\omega$ 10%	0.0884	0.0067	0.0898	0.3178
opt. Std. 15%	0.0555	0.0043	0.0671	0.2085

By using an entropy measure, there is no need to utilize data from over one rotation of the compressor. This entropy can be computed directly with the data present and hence has the same sampling frequency as the input. Therefore, we can associate the state of fluid flow with one characteristic number. The Shannon entropy is commonly used in information theory and measures the amount of information contained in a message. Here, one uses the entropy of a signal and classifies its predictability by a low entropy value and its randomness or amount of disorder by a large entropy value. The entropy is computed as

$$\zeta_y = - \sum_{i=1}^{k_b} \{p_i \times \log_2 (p_i)\}, \quad (45)$$

where  $k_b = 1 + \log(\phi_y)$  is the number of bins for the construction of the histogram,  $\phi_y$  is the set of data to be used for the computation, and  $p_i$  is the bin probability. An extension to the Shannon entropy is the spectral entropy, which can be

used to characterize the distribution of energy in a signal. The spectral entropy can be computed as

$$\zeta_\omega = - \sum_{f=-f_s/2}^{f=f_s/2} \text{PSD}_n(f) \log_2 \{\text{PSD}_n(f)\}, \quad (46)$$

where PSD is the Power Spectral Density,  $f$  is the frequency, and  $\text{PSD}_n(f) = \text{PSD}(f) / \sum_{f=-f_s/2}^{f=f_s/2} \text{PSD}(f)$  is the normalized PSD.

By assuming equivalent flow condition at a given time for a set of blade passages, we artificially increase the spectral entropy value, due to the variation of flow energy among different blade passages at a given time. The entropy can be assessed at each sensor location and hence provides a snapshot of the flow characteristics. This is shown schematically in Figures 17 and 18 which depict the computed spectral entropy of the leading sensor (Sensor 2) using (46). For the first part of the time history, no injection is used, while, for the second part, injection is used in some random fashion (on/off). In

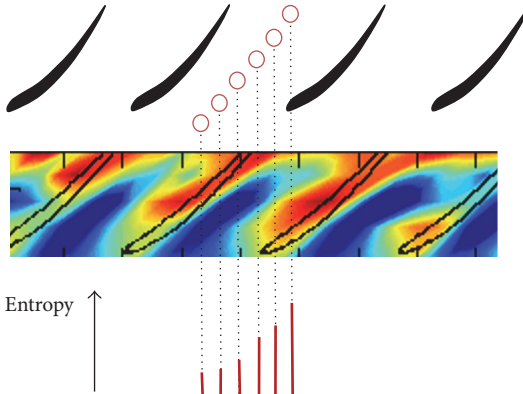


FIGURE 17: Entropy as description for current state of flow within a blade passage.

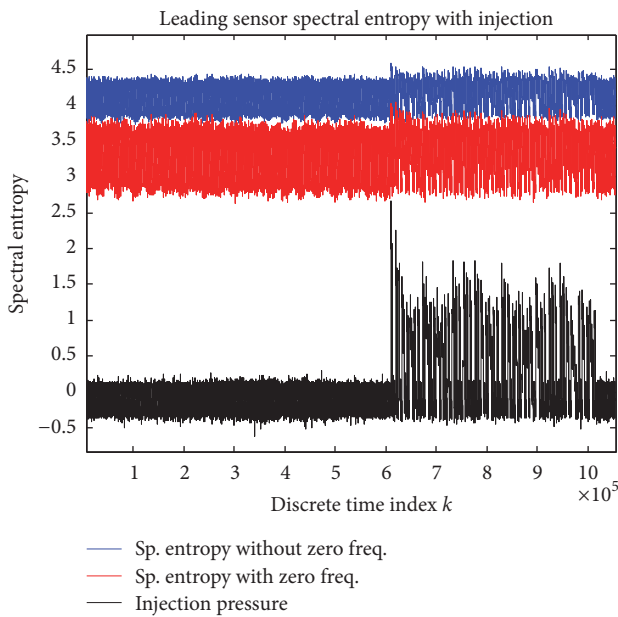


FIGURE 18: Spectral entropy for leading sensor. The first part of time series is without injection; second part is with injection.

information theory, often the zero frequency component of the spectral entropy is disregarded in order to measure a signal's true disorder. Figure 18 depicts the spectral entropy with (red) and without (blue) the zero frequency component. For the purpose of system identification, from this figure, we can safely assume that the inclusion of the zero frequency component has no effect on the inferred system dynamics. It should be noted that the disadvantage of using an entropy measure as the measured quantity—for characterizing the flow—is that it increases the computational cost compared to the correlation coefficient approach and hence is only useful for offline work.

Figure 19 shows the spatial distribution of the spectral entropy within a blade passage using the seven sensors as given in Figure 2. The entropy values are given for two cases, without air injection and with air injection, for three different

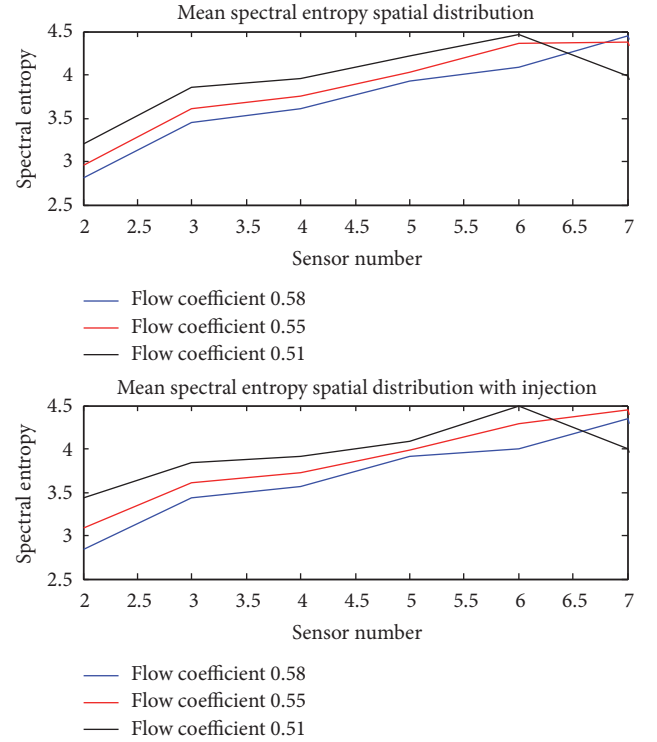


FIGURE 19: Spectral entropy spatial distribution within a blade passage with and without injection.

TABLE 4: Identification results for dynamics in blade passage.

	$\phi = 0.51$ [Hz]	$\phi = 0.55$ [Hz]	$\phi = 0.58$ [Hz]
ARX	52.4	90.4	101.6
ARX-optimum	54.3	90.4	116.5
ARMAX-optimum	54.4	90.4	116.7

flow coefficients. From Figure 19, it appears that the injection affects primarily the entry of the blade passage where the spectral entropy level is raised, primarily for a flow coefficient close to stall (flow coefficient = 0.51). There is little effect due to injection into the end of the blade passage for all other flow coefficients.

Utilizing the optimized identification approaches for the ERA with ARX and ARMAX base models, the identification results for the dynamics of the flow at the entry of the blade passage are reduced to the fundamental natural frequency and given in Table 4.

The identification utilized 45 Markov parameters to construct the Hankel matrix given in (30) resulting in state-space systems with three states, for each flow coefficient. The optimization parameters are the same as those given for the simulation work stated earlier. Considering the resulting natural frequencies of the extracted state-space models, it is evident that these frequencies greatly reduce in magnitude as they approach the stall limits. The stall frequency is between 40% and 50% of the rotating frequency ( $\sim 40$  Hz). As future work, the convergence to this stall frequency will be investigated.

## 7. Conclusions

In this work, we propose a system identification algorithm utilizing a TS based realization. The TS optimization along with the system identification algorithm is used to investigate two different model structures and their characteristics applied to an axial compressor system. In particular, three dynamical models are extracted which characterize input-output behavior at different levels of the compressor system. One of these models describes the relationship between air injection at the blade tip and the resulting overall compressor dynamics represented by the computed change in flow coefficient. Considering the presented results: injection at the tip of the leading edge of the compressor blade has an influence on the overall dynamics of the compressor. These types of coupling dynamics may be of interest in developing more efficient control schemes for compressor control. Such controllers can contribute to extending the stall margin improvement (SMI) and run axial compressors at higher efficiencies. Another model extracted using the proposed identification algorithm captures the dynamics between the throttle movement and the overall dynamics as measured by the change in the computed flow coefficient—using measured data points. The proposed identification scheme embeds prior knowledge of the compressor and therefore guides the identification to more accurate results. Finally, the proposed identification algorithm is used to infer a model relating the air injection—treated as an input—at the blade time to the resulting flow dynamics near the tip of the compressor blade. At this stage, such models relating the air injection to flow characterizations near the tip may help in gaining a better understanding of the effect from the air injection, its reach into the blade passage, and its potential stall dynamics at this location. The proposed identification scheme with an embedded TS optimization algorithm as presented in this work seems to be able to aid in developing any of the three models stated above.

## Appendix

Discrete time state-space model characterizing the dynamics between throttle movements and pressure rise coefficient changes is

$$A = \begin{bmatrix} 1.0204 & 0.0710 & 0.0371 \\ -0.0710 & 0.8479 & -0.1963 \\ 0.0371 & 0.1963 & 0.8667 \end{bmatrix},$$

$$B = \begin{bmatrix} 0.0839 \\ 0.1028 \\ -0.2311 \end{bmatrix}, \quad (A.1)$$

$$C = [-0.0839 \ 0.1028 \ 0.2311],$$

$$D = [-0.1259].$$

## Conflicts of Interest

The authors declare that they have no conflicts of interest.

## Acknowledgments

This research was supported by a generous grant from the National Science Foundation of China on Project no. 51306178.

## References

- [1] K. L. Suder, M. D. Hathaway, S. A. Thorp, A. J. Strazisar, and M. B. Bright, "Compressor stability enhancement using discrete tip injection," *Journal of Turbomachinery*, vol. 123, no. 1, pp. 14–23, 2001.
- [2] J. C. Li, F. Lin, Z. T. Tong, C. Q. Nie, and J. Y. Chen, "The dual mechanisms and implementations of stability enhancement with discrete tip injection in axial flow compressors," *Journal of Turbomachinery*, vol. 137, no. 3, Article ID 031010, 2015.
- [3] I. J. Day, "Active suppression of rotating stall and surge in axial compressors," *Journal of Turbomachinery*, vol. 115, no. 1, pp. 40–47, 1993.
- [4] J. Li, F. Lin, S. Wang, J. Du, C. Nie, and J. Chen, "Extensive experimental study of circumferential single groove in an axial flow compressor," in *Proceeding of the ASME Turbo Expo 2014: Turbine Technical Conference and Exposition, GT, 14*, Düsseldorf, Germany, June 2014.
- [5] T. Houghton and I. Day, "Enhancing the stability of subsonic compressors using casing grooves," in *Proceeding of the asme Turbo Expo*, pp. 39–48, Orlando, Fla, USA, June 2009.
- [6] T. Houghton and I. Day, "Stability enhancement by casing grooves: The importance of stall inception mechanism and solidity," in *ASME Turbo Expo 2010: Power for Land, Sea, and Air, GT, 10*, pp. 2383–2391, Glasgow, UK, June 2010.
- [7] J.-N. Juang and R. S. Pappa, "An eigensystem realization algorithm for modal parameter identification and model reduction," *Journal of Guidance, Control, and Dynamics*, vol. 8, no. 5, pp. 620–627, 1985.
- [8] M. P. Schoen, S. Chinvorarat, and C.-H. Kuo, "Eigensystem realization with modified genetic algorithm for system identification of noise corrupted processes," in *Proceeding of the asme International Mechanical Engineering Congress and Exposition, IMECE2006*, Chicago, Ill, USA, November 2006.
- [9] B. Ramkumar, M. P. Schoen, and F. Lin, "Hybrid enhanced continuous tabu search and genetic algorithm for parameter estimation in colored noise environments," *Expert Systems with Applications*, vol. 38, no. 4, pp. 3909–3917, 2011.
- [10] J.-N. Juang, C.-W. Chen, and M. Phan, "Estimation of Kalman filter gain from output residuals," *Journal of Guidance, Control, and Dynamics*, vol. 16, no. 5, pp. 903–908, 1993.
- [11] C.-H. Kuo, M. P. Schoen, S. Chinvorarat, and J.-K. Huang, "Closed-Loop System Identification by Residual Whitening," *Journal of Guidance, Control, and Dynamics*, vol. 23, no. 3, pp. 406–411, 2000.